

# Carnegie Mellon University

CARNEGIE INSTITUTE OF TECHNOLOGY

## THESIS

SUBMITTED IN PARTIAL FULFILLMENT OF THE REQUIREMENTS

FOR THE DEGREE OF **Doctor of Philosophy**

### TITLE

**CAPILLARY KINETICS BETWEEN MULTI ASPERITY SURFACES**

**PRESENTED BY EMRECAN SOYLEMEZ**

**ACCEPTED BY THE DEPARTMENT OF**

**MECHANICAL ENGINEERING**

\_\_\_\_\_  
ADVISOR, MAJOR PROFESSOR

\_\_\_\_\_  
DATE

\_\_\_\_\_  
DEPARTMENT HEAD

\_\_\_\_\_  
DATE

**APPROVED BY THE COLLEGE COUNCIL**

\_\_\_\_\_  
DEAN

\_\_\_\_\_  
DATE

# **CAPILLARY KINETICS BETWEEN MULTI ASPERITY SURFACES**

Submitted in partial fulfillment of the requirements for

the degree of

Doctor of Philosophy

in Mechanical Engineering

Emrecan Soylemez

B.S., Mechanical Engineering, Istanbul Technical University, 2007

M.S., Mechanical Engineering, Carnegie Mellon University, 2010

Carnegie Mellon University

Pittsburgh, Pennsylvania

December, 2014

© Emrecan Soylemez 2014  
All Rights Reserved



# ACKNOWLEDGEMENTS

I would like to thank my family (my mother Betul Soylemez, my father Selami Soylemez, and my sister Esra Soylemez). They loved and supported me throughout my entire life. They provided me anything I want for my education. Also, my father inspired and encouraged me for a graduate study.

My interest and incentive for capillary adhesion study has been triggered by my Ph.D. advisor Professor Maarten P. de Boer. I am grateful and thankful to him for his excellent guidance. His encouragement and appreciation to my work stimulated me to move forward in this project.

I also would like to thank my thesis committee members: Professor Maarten P. de Boer, Prof. Alan J. H. McGaughey, Prof. Craig Maloney, and Prof. Stephen Garoff for their help and advice for my study. I am also thankful to my M.S. advisor Professor Jack Beuth for his great lectures that built up my solid mechanics knowledge, and I appreciate his advising skills to help me understand how to do a research study. I would like to thank Professor W. Robert Ashurst for his help to build the experimental setup. I also want to thank Dr. Frank W. DelRio for sharing his expertise at multi-asperity adhesion experiments. I would like to thank Udom Sae-Ueng, Professor Alex Evilevitch, Dr. Tom A. Stewart, and Professor. May Nyman for their collaboration in my first year research project.

I would like to thank Emre Biyikli and Gunay Orbay for their help in my numerical modeling codes. I am also grateful to Ryan Pocratsky for his valuable suggestions and help when I need a quickly accessible second thought. I want to thank Christa Orvik, Robert Winkelman, and Sara Saheb Kash for their contribution to the Inteferometer User Guide. I would like to thank my research group members Dr. Sidharth S. Hazra, Dr. Vitali Brand, Mohamed Saleh, Ryan Pocratsky, Sameer Shroff, Ramesh Shrestha, Changho Oh, and Prince Singh for their help and friendship.

I am thankful to machine shop staff Ed Wojcichowski, Jim Dillinger, and John Fulmer for their master work at my custom experimental setup parts. I want to thank Chris Hertz,

Michael Scampone, Christine Lambrou, Melissa Hyzy, Ginny Barry and Bobbi Kostyak for their help and support on organizational related issues.

I would like to thank my friends Recep Onler, Bekir Bediz, Dr. Bulent Arda Gozen, Emrullah Korkmaz, Dr. Yigit Isbilioğlu, Batuhan Arisoy, Dr. Onur Ozcan, Korhan Sahin, Mehmet Ersin Yumer, Erdinc Tatar, Dr. Gunay Orbay, Melis Hazar, Tugce Yuksel, Onur Albayrak, Dr. Bilsay Sumer, Dr. Cagdas Onal, Arslan Ovezgylyjov, Jiawei Shi, Pengfei Li, Francisco Ramirez, Baoan Liu, Jason Fox, Jeremiah Mpagazehe, Iacopo Gentilini, Erva Ulu, Nurcan Gecer Ulu, Lina Gonzalez, Billy Epting, Mike Burkholder, Iryna Zenyuk, Seong Jin An, Siddharth Komini Babu, Arjun Kumar, Pratiti Mandal, Wee Liat Ong, Keith Regner, Shubhaditya Majumbar, Lili Ehrlich, Kevin Parrish, Ankit Jain, Sudanshu Nahata, Anirban Roy, Adam Sifounikas, Enes Calayir, Ekin Sumbul, Berkin Akin, Sercan Yildiz, Omer Ozdemir, Beril Cagla Cakir, Zahid Kisa, Ahmet Bakan and Hakan Gunaydin.

Finally, I gratefully acknowledge National Science Foundation funding through CMMI Grant # CMMI 1030322. Also, I acknowledge the Sandia National Laboratories through Award No. 1270979 for their contribution to the experimental setup. I also appreciate the technical staff in the Microelectronics Development Laboratory at Sandia National Labs in Albuquerque, NM, 87108 for fabricating the experimental samples.

# ABSTRACT

Capillary bridge formation between adjacent surfaces in humid environments is a ubiquitous phenomenon. Capillary forces are important in nature (granular materials, insect locomotion) and in technology (disk drives, adhesion). Although well studied in the equilibrium state, the dynamics of capillary formation merit further investigation. Here, we show that microcantilever crack healing experiments are a viable experimental technique for investigating the influence of capillary nucleation on crack healing between rough surfaces. To demonstrate the effects, a custom micromachine characterization system is built that allows for full environmental control (pressure, humidity, and gas composition) while retaining full micromachine characterization techniques (long working distance interferometry, electrical probe connectivity, actuation scripting capability). The system also includes an effective *in situ* surface plasma cleaning mechanism. The average spontaneous crack healing velocity,  $\bar{v}$ , between plasma-cleaned hydrophilic polycrystalline silicon surfaces of nanoscale roughness is measured. A plot of  $\bar{v}$  versus energy release rate,  $G$ , reveals log-linear behavior, while the slope  $|d[\log(\bar{v})]/dG|$  decreases with increasing relative humidity. An interface model that accounts for the nucleation time of water bridges by an activated process is developed to gain insight into the crack healing trends. This methodology enables us to gain insight into capillary bridge dynamics, with a goal of attaining a predictive capability for this important microelectromechanical systems (MEMS) reliability failure mechanism.

A variety of alcohol vapors significantly reduce or perhaps eliminate wear in sliding micro-machined contacts. However, these vapors may increase adhesion due to the capillary forces. Equilibrium adhesion energies at various partial pressures are found for *n*-pentanol (long chain molecule) and ethanol (short chain molecule). For low partial pressures ( $p/p_s=0.3$ ), adhesion energy of *n*-pentanol is even larger than water.

# TABLE OF CONTENTS

|   |      |
|---|------|
| ACKNOWLEDGEMENTS.....   | i    |
| ABSTRACT.....   | iii  |
| TABLE OF CONTENTS.....  | iv   |
| LIST OF TABLES.....   | viii |
| LIST OF FIGURES AND ILLUSTRATIONS.....  | ix   |
| NOMENCLATURE.....   | xix  |
| Chapter I: Introduction.....  | 1    |
| 1.1 MOTIVATION.....   | 1    |
| 1.2 THEORETICAL BACKGROUND.....   | 2    |
| 1.2.1 Single Asperity Contact Models.....   | 3    |
| 1.2.2 Capillary Forces.....   | 5    |
| 1.3 EXPERIMENTAL BACKGROUND.....  | 12   |
| 1.4 SINGLE ASPERITY CAPILLARY CONDENSATION KINETICS: REVIEW OF<br>THEORIES AND EXPERIMENTS.....                         | 18   |
| 1.4.1 1D Molecular Gas Diffusion Theory.....  | 18   |
| 1.4.2 Mass Transfer Theory Using Knudsen Diffusion.....   | 21   |
| 1.4.3 Experiments Measuring the Capillary Condensation Kinetics of Contacting Asperities<br>.....                       | 25   |
| 1.4.4 Theory Modification: Adsorption and Surface Flow Limit Meniscus Growth Rate ...                                   | 25   |
| 1.4.5 Theory for a Thermally Activated Gas-Liquid Phase Transition Between Non-<br>Contacting Surfaces.....             | 30   |
| 1.4.6 Experiments with Non-Contacting Surfaces - Exploring the Thermally Activated Gas-<br>Liquid Phase Transition..... | 33   |

|  |    |
|--|----|
| 1.5 SUMMARY .....  | 38 |
| 1.6 THESIS GOALS AND KEY RESULTS .....   | 39 |
| 1.7 CONTRIBUTIONS .....  | 41 |
| Chapter II: Probing MEMS in an Environmentally Controlled Chamber using Long Working<br>Distance Interferometry .....            | 43 |
| 2.1 INTRODUCTION .....   | 43 |
| 2.2 DESCRIPTION OF SYSTEM COMPONENTS .....   | 45 |
| 2.2.1 Main Chamber .....   | 45 |
| 2.2.2 Load-Lock Chamber .....  | 47 |
| 2.2.3 Environmental Control.....   | 50 |
| 2.2.4 Optical Detection System .....   | 52 |
| 2.3 PRELIMINARY RESULTS.....   | 54 |
| 2.3.1 System Qualification.....  | 54 |
| 2.3.2 Crack Healing Experiment.....  | 56 |
| 2.4 CONCLUDING REMARKS.....  | 60 |
| Chapter III: Experiments of Water, <i>n</i> -Pentanol, and Ethanol Capillary Bridge Kinetics at Multi<br>Asperity Surfaces ..... | 61 |
| 3.1 INTRODUCTION .....   | 61 |
| 3.2 WATER EXPERIMENTS.....   | 62 |
| 3.3 DISCUSSION.....  | 69 |
| 3.4 ALCOHOL EXPERIMENTS.....   | 72 |
| 3.5 COMPARISON OF EQUILIBRIUM ADHESION VALUES OF WATER, <i>n</i> -<br>PENTANOL, AND ETHANOL.....                                 | 78 |
| 3.5.1 Surface Roughness Effect .....   | 80 |
| 3.5.2 Kelvin Radius and Surface Tension Effects .....  | 83 |
| 3.6 CHAPTER SUMMARY.....   | 85 |

|   |     |
|---|-----|
| Chapter IV: First Order Model of the Crack Healing at Various Partial Pressures .....                           | 86  |
| 4.1 SURFACE ROUGHNESS CHARACTERIZATION .....  | 86  |
| 4.2 MODEL DESCRIPTION .....   | 88  |
| 4.3 MODEL IMPLEMENTATION.....   | 90  |
| 4.4 MODEL RESULTS .....   | 93  |
| 4.5 CHAPTER SUMMARY.....  | 94  |
| Chapter V: Modeling of Crack Healing at Various Partial Pressures Between the Rough<br>Nanoscale Surfaces ..... | 96  |
| 5.1 INTRODUCTION .....  | 96  |
| 5.2 SURFACE TOPOGRAPHY MAPS AND INTERFACIAL PARAMETERS .....  | 97  |
| 5.3 CONSTITUTIVE LAWS FOR DRY CONDITIONS.....   | 99  |
| 5.4 PARALLEL PLATE MODEL .....  | 107 |
| 5.4.1 Parallel Plate Model Description .....  | 107 |
| 5.4.2 Parallel Plate Model Results for Dry conditions.....  | 109 |
| 5.5 S-SHAPED BEAM MODEL.....  | 111 |
| 5.5.1 S-shaped Beam Model Description .....   | 111 |
| 5.5.2 S-shaped Model Results.....   | 115 |
| 5.6 WET CONDITIONS – CRACK HEALING BEAM MODEL .....   | 119 |
| 5.7 CRACK HEALING MODEL RESULTS .....   | 121 |
| 5.8 CHAPTER SUMMARY.....  | 127 |
| Chapter VI: Summary and Suggestions for Future Work.....  | 128 |
| BIBLIOGRAPHY.....   | 130 |
| APPENDICES .....  | 142 |
| Appendix A.....   | 143 |
| Appendix B.....   | 165 |

|                  |     |
|------------------|-----|
| Appendix C ..... | 169 |
| Appendix D ..... | 171 |
| Appendix E ..... | 174 |
| Appendix F.....  | 177 |

# LIST OF TABLES

|  |     |
|--|-----|
| <b>Table 2.1:</b> Experiments performed.....                                   | 58  |
| <b>Table 5.1:</b> Summary of model results for dry conditions.....             | 110 |
| <b>Table A1:</b> Compensating plate selection to eliminate the bull’s eye..... | 151 |
| <b>Table B1:</b> Components list.....  | 153 |

# LIST OF FIGURES AND ILLUSTRATIONS

**Figure 1.1:** Sphere vs flat surface contact geometry.  $R$  is the radius of sphere,  $F_{ext}$  is the externally applied force, and  $a$  is the contact radius.....3

**Figure 1.2:** Force curves as a function of displacement are plotted for three models. Hertz, JKR and DMT model curves are plotted with black, red and blue lines, respectively.....5

**Figure 1.3:** Definition of principal radii of curvature ( $r_a$  and  $r_m$ ) for a saddle-shaped meniscus...6

**Figure 1.4:** Liquid film thickness in equilibrium with a spherical shaped meniscus.  $R$ =meniscus curvature radius (m), and  $h_f$ =liquid film thickness (m).....9

**Figure 1.5:** Comparison of the equation 1.15 and 1.28 as a function of  $H$ . Dashed black line is calculated according to equation 1.15 and solid black and blue line are calculated according to equation 1.28. Liquid film thickness is 0.1 nm for the blue line and 1 nm for the solid black line.....12

**Figure 1.6:** Schematic diagram of surface force apparatus (SFA).....15

**Figure 1.7:** Typical force versus piezo position curve.....16

**Figure 1.8:** Schematic cross-section of adhered microcantilever configured in the  $S$  shape.....17

**Figure 1.9:** Schematic cross section of the surfaces in the equivalent sphere-on-a-flat-surface configuration in adhesive contact with a condensed annulus.  $A = 2\pi x[R \cos\phi - (R^2 - x^2)^{1/2}]$  and  $V \approx 4\pi Rr^2$  [73].....19

**Figure 1.10:** Comparisons of different diffusion theory calculations. The trends show the predicted meniscus radius dependence on time assuming an asperity radius  $R=2$  cm. Solid blue line is calculated by equation 1.34, solid red line is calculated by equation 1.40 by using Knudsen diffusion coefficient, solid black line is calculated by equation 1.40 by using bulk diffusion coefficient, solid green line is calculated by equation 1.37, Rabinovich data shown as green circles are reproduced from Fig. 11 in ref [74], and Kohonen data shown as blue triangles are reproduced from Fig. 3 in ref [73].....23

**Figure 1.11:** Kohonen calculations (equation 1.34) are shown with blue line, Sirghi calculations (equation 1.40) for bulk diffusion are shown with black line, and red line represents Knudsen diffusion approach (equation 1.40). Here  $R= 250$  nm and  $RH=50\%$ .....24

**Figure 1.12:** Comparisons of the derivative of Kohonen and Rabinovich methods. Dashed orange line is the equation 1.34 curve.....24

**Figure 1.13:** Schematic of the capillary water meniscus at the contact between completed wetting surfaces of AFM tip and sample [37].....28

**Figure 1.14:** Schematic of the liquid droplet on a flat solid surface. At equilibrium three interfacial surface tensions are counterbalanced.....30

**Figure 1.15:** The critical nucleus for capillary condensation in three dimensions.  $R^*$  represents the lateral extension of the critical nucleus. The total curvature of the meniscus is equal to  $2/H_c$  [77].....32

**Figure 1.16:** Free energy barrier as a function of the normalized width of the pore,  $H/H_c$ .....32

**Figure 1.17:** The steps of the evaporation experiment. Left row shows the schematic of the capillary condensate. Middle left row FECO images of adjacent odd-order and even-order fringes of the experiment steps. Middle right row is schematics of even-order fringes only, which give the refractive index profile  $n(x)$ . Right row shows the refractive index profiles  $n(x)$  [61]...34

**Figure 1.18:** Capillary bridges in the contact area between the AFM tip and the sample [79]...35

**Figure 1.19:** **a)** Friction force as a function of  $\log v$  for four different temperatures.  $v_c$  points out the critical velocity where the capillary forces are effective. **b)**  $\ln \tau$  as a function of  $1/T$ . The experimental data (scattered circles) are fitted (solid line) with the Arrhenius law [Eq. (1.62)]. A correlation coefficient of 0.997 is obtained [57].....36

**Figure 2.1:** A computer-aided design (CAD) rendering of the Environmental Interferometer Microprobe Station.....46

**Figure 2.2:** **(a)** Optical image of the Environmental Interferometer Microprobe Station. **(b)** Optical close-up of area imaged inside the main chamber, including electrical probes that allow in-situ actuation of micromachined devices. **(c)** Interferogram of initially freestanding microcantilevers adhered by capillary forces with  $p/p_{\text{sat}} \approx 1$ .....47

**Figure 2.3:** **(a)** Load-lock chamber interior indicating sample holder, plasma electrode Ti meshes and platen fork for transferring samples. (white boroelectric heater is below the sample holder) **(b)** View of glowing plasma inside the load-lock chamber through viewport. **(c)** RF plasma generator box with parameters displayed.....49

**Figure 2.4:** Atmospheric pressure vapor delivery system schematic. Arrows on the various lines show the direction of normal  $N_2$  carrier gas flow.....51

**Figure 2.5:** **(a)** Deflection of a silicon wafer over a 500 mm length. For this single linescan, the root mean square (RMS) error per pixel from a linear fit is 1.2 nm. **(b)** RMS error versus linescan number for 100 linescans taken at 8 s intervals.....53

**Figure 2.6:** Measured RH and temperature values of the entry and exit lines. Entry lines data are solid and exit lines data are dotted. RH data is shown on the left y axis in blue color, and temperature data is shown at the right y axis in red color.....55

**Figure 2.7:** Measured RH and temperature values of the entry and exit lines from the high temperature experiments. Entry lines data are solid and exit lines are dotted. RH data is shown on the left y axis in blue color, and temperature data is shown at the right y axis in red color. **a)** Rh starts at 30%. Then it increases and stays for some time at 60%,70%, and 80% RH, sequentially. **b)** This experiment shows 60% RH is stable during 300 min.....56

**Figure 2.8:** Interferograms of crack length  $s$  vs. time at 61% RH ( $p/p_s$ ) for sample 3. **a)** At 0<sup>th</sup> min. **b)** At 25<sup>th</sup> min. **c)** At 100<sup>th</sup> min.....58

**Figure 2.9:** Sample 1 RH and adhesion data over time. Solid lines represent RH data at the chamber entrance (blue) and exit (red), and dashed lines represent adhesion data for different individual microcantilevers.....59

**Figure 2.10:** Sample 2 RH and adhesion data over time. Solid lines represent RH data at the chamber entrance (blue) and exit (red), and dashed lines represent adhesion data for different individual microcantilevers.....59

**Figure 2.11:** Sample 3 RH and adhesion data over time. Solid lines represent RH data at the chamber entrance (blue) and exit (red), and dashed lines represent adhesion data for different individual microcantilevers.....59

**Figure 2.12:** Sample 3 RH and adhesion data over time. Solid lines represent RH data at the chamber entrance (blue) and exit (red), and dashed lines represent adhesion data for different individual microcantilevers.....59

**Figure 3.1:** Cross-section schematic geometry of the microcantilever (a) standing freely and (b) in the  $S$  shape. Interferograms (c) of Cantilevers 5-14 at 29% RH (no crack healing) and (d)-(f) after increasing exposure to humid conditions.....64

**Figure 3.2:** RH and crack length data over time. The solid blue lines indicate RH, while the dashed lines represent crack length data for different individual microcantilevers. The vertical solid black line represents onset of steady state RH. (a) Crack healing data of Cantilever 9 (blue squares) and Cantilever 10 (orange triangle markers) when RH is increased to 60.5% RH from 29% RH. (b) Crack healing data of Cantilever 10 (orange triangles) and Cantilever 14 (red crosses) when the 60.5% RH is increased to 87.5% RH.....66

**Figure 3.3:** Crack healing data over time. The solid lines indicate RH at the chamber entry, while dashed lines represent energy release rate  $G$  data for different individual microcantilevers. Data for  $G$  after increasing RH (a) from 29 to 60.5%. (b) from 60.5 to 87.5%.....67

**Figure 3.4:** Average crack healing velocity  $\bar{v}$  as a function of energy release rate  $G$ . Different cantilever responses are plotted with different color and marker types for 60.5% and 87.5% RH cases. Solid lines are semi-empirical fit.....69

**Figure 3.5:** (a) Idealized crack tip region schematic to help visualize the effect of roughness. (b) The crack tip region is further simplified so that all suspended asperities in the HPZ nucleate at the same time due to the roughness.....71

**Figure 3.6:** Crack healing data over time. Colored lines represent energy release rate  $G$  data for different individual microcantilevers. Data for  $G$  after increasing  $p/p_s$  (a) from 0 to 0.3. (b) from 0.3 to 0.5. (c) from 0.5 to 0.6. (d) from 0.6 to 0.8. (d) from 0.8 to 0.9. (d) from 0.9 to 0.95.....75

**Figure 3.7:** Average crack healing velocity  $\bar{v}$  as a function of energy release rate  $G$ . Different cantilever responses are plotted with different color and marker types. (a) for  $p/p_s=0.3$  case. (b) for  $p/p_s=0.5$  case. (c) for  $p/p_s=0.8$  case. (d) for  $p/p_s=0.9$  case. (e) for  $p/p_s=0.95$  case. It is again seen that  $|d[\log(\bar{v})]/dG|$  decreases as  $p/p_s$  increases.....77

**Figure 3.8:** Crack healing data over time. Colored lines represent energy release rate  $G$  data for different individual microcantilevers. Data for  $G$  after increasing  $p/p_s$  (a) from 0 to 0.9. (b) from 0.9 to 0.95.....78

**Figure 3.9:** Average crack healing velocity  $\bar{v}$  as a function of energy release rate  $G$ . Different cantilever responses are plotted with different color and marker types. (a) for  $p/p_s=0.9$  case. (b) for  $p/p_s=0.95$  case.....78

**Figure 3.10:** Adhesion energy at equilibrium vs partial pressure data. Water,  $n$ -pentanol and ethanol were represented by marks with blue circle, black square and red triangle, respectively.....79

**Figure 3.11:** AFM images of the lower counterfaces over  $5 \times 5 \mu\text{m}^2$ . **a&d)** 3D&2D of the topography for the sample of the water experiment. **b&e)** 3D&2D illustration of the topography for the sample of the  $n$ -pentanol experiment. **c&f)** 3D&2D illustration of the topography for the sample of the ethanol experiment.....81

**Figure 3.12:** AFM images of the upper counterfaces over  $5 \times 5 \mu\text{m}^2$ . **a&d)** 3D&2D of the topography for the sample of the water experiment. **b&e)** 3D&2D illustration of the topography for the sample of the  $n$ -pentanol experiment. **c&f)** 3D&2D illustration of the topography for the sample of the ethanol experiment.....82

**Figure 3.13:** AFM image of the upper counterface of ethanol experiment's sample over  $2 \times 2 \mu\text{m}^2$ . Red circles indicate the possible SiC particles.....83

**Figure 3.14:** Comparison of the water and  $n$ -pentanol force values (equation 1.15) as a function of  $H$ . Blue line represents water, and black line represents  $n$ -pentanol.  $R=62 \text{ nm}$  and  $p/p_s=0.6$ .....84

**Figure 4.1:** AFM images of polysilicon surface of sample 1. **a)**  $5 \mu\text{m}^2$  surface area **b)**  $1 \mu\text{m}^2$  surface area **c)** Cross sectional image along the black line shown in (b).....87

**Figure 4.2:** Array of uniform asperities with areal density  $n_{asp}=1/(8Rz_{max})$  contacting a plane, with liquid bridges of radius  $r_K$  providing adhesive energy [68].  $z_{max}$  is the largest separation between the substrate and the rough surface.  $l_{asp}$  is the asperity spacing along the length.....88

**Figure 4.3:** Illustration of crack healing with uniformly distributed asperities of equal height. (a) At low RH, the crack tip region is illustrated in equilibrium. (b) When RH is increased, capillaries at Asperities 1 and 2 grow, but induce only a small beam deflection. (c) Asperities 3 to 5 are nucleated sequentially, but Asperity 1 does not yet make contact. (d) The capillary force at each asperity brings the beam closer to the substrate. The resulting deflection due to the forces at Asperities 1-5 cause Asperity 1 to make contact.....90

**Figure 4.4:** Force-displacement curve according to Eq. (1.15) with  $R=62 \text{ nm}$  and  $\text{RH}=60.5\%$ . At  $H=2r_K$ , no capillary bridge can form. With decreasing  $H$  (A→B), a liquid capillary bridge nucleates after time  $\tau$  determined by equation 1.59 (B→C). This will exert force on the microcantilever, causing capillary growth, further increasing the force (D). As other capillaries nucleate, point D will move further up the curve. The maximum capillary force between two surfaces occurs at contact (E).....92

**Figure 4.5:** Numerical model results. The average velocity  $\bar{v}$  for the cases of  $\text{RH}=60.5\%$  and  $87.5\%$ , and pitch=75, 125 and 250 nm are calculated. Shaded rectangular areas indicate the experimental adhesion and time realms, and the solid line within indicates the approximate experimental trend.....94

**Figure 5.1:** Topography of the sample that has been used at the experiment. **a&c)** 3D&2D AFM images of the lower counterface over  $1 \times 1 \mu\text{m}^2$ . **b&d)** 3D&2D AFM images of the upper counterfaces over  $1 \times 1 \mu\text{m}^2$ .....98

**Figure 5.2:** Schematic of a deformable elastic sphere and a rigid flat surface.  $z_0$  is the interatomic distance. **(a)** Non-contacting illustration  $H \geq z_0$ , **(b)** contacting  $H < z_0$ .....100

**Figure 5.3:** Schematic of a deformable elastic sphere and a rigid flat surface.  $z_0$  is the interatomic distance,  $\delta_t$  is the range of the constant attractive region for MD model. **(a)** Non-contacting illustration  $h_0 > 0$ , **(b)** contacting  $h_0 < 0$ .....103

**Figure 5.4:** Blue dashed lines are the curves for adhesive force versus  $\omega$  for the **(a)** DMT, **(b)** MD and **(c)** MMD models. Red dotted lines are the repulsive forces due to Hertzian contact. Black solid lines are the sum of the attractive and repulsive forces. **(d)** shows the total force applied for each model.....106

**Figure 5.5:** Parallel plate schematic. The plates are rigid bodies, while the spheres, distributed at different heights with constant radius, are elastic. Dimension  $\bar{H}$  is the average surface separation.....108

**Figure 5.6:** Force-average separation curve for a parallel plate model with different asperity normal height distribution. Blue line represents the results with no cut-off, and red line represents for the same distribution with  $2\sigma$  cut-off.....109

**Figure 5.7:** S-Shape beam model schematic with directions indicated. **a)** Slice of the S-Shape model in the longitudinal direction. **b)** Cross section schematic of A-A'.....112

**Figure 5.8:** S-Shape beam model simulated surface topography with a cutoff at  $2.6\sigma$ ,  $\sigma=2.1$  nm. **a)** 3D view of the asperity distribution. **b)** Front view of the asperity distributions. Right end is near the crack tip.  $\bar{H}_{eq}$  sets the gap at the right end between the flat surface and the average height of the asperities. Red line represents the plane of the  $z_0$  distance where the repulsive forces start to apply when the asperities contact.....113

**Figure 5.9:** Free-body diagram for an s-shaped beam. The force and moment are provided by the support post on the left-hand side. On the right-hand side, the moment and the reaction force occur at the crack tip.....114

**Figure 5.10:** Illustration of the crack healing at the model. Black line represents the initial deflection  $w_i$ , and red line represents the final cantilever shape  $w_f$ .....115

**Figure 5.11:** Illustration of the asperity column shifting to simulate different distributions.....116

**Figure 5.12:** S-Shape Beam model crack healing result with  $2\sigma$  cutoff ( $\sigma =7.40$  nm) (using DMT model). 50 different asperity distributions have been simulated.....117

**Figure 5.13:** Cantilever deflection shapes are shown according to Figure 5.11 data. **a)** Cantilever shape after healing occurs, **b)** cantilever shape without healing event. Black dashed line is the axis showing the  $\bar{H}_{eq}$  level.....118

**Figure 5.14:** S-Shape Beam model crack healing results with  $1.9\sigma$  cutoff ( $\sigma =17.5$  nm) (using DMT model). 50 different asperity distributions have been simulated.....118

**Figure 5.15:** Schematic of an elastic sphere and a rigid flat surface.  $z_0$  is the intermolecular separation,  $H_c$  is the range of the constant Laplace pressure. (a) Non-contacting illustration  $\omega>0$ , (b) contacting  $\omega < 0$ .....120

**Figure 5.16:** Crack healing model results at RH=60.5%. Average velocity calculations are based on equation 5.30. Markers show the results for fifty different shifted distributions of the asperities. Gray shaded area represents the experimental trend.....122

**Figure 5.17:** Schematic of a capillary bridge with adsorbed liquid film between an elastic sphere and a rigid flat surface.  $z_0$  is the intermolecular separation,  $H_c$  is the range of the constant Laplace pressure.  $H = \omega - z_0$ .....123

**Figure 5.18:** Crack healing model results at RH=60.5% with  $h_f = 1$  nm. Average velocity calculations are based on equation 5.30. Markers show the results for fifty different shifted distributions of the asperities. Gray shaded area represents the experimental trend.....123

**Figure 5.19:** Crack healing model results at RH=60.5% with  $h_f = 0.5$  nm. Average velocity calculations are based on equation 5.30. Markers show the results for fifty different shifted distributions of the asperities. Gray shaded area represents the experimental trend.....124

**Figure 5.20:** Energy barrier and nucleation time curves at 60.5% RH level in the range of 0 to  $H_c$ . **a)** Energy barrier vs gap is plotted with blue and red lines by equation 5.26 and 5.29, respectively. **b)** Nucleation time vs gap is plotted with blue and red lines by equation 5.27 and 5.30, respectively.....125

**Figure 5.21:** Crack healing model results at RH=60.5% with  $h_f = 0.5$  nm. Average velocity calculations are based on equation 5.30. Markers show the results for fifty different shifted distributions of the asperities. Gray shaded area represents the experimental trend.....126

**Figure 5.22:** Energy barrier and nucleation time curves at 87.5% RH level in the range of 0 to  $H_c$ . **a)** Energy barrier vs gap is plotted with blue and red lines by equation 5.26 and 5.29, respectively. **b)** Nucleation time vs gap is plotted with blue and red lines by equation 5.27 and 5.30, respectively.....126

**Figure 5.23:** Crack healing model results at RH=87.5% with  $h_f = 0.5$  nm. Average velocity calculations are based on equation 5.30. Markers show the results for fifty different shifted distributions of the asperities. Gray shaded area represents the experimental trend.....127

**Figure A1:** Schematic layout of the interference microscope.....132

**Figure A2:** Picture of the DC power supply.....132

**Figure A3:** “TalkToLED.bat” shortcut symbol.....133

**Figure A4:** Command window for LED brightness.....133

|  |     |
|--|-----|
| <b>Figure A5:</b> NIMAX shortcut symbol.....   | 134 |
| <b>Figure A6:</b> Screenshot of the “PCI-6733 (Device 1)” in the menu.....   | 134 |
| <b>Figure A7:</b> Alignment tools. (a) two small paper circles (1.5” and 1” in diameter) each with a small pinhole in its center. (b) a bull’s eye level. (c) a set of Allen wrenches..... | 135 |
| <b>Figure A8:</b> Interferometer microscope right hand side picture.....   | 136 |
| <b>Figure A9:</b> Interferometer microscope right hand side picture.....   | 137 |
| <b>Figure A10:</b> Interferometer microscope right hand side picture.....  | 138 |
| <b>Figure A11:</b> Interferometer microscope center picture.....   | 139 |
| <b>Figure A12:</b> Interferometer microscope center picture.....   | 140 |
| <b>Figure A13:</b> Interferometer microscope center picture.....   | 141 |
| <b>Figure A14:</b> Interferometer microscope center picture.....   | 142 |
| <b>Figure A15:</b> Shortcut symbol of 1394Camera Demo.....   | 142 |
| <b>Figure A16:</b> Grabbed image.....  | 143 |
| <b>Figure A17:</b> Shortcut of ESP-util.....   | 143 |
| <b>Figure A18:</b> ESP-util menu.....  | 144 |
| <b>Figure A19:</b> ESP-util pop up window.....   | 144 |
| <b>Figure A20:</b> ESP-util controlling is enable for three channels.....  | 144 |
| <b>Figure A21:</b> Symbol of Jog.....  | 145 |
| <b>Figure A22:</b> Jog window.....   | 145 |
| <b>Figure A23:</b> Reference side picture of the interferometer.....   | 147 |
| <b>Figure A24:</b> Reference side picture of the interferometer.....   | 149 |
| <b>Figure A25:</b> Bull’s eye patterned fringes.....   | 149 |
| <b>Figure A26:</b> Compensating plates.....  | 150 |
| <b>Figure A27:</b> Compensating plate locations.....   | 150 |

|   |     |
|---|-----|
| <b>Figure A28:</b> WinLens3D screenshot for a specific schematic.....   | 151 |
| <b>Figure A29:</b> Image of replaced LED Light Source.....  | 152 |
| <b>Figure B1:</b> Picture of the contact angle goniometer set up.....   | 154 |
| <b>Figure B2:</b> CAM 100 window. Red line is aligned with the substrate.....   | 155 |
| <b>Figure B3:</b> CAM 100 window. Blue rectangular is aligned according to the droplet.....   | 155 |
| <b>Figure B4:</b> CAM 100 window. Calculated contact angles: left CA=53.43, right CA=47.95 and mean CA=50.69.....   | 156 |
| <b>Figure D1:</b> Flow line schematic after chilled mirror hygrometer adaptation.....   | 160 |
| <b>Figure D2:</b> a) Sensor box image. b) Image of the sensor box interior.....   | 160 |
| <b>Figure E1:</b> Free-body diagram for an <i>s</i> -shaped beam. The force and moment are provided by the support post on the left-hand side. On the right-hand side, the moment and the reaction force occur at the crack tip.....  | 162 |
| <b>Figure S1.</b> Crack length <i>s</i> versus time on five different cantilevers taken at 5 s intervals after increasing RH from 0 to 62%. The solid line indicates RH at the chamber entry, while dashed lines represent crack length <i>s</i> data for different individual microcantilevers. In this particular experimental trial, the exit line reached steady state at 27 min (not shown), and the environment temperature was 21°C, which is 3°C less than the conditions for the 1 min resolution experiments shown in the main text. These differences may explain the longer period before crack healing begins. In any case, the crack healing velocity is only calculated after previous healing had already been observed, as explained in the main text. The plot clearly shows that crack healing occurs in discrete steps..... | 165 |
| <b>Figure S2.</b> Crack length <i>s</i> versus time on five different cantilevers taken at 10 s intervals after increasing RH from 69 to 89.5%. The solid line indicates RH at the chamber entry, while dashed lines represent crack length <i>s</i> data for different individual microcantilevers. The plot again shows that crack healing occurs in discrete steps.....  | 166 |
| <b>Figure S3.</b> Average crack healing velocity $\bar{v}$ as a function of energy release rate <i>G</i> . Different cantilever responses are plotted with colors and marker types corresponding to Figure S1. In this case, a non-zero $\bar{v}$ extends out nearly to $G=4$ mJ/m <sup>2</sup> , possibly indicating a smaller surface roughness.....  | 166 |
| <b>Figure S4.</b> Average crack healing velocity $\bar{v}$ as a function of energy release rate <i>G</i> . Different cantilever responses are plotted with colors and marker types corresponding to Figure S2.....  | 167 |

**Figure S5.** Circle data points represent the AFM topography data across the asperity. Solid line is a curve fit by using a circular arc shape assumption.  $R=81.3$  nm for this given data. As stated in the main text, the average value of  $R$  is 124 nm and the standard deviation is 43 nm.....167

# NOMENCLATURE

|               |   |
|---------------|---|
| $a$           | contact radius (m)  |
| $\alpha$      | microscopic tilting angle at the point of contact with the meniscus (rad) |
| $c$           | the radius of projected area of the meniscus or Dugdale zone (m)          |
| $d$           | distance between surfaces (m)   |
| $d_c$         | contact diameter (m)  |
| $\delta$      | displacement between two bodies (m)                                       |
| $\delta_t$    | Dugdale zone distance (m)   |
| $\Delta x$    | distance between two asperities (m)                                       |
| $\eta$        | viscosity (Pa·s)  |
| $\gamma_L$    | surface tension of the liquid (N/m)                                       |
| $\gamma_{LV}$ | surface tension of the liquid-vapor interface (N/m)                       |
| $h_f$         | liquid film thickness on the substrate (m)                                |
| $k_B$         | Boltzmann constant (J/ K)   |
| $l_{asp}$     | asperity spacing (m)  |
| $\lambda$     | Maugis' adhesion parameter  |
| $\mu$         | chemical potential (J/mol)  |
| $\mu_0$       | friction coefficient  |
| $n$           | number of moles (mol)   |
| $n_i$         | index of refraction   |
| $n_{asp}$     | areal density of the asperities ( $1/\mu\text{m}^2$ )                     |
| $n_{wet}$     | areal density of the wetted asperities ( $1/\mu\text{m}^2$ )              |
| $n_{c,wet}$   | areal density of contacting wetted asperities ( $1/\mu\text{m}^2$ )       |
| $\nu$         | Poisson's ratio   |
| $\omega$      | interpenetration (m)  |
| $p$           | pressure (Pa)   |
| $p_s$         | saturated vapor pressure (Pa)   |
| $p/p_s$       | partial vapor pressure  |
| $r$           | radius of curvature at liquid vapor interface (m)                         |
| $r_a$         | azimuthal meniscus radius (m)   |
| $r_e$         | effective meniscus radius (m)   |
| $r_K$         | Kelvin radius (m)   |
| $r_m$         | meridional meniscus radius (m)  |
| $\rho$        | density ( $\text{kg}/\text{m}^3$ )  |
| $s$           | crack length (m)  |
| $\sigma$      | root mean square of the asperity heights (m)                              |
| $\sigma_0$    | constant stress in Dugdale zone ( $\text{N}/\text{m}^2$ )                 |
| $t$           | time (s)  |
| $\tau$        | condensation growth time or nucleation time (s)                           |
| $\tau_{asp}$  | capillary density nucleation rate ( $1/\mu\text{m}^2 \text{ min}$ )       |
| $1/\tau_0$    | one over attempting frequency (s)   |

|                    |  |
|--------------------|--|
| $v$                | volume ( $\text{m}^3$ )  |
| $v_0$              | critical AFM tip velocity (m/s)  |
| $v_m$              | volume of a particle (atoms or molecules) ( $\text{m}^3/\text{particle}$ )   |
| $v_t$              | AFM tip velocity (m/s)   |
| $\bar{v}$          | average crack healing velocity (m/s)   |
| $v_x$              | velocity of the liquid film (m/s)  |
| $w$                | width of the cantilever (m)  |
| $w_i$              | cantilever beam deflection with no loading (m)   |
| $w_j$              | cantilever beam deflection with single point loading (m)   |
| $z_0$              | intermolecular distance (m)  |
| $z_{\text{max}}$   | maximum gap between the uniformly distributed asperities and the flat surface (m)  |
|                    |  |
| $A$                | area of annular shell of the meniscus ( $\text{m}^2$ )   |
| $A_H$              | Hamaker constant (J)   |
| $A_w$              | constant as a function of the thermodynamic equilibrium value of the thickness of adsorbed water layer on the flat surface (N/m) |
| $AR$               | capillary bridged asperity density ratio to areal asperity density   |
| $C$                | mass concentration ( $\text{kg}/\text{m}^3$ )  |
| $D$                | diffusion coefficient ( $\text{m}^2/\text{s}$ )  |
| $D_k$              | Knudsen diffusion coefficient ( $\text{m}^2/\text{s}$ )  |
| $\Delta\Omega$     | energy barrier (J)   |
| $E$                | Young's modulus (GPa)  |
| $E^*$              | reduced Young's modulus (GPa)  |
| $F_c$              | capillary adhesion force (N)   |
| $F_F$              | friction force (N)   |
| $F_N$              | normal force (N)   |
| $G$                | energy release rate ( $\text{J}/\text{m}^2$ )  |
| $G_f$              | free energy (J)  |
| $\Gamma$           | adhesion energy per unit area ( $\text{J}/\text{m}^2$ )  |
| $H$                | meniscus height at nucleation or gap between two surfaces (m)  |
| $H_c$              | meniscus height at thermodynamic equilibrium or critical gap distance (m)  |
| $\bar{H}$          | average surface separation (m)   |
| HPZ                | healing process zone length (m)  |
| $\mathbb{H}$       | hardness coefficient (GPa)   |
| $J_w$              | net inward flux ( $\text{mol}/(\text{m}^2\cdot\text{s})$ )   |
| $K$                | effective elastic modulus (GPa)  |
| $M_w$              | molecular weight of the liquid (kg/mol)  |
| $N_A$              | Avagadro's constant  |
| $N_{\text{c,wet}}$ | nucleated contacting asperities  |
| $\Omega$           | grand potential of partially filled liquid vapor (J)   |
| $\Omega_v$         | grand potential of vapor (J)   |
| $\Pi$              | disjoining pressure (Pa)   |
| $P$                | pressure (Pa)  |
| $P_c$              | capillary pressure (Pa)  |

|           |   |
|-----------|---|
| $Q$       | heat transfer (J)                                       |
| $\dot{Q}$ | rate of change of mass (kg/s)                           |
| $R$       | radius of the sphere or asperity (m)                    |
| $R_T$     | radius of the AFM tip (m)                               |
| $R^*$     | lateral extension of the critical nucleus (m)           |
| $R_g$     | ideal gas constant (J/(mol·K))                          |
| $RH$      | relative humidity                                       |
| $T$       | temperature (K)   |
| $V$       | volume of the annulus of the meniscus (m <sup>3</sup> ) |
| $V_m$     | molar volume (m <sup>3</sup> /mol)                      |
| $W$       | work done on the system (J)                             |
| $W_{asp}$ | work of adhesion for an individual asperity (J)         |

# Chapter I: Introduction

## 1.1 MOTIVATION

In “Status of the MEMS industry 2013 [1], Yole Developpement reported that in 2012 \$11 billion was spent on the microelectromechanical (MEMS) sector. It also projected that this growing market will manage \$22.5 billion annual sales by 2018. Despite these stunning parameters, mass production of MEMS components for use in commercial applications contribute to the market as a small portion, because not all device concepts are reliable enough to meet the expectations of the consumers.

While a plethora of concepts have been explored, a large portion of MEMS devices have been constrained due to the reliability issues experienced during the use of these devices. Micro- and Nanoelectromechanical Systems (MEMS and NEMS) can be categorized into four classes [2]. These include:

Class I: Mechanisms with no moving parts (accelerometers, pressure sensors, ink jet print heads, strain gauges and microphones).

Class II: Mechanisms with moving parts still no rubbing or impacting (gyroscopes, comb drives and RF oscillators).

Class III: Mechanisms with moving parts including impacting surfaces (The Texas Instruments Digital Mirror Device (DMD) [3], Qualcomm mirasol display [4], ohmic [5] and capacitive microrelay switches [6]).

Class IV: Mechanisms with moving parts likewise impacting and rubbing surfaces (optical switches, scanners and lock discriminators).

Class IV devices are still struggling to overcome the reliability issues before appearance in the MEMS market. Reliability issues are due to [7] particle contamination leading to fix the device to the substrate, particles inducing third body wear changing the motion tolerance,

particulate contamination impeding the motion, and adhesion of rubbing or contacting surfaces. Solving these problems will make it possible to fabricate new devices with higher performance and better functionality. Consequently, the number of fabricated units will increase dramatically in the MEMS market. Examples of units that can be fabricated include corner cube reflectors for free-space optical switching [8], friction-based actuators [9] and gears [10] for microrobotics and micromanipulation applications, rotating platforms for directional detection of electromagnetic radiation ranging from X-ray to communications wavelengths or acoustic signals [11], and microscale Fourier Transform InfraRed spectrometers [12].

Adhesion of contacting surfaces is an important failure mechanism. Capillary forces are among the strongest contributors of the adhesion forces. While capillary adhesion *equilibrium* values have been widely studied [13], there is a lack of understanding of capillary adhesion *dynamics*.

*The subject of this thesis dissertation is to measure and provide fundamental understanding of capillary bridge dynamics with a goal of helping to improve reliability of Class III and IV MEMS devices.*

## **1.2 THEORETICAL BACKGROUND**

Surfaces of solid materials exhibit height differences which are either large or small. Convex points on the surface are called asperities, while concave points are called valleys. The character of the surface can be measured and is referred to as surface roughness. When two nominally flat surfaces contact each other, the real contacting area is determined by the surface roughness [14], the mechanical and adhesive properties of the surface and the applied load [15]. The work of adhesion between the two surfaces can be determined from the integral of the force-displacement curve as separation occurs. The associated force is a result of interatomic interactions at contacting asperities [16].

Contacting asperities of rough surfaces can be studied by single asperity contact models to understand the adhesion characteristics of the surfaces.

## 1.2.1 Single Asperity Contact Models

The contact between an elastic smooth sphere and a rigid flat surface without any adhesion or surface force contribution, as shown in Figure 1.1, is calculated in the Hertz theory. Under externally applied force,  $F_{ext}$ , the contact radius  $a$  and the displacement  $\delta$  are given by [17–19]

$$a = \sqrt[3]{\frac{R F_{ext}}{K}} \quad \text{and} \quad (1.1)$$

$$\delta = \frac{a^2}{R} \quad (1.2)$$

in which  $R$  is the radius of the sphere, and  $K = 4/3[(1 - \nu_1^2)/E_1 + (1 - \nu_2^2)/E_2]$  is the effective elastic modulus.  $E_1$  and  $E_2$  are the Young's moduli and  $\nu_1$  and  $\nu_2$  are the Poisson's ratios for the sphere and flat surfaces, respectively.

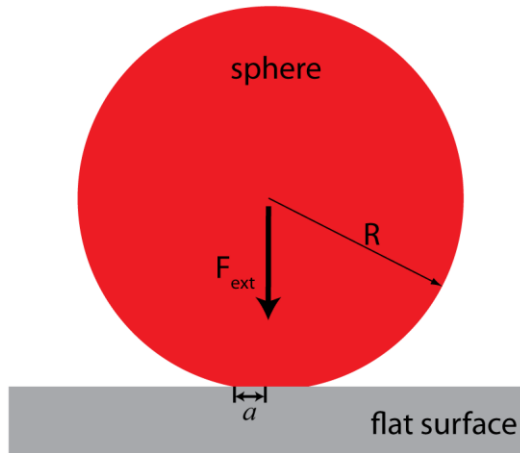


**Figure 1.1:** Sphere vs flat surface contact geometry.  $R$  is the radius of sphere,  $F_{ext}$  is the externally applied force, and  $a$  is the contact radius.

In reality, even at zero external loading case contact area forms because interatomic attractive forces such as van der Waals forces attract surfaces together. Hertz theory has been modified to include adhesion effects. One of the most commonly used models is the Johnson, Kendall, and Roberts (JKR) model [20]. This model assumes that short range interaction forces exist only inside the contact area [21]. Equations are derived from the balance between the

elastic strain energy and the loss in surface energy. For a known contact radius the corresponding force can be calculated as:

$$F_{JKR} = F_{ext} - \sqrt{6\pi a^3 \Delta\gamma K}, \quad (1.3)$$

where  $\Delta\gamma$  is the surface energy. The contact radius becomes

$$a = \sqrt[3]{\frac{R F_{JKR}}{K}}, \quad (1.4)$$

while the displacement equation becomes

$$\delta_{JKR} = \frac{a^2}{R} - \sqrt{\frac{8\pi\Delta\gamma}{3K}}. \quad (1.5)$$

Another widely used theory that accounts for the long range interaction forces outside of the contacting area is Derjaguin, Muller, and Toporov (DMT) model. This model applies the Hertz theory in the contacting area. However, the DMT model adds adhesion forces outside of the contacting region [22]. Force  $F_{DMT}$ , contact radius  $a$ , and the deformation  $\delta_{DMT}$  are given by

$$F_{DMT} = F_{ext} - 2\pi R \Delta\gamma, \quad (1.6)$$

$$a = \sqrt[3]{\frac{R F_{DMT}}{K}}, \text{ and} \quad (1.7)$$

$$\delta_{DMT} = \frac{a^2}{R}. \quad (1.8)$$

The three different models are plotted in Figure 1.2 using values  $R=124$  nm,  $\Delta\gamma=33.16$  mJ/m<sup>2</sup>,  $K=115.4$  GPa, and  $z_0=0.2$  nm. Forces are similar in the contact. However, adhesive forces only occur for the JKR and DMT models, as clearly seen at 0 displacement.

Tabor came up with a parameter showing the JKR and DMT models represent two extreme cases [23]. Rigid small spheres are modeled accurately by the DMT model. On the other hand, the JKR model predicts better for large flexible sphere contact cases. The more advanced model for the transition of JKR-DMT is known as the Maugis-Dugdale (MD) model [24]. These models are valid for dry environment conditions. However, our focus in this thesis is on the effect of capillary forces on adhesion. This is discussed next.

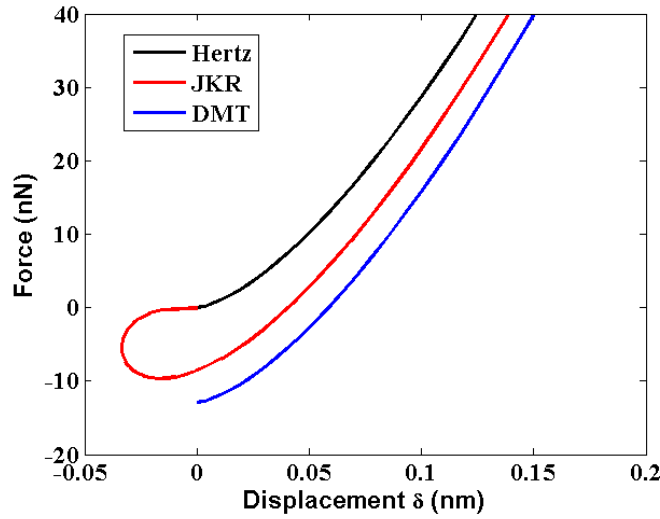


**Figure 1.2:** Force curves as a function of displacement are plotted for three models. Hertz, JKR and DMT model curves are plotted with black, red and blue lines, respectively.

## 1.2.2 Capillary Forces

When contacting surfaces are exposed to the undersaturated vapor of a condensable substance, the substance may spontaneously condense into a liquid state and form curved menisci that fill nanometer-scale gaps [25]. The curved meniscus induces a pressure difference across the liquid-vapor interface. The expression relating the pressure to the meniscus curvature is known as the Laplace equation [26,27],

$$\Delta P = \gamma_L \left( \frac{1}{r_a} + \frac{1}{r_m} \right). \quad (1.9)$$

Here,  $r_a$  (the azimuthal radius) and  $r_m$  (the meridional radius) are the principal radii of curvature of the surface, and  $\gamma_L$  is the surface tension of the liquid [28]. Asperity contact mechanisms are modeled as a sphere-flat surface interaction, as shown in Figure 1.3. The sign of  $r_a$  is positive because the center is inside the meniscus, while  $r_m$  is negative because the center is outside the meniscus. Equation 1.9 can be simplified using  $r_e$ , the effective radius. Accordingly,

$$\Delta P = \gamma_L \left( \frac{1}{r_e} \right). \quad (1.10)$$

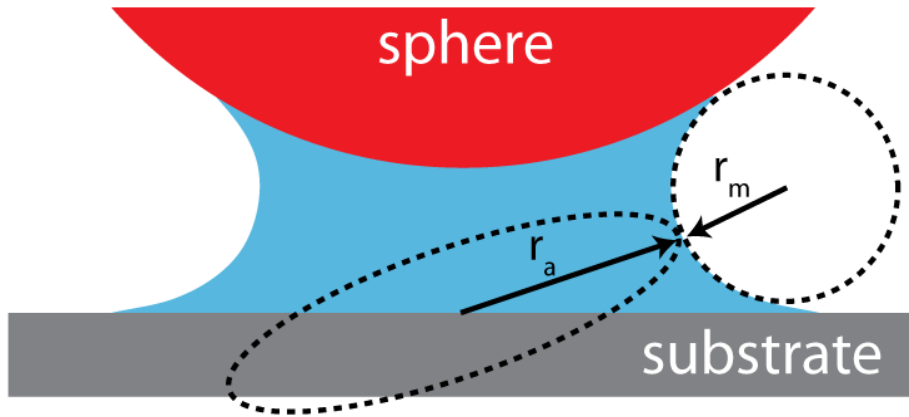


**Figure 1.3:** Definition of principal radii of curvature ( $r_a$  and  $r_m$ ) for a saddle-shaped meniscus[29].

In thermodynamic equilibrium  $r_e$  equals the Kelvin radius  $r_K$ . The Kelvin equation is derived using thermodynamics and the Young-Laplace equation [25]. First, for a reversible process at constant temperature, the mechanical pressure change affects the free energy  $G_f$  of a substance as

$$\Delta G_f = \int V_m dP. \quad (1.11)$$

Assuming constant molar volume of the liquid substance  $V_m$ , and substituting the Young-Laplace equation with pressure change  $\Delta G_f$  becomes

$$\Delta G_f = \gamma_L V_m / r_e. \quad (1.12)$$

Relating the free energy of a substance to its vapor pressure is acceptable for ideal gas condition assumption. Hence,

$$\Delta G_f = R_g T \ln(p/p_s). \quad (1.13)$$

Here  $R_g$  is ideal gas constant,  $T$  is temperature,  $p$  is the vapor pressure, and  $p_s$  is the saturated vapor pressure. At thermodynamic equilibrium,  $\Delta G_f$  for the vapor and the liquid are the same. The equality of equations 1.12 and 1.13 gives the Kelvin equation [27],

$$r_K = \frac{\gamma_L V_m}{R_g T \ln(p/p_s)} = \frac{0.53}{\ln(p/p_s)} \text{ nm}. \quad (1.14)$$

Here, 0.53 nm is the value for water as the substance at room temperature with  $\gamma_L=0.073$  N/m,  $V_m=0.018$  L/mol,  $T=300$  K, and  $R_g=8.314$  J/(mol·K).

For a sphere-flat geometry, with the assumption that the sphere radius  $R \gg |r_K|$ ,  $|r_a| \gg |r_m|$ , so  $r_m$  closely approaches  $r_K$ . Then, assuming the sphere and the flat are both elastically rigid, the capillary force  $F_c$  under thermodynamic equilibrium can be found from the Laplace and Kelvin equations as [28]

$$F_c = 4\pi R \gamma_L \cos\theta \left[ 1 - \frac{H}{2|r_K| \cos\theta} \right]. \quad (1.15)$$

Here,  $\theta$  is the contact angle between the meniscus and the surface, and  $H$  is the separation between two bodies. The work of adhesion can be calculated for the multi-asperity surfaces based on equation 1.15. The work of adhesion for an individual asperity,  $W_{asp}$ , is the work done while separating an asperity subject to the equilibrium capillary force from a substrate. For the case where all the asperities are uniform on one surface vs. flat surface, the work of adhesion is

$$\Gamma = n_{asp} W_{asp} = 4\pi n_{asp} R |r_K| \gamma_L \cos\theta^2, \quad (1.16)$$

where  $n_{\text{asp}}$  is the areal density of the contacting asperities. Calculation of work of adhesion with equation 1.16 is a satisfactory first order model. However, more advanced models need to consider the liquid vapor adsorption on the surfaces [30].

Thin liquid films accumulate on a substrate as a result of vapor pressure. In the absence of external forces, the pressure in the liquid film is equal to the pressure of the bulk phase that formed the film. Thus, the interlayer thickness can change without change of free energy. When overlapping sets in at the film as a result of external forces, the situation must change. This leads to the hydrostatic pressure difference between in a thin film and in the contiguous bulk phase from which the interlayer is called the disjoining pressure,  $\Pi$  [31]. Following Derjaguin and Churaev, non-zero external forces arise from three different factors. These are (i) van der Waals forces, (ii) macroscopic electrostatic field created by nonuniform distribution of positive and negative ions, and (iii) forces as a function of special structure of interfacial layers.

Mate explored disjoining pressure in perfluoropolyether lubricants and used the van der Waals force to obtain expressions for  $\Pi$  [32]. The van der Waals force between atoms and/or molecules has contributions from three different forces. Each exhibits a  $1/z^6$  dependence, where  $z$  is the distance between the atoms or molecules [33]. The potential energies, which lead to van der Waals forces, are the Keesom energy, the Debye energy and the London dispersion energy. The interaction types of these potentials are dipole-dipole, dipole-non-polar and dipole-induced dipole, respectively. In order to apply the van der Waals forces between macroscopic bodies, derivations for different geometries are available in the literature. Between two flat surfaces, the force per unit area is

$$F = -\frac{A_H}{6\pi d^3}, \quad (1.17)$$

in which  $A_H$  is the Hamaker constant, and  $d$  is the distance between the surfaces. If the force is negative (positive), it means an attractive (repulsive) force exists between surfaces. The Hamaker constant is calculated by summing forces over all the molecules in the adjacent bodies. It is always positive between two identical bodies in a medium and between any two condensed

bodies in vacuum or in air. It is negative whenever the dielectric properties of the intervening medium are intermediate between those of the two interacting media [26].

Liquid film interactions, which lead to a disjoining pressure, have negative  $A_H$  values. An example is a water film on muscovite mica surface in an air environment. The index of refraction,  $n_i$ , values are 1.333 [34], 1.58-1.62 [35] and 1.00029 [34], for water, mica and air, respectively. The relative dielectric constant,  $\epsilon_r$  equals the square of the index of refraction, i.e.  $\epsilon_r = n_i^2$ . Therefore,  $A_H$  becomes negative. Another example, which is the situation in our study, is a water film on top of  $\text{SiO}_2$  surface in air. Their  $n_i$  values are 1.333 [34], 1.4584 [35] and 1.00029 [34], respectively.  $A_H$  for this case is  $-1 \times 10^{-20}$  (J) [33]. Negative  $A_H$  values are generally expected for liquid films adsorbed on a solid surface in a gas environment. For van der Waals forces only,  $\Pi$  can be written as

$$\Pi = -\frac{A_H}{6\pi h_f^3} \quad , \quad (1.18)$$

where  $h_f$  is the liquid film thickness.

Following Mate [32], we now derive the relation between disjoining pressure and capillary pressure  $P_c$  for surface with a pore. We consider Figure 1.4, in which a liquid layer is in contact with liquid on a flat surface at pressure  $P_s$  and is in the pore region at pressure  $P_p$ .

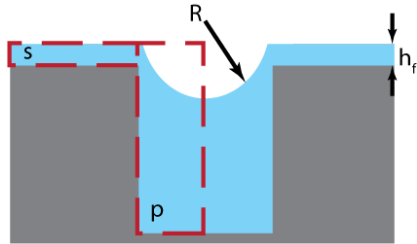


**Figure 1.4:** Liquid film thickness in equilibrium with a spherical shaped meniscus.  $R$ =meniscus curvature radius (m), and  $h_f$ =liquid film thickness (m).

Taking the entire region in Figure 1.4 as the system, the first law can be written as

$$dE = dU + \delta Q - \delta W, \quad (1.19)$$

where  $E$  is the total energy of the system,  $U$  is the internal energy in the system (due to the interaction of the liquid layer with the surface),  $Q$  is the heat transfer into the system and  $W$  is the work done by the system. We take  $\delta Q = \delta W = 0$  (no heat or work transferred into the system).

We now separate the system into two parts. One is associated with the surface (Region s) and the other with the pore (Region p). Writing the associated energy terms gives

$$dE = dE_s + dE_p = (dU_s - P_s dV_s) + (dU_p - P_p dV_p), \quad (1.20)$$

where  $P$  is pressure and  $V$  is volume and the subscripts refer to the respective regions. Now we identify the internal energy change in each region with the chemical potential  $\mu$  (J/mole), rearrange the terms and write

$$dE = \mu_s dn_s + \mu_p dn_p - P_s dV_s - P_p dV_p, \quad (1.21)$$

where  $n$  is the number of moles of liquid. Taking the liquid volume and density to be constant,  $dn_s = -dn_p = dn$ , and  $dV_s = -dV_p = dV$ . At equilibrium,

$$0 = (\mu_s - \mu_p)dn - (P_s - P_p)dV. \quad (1.22)$$

Here for example, *net* work done within the system,  $(P_s - P_p)dV$ , results in a *net* increase in the system's internal energy,  $(\mu_s - \mu_p)dn$ .

Now we consider the signs of the terms. We rewrite equation 1.22 as

$$(\mu_s - \mu_p)dn = (P_s - P_p)dV. \quad (1.23)$$

Because curvature is zero in the surface region and negative in the pore region, the  $(P_s - P_p)$  term is positive. The value of  $\mu_p$  (in the bulk) can be neglected because the pore region is equal

to bulk liquid, and the value of  $\mu_s$  (on the surface) increases as the film thickness decreases. This is because molecules in a thicker film will have less interaction with the surface (here we take the liquid-surface interaction to be unfavorable). Hence the  $(\mu_s - \mu_p)$  term is also positive. The signs of  $dn$  and  $dV$  are the same. Therefore, the signs agree, and the situation makes physical sense. The situation can also be considered as follows: The negative pressure in the pore pulls the liquid in, but this is offset by the increase in the internal energy of the liquid over the surface.

In Figure 1.4  $R < 0$ , so  $P_s = 0$  and  $P_p = -2\gamma/R_a > 0$ .  $(P_s - P_p)$  can be recognized as the opposite of the capillary pressure, i.e.,

$$P_c = -(P_s - P_p). \quad (1.24)$$

Meanwhile, the term  $(\mu_1 - \mu_2)dn$  represents the difference in chemical potential of the liquid in the surface relative to the pore. Associating this with the disjoining pressure,  $\Pi$ , we write

$$\Pi dV = -P_c dV, \quad \text{or} \quad (1.25)$$

$$\Pi = -P_c. \quad (1.26)$$

Disjoining pressure has the same sign as capillary pressure in much [32,36,37] but not all [29] of the literature. Therefore, the sign in equation 1.18 can be changed

$$\Pi = \frac{A_H}{6\pi h_f^3} \Rightarrow \Pi = P_c. \quad (1.27)$$

***To summarize, the disjoining pressure can be thought of as the pressure that opposes the flow due to the capillary forces, and it is due to the difference in chemical potential of the liquid film on the surface relative to that over the asperity or pore.***

Disjoining pressure also affects the capillary adhesion force. Equation 1.15 can be revised as [38]

$$F_c = 4\pi R\gamma_L \left(1 + \frac{h_f}{|r_K|}\right) \cos\theta \left[1 - \frac{H}{2(|r_K|+h_f)\cos\theta}\right]. \quad (1.28)$$

This relationship is plotted in Figure 1.5 for  $2|r_K|=2.1$  nm (corresponding to 60% RH), and for two different liquid film thickness values  $h_f$ .

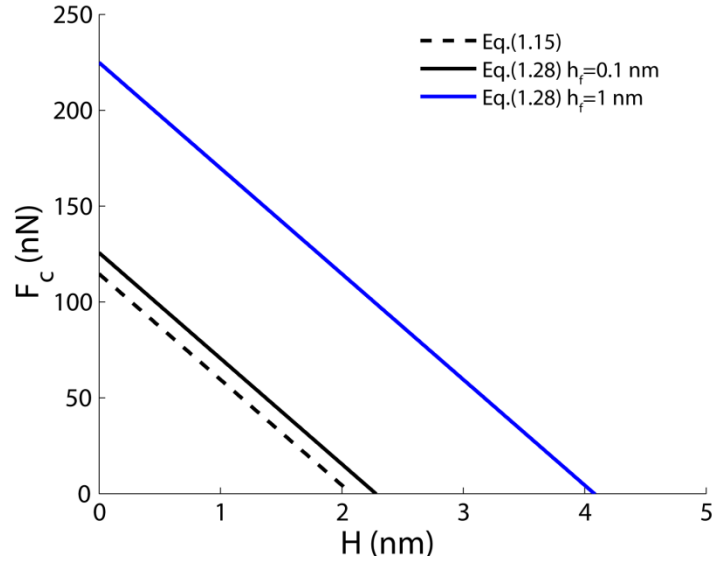


**Figure 1.5:** Comparison of the equation 1.15 and 1.28 as a function of  $H$ . Dashed black line is calculated according to equation 1.15 and solid black and blue line are calculated according to equation 1.28. Liquid film thickness is 0.1 nm for the blue line and 1 nm for the solid black line.

### 1.3 EXPERIMENTAL BACKGROUND

Capillary bridge formation between adjacent surfaces in humid environments is a ubiquitous phenomenon. For example, it can be observed in studies of granular materials [39], friction [40], insect adhesion [41], the head/disk system [32], soil mechanics [42], nanolithography [43], colloidal physics [44], and microelectromechanical systems (MEMS) devices [45,46].

MEMS fabrication techniques generally offer smooth surfaces with root mean square (rms) less than 10 nm [28]. The Kelvin radius is also on the nanometer scale for water for  $0.1 <$

$p/p_s < 0.95$ . Thus, it is expected that capillary forces will play an important role in MEMS adhesion mechanics.

The surface forces apparatus (SFA) and the atomic force microscope (AFM) have been used to measure equilibrium capillary forces. These techniques can be used to quantify the maximum capillary force (at contact), but not the full force-distance curve [47]. At thermodynamic equilibrium, the accuracy of Kelvin equation was shown directly with SFA experiments, where bridge radii of curvature is as small as 5 nm for water bridge [48] and 4 nm for cyclohexane [13]. On the other hand, direct imaging of the capillary bridge by environmental scanning electron microscopy (ESEM) revealed a radius of curvature values that was orders of magnitude larger than  $r_K$  [49]. One possible reason is an electrostatic pressure at the liquid-vapor interface due to the charging effect on the water meniscus [50]. Another reason might be the thicker liquid film on the substrate. Ionized water molecules due to the collision of electrons emitted by the sample may adsorb on the charged substrate [51]. The thicker liquid film would increase the disjoining pressure, and thus increase the volume of the meniscus bridge.

Moreover, the Laplace pressure has been found the dominant factor for  $p/p_s > 0.7$  for cyclohexane, *n*-hexane and water vapors on mica surfaces as a result of the SFA experiments [52]. In contrast, application of the continuum theory at the nanoscale for relative humidity (RH) < 0.7 ( $r_K < 1.5$  nm) fails to predict experimental results [53] due to the discrete molecular nature of the liquid [54]. On the other hand, the modified meniscus model that accounts for water adsorption effects on capillary forces agrees with the experimental AFM data in the  $p/p_s$  range from 0.15 to 0.95 [55]. The varying meniscus geometry [28] of the liquid for the non-contacting asperities should also be kept in mind to calculate the capillary forces accurately. However, there is a lack of understanding in the dynamics of capillary condensation. This is because there are large discrepancies between theory and experiments with respect to meniscus nucleation and evolution toward thermodynamic equilibrium explanations. The surface force apparatus (SFA) [56] and atomic force microscopy (AFM) [57] are the main experimental setups to investigate nanoscale water bridge dynamics. Avalanche angles have been also studied in a rotating drum with variation of  $p/p_s$  as a function of time [58]. Furthermore, a recent study shows that the crack healing rate of a microcantilever as a function of time depends on time and water partial pressure  $p/p_s$  [59]. These experimental methods will be reviewed next.

The SFA experiments involve the two curved back-silvered muscovite mica, which are held in a crossed-cylinder geometry as shown in Figure 1.6 [60]. There, a piezoelectric cylinder enables the surface separation movements as precise as  $1 \text{ \AA}$  [61]. Furthermore, capillary bridges can be observed with Fringes of Equal Chromatic Order (FECO) [62] using the standard three-layer interferometer equation [63]. A unique power of multiple-beam interferometry is that for the even-order fringes, the shift in wavelength is nearly proportional to the square of the refractive index of the intervening medium, while for odd-order fringes shift in wavelength is almost independent of the refractive index of the medium [13]. Therefore, while a liquid meniscus between the surfaces causes a break in the even-order fringes, the odd-order fringes remain substantially unaffected. A sphere near a flat surface is an equal model to these two cylinders. The sphere radius  $R$  is usually  $\sim 2 \text{ cm}$ .

The experiments begin by purging the chamber with nitrogen, and then sealing it. Mica surfaces are brought into molecular contact to measure contact wavelength of several odd- and even-order FECO fringes. The shift of the wavelengths during the vapor equilibrium experiments are analyzed according to initial molecular contact points. When thermodynamic vapor equilibrium in the chamber is achieved, the mica surfaces are brought toward each other until they jump into contact due to van der Waals forces. Condensation rapidly occurs in the contact region. Then, surfaces are separated until rapid capillary bridge evaporation occurs. If the surfaces are quickly brought closer during the rapid evaporation stage, the bridge grows again. Approach and separation of the surfaces are tested a few times, and the maximum height of the capillary bridge is obtained.

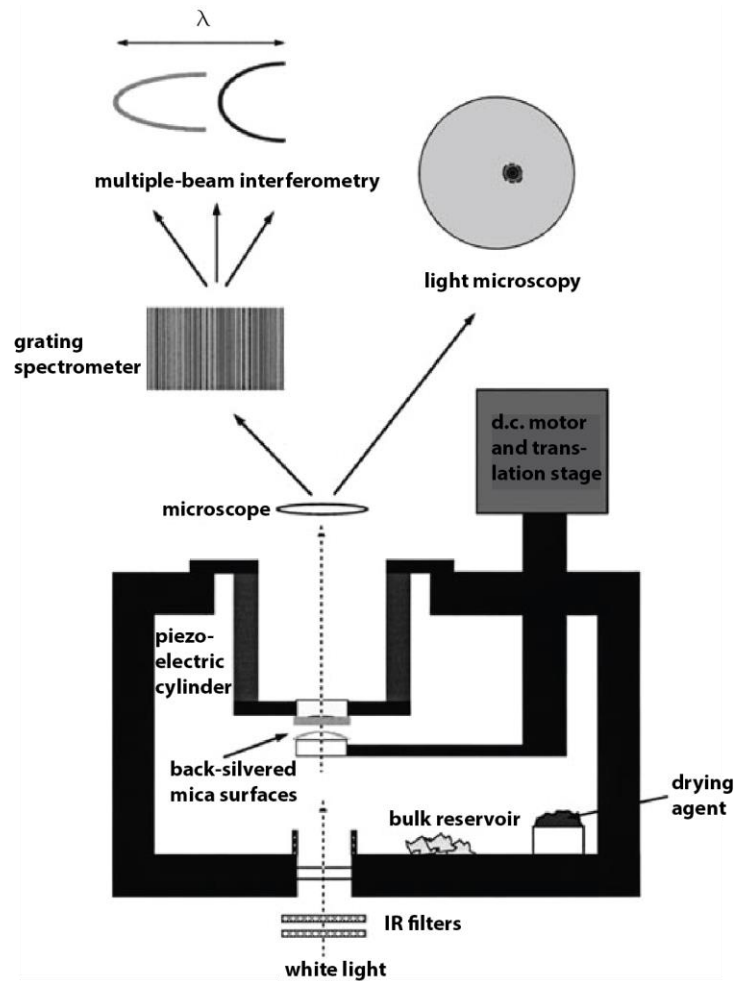


**Figure 1.6:** Schematic diagram of surface force apparatus (SFA)[60].

Another method to investigate the capillary nucleation dynamics is by AFM. Two common methods are employed to measure capillary forces. These are (i) force-distance curves and (ii) friction force measurements.

The AFM system usually has a laser system, a photo detector, a cantilever with a probe, a piezoelectric actuator (piezo) , and a controller [64]. The laser is focused on the back side of the cantilever, and the reflection is captured by a photo detector to detect the cantilever deflection and torsional rotation variations. Cantilevers usually are 50-500  $\mu\text{m}$  long and 10-50  $\mu\text{m}$  width and are made out of silicon. At the end of the cantilever, there is usually a probe with  $\sim 10$  nm radius. Microspheres can also be attached as desired [65]. The piezo has  $\sim 1$   $\text{\AA}$   $z$ -resolution, and

it can raster the surface with  $\sim 10\text{-}100\ \mu\text{m}$  range in the  $xy$  plane. A controller regulates, collects, and processes the data, and drives the piezo scanner.

To obtain the force-distance curve (i) as shown in Figure 1.7, the cantilever is moved up and down by applying a voltage to the piezo while measuring the cantilever deflection [33]. Adhesion forces are determined in the following way [66]: First the zero force line is derived from the noncontact approach region of the force-distance curve, and it fits to a line. Second, the contact part of the force curve from the retraction also fits to a line. Then the distance point of the jump-out of contact is determined. The difference in the forces of the contact and noncontact straight lines at the jump-out position is taken as the adhesion force. For example, Tabrizi et al. observed forces changing from 90 to 160 nN for RH 0.1 to 0.8 respectively on silicon wafer with silicon nitride tip ( $R \leq 10\ \text{nm}$ ) by this method [66].

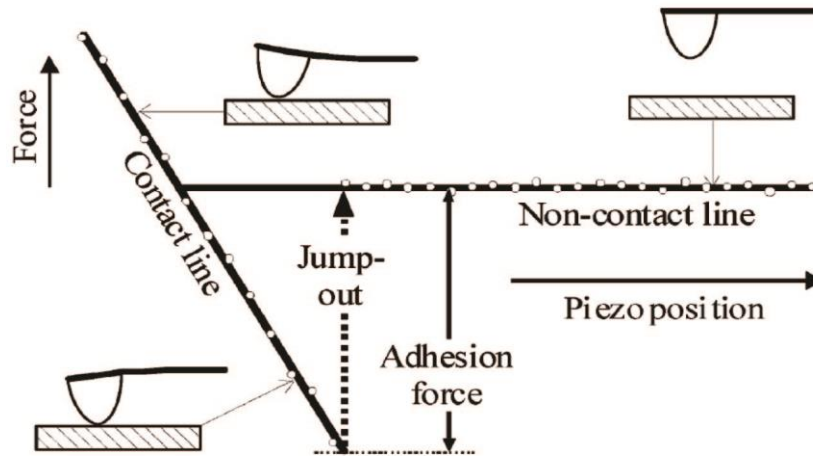


**Figure 1.7:** Typical force versus piezo position curve [66].

On the other hand, friction force measurements (ii) focus on torsion of the cantilever. During the contact mode scan, torque is applied due to friction, and it can be detected with photo detector. The relation between the friction force measurements and adhesion forces are described in Section 1.4.6.

While the above methods measure meniscus interactions with single asperities, real surfaces consist of multiple asperities. In principle, therefore, such measurements will shed light

on the capillary interactions in multi-asperity surfaces. MEMS cantilevers consist of multiple asperities. However, to date there are no reported studies on dynamics of adhesion in MEMS. The work of adhesion of MEMS cantilevers can be readily and accurately measured [46,67]. Cantilevers can be actuated to bring the free end into contact with the substrate by applying mechanical or electrostatic forces. Once contact occurs, surface interactions are sufficient to keep the cantilever attached to the substrate. The non-adhered length from the support post to the point at which the beam comes into contact with the substrate is referred to as the crack length  $s$  as in Figure 1.8. The adhesion energy per unit area  $\Gamma$  of a given cantilever is calculated according to

$$\Gamma = \frac{3}{2} E \frac{h^2 t^3}{s^4}. \quad (1.29)$$

Here,  $E$  is Young's Modulus,  $h$  is the distance between surfaces, and  $t$  is the cantilever thickness. Near the crack tip, the distance between surfaces is in the range of  $r_K$ ; this enables the meniscus formation between asperities of the two surfaces. Crack healing can be observed when the vapor pressure is increased in the environment. Equilibrium adhesion data for water over the partial pressure range  $0.3 < p/p_s < 0.95$  corresponds to  $1 < \Gamma < 30$  (mJ/m<sup>2</sup>) [68].

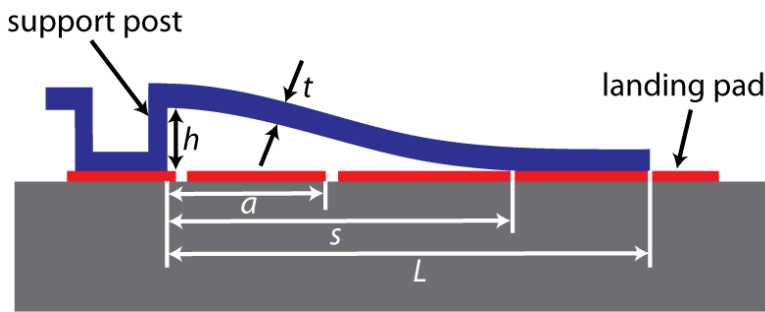


**Figure 1.8:** Schematic cross-section of adhered microcantilever configured in the S shape.

Molecular simulation studies are also investigated to understand the physical formation of the capillary meniscus. AFM force distance curves have been simulated by considering the adsorbed film layer on the surface [69] or not [70], both studies are in qualitative agreement with

the force-distance curves in the AFM experiments. Recently capillary condensation between two silica particles with a diameter of 4 nm has been illustrated by molecular simulation [71]. Attractive forces at different RH levels have been estimated at specified distances, and this study also has explained that meniscus volume changes while the distance between silica particles varies. Although molecular simulation studies help insightful understanding of capillary bridge forces in equilibrium, the dynamics of the capillary bridge have been only studied by experimental and theoretical works [72].

## **1.4 SINGLE ASPERITY CAPILLARY CONDENSATION KINETICS: REVIEW OF THEORIES AND EXPERIMENTS**

When an asperity first makes contact with a surface in an environment in which  $p/p_s > 0$ , the meniscus volume will be less than its equilibrium value. One route for capillary meniscus growth is through diffusion of vapor through the atmosphere and into the meniscus. Two closely related theoretical approaches due to (i) Kohonen [73] and Rabinovich [74] (Section 1.4.1) and (ii) Sirghi [37] (Section 1.4.2) are presented below. The different approaches agree relatively well numerically. However, discrepancies between Kohonen's and Rabinovich's theory exist and are resolved here. Importantly, the diffusion theories predict condensation rates at the nanoscale that are orders of magnitude less than those observed experimentally. That issue (Section 1.4.3) and a possible resolution (Section 1.4.4) are discussed. A different theory, which considers the nucleation time of a meniscus when one surface is in close proximity with another (but not in contact), is described in Section 1.4.5. Experiments in which this situation exists are discussed in Section 1.4.6.

### **1.4.1 1D Molecular Gas Diffusion Theory**

In Kohonen et al. [73], a quasi-one-dimensional diffusion theory is developed to estimate the growth time of a meniscus for an asperity that has just made contact with a surface. (Because a thin liquid layer exists on each surface, meniscus nucleation occurs immediately and need not be considered). Assuming steady state conditions with position  $x$  defined as in Figure 1.9 below, the rate of change of mass of the liquid,  $\dot{Q}$ , is,

$$dC = \frac{\dot{Q}}{D} \frac{dx}{A}, \quad (1.30)$$

where  $C$  is the vapor concentration at location  $x$ ,  $D$  is the vapor diffusion coefficient, and  $A$  is the area of annular shell at  $x$ . The vapor concentration can be converted to pressure using the ideal gas law. Accordingly,

$$p = \frac{C R_g T}{M_w}, \quad (1.31)$$

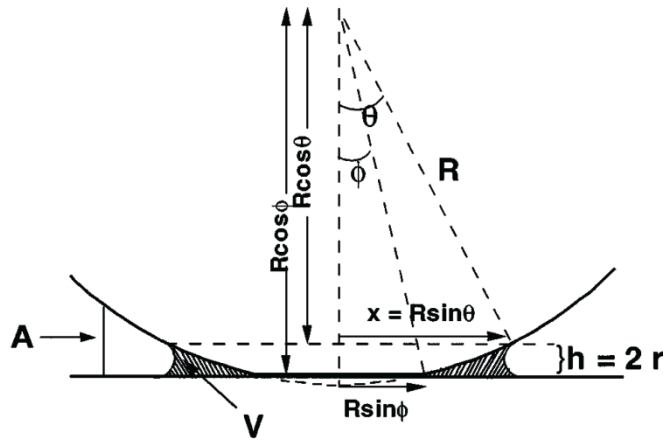


**Figure 1.9:** Schematic cross section of the surfaces in the equivalent sphere-on-a-flat-surface configuration in adhesive contact with a condensed annulus.  $A = 2\pi x[R \cos\phi - (R^2 - x^2)^{1/2}]$  and  $V \approx 4\pi Rr^2$  [73].

where  $M_w$  is the molecular weight of the liquid. Substituting equation 1.31 into equation 1.32 and integrating between the limits  $x=a$  and  $x=b$  results in

$$p_b - p_a = \frac{\dot{Q} R_g T}{D M_w} \int_a^b \frac{dx}{A}, \quad (1.32)$$

where  $a=R\sin\theta$  is at the meniscus liquid/vapor interface, and  $b=R$ . If  $R$  is large enough  $p_b=p$ , while  $p_a$  can be calculated using the Kelvin equation 1.14. Note that  $A$  remains inside the integral because it depends on  $x$ . Note also that the pressure gradient is not linear because the height  $h$  is

changing (it can be found by integrating equation 1.32 from  $a$  up to increasing values of  $b$ , though that is not done here).

$\dot{Q}$  can be written as a function of time instead of  $x$  as

$$\dot{Q} = \rho \left( \frac{dV}{dr} \right) \frac{dr}{dt} , \quad (1.33)$$

where  $\rho$  is the liquid density,  $r$  is the meniscus radius and  $V \approx 4\pi Rr^2$ . Substituting equation 1.33 into equation 1.32, and calculating the integral gives

$$\frac{dr}{dt} = \frac{DM_w p_0}{R_g T \rho} G(r, R, \phi) [RH - \exp(-\gamma_L v_m / k_B T r)] \quad (1.34)$$

where  $k_B$  is the Boltzmann constant, and the liquid specific volume on a molecular basis is  $v_m$ . Here,  $v_m = M_w / \rho N_A$  (the value for water is  $v_m = 2.99 \times 10^{-29}$  m<sup>3</sup>/molecule), where  $\rho$  is the liquid density and  $N_A$  is the Avagadro constant. Also,

$$G^{-1}(r, R, \phi) = 4Rr \int_a^R \frac{dx}{A} . \quad (1.35)$$

An expression for  $G$  is given in Kohonen et al.[73]. However, it appears to be incorrect due to a typographical error. As verified using Mathematica 8.0, the correct result is given by Rabinovich et al. [74] as

$$G^{-1}(r, R, \phi) = \frac{4r}{\sin^2 \phi} \left\{ 0.5 \cos \phi \ln \left[ 1 - \left( \cos \phi - \frac{2r}{R} \right)^2 \right] - 0.5 \ln \left( \frac{1 + \cos \phi - \frac{2r}{R}}{1 - \cos \phi + \frac{2r}{R}} \right) + \cos \phi \ln \left( \frac{\cos \phi}{\frac{2r}{R}} \right) \right\} . \quad (1.36)$$

Rabinovich et al. [74] compare their  $r$  vs  $t$  theoretical curve with that of Kohonen et al [73]. The radius  $R$  is taken to be 2 cm, and  $\phi$  the initial meniscus angle is taken as 0.015 rad<sup>1</sup>. Data points indicated by green circles and blue triangles in Figure 1.10 were taken from plots of theory in the Rabinovich [74] and Kohonen [73] papers, respectively. The results indicated by the green and blue solid lines were calculated by the present author using equations 1.34 and 1.36. To calculate the green solid line, the RHS of equation 1.34 was simply multiplied by time according to

$$r = \left( \frac{DM_w p_0}{R_g T \rho} G(r, R, \phi) \left[ RH - \exp\left(-\frac{\gamma_L v_m}{k_B T r}\right) \right] \right) t + r_0, \quad (1.37)$$

where  $r_0=20$  nm is the radius of meniscus at time  $t=0$  (this value is found from the volume expelled due to the  $\approx 3$  nm thick water layer at the point of contact). The  $r$  vs  $t$  dependence is found by assuming values of  $r$  and finding the corresponding  $t$  values. This method appears to agree well with the green circles.

In equation 1.37,  $G$  depends on  $r$ , and furthermore,  $r$  is in the exponential term. Hence, equation 1.34 should be numerically integrated. This was done for the blue solid line, and it is seen that the numerical integration agrees well with Kohonen's theoretical curve as indicated by the blue triangles. Therefore, Kohonen's theoretical curve is correct even though his expression for  $G$  (equation 1.35) is incorrect due to a typo. The later paper by Rabinovich [74] corrects the expression for  $G$ , but then appears to integrate incorrectly, resulting in an incorrect result. It was important to resolve the discrepancy to be confident that the theoretical results plotted here are correct.

## 1.4.2 Mass Transfer Theory Using Knudsen Diffusion

Sirghi et al.[37] proposed that Knudsen rather than bulk diffusion should be used in calculations because the gap becomes small as the vapor reaches the meniscus. That is, diffusing

---

<sup>1</sup> Rabinovich et al. draws theoretical curves with  $\phi=0.012$  rad, however Kohonen et al. uses  $\phi=0.015$  rad. The author used  $\phi=0.015$  in the equations to plot figures in this study consistently. In any case, the slight change of the angle imparts a negligible change in the results.

molecules are more likely to strike the wall than each other. This is especially true for AFM tips, which are on the order of 10-100 nm. In comparison, the mean free path of a water molecule,  $\lambda_w$ , is 50 nm at standard temperature and pressure (STP).

Sirghi et al. defines net inward flux as

$$J_w = \frac{D_k}{k_B T} \frac{dp}{dx}, \quad (1.38)$$

where  $D_k$  is the Knudsen diffusion coefficient of vapor molecules. Continuity rules are followed, and the mass flow is constant while the gap height is changing. Then,  $dp/dx$  can be written in terms of  $dp/da$  at the meniscus. Equation 1.39 indicates the calculation for Knudsen diffusion

$$D_k(a) = \frac{2r}{3} \left( \frac{8R_g T}{\pi \rho v_m n} \right)^{1/2}, \quad (1.39)$$

The derivative of the meniscus radius ( $r$ ), which can be compared with equation 1.34, is

$$\frac{dr}{dt} = D_k \frac{v_m}{k_B T} \frac{2v_s}{R} [RH - \exp(-\gamma_L v_m / k_B T r)]. \quad (1.40)$$

Again numerically integrating, the result of the Knudsen diffusion curve is indicated by the red line in Figure 1.10. It is not so different from the other curves for a large sphere ( $R=2$  cm). Figure 1.11 illustrates the Knudsen diffusion effect on capillary condensation at  $R=250$  nm and  $RH=0.5$ . Here it is clear that for nanometer-scale asperities, capillary condensation is expected to be rapid. However, the slower Knudsen diffusion rate decreases the rate by approximately a factor of 100 from  $\sim 1$  to  $\sim 100$   $\mu$ s.

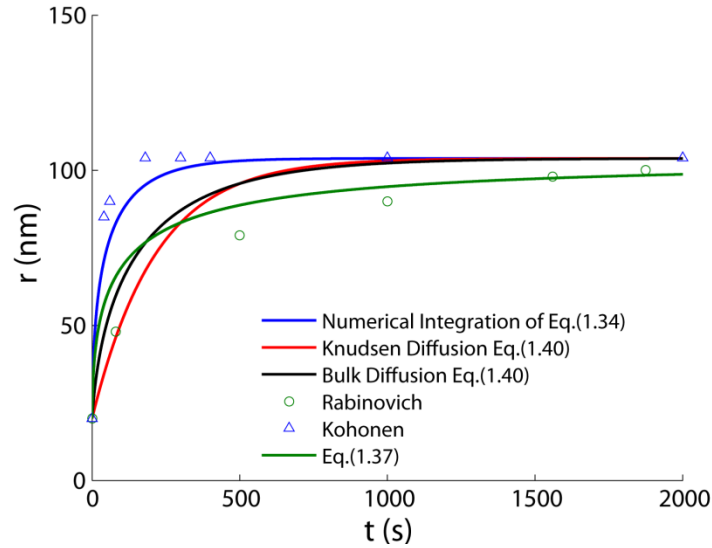


**Figure 1.10:** Comparisons of different diffusion theory calculations. The trends show the predicted meniscus radius dependence on time assuming an asperity radius  $R=2$  cm. Solid blue line is calculated by equation 1.34, solid red line is calculated by equation 1.40 by using Knudsen diffusion coefficient, solid black line is calculated by equation 1.40 by using bulk diffusion coefficient, solid green line is calculated by equation 1.37, Rabinovich data shown as green circles are reproduced from Fig. 11 in ref [74], and Kohonen data shown as blue triangles are reproduced from Fig. 3 in ref [73].

Figure 1.12 further demonstrates that numerical integration is needed. When equation 1.34 is plotted as a function of  $r$ , it coincides with the derivative of Kohonen’s numerically integrated curve. The green line in Figure 1.12 is the derivative of the green solid line in Figure 1.10 and is not in agreement with equation 1.34. Hence, it appears that the blue solid line is the correct result.

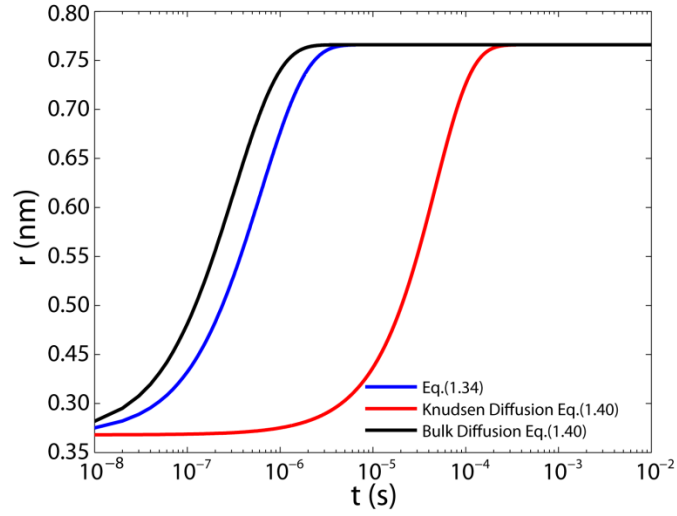


**Figure 1.11:** Kohonen calculations (equation 1.34) are shown with blue line, Sirghi calculations (equation 1.40) for bulk diffusion are shown with black line, and red line represents Knudsen diffusion approach (equation 1.40). Here  $R= 250$  nm and  $RH=50\%$ .

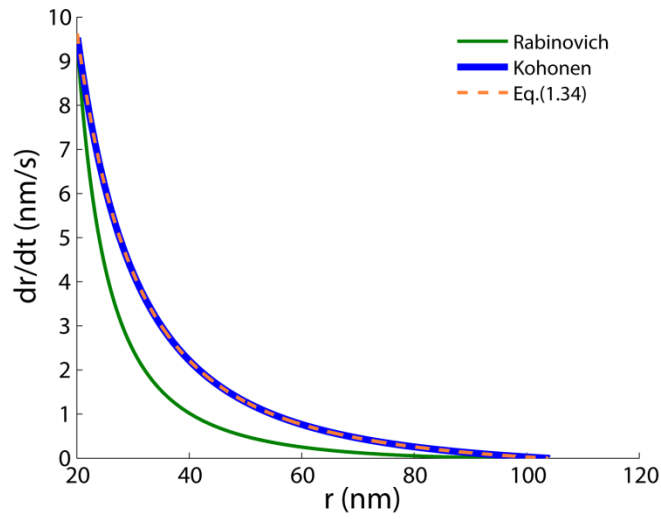


**Figure 1.12:** Comparisons of the derivative of Kohonen and Rabinovich methods. Dashed orange line is the equation 1.34 curve.

### 1.4.3 Experiments Measuring the Capillary Condensation Kinetics of Contacting Asperities

Experimentally, AFM and SFA have been used to detect the pull-off force dependence on time after contact is made. The pull-off force is taken as a measure of the capillary force, and the change of the pull-off forces with time indicates the kinetics of the capillary condensation.

Kohonen et al. [73] used the SFA with crossed cylinder mica surfaces with  $R=2$  cm radius. They investigated *n*-pentane, *n*-hexane, cyclohexane and water at high partial pressures ( $p/p_s = 0.9945-0.9975$ ) at room temperature. At room temperature, the saturation pressures of these liquids are 68, 20, 13 and 3.2 kPa, respectively, and it is observed in experiments that substances with a higher saturation pressure reach equilibrium in a shorter time. Kohonen's experiments agree well with his molecular diffusion approach. The main reason may be the very high  $p/p_s$  conditions. That is, the equilibrium radii are on the order of 100 nm. Hence, the large gap between the mica surfaces is compatible with the molecular diffusion theory.

However, for  $\mu\text{m}$ - and  $\text{nm}$ -scale asperity tips, the theoretical predictions for  $dr/dt$  are orders of magnitude faster than the time required to attain the full capillary force in measurements performed by Rabinovich [74] and Sirghi [37]. A revised theory by Sirghi [37] that attempts to resolve this discrepancy is discussed next.

### 1.4.4 Theory Modification: Adsorption and Surface Flow Limit Meniscus Growth Rate

The flow of a thin liquid film on the surface has been studied with the concepts of disjoining and capillary pressure by Mate [32] and Israelachvili [5 (Chptrs. 11&14)], and was reviewed in Section 1.2.2. Wei and Zhao first followed these concepts to explain the capillary condensation equilibrium time as a result of surface adsorption and transport of water molecules [36]. More recently Sirghi [37] developed a similar technique, and his method is followed below.

The disjoining pressure,  $\Pi$ , represents the difference in interaction energy per unit volume between molecules in a liquid film with respect to molecules in a bulk liquid and can be

understood in the following sense. Negative pressure in a meniscus acts to draw liquid into a capillary bridge spanning two surfaces. However, as the liquid layer becomes thinner, its free energy per mole,  $\mu$ , increases because relatively more molecules are at the surface (where they make fewer bonds). Effectively, there is an opposing pressure,  $\Pi$ , that prevents all the liquid from being drawn in.

Now let us consider the disjoining pressure on a vertically aligned surface extending above and perpendicular to a bulk liquid. As height increases above the horizontal bulk liquid surface, the partial pressure of the vapor will decrease (just as air pressure decreases with altitude). Using this idea, Israelachvili [5 (Chptr.11)] shows that at thermodynamic equilibrium, the disjoining pressure  $\Pi$  of a liquid film is

$$\Pi(h_0) = \frac{k_B T}{v_m} \ln(p/p_s), \quad (1.41)$$

where  $h_0$  is the liquid film equilibrium thickness. The expression

$$\Pi(h_f) = \frac{A_w}{h_f} \quad (1.42)$$

defines the disjoining pressure as a function of film thickness, and is valid for water ( $h_f < 40$  nm) on glass or silica surfaces [37]. Here,  $A_w < 0$  is a constant with units of N/m.

According to the Kelvin equation, the capillary pressure across the liquid-vapor interface at thermodynamic equilibrium has the value

$$P_c = \frac{\gamma_L}{r_K} = \frac{k_B T}{v_m} \ln(p/p_s) . \quad (1.43)$$

Hence, in equilibrium, the disjoining pressure and the capillary pressure are equal to the equilibrium value.

$$P_c = \Pi(h_0) = \frac{A_w}{h_0} = \frac{\gamma_L}{r_K} \quad (1.44)$$

When an asperity first makes contact with a surface, the capillary radius will be very small and negative. Hence, the capillary pressure will be very large and negative, and act to draw liquid from the adsorbed layer. The driving force for this process is the difference between the disjoining pressure of the liquid film and the capillary pressure in the meniscus,

$$\Pi(h_f) = \frac{k_B T}{v_m} \ln(p/p_s) - \frac{\gamma_L}{r} . \quad (1.45)$$

Following Sirghi [37], the gradient of disjoining pressure in the  $x$  direction is

$$\frac{d\Pi}{dx} = \frac{d\Pi}{dh} \frac{dh}{dx} , \quad (1.46)$$

where

$$\frac{d\Pi}{dh} = -\frac{A_w}{h^2} = -\frac{\gamma_L h_0}{r_K h^2} , \text{ and} \quad (1.47)$$

$$\frac{dh}{dx} = \tan(\alpha) . \quad (1.48)$$

At this point, Sirghi proposes  $\alpha$  as a “microscopic tilting angle” of the adsorbed water layer at the point of contact with the meniscus as shown in Figure 1.13.

If the thin liquid film is assumed to be a Newtonian fluid, the motion of the liquid film can be derived from Navier-Stokes equation for an infinitesimal volume as

$$\eta \frac{d^2 v_x}{dz^2} = \frac{d\Pi}{dx} , \quad (1.49)$$

where  $\eta$  is the viscosity of the surface water and  $v_x$  is the velocity of the liquid in thin film. Applying the boundary conditions of no slippage of liquid at the solid liquid interface,  $v_x=0$  at  $z=0$ , and no air shear or other stress at the liquid-air interface,  $dv_x/dz=0$  at  $z=h$ , it is found that

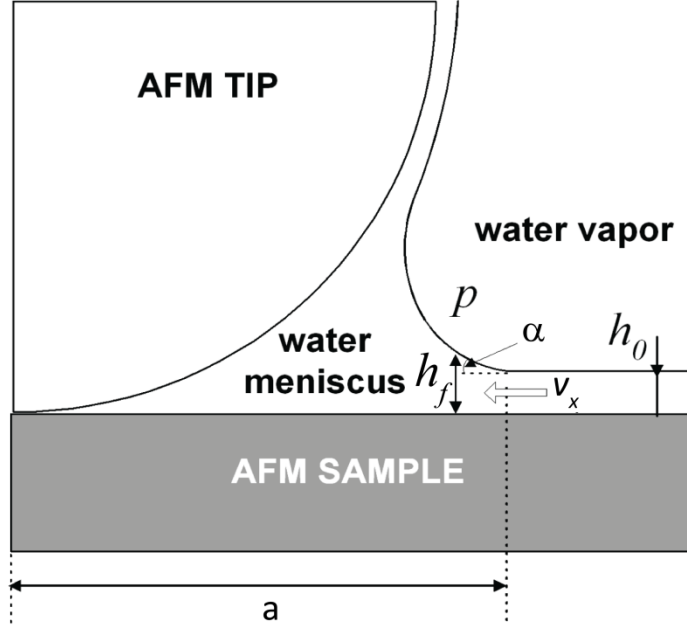


**Figure 1.13:** Schematic of the capillary water meniscus at the contact between completed wetting surfaces of AFM tip and sample [37].

$$v_x(z) = \frac{1}{\eta} \frac{d\Pi}{dx} (h_f z - z^2/2), \quad (1.50)$$

where  $h_f$  is the thickness of the liquid film and  $z$  is the distance from the liquid-solid interface. The average velocity of water molecules is

$$\langle v_x \rangle = \frac{1}{h_f} \int_0^{h_f} v_x(z) dz = \frac{h_f^2}{3\eta} \frac{d\Pi}{dx} \quad (1.51)$$

By substituting equation 1.46 to 1.48 into equation 1.51, the average velocity becomes

$$\langle v_x \rangle = \frac{\gamma_L h_0}{3\eta r_K} \tan(\alpha). \quad (1.52)$$

Once the average velocity is calculated, the growth time  $\tau$  can be found by dividing the meniscus volume, which needs to be filled, by the volumetric rate of entry into the meniscus (i.e., the product of the meniscus entry area and the average velocity).

$$\tau = \frac{4\pi R r_K^2}{2\pi a h_0 \langle v_x \rangle} = \frac{R^{1/2} r_K^{3/2}}{h_0 \langle v_x \rangle} \quad (1.53)$$

To make a reasonable estimate of  $\tau$ , good values of the parameters  $h_0$ ,  $\eta$  and  $\alpha$  are needed. Liquid film thickness values are very sensitive to material and surface conditions, so a literature search may not provide accurate values. Separate experiments need to be conducted to find the film thicknesses. The viscosity of the water at the nanoscale has not yet been well understood. Reported values can be very different from each other:  $\eta=35$  Pa•s in [75] and  $\eta=1.5$  kPa•s in [76]. This can be compared with the bulk value of  $\eta=0.001$  Pa•s. Also, the microscopic contact angle demands further study to obtain precise values. Sirghi et al. used  $\eta=35$  Pa•s,  $\tan(\alpha)=0.01$ ,  $h_0=0.3$  nm, and  $r_K=0.78$  nm (RH=50%). When equation 1.53 is calculated for  $R=250$  nm according to the case where Figure 1.11 is plotted, the meniscus growth time is computed as 13.5 ms. This is two orders of magnitude slower than Knudsen diffusion approach. Although Sirghi's method provides a reasonable estimate of the growth time of micro- and nanoscale capillary condensation, there is uncertainty because good values of thin liquid film viscosity are not well known.

In summary, neither Rabinovich [74] nor Sirghi's [37] experiments with small tip radius (3.3  $\mu\text{m}$  or 30 nm, respectively), fit diffusion theory (as presented in Sections 1.4.1 and 1.4.2) well. Sirghi hypothesizes that this is due to the serial stages of the growth. Growth by diffusion is slowed because condensation occurs on the nearby surfaces. Then the motion of the liquid film towards to capillary meniscus, driven by the gradient in the disjoining pressure, is slow compared to diffusion. The calculated time is large because the viscosity of a thin water film is taken to be four orders of magnitude slower than that of bulk water. To test his hypothesis, Sirghi conducted experiments in which he moved an AFM tip back and forth at different speeds, then pulled the tips from the surface [37]. In each case the contact time was the same, but the pull-off forces decreased with increasing speed. This supports his hypothesis, because the liquid cannot flow quickly enough into the moving meniscus.

## 1.4.5 Theory for a Thermally Activated Gas-Liquid Phase Transition Between Non-Contacting Surfaces

A completely different theory is reviewed in this section. The case of two parallel surfaces brought into close proximity is considered. If the surfaces remain separated by less than  $|2r_K|$ , thermodynamic equilibrium does not prevail – eventually a meniscus will nucleate. This can qualitatively be understood in the sense that when two surfaces are in such close proximity, the vapor partial pressure can exceed the bulk value because molecules that evaporate immediately encounter another surface rather than diffusing into the bulk vapor. Theory and experiments for the capillary nucleation time are reviewed next.

The thermally activated first order gas-liquid phase transition theory is due to Restagno et al. [77]. Bulk energies due to vapor and liquid phases, and interfacial energies due to the solid-liquid  $\gamma_{SL}$ , liquid-vapor  $\gamma_{LV}$ , and solid-vapor  $\gamma_{SV}$ , between the parallel plates are considered in a macroscopic formulation. Figure 1.14 shows the equilibrium condition for a liquid droplet on a flat surface. Perfect wetting situation is assumed. According to the Young-Laplace equation, when the contact angle,  $\theta$ , is zero,

$$\gamma_{SV} = \gamma_{SL} + \gamma_{LV}. \quad (1.54)$$

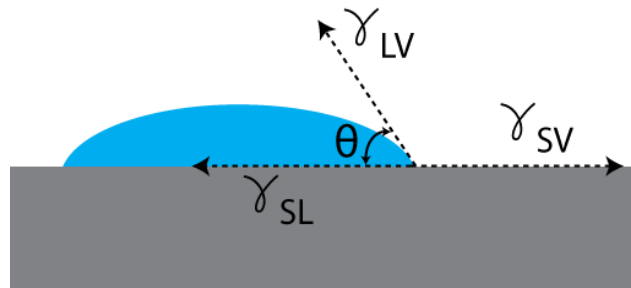


**Figure 1.14:** Schematic of the liquid droplet on a flat solid surface. At equilibrium three interfacial surface tensions are counterbalanced.

The grand potential  $\Omega$  of a pore for a nucleated capillary bridge can be written as

$$\Omega = -p_V V_V - p_L V_L + \gamma_{SV} A_{SV} + \gamma_{SL} A_{SL} + \gamma_{LV} A_{LV}, \quad (1.55)$$

where  $V_V$  and  $V_L$  are the volume of gas phase and liquid phase, respectively,  $p_V$  and  $p_L$  are the pressure of the vapor and liquid, respectively, and  $A_{SV}$ ,  $A_{SL}$  and  $A_{LV}$  are the total solid-vapor, solid-liquid and liquid-vapor surface area, respectively. The grand potential of a pore only with vapor existence can be defined as follows

$$\Omega_v = -p_V V_V - p_V V_L + \gamma_{SV} A_{SV} + \gamma_{SV} A_{SL}. \quad (1.56)$$

The difference between equation 1.55 and 1.56 gives the excess grand potential of the system  $\Delta\Omega_{\text{tot}}$ . By substituting equation 1.54 into equation 1.57, following equation is obtained

$$\Delta\Omega_{\text{tot}} = \gamma_{LV} A_{LV} - \gamma_{LV} A_{SL} + \Delta\mu\Delta\rho V_L \quad (1.57)$$

where  $\Delta\mu\Delta\rho$  is a replacement for  $p_V - p_L$ .  $\Delta\mu = \rho_L - \rho_v$  is the density difference between liquid and vapor respectively, and  $\Delta\mu = \mu_{\text{sat}} - \mu$  is the chemical potential difference between saturated condition and vapor condition. The volume and surface area are calculated in cylindrical coordinates as a result of circular symmetry (see Figure 1.15). Then,

$$\Delta\Omega_{\text{tot}} = \Delta\mu\Delta\rho 2\pi \int_0^{H/2} dz \dot{\rho}^2(z) - 2\pi\gamma_{LV} \dot{\rho}^2\left(\frac{H}{2}\right) + 2\pi\gamma_{LV} \int_0^H dz \dot{\rho}(z) \sqrt{1 + \dot{\rho}_z^2}, \quad (1.58)$$

where  $\dot{\rho}(z)$  is the position of the liquid-vapor interface, and the index  $z$  denotes differentiation. Here,  $\Delta\mu\Delta\rho$  represents the pressure difference between vapor and liquid; this can be related with Young-Laplace equation Eq. (1.10). Then  $\Delta\mu\Delta\rho \cong \gamma_{LV} r_K$ . Equation 1.57 cannot be solved analytically; however, there is a critical gap between the plates, and after that point nucleation is not expected. Moreover, a dimensionless function,  $f(H/H_c)$ ,  $\Delta\Omega_{\text{tot}} = \gamma_{LV} H_c^2 f(H/H_c)$  can be assumed. Here  $H_c$  is the critical separation which can be identified with  $|2r_K|$ . Lateral extension of the critical nucleus  $R^*$ , is much bigger than  $H$ , so the liquid-vapor interface can be assumed as semicircular shape. Then  $V_L = \pi R^{*2} H - \frac{\pi^2}{4} R^* H^2 + \frac{\pi}{6} H^3$ ,  $A_{SL} = 2\pi R^{*2}$ , and  $A_{LV} = 2\pi^2 R^* H - \pi H^2$  [77]. Redefined area and volume terms are substituted in equation 1.57, and the energy barrier for capillary bridge nucleation is given in the following equation

$$\Delta\Omega = \gamma_{LV}H^2 \left( \frac{\pi^2}{8} \frac{[1-(H/2H_c)]^2}{1-(H/H_c)} + \frac{H}{3H_c} - 1 \right). \quad (1.59)$$

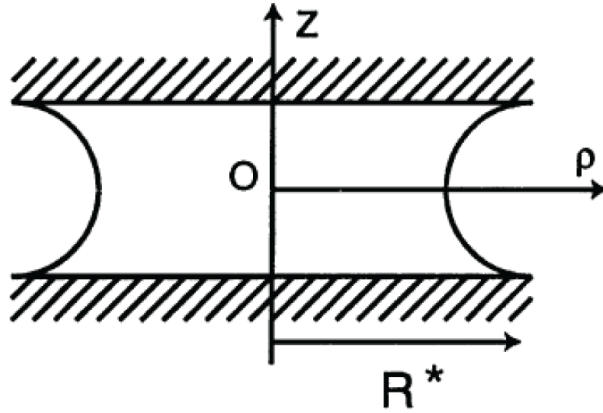


**Figure 1.15:** The critical nucleus for capillary condensation in three dimensions.  $R^*$  represents the lateral extension of the critical nucleus. The total curvature of the meniscus is equal to  $2/H_c$  [77].

Note that equation 1.59 diverges when  $H \rightarrow H_c$  as shown in Figure 1.16. This is expected because the meniscus will evaporate for  $H > |2r_K|$ . On the other hand, as  $H \rightarrow 0$ ,  $\Delta\Omega \rightarrow 0$ , as expected.

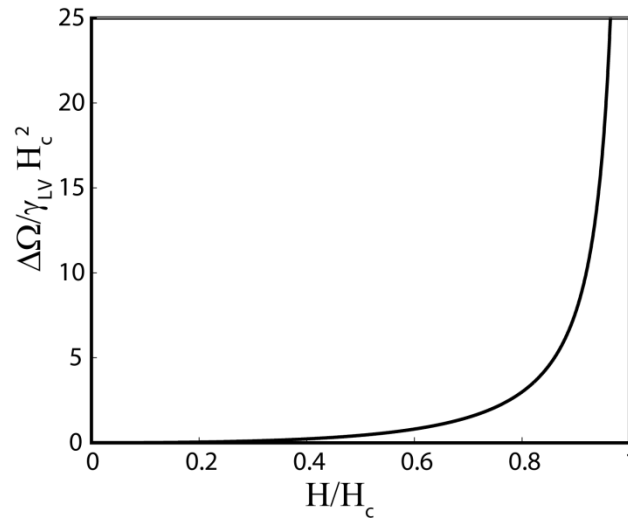


**Figure 1.16:** Free energy barrier as a function of the normalized width of the pore,  $H/H_c$ .

### 1.4.6 Experiments with Non-Contacting Surfaces - Exploring the Thermally Activated Gas-Liquid Phase Transition

A capillary bridge condensation and evaporation study between non-contacting surfaces with the SFA was reported by Maeda and Israelachvili [56]. They focused on evaporation of the capillary bridge [61]. The distance between surfaces  $H$  was adjusted initially less than  $2|r_k|$  to preserve the capillary bridge after jumping into contact as seen in Figure 1.17 B below [61]. A bulk liquid index of refraction was observed throughout the diameter of the condensate, indicating a capillary bridge. The diameter of the condensates varied from 40 to 0  $\mu\text{m}$  where the vapor is cyclohexane with  $p/p_s=0.938$  ( $r_k=17.1$  nm). Figure 1.17 C to F shows that when  $H>2|r_k|$ , the index of refraction decreases at the perimeter of the condensate as a result of evaporation, and finally the capillary bridge disappears. This evaporation time was only a few seconds, and was shorter at lower  $p/p_s$  and higher  $H$  values.

While studying evaporation of the capillary bridge, condensation of the liquid bridge can be observed in a hysteresis loop of index of refraction  $n$  [56]. The n-hexadecane bridge neck diameter was studied in this loop at  $p/p_s=0.88$  ( $2|r_k|\sim 50$  nm) [56]. Bridge evaporation starts at  $H>2|r_k|$ , and continues at the same separation until the bridge disappears. However, at nucleation and condensation formation  $H$  decreases until  $H\approx 2|r_k|$  to observe the capillary bridge. In the same study, the bridge evaporation time took 25 s from 10 to 0  $\mu\text{m}$  gap [56]. Moreover, when the surfaces are kept in contact for a longer time, the volume of the condensate increases. The result is a larger snap distance  $H_c$  [56].

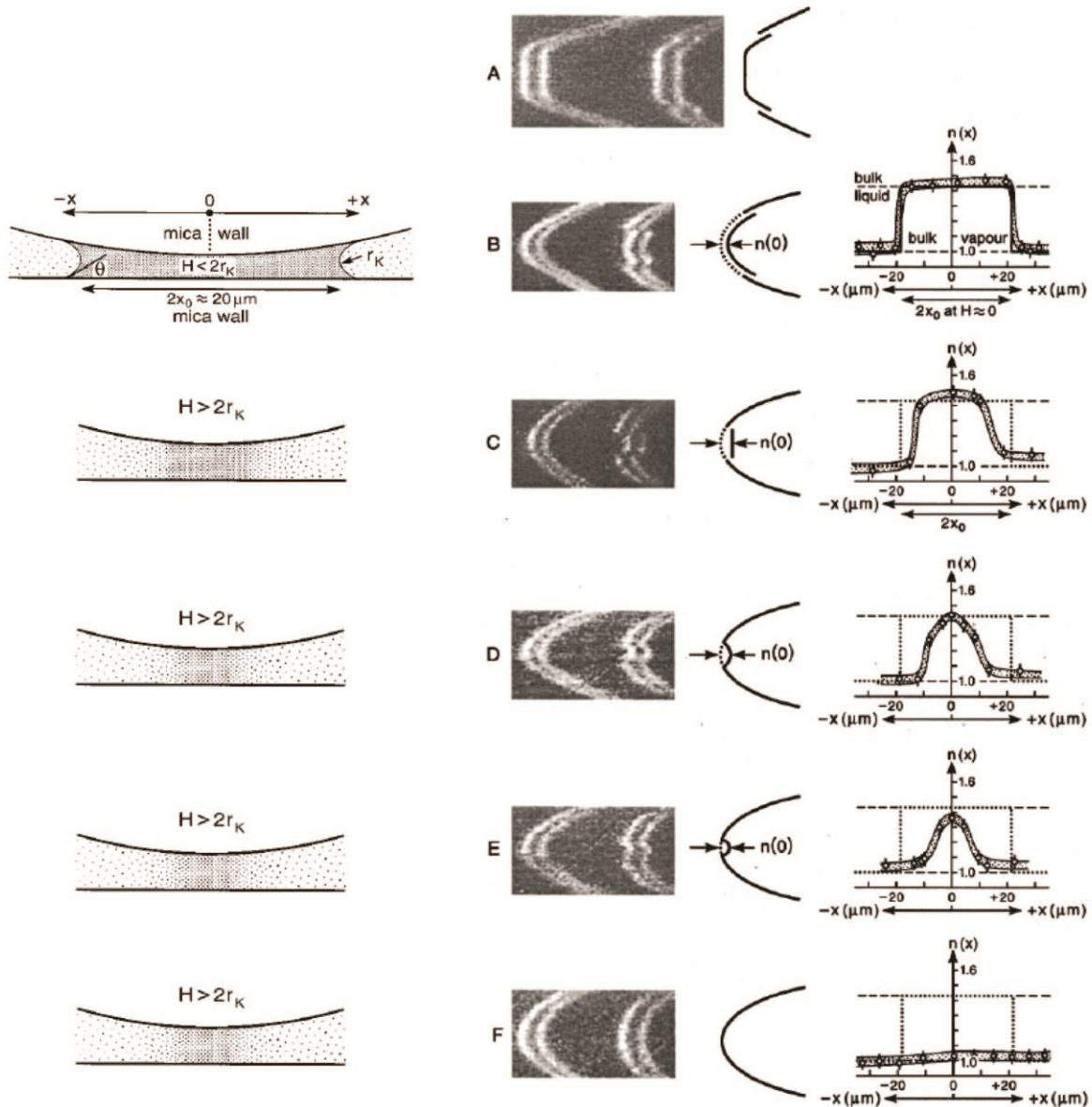


**Figure 1.17:** The steps of the evaporation experiment. Left row shows the schematic of the capillary condensate. Middle left row FECO images of adjacent odd-order and even-order fringes of the experiment steps. Middle right row is schematics of even-order fringes only, which give the refractive index profile  $n(x)$ . Right row shows the refractive index profiles  $n(x)$ [61].

In a different study using AFM, Szoszkiewicz and Riedo interpreted their results with the thermally activated gas-liquid phase transition theory reviewed in Section 1.4.5 [57]. AFM friction force was investigated as a function of the adhesion forces and the friction coefficient [78]. Adhesion forces were found as a result of Hertz contact theory between the AFM tip and

the sample and the capillary water bridges in the contacting area [79]. It is assumed that there are multiple asperities between the AFM tip ( $R_T > 10$  nm) and the surface as shown in Figure 1.18 [79,80]. Riedo et al. gave experimental and theoretical evidence [78,79] that these asperities can nucleate more capillary bridges with slower velocities, higher  $p/p_s$  conditions and higher normal loads [78,79]. Based on Hertz mechanics, the equation used for the friction force calculation is:

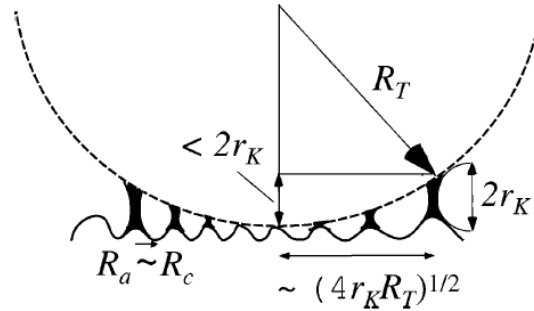


**Figure 1.18:** Capillary bridges in the contact area between the AFM tip and the sample [79].

$$F_F \cong \mu_0 (F_N + F_c)^{2/3} . \quad (1.60)$$

Here,  $F_F$  is the friction force,  $\mu_0$  is the friction coefficient,  $F_N$  is the normal load. The adhesion force  $F_c$  is found from Equation 1.61 as a function of velocity, relative humidity, AFM tip radius, normal load and surface roughness.

$$F_c \cong 8\pi\gamma_L R_T \left(1 + K F_N^{2/3}\right) \left(\frac{V_M}{\lambda R_c^2}\right) \frac{\ln \frac{v_0}{v_t}}{\ln \frac{p_s}{p}} \quad (1.61)$$

Here  $R_T$  is the AFM tip radius,  $V_M$  is the molecular volume of the liquid,  $K$  is the effective elastic modulus for the counterfaces,  $\lambda$  is the width of the distribution between the asperities,  $R_c$  is the capillary radius,  $v_0$  is a critical velocity [78], and  $v_t$  is the tip velocity.

Szozzkiewicz and Riedo [57] assumed an Arrhenius dependence for equation 1.59 to describe the influence of the temperature on nucleation time  $\tau$ , yielding,

$$\tau = \tau_0 \exp[\Delta\Omega/k_B T], \quad (1.62)$$

where  $1/\tau_0$  is the attempt frequency. Their data for  $\tau$  was found by plotting friction versus  $\log(v_t)$ , where  $v_t$  is the tip velocity, as seen in Figure 1.19 a. Above a critical velocity, there is only a weak dependence of friction on velocity. Below the critical velocity, friction rises rapidly as  $v_t$  decreases. The critical velocity is then taken to be a measure of the mean capillary nucleation time through the relationship

$$\tau = d_c/v_c, \quad (1.63)$$

where  $d_c$  is the contact diameter. Experiments were conducted with  $R_T=25$  nm between a soda lime glass substrate and silica tip. Nucleation times were found in the 0.7 to 4.2 ms range. The resulting plot is shown in Figs. 1.19 (b), and when  $\tau$  is plotted versus temperature an Arrhenius relationship is observed.

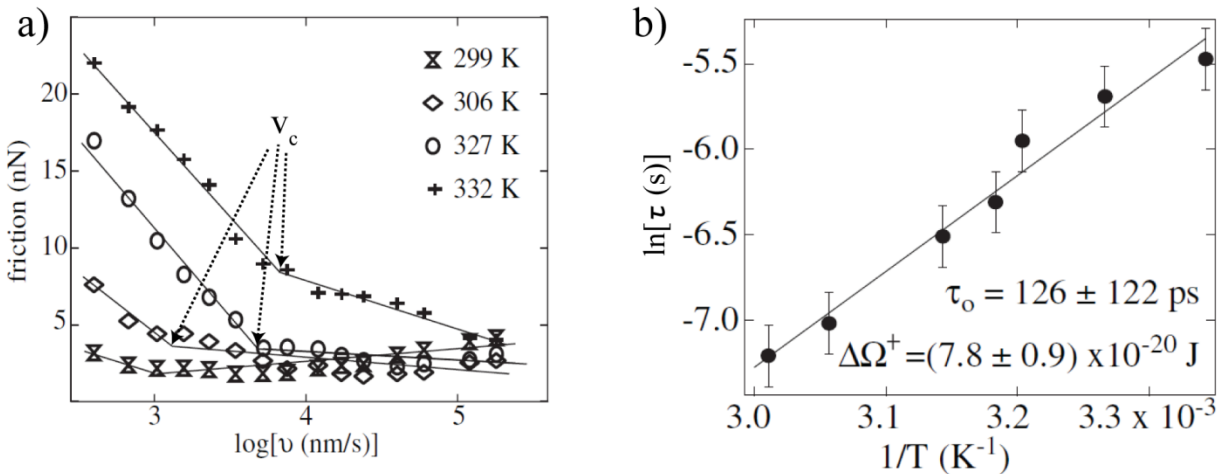


**Figure 1.19:** **a)** Friction force as a function of  $\log v$  for four different temperatures.  $v_c$  points out the critical velocity where the capillary forces are effective. **b)**  $\ln\tau$  as a function of  $1/T$ . The experimental data (scattered circles) are fitted (solid line) with the Arrhenius law [Eq. (1.62)]. A correlation coefficient of 0.997 is obtained [57].

To assess the data from a theoretical standpoint, the grand canonical thermally activated energy barrier was applied [57]. To find the nucleation time at a given partial pressure, values for  $\tau_0$  and  $H$  are needed. The attempt frequency for water is chosen as the pre-exponential factor because a surface water layer will be the source of the capillary bridge nucleation [57]. Tamura and Ichinokawa derived a coupled relation between surface vibrational modes and bulk vibrational modes for a small droplet [81]. Then Boyd et al. calculated the surface vibration modes and found that for small droplets such as 1.5 nm radius corresponds to ~750 GHz frequency and 2.9 nm radius corresponds to 200 GHz frequency [82]. Szoskiewicz and Riedo take  $1/\tau_0 = 45$  GHz [83].

To estimate  $H$ , Szoskiewicz and Riedo follow Iwamatsu and Horii's [84] approach, which predicts capillary condensation at  $H=3h_f$ , where  $h_f$  is the water film thickness on the surface. Capillary condensation occurs due to van der Waals forces because a water meniscus spontaneously coalesces at that distance [84]. This spontaneous time is assumed to be associated with the mean capillary nucleation time. The value of  $h_f$  is estimated as

$$H_f=[(-A_H r_K)/(6\pi\gamma_L)^{1/3}], \quad (1.64)$$

where  $A_H = 10^{-20}$  J for their experimental conditions in which  $p/p_s=0.37$ , and hence  $r_K \cong 0.5$  nm. The resulting value of  $h_f$  is about 0.16 nm, and it corresponds to  $H=0.48$  nm. The calculated energy barrier from equation 1.59 is  $2.7 \times 10^{-20}$  J. This value agrees well with the experimental value of  $7.8 \times 10^{-20}$  J, but the calculated and experimental values of nucleation times according to these energy barrier values differ by five orders of magnitude. This large difference is due to the exponential term, which is very sensitive to small changes in energy barrier. The energy barrier in turn is very much dependent on the estimate of  $H$ .

Greiner et al. showed the isothermal environment difference from the local heated region experimentally [85]. They used the AFM friction force experiments to detect the capillary bridge formations. 20 nm radius AFM tip and silicon wafer were used as surfaces with varying AFM tip temperatures from 25 to 120 °C. In the same way that Szoskiewicz et al. calculated, they found attempting frequency as ~100 kHz and energy barrier as  $\sim 4.7 \times 10^{-20}$  J. Attempting frequency decreased as a result of cooler environment with lower kinetics around the capillary bridge.

More recently a novel custom AFM with a quartz tuning fork (QTF) has been used to measure capillary nucleation across a gap [86]. In this experiment, Arrhenius behavior was also measured, similar to the above work [57,58,85], and also as predicted theoretically [77]. High quality factor  $\sim 1000$  of the tip provides a known rate approach mechanism and a constant surface separation [86]. However, a drift rate of 10 pm/s compared to an approach rate of 75 pm/s introduces some uncertainty into the reported results. Stepwise discrete approach with 0.15 nm step size stops for a 2 s time interval, and during the waiting time capillary nucleation is detected as a lateral amplitude drop. This technique avoids asperities with large gaps that require longer than 2 s to nucleate the capillary bridges

In summary, SFA and AFM are the two methods that have been practiced to investigate non-contacting asperity bridge dynamics. For a single big ( $\sim$ cm) asperity, SFA is capable to observe the capillary bridging, but it is not applicable to multi-asperity bridging experiments. AFM friction experiments point out the capillary formation as a function of velocity, and Szoszkiewicz explains the capillary force increment with time as a result of multi-asperity bridging formation on the rough surface of the substrate [57]. There is an issue with Szoszkiewicz's approach. It is assumed that there are non-contacting capillary bridges between contacting AFM tip and the substrate. Szoszkiewicz's results can also be evaluated according to Sirghi's approach discussed in Section 1.4.6. There is still lack of study to show the multi asperity or nano scale non-contacting bridge formation dynamics.

## 1.5 SUMMARY

At thermodynamic equilibrium in vapor environments, the Kelvin equation (1.14) is accurate over a wide range of  $p/p_s$  and for many different liquids. Indeed, this equation has been verified with many different sphere sizes including the cm [13], micrometer [74] and nanometer scales [83]. However, the dynamics of the capillary bridge nucleation and growth lack understanding, especially at the micro- and nanometer scales.

Single asperity vs. surface capillary bridge dynamics experiments are available in the literature [37,57,73,74]. Theories, which try to explain the experiments, include bulk gas diffusion [73], Knudsen diffusion [37], surface liquid flow effect on capillary growth rate [37],

and energy barrier to reach the liquid bridge form [57]. None explain the experiments in a fully satisfactory manner at the micro- and nanometer scales.

In principle, micro- and nanometer capillary dynamic single asperity experiments and theory will help predict capillary dynamics of real surfaces, which always exhibit roughness. However, very few if any such experiments have been conducted. Therefore, it is important to develop protocols and conduct experiments that measure dynamic capillary effects of multi-asperity surfaces.

## 1.6 THESIS GOALS AND KEY RESULTS

The purpose of this study is to investigate the kinetics of the capillary nucleation in multi-asperity surfaces by constructing a test system (Chapter 2), conducting experiments (Chapter 3), and explaining the results with theoretical studies (Chapters 4 & 5).

Experimental studies in the literature tend to study capillary growth dynamics at single asperities. There is not yet a reported study in the literature for multi-asperity nanoscale surface capillary dynamics. We aim to investigate capillary condensation dynamics between nano-scale multiasperity surfaces. Microcantilever crack healing experiments are conducted and surface adhesion energy measurements are tracked over time after a step change in humidity is applied.

**In Chapter II, we give the details of the experimental samples and setup.** To establish the effects of capillary nucleation and growth on adhesion in the microcantilever crack healing experiments, a smooth surface (2 nm root mean square roughness) is beneficial. Our samples are fabricated through chemical vapor deposition to attain a smooth surface. We built up the environmental chamber to control the vapor partial pressure precisely, and to keep the sample surface clean during the experiments. To maximize the capillary adhesion forces due to hydrophilic surfaces, we built and attached a plasma cleaning system to the chamber. To observe the crack healing events inside the chamber, we utilized a long-working distance interferometer above the chamber. We tested the system to make sure that the deflection data used to quantify adhesion is reliable, consistent, and repeatable.

**In Chapter III, we analyze the crack healing data in detail.** Crack healing data as a function of time was interpreted as an average crack healing velocity,  $\bar{v}$ . We discovered that a plot of  $\bar{v}$  versus energy release rate,  $G$ , reveals log-linear behavior, while the slope  $|d[\log(\bar{v})]/dG|$  decreases with increasing relative humidity. We explained the trend with capillary nucleation mechanisms, and we proposed an empirical fit to estimate the  $\bar{v}$  as a function of  $G$ .

**In Chapter III, we also explore the adhesion energy at different partial pressures of alcohol vapors that can be used as lubricants in MEMS devices.** We obtain equilibrium adhesion energy values for *n*-pentanol and ethanol. Then, we compare them with water experiments. We explain the differences and similarities by analyzing the surface roughness and Kelvin radius  $r_K$ .

**In Chapter IV, crack healing experiments are interpreted with a first order numerical model.** Equally spaced asperities at the same height with the same radius are modeled as a multi-asperity surface. Then, the cantilever with multi-asperities modeled against a flat surface. Asperity pitch variation effects are studied. Although the interface model is oversimplified, the log-linear trend and decreasing slope in increasing RH behaviors are captured qualitatively.

**In Chapter V, the first order model is improved, and a more realistic model is presented to estimate the crack healing trends quantitatively.** The first improvement is a better interface description. Surface roughness of the experimental samples were implemented by applying a Gaussian distribution of the asperity heights. Furthermore, we realized that liquid film adsorption is playing an important role. Therefore, we incorporated the effect of adsorbed liquid films on the surfaces to nucleate more capillary bridges. Finally, to attain good quantitative agreement, the capillary nucleation time theoretical equation has been modified. This equation diverged very quickly as a function of gap. This meant our model could only predict a small portion of the experimental data range. We presented our numerically fit capillary nucleation time equations and show good agreement with capillary crack healing rate trends.

## 1.7 CONTRIBUTIONS

We identify contributions to date and expected contributions in the capillary dynamics and capillary adhesion between multi-asperity surfaces. Two articles so far published in Review of Scientific Instruments [59] and Langmuir [87]. Two other journal articles are in preparation.

- Kohonen's [73] theoretical curve of diffusion is correct even though his expression for  $G$  (equation 1.35) is incorrect due to a typo. The later paper by Rabinovich [74] corrects the expression for  $G$ , but then appears to integrate incorrectly, resulting in an incorrect result (Chapter 1).
- It is possible to build a system that can control the partial pressures of water and alcohol vapors. The partial pressure can also be controlled at temperatures up to 50 °C (Chapter 2).
- In situ surface plasma cleaning is an effective way to observe the capillary adhesion effects at low partial pressures (Chapter 2).
- Chilled mirror hygrometer is a promising technique to measure the partial pressures of the alcohols (Appendix D).
- Observations of cantilever deflections by long working distance interferometry can be accomplished without interfering with experiments (Chapter 2).
- After steady state environment conditions are attained, microcantilever crack healing continues. This implies the capillary nucleation until the equilibrium can be detected and crack healing rates can be quantified at constant RH with the experimental system (Chapter 3).
- Microcantilever crack healing experiments verify that capillary condensation takes a longer time at large gaps compared to capillary growth times (Chapter 3).
- Adhesion energies of ethanol and  $n$ -pentanol vapor at different partial pressures have been obtained. Comparisons with water are explained in terms of the Kelvin radius and the surface tension differences (Chapter 3).
- Surface roughness effects on adhesion have been verified by water, ethanol and  $n$ -pentanol vapor experiments. Particles on ethanol sample causes order of magnitude less adhesion values compared to  $n$ -pentanol and water samples (Chapter 3).

- Qualitative agreement with the crack healing experiments is explained in terms of a simplified description of the interface and implemented with a numerical model (Chapter 4).
- Quantitative agreement with the crack healing experiments are demonstrated with more advanced numerical models that take into account more details of the interface as well as the adsorbed film layer. Also an empirical modification of nucleation rate theory is found to be necessary to attain good agreement with the data

**Journal contributions to date:**

1) E. Soylemez, and M. P. de Boer, "Capillary-Induced Crack Healing Between Surfaces of Nanoscale Roughness," *Langmuir*, vol. 30, 11625-11633, 2014.

2) E. Soylemez, R. A. Plass, W. R. Ashurst, and M. P. de Boer, "Probing MEMS in an environmentally controlled chamber using long working distance interferometry," *Review of Scientific Instruments*, vol. 84, 2013.

3) E. Soylemez, and M. P. de Boer, "Partial Pressure Effects of Water, *n*-Pentanol and Ethanol on Crack Healing in Oxidized Polysilicon," *to be submitted*.

4) E. Soylemez, and M. P. de Boer, "Modeling of Capillary-Induced Crack Healing at Various Partial Pressures Between the Rough Nanoscale Surfaces," *to be submitted*.

**Other journal contribution published during the Ph.D. work**

5) E. Soylemez, M. P. de Boer, U. Sae-Ueng, A. Evilevitch, T. A. Stewart, and M. Nyman, "Photocatalytic Degradation of Bacteriophages Evidenced by Atomic Force Microscopy," *PloS one*, vol. 8, p. e53601, 2013.

# **Chapter II: Probing MEMS in an Environmentally Controlled Chamber using Long Working Distance Interferometry**

## **2.1 INTRODUCTION**

The environment in which micro- and nanoscale devices operate can strongly influence their performance. This is particularly true if mechanical contact, whether intended or not, occurs. Organic vapors can rapidly flow into the narrow channels of such devices [88], and often have beneficial effects. Perfluorodecanoic acid enables billions of cycles in micromirror displays [89], and a variety of alcohol vapors significantly reduce or perhaps eliminate wear in sliding micromachined contacts [90,91]. Organic vapors in the environment can instead degrade micromachined devices. For example, a hydrocarbon contaminant forms a carbonaceous deposit in microrelay devices, increasing their resistance [92–94].

Water vapor has a strong effect on micromachined device performance. The relative humidity (RH) level strongly increases the adhesion of surfaces that are hydrophilic (contact angle  $< 90^\circ$ ) [68,95]. Polycrystalline silicon (polysilicon) friction and wear are likewise strongly influenced by RH level [96–98]. Another important effect is anodic oxidation, in which an oxide is induced to grow on a polysilicon surface subject to an electric field in air. Its growth is strongly enhanced as RH increases [99,100].

Environment affects materials due to corrosion or oxidation. Water vapor induces stress corrosion cracking in glass [101]. Silicon oxidizes rapidly, and therefore the issue of vapor-induced crack growth in micromachined polysilicon has been of much interest [102–104]. A thin film of water or any vapor readily adsorbs to surfaces, and the film thickness can be extracted from effective mass changes in a resonant device [105].

Ambient pressure will strongly affect performance. Due to the thermal conductivity of gas at atmospheric pressure, thermal actuators require significantly more current to achieve a give force or displacement in air than in vacuum [106]. It is well known that mechanical damping is significantly affected by ambient pressure greater than  $\sim 10^{-4}$  Torr [107].

Because of these many effects, it is useful to examine the performance of micro- and nanodevice in controlled environmental conditions in a general purpose instrument. MEMS devices are usually exposed to air after fabrication. In air, adventitious hydrocarbons adsorb on the surface in an uncontrolled and non-uniform fashion. In controlled tests, the device surface and the chamber ideally will be pristine. Subsequently, a controlled amount of contaminant or vapor partial pressure will be introduced. It is often useful to characterize the device performance by applying electrical signals and monitoring device deflections in both in-plane and out-of-plane directions (parallel and perpendicular to the substrate, respectively). Preferably, wire-bonding of the device will not be needed, as this requires further process steps.

Several instruments exist that have some of these capabilities. For example, Lakeshore Instruments [108] and MMR Technologies [109] probe station chambers control temperature while devices are actuated at over a broad frequency range. The chamber described in this chapter is unique in that it combines the following attributes:

- (1) a plasma chamber for cleaning devices is directly connected to it,
- (2) imaging of micromachined devices is enabled by a long-working distance interferometer with 5, 10 and 20 X objectives. Electrical signals can be applied through probes and device motion can be measured in 3-dimensions using a CCD camera integrated with scripting software.
- (3) it is constructed with all ultra-high vacuum (UHV)-compatible hardware, enabling high temperature (200 °C) bake-outs and high speed pumping such that a pressure of  $10^{-9}$  Torr is attainable, and
- (4) clean gases, vapors or contaminant gases can be introduced at controlled levels.

In the following, we detail the construction of an Environmental Interferometric Microprobe station. To demonstrate the performance of the system, we plasma clean microcantilevers in the adjacent load lock, and then directly transfer them into the main chamber.

Thereafter, water vapor is introduced. Adhesion is an important reliability concern in micro- and nanoscale devices, but is usually measured at equilibrium. In Section 2.3.2, we present new data on adhesion energy of plasma-cleaned microcantilevers as a function of time at a fixed humidity level.

## **2.2 DESCRIPTION OF SYSTEM COMPONENTS**

The system consists of (a) a main chamber, (b) a load lock with plasma cleaning and sample transfer mechanism, (c) a vapor delivery system and (d) an optical interferometer. Figure 2.1 is a rendering of the system indicating (a), (b) and (c) above, as well as important subcomponents. The interferometer is seen in Figure 2.2a.

### **2.2.1 Main Chamber**

As seen in the center of Figure 2.1, the main chamber body is a stainless steel 8 inch extended spherical body (Kimball Physics model MCF800-ExtOct-G2C8) with eight equally separated 2.75 inch CF (Conflat) flange ports. One flange port is connected to inlet of the vapor delivery system (entry RH sensor), and another connects to the vapor delivery system outlet (exit RH sensor). Four of the other 2.75 inch flanges are used for electrical probe connections (XYZ manipulator & electrical feedthrough), as described below. Another 2.75 inch flange is available for pumping into the UHV realm with a Thermionics ion pump (model HP-020/IH, not shown), and the last is used for sample transfer from the load lock chamber, as described below.

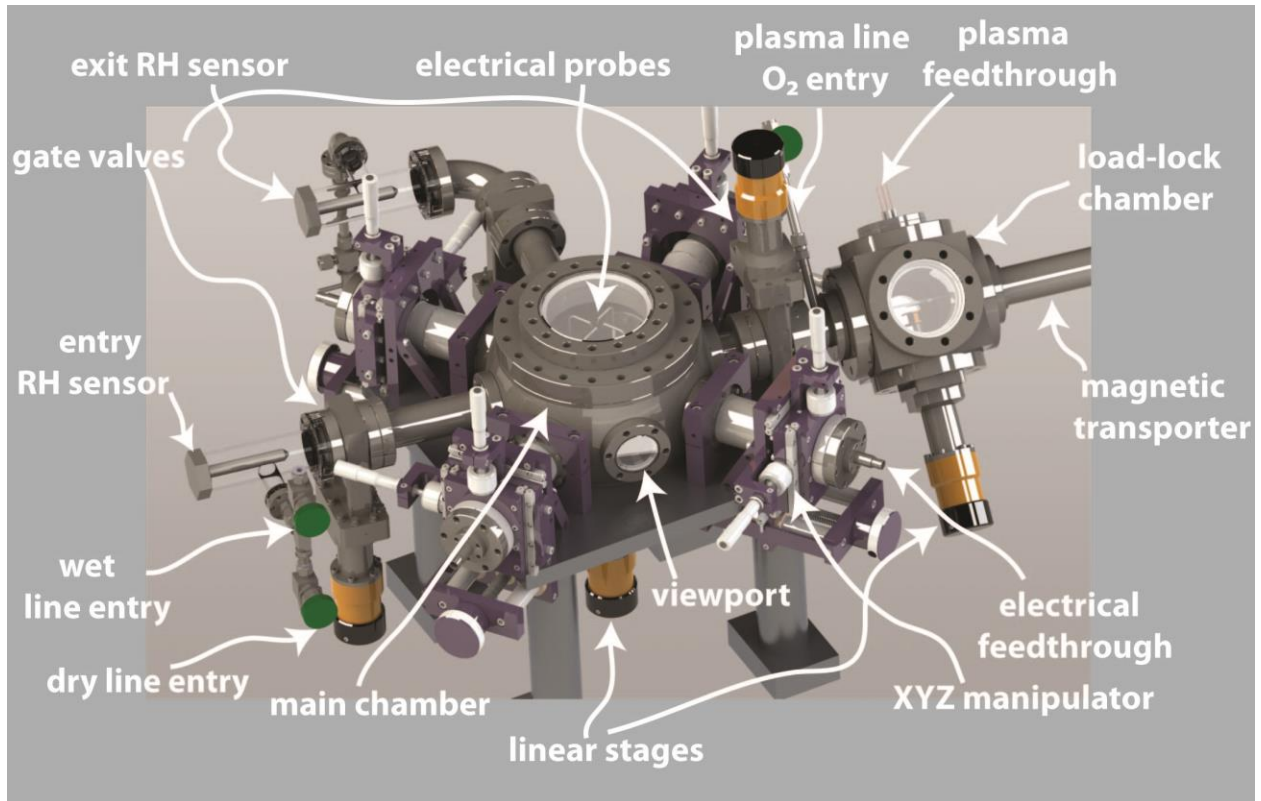


**Figure 2.1:** A computer-aided design (CAD) rendering of the Environmental Interferometer Microprobe Station.

At the bottom of the chamber there is an 8 inch MDC multiport flange (model MAF800-6-133T) including five circumferential 1.33 inch CF flange ports and one central 2.75 inch CF flange port. These are used for sample heating and temperature sensor feedthroughs and for a vertically-aligned linear stage feedthrough (linear stage), respectively. The MDC linear stage (model HLM-275-3) is used to accept the sample from the load lock and elevate it into the focal plane for the optical microscope objective. The top of the chamber is a 6 inch MDC (model VP-400QZ) viewport for optical observation of the samples.

Figure 2.2 is an optical image of the system, now including the optical interferometer. The four UHV compatible electrical probes are mounted on Thermionics (model EC-1.39-2) XYZ welded bellows micromanipulators, one of which is annotated in Figure 2.2a. The probe tips can be seen in Figure 2.2b. Their positional accuracy is  $\sim 2.5 \mu\text{m}$  along the  $x$ - and  $y$ -axes (in-plane), and

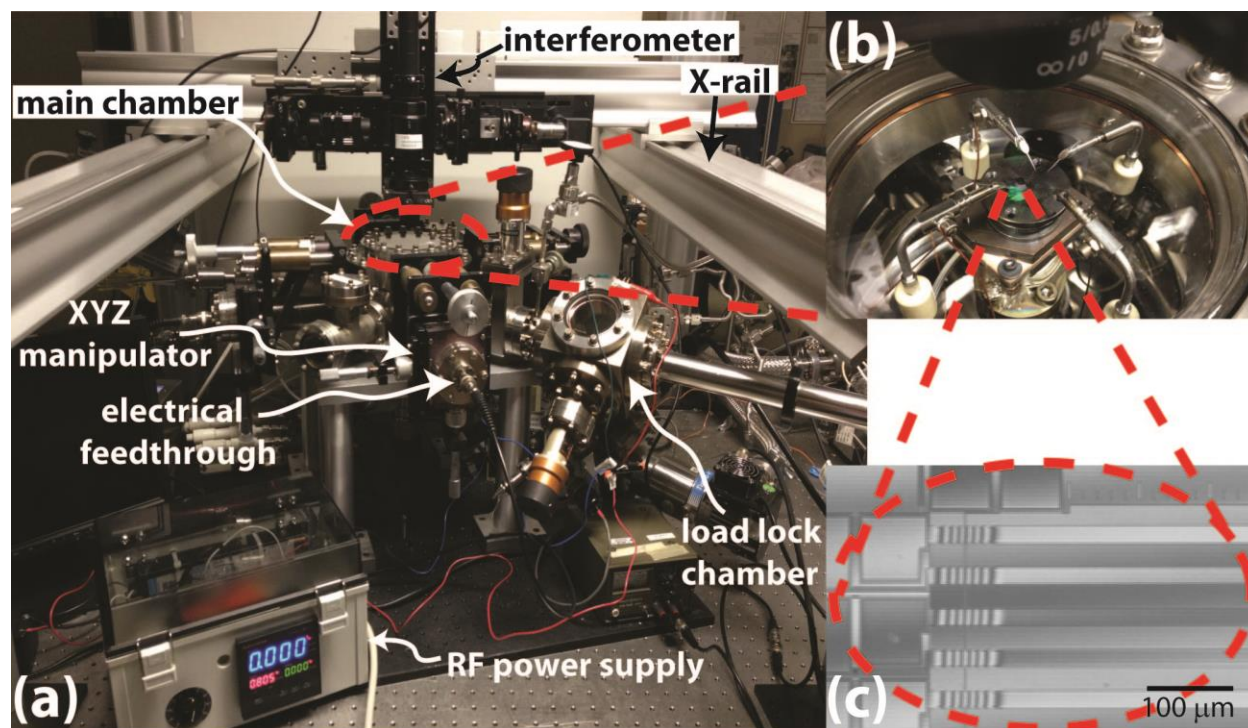


**Figure 2.2:** (a) Optical image of the Environmental Interferometer Microprobe Station. (b) Optical close-up of area imaged inside the main chamber, including electrical probes that allow in-situ actuation of micromachined devices. (c) Interferogram of initially freestanding microcantilevers adhered by capillary forces with  $p/p_{\text{sat}} \approx 1$ .

$\sim 13 \mu\text{m}$  along the vertical  $z$ -axis. MDC (model BNC-133) electrical feedthroughs are mounted to the ends of each XYZ manipulator. MDC kapton-coated 0.021 inch diameter cables are connected from electrical feedthroughs to the electrical probes. An s-shaped electrical probe body is assembled from stainless steel rod. To insulate it electrically from the main chamber walls, the body is cut into two pieces, and an MDC ceramic standoff (model 607602) connects them mechanically. Signatone (model SE-T) probes are used to make contact with the actuation pads of the micromachined devices.

With this hardware, the main chamber can reach a pressure as low as  $10^{-9}$  Torr. Details on the pumping system are given in Section 2.2.3.

### 2.2.2 Load-Lock Chamber

Hydrocarbon contaminants can be removed by plasma cleaning of samples. However, to avoid re-adsorption, they must subsequently be transferred to the main chamber without

exposure to air. The load-lock chamber is constructed with these objectives in mind. As seen in Figure 2.1, the load lock chamber body is an MDC cube (model CU250-6), and it is connected to the main chamber by an MDC gate valve (model GV-1500 V), which isolates the two chambers while a sample is cleaned.

A front-mounted MDC viewport (model VP-250) enables sample entry and visual inspection. A platen sample holder (MDC SAM-1), to which the sample is affixed, is connected to a vertically aligned heavy duty linear motion MDC feedthrough (model HLM-275-3), as annotated in Figure 2.1. Its three-inch linear range enables it to extend into the plasma (described next), and to be withdrawn so that the sample holder can be picked up by a transporter which conveys it into the main chamber as described below.

A standard electrical feedthrough (Kurt J. Lesker model EFT0543053) with sealed copper wires for plasma generation is mounted through the top of the load lock. A simple radio-frequency (RF) plasma generator supplies power to the electrodes inside the load lock chamber, as shown in Figure 2.3a. Regarding the electrodes, the copper wires are cut as short as possible inside the chamber and are connected to titanium rods. These titanium rods, which form the anode and the cathode of the plasma, are covered with Unique Wire Weaving Co. titanium meshes (0.016" diameter, 20x20 wires/inch, twill). The Ti material is chosen to minimize sputtering during the plasma treatment [110]. The surface area of the meshes is as large as possible within the limits of the chamber geometry to improve plasma stability and to minimize its power density.

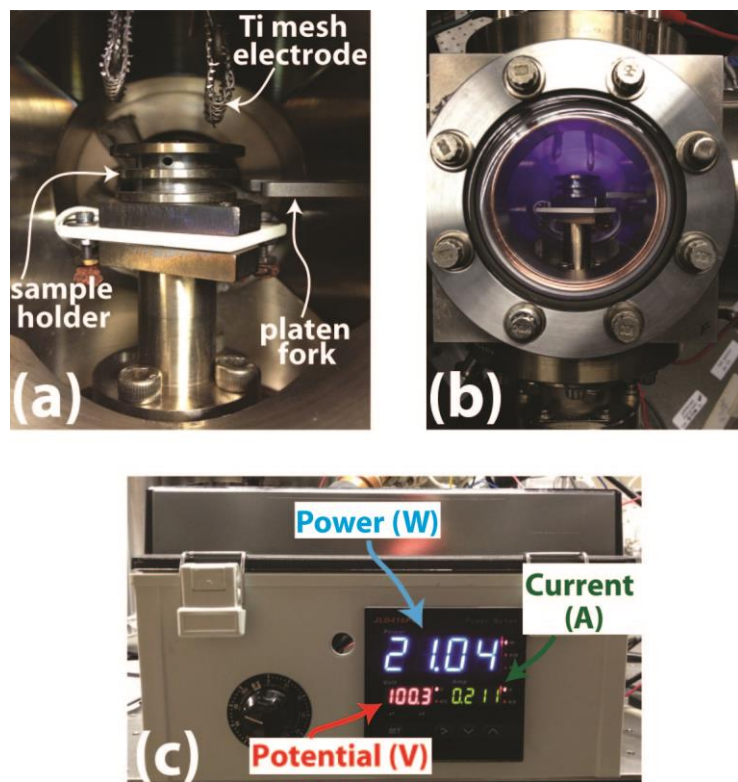


**Figure 2.3:** (a) Load-lock chamber interior indicating sample holder, plasma electrode Ti meshes and platen fork for transferring samples. (white boroelectric heater is below the sample holder) (b) View of glowing plasma inside the load-lock chamber through viewport. (c) RF plasma generator box with parameters displayed.

The custom RF power supply consists of three components: a voltage output transformer, a fluorescent light ballast and a power meter. The 120 VAC line voltage is connected to a variable voltage output transformer (model 6994K32) to control the power supplied to the ballast. A Philips ballast (model Advance Centium ICN-2P60-SC) is used to establish an output voltage with amplitude up to 1500 V AC operating at 77 kHz, as measured by an oscilloscope with a 100X attenuation probe. A Coldfusion power meter (model HB416PVA) is connected in parallel with the plasma electrode cables to monitor the power, voltage and current drawn by the ballast during plasma processing. Accordingly, the measurement of power used by the ballast is approximately the power delivered into the plasma. Since it is not necessary to precisely characterize the plasma conditions, the approximate measurements suffice. These components are held in a NEMA 4X/13 polycarbonate box (model McMaster-Carr Part number 7335K21), as

seen in Figure 2.3c. For plasma cleaning, high purity O<sub>2</sub> gas is supplied through a variable rate leak valve (Agilent model 951-5106).

Opposite the gate valve, a magnetically-coupled transporter (MDC model MT-24) is connected to transfer the samples from the load-lock chamber to the main chamber along a horizontal linear path. An MDC platen fork (model FOR-1), designed to grasp the sample holder, is attached to the end of the transporter arm. In the main chamber, the 2.75 inch MDC viewport (model VP-150QZ) enables observation of the main chamber linear actuator position. This aids the sample transfer from the transporter to the main chamber linear actuator.

### **2.2.3 Environmental Control**

Vacuum is established in the main chamber before an experiment to minimize the adventitious hydrocarbons. A Varian dry scroll roughing pump (model SH-110) backs a Varian (model V 70LP) turbo pump. A single pumping system is used. The load lock to main chamber gate valve must be open in order to pump on the main chamber. Using the dry scroll pump alone, a medium vacuum level of 60 mTorr is measured by a thermocouple gauge. Without a bakeout, the turbo pump further reduces the pressure to  $\sim 10^{-7}$  Torr in the load lock chamber and  $\sim 10^{-6}$  Torr in the main chamber, as measured by a cold cathode ion gauge (MKS model 423 I-MAG). After a UHV bakeout conducted at 200 °C, the main chamber reaches a pressure of  $10^{-9}$  Torr with the help of the ion pumping as mentioned above.

Besides attaining high vacuum, vapors can be delivered into the system at atmospheric pressure. A schematic of the vapor delivery system is shown in Figure 2.4. A high purity nitrogen tank is regulated to below 5 psi. To obtain the desired stable pressure, two stage pressure reducing Swagelok valve (model KCY) is connected to the cylinder. Then, the line is connected to another high precision pressure reducing regulator (Equilibar Type 10 LR). Gilmont ball type gas flow meters and needle flow valves control the mix ratio and hence the partial pressure of vapor in the line. To ensure the “wet” N<sub>2</sub> line is fully vapor saturated the nitrogen sequentially passes through two fritted bubblers filled with deionized (DI) water. A vapor-saturated N<sub>2</sub> line mixes with a dry N<sub>2</sub> line at the vapor entry chamber. The vapor entry chamber is initially isolated from the main chamber to allow the mixture to stabilize before

entering the main chamber. The entry line and exit line are then opened to allow continuous flow through the chamber.

There is also a vent line through a third flow meter for clean, controlled venting of the load lock and main chamber. Finally, isolation valves upstream from the mix point of the “wet” and “dry” lines are needed to eliminate cross contamination of these lines when one is running under either fully dry or full vapor saturated conditions.

Water vapor experiments are monitored by calibrated Vaisala RH and temperature sensors (models HMT334 and HMP234). The needle flow valves are adjusted according to the desired RH level. The partial pressure  $p/p_s$  can be controlled from 0 to 1 (corresponding to RH from 0 to 100%). One sensor is mounted in the vapor entry chamber, and the other one is in the vapor exit chamber. The sensor data are recorded via an RS-232 interface.

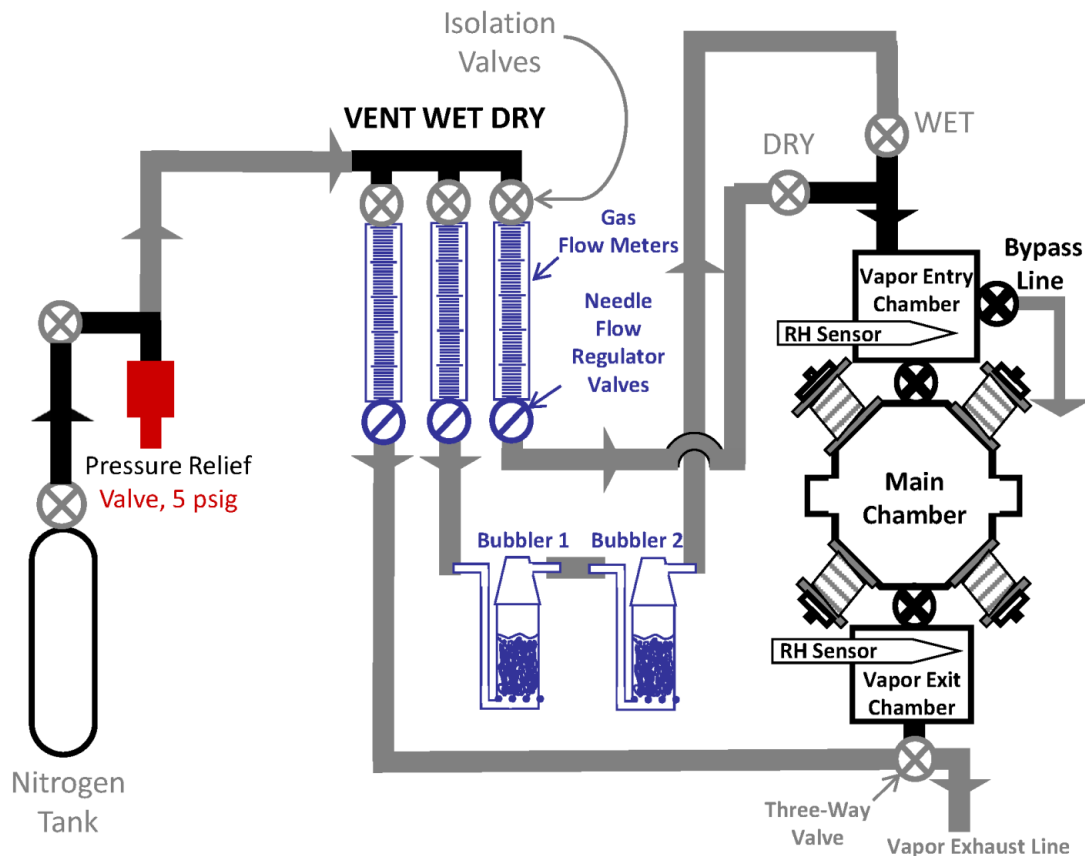


**Figure 2.4:** Atmospheric pressure vapor delivery system schematic. Arrows on the various lines show the direction of normal N<sub>2</sub> carrier gas flow.

## 2.2.4 Optical Detection System

A detailed explanation of the long working distance interference microscope can be found in the article by Sinclair [111], and the user guide is prepared (Appendix A). As described there, a quartz compensating plate of optical thickness equal to the viewport glass is placed in the interferometer reference arm in order to optimize contrast. As shown in Figure 2.2a, Newport optical X-rails (X-95 series) support the microscope. Positioning in the xy-plane is accomplished by sliding the microscope on the rails. The free working distance (~2.5 centimeters with a 5X objective) coupled with the low-profile electrical probe design enables interferometry through the chamber viewport, as seen in Figure 2.2c. There remains ~1.25 cm vertical height from the bottom of the viewport to the sample. This provides ample room to move probes laterally between the window and the sample. This configuration also works with 10X and 20X objectives [111].

To minimize vibrations, the entire system is mounted on a Newport optical table (model RS 4000). Nonetheless, due to laboratory air currents and due to mechanical coupling through connections such as the pump roughing lines, the gas feed lines and electrical cables, vibrations are inevitable. Much work was done to understand and minimize these noise sources. Vibrations transmitted through the Swagelok gas feed lines were reduced by making the final connection to the table with flexible lines. Also, gas feed line ceiling connections were made with rubber dampers.

Using phase stepping interferometry (PSI) [112], multiple measurements of the same surface were used to quantify the interferometer precision. One hundred line scans, each 200 pixels (~2.5  $\mu\text{m}/\text{pixel}$  with a 5X objective) were taken along the same region. Figure 2.5a illustrates a single linescan on a silicon wafer, which is expected to be optically flat. A linear best fit to this data was determined, with a result of 1.2 nm rms error per pixel. In this fit, the slope is removed because it only represents the relative tilt between the reference surface and the sample, while the first data point is set equal to zero. The average rms noise for one hundred scans, taken at 8 s time intervals, was 2.0 nm/pixel, as seen in Figure 2.5b. Some of the data show higher noise of up to 7 nm/pixel. This could be directly attributed to transient laboratory vibrations, which cause the phase shifting of the interferometer reference surface to be

inconsistent, introducing error into the PSI algorithm. One method of dealing with this is to determine if the linescan data from each of the five phases are within a certain tolerance of  $\pi/2$  before accepting data.

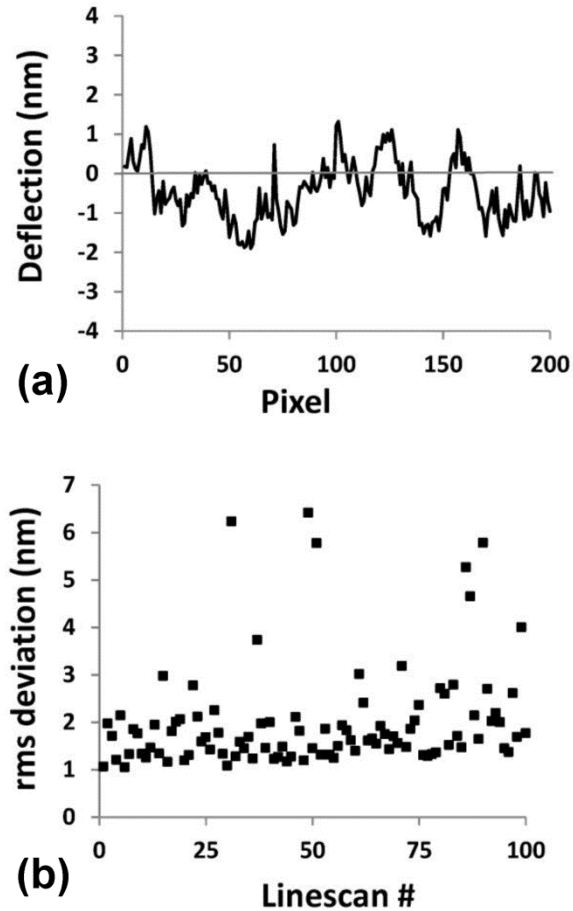


**Figure 2.5:** (a) Deflection of a silicon wafer over a 500 mm length. For this single linescan, the root mean square (RMS) error per pixel from a linear fit is 1.2 nm. (b) RMS error versus linescan number for 100 linescans taken at 8 s intervals.

## 2.3 PRELIMINARY RESULTS

### 2.3.1 System Qualification

Plasma conditions were first established by ensuring that negligible material sputtered from the Ti/Cu electrodes onto a glass slide, as evaluated visually. Minimizing the length of the Cu electrodes and covering them with the Ti mesh significantly improved the clarity of the glass slide. At 15 W (voltage output transformer power) and 60 minutes, however, some sputtering deposit was still visible. By decreasing power to 3.8 W while keeping time at 60 minutes, slides remained optically transparent. Actual plasma treatments were done at 2.9 W for 30 minutes.

Next, we evaluated sample cleanliness with respect to hydrocarbon contamination by measuring the contact angle of DI water on Si (100) blanks before and after plasma cleaning in the load lock. Contact angle (CA) was measured on a custom-built apparatus (Appendix B). Before the plasma treatment, Si blank samples had contact angles of  $70^\circ$ . We loaded a Si blank into the load lock chamber, and introduced  $O_2$  at 250 mTorr pressure. An  $O_2$  plasma was ignited with output ballast voltage at 1300 V amplitude, as observed in Figure 2.3c. After ignition, the voltage was dropped to 600 V and a voltage output transformer power of  $\sim 3$  Watt was maintained for 1 minute.

Immediately following the plasma treatment, the CA was  $0^\circ$  in laboratory air. For a sample that was plasma cleaned and then left in laboratory air for 24 hours, a  $24^\circ$  contact angle was measured. Another sample was placed in the load lock and cleaned under the same plasma conditions. Then the gate valve was opened, and the sample was transferred to the main chamber. The main chamber was then vented with  $N_2$ . After 24 hours, the sample was removed, and the CA was  $0^\circ$ . This experiment was repeated, but now we purged continuously with  $N_2$  for 17 hours. Again, a  $0^\circ$  CA was measured. Hence, the chamber indicates a  $0^\circ$  contact angle after long exposures, indicating a “clean” hydrophilic surface.

Another important system qualification is the stability of RH and temperature with respect to time. Figure 2.6 shows RH and temperature values of the entry and exit lines over a 102 hour period. It includes long periods of stable RH values in which entry and exit sensor

readings are not changing by more than  $\pm 2\%$ . This data shows that laboratory temperature control is  $\sim \pm 0.5^\circ\text{C}$ .

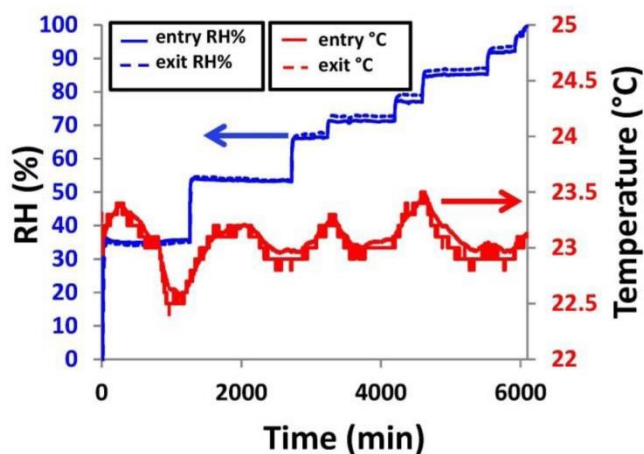


**Figure 2.6:** Measured RH and temperature values of the entry and exit lines. Entry lines data are solid and exit lines data are dotted. RH data is shown on the left y axis in blue color, and temperature data is shown at the right y axis in red color.

Also, we demonstrated a high temperature environment control by heating up the chamber with heating tapes. Heating tapes were covered by aluminum foil to prevent heat loss to the laboratory air. Uniform temperature at the surrounding region of the chamber has been obtained. Temperature measurements have been taken by thermocouples at various locations. Then, Variac voltage transformers that control the heating tape power were adjusted. Figure 2.7 shows RH and temperature values of the entry and exit lines for two different cases. The key thing to keep the constant RH is to eliminate any local condensation spots through the line. The humidified flow after the gas bubblers can condensate at a local colder spot right before the main chamber. This would cause a sudden RH jumps at the main chamber. It is crucial to satisfy the uniform heat distribution outside the chamber.

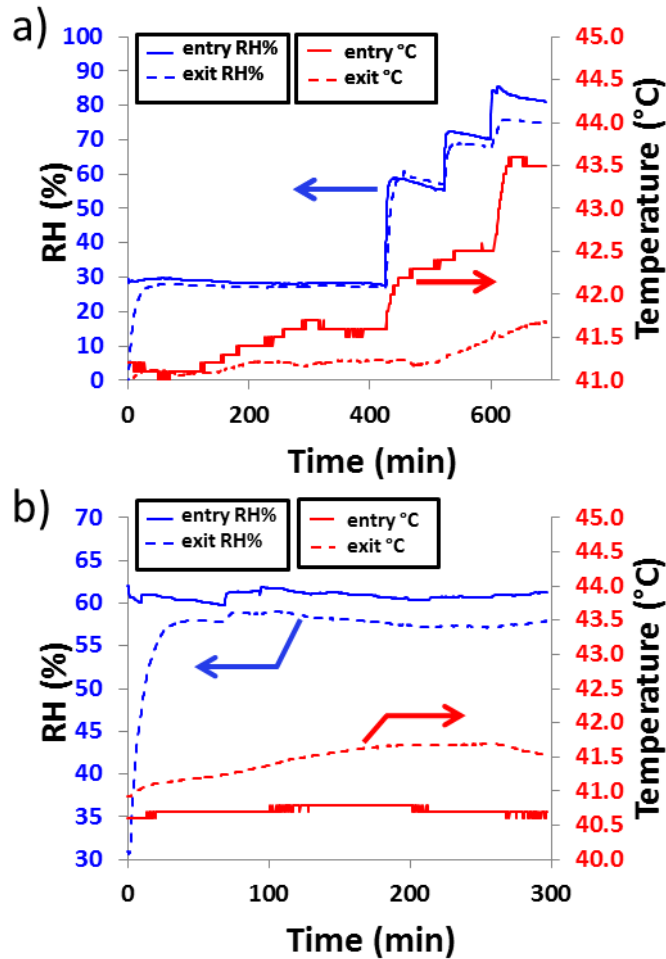


**Figure 2.7:** Measured RH and temperature values of the entry and exit lines from the high temperature experiments. Entry lines data are solid and exit lines are dotted. RH data is shown on the left y axis in blue color, and temperature data is shown at the right y axis in red color. **a)** Rh starts at 30%. Then it increases and stays for some time at 60%,70%, and 80% RH, sequentially. **b)** This experiment shows 60% RH is stable during 300 min.

### 2.3.2 Crack Healing Experiment

As a demonstration of the new measurement capability, we investigate the spontaneous crack healing of microfabricated cantilevers adhered to a substrate at fixed RH. Capillary adhesion adversely affects micro/nanoelectromechanical systems (MEMS/NEMS) reliability. The smooth surface of microcantilevers, which is often less than 5 nm root mean square (rms) roughness, enables effects of capillary nucleation and growth on adhesion of rough surfaces to be observed [68]. Various models [113,114], and experimental results [68,115] have been reported

with respect to the *equilibrium* adhesion energy between wetted smooth surfaces. The new data investigates the adhesion energy dependence on time.

The microcantilevers were fabricated at Sandia National Laboratories in the SUMMiT V<sup>TM</sup> process [116] and released and supercritically dried [117] at Carnegie Mellon University (Appendix C). As imaged by interferometry, twenty freestanding cantilevers of lengths from 1,050 to 2,000  $\mu\text{m}$  in 50  $\mu\text{m}$  increments were obtained from a given chip. As schematically represented in Figure 1.8, the height of the step-up support post is  $h=1.8 \mu\text{m}$ , the cantilever width is  $w=20 \mu\text{m}$  and the cantilever thickness is  $t=2.5 \mu\text{m}$ . An electrically isolated pad of 50  $\mu\text{m}$  length near the support post was used to actuate the cantilevers.

The cantilevers were placed in the load lock chamber, and O<sub>2</sub> plasma treated at 2.9 W for 30 min. After cleaning the sample, it was transferred to the main chamber, where the environment was at about 100 mTorr pressure. After the plasma treatment the cantilevers were again imaged by interferometry and were mostly in the arc shape, i.e., contacting the substrate only at their tips [67]. They were brought further into contact with the substrate by electrostatic actuation. Most cantilevers then remained adhered in the “S-shape”, in which the cantilever is in nominal contact with the substrate beyond the crack tip at  $s$ . We increased RH gradually and observed the crack lengths with time using interferometry as shown in Figure 2.8. Crack length data was taken at 10 min intervals until no further change was detected. Figure 2.7 shows the RH values during the experiment, which are at 34.7, 53.6, 71.5, 77.1, 85.2, 92.1, and 96.7 %. Figure 2.9 displays the measured crack length data over time at 54 % RH condition. After 13.6 minutes, the RH value had increased by 95% of its total change from 35% RH to 54% RH, as seen in Figure 2.9. Crack healing persisted for the cantilevers until 500 min, indicating that the new RH level was achieved in a time much shorter than the time required to achieve crack equilibrium. The equilibrium crack lengths  $s$  decreased about 42, 120, 36 and 77  $\mu\text{m}$  for four different cantilevers, respectively.

We present here three different samples’ crack healing data. Experiment conditions are summarized in Table 2.1. Each sample was monitored in a humid environment and 6 to 18 minutes were required to establish vapor pressure equilibrium conditions. For the first two

samples, cantilever deflection data were collected at 10 min intervals, while data for the third sample data were collected at 1 min intervals.

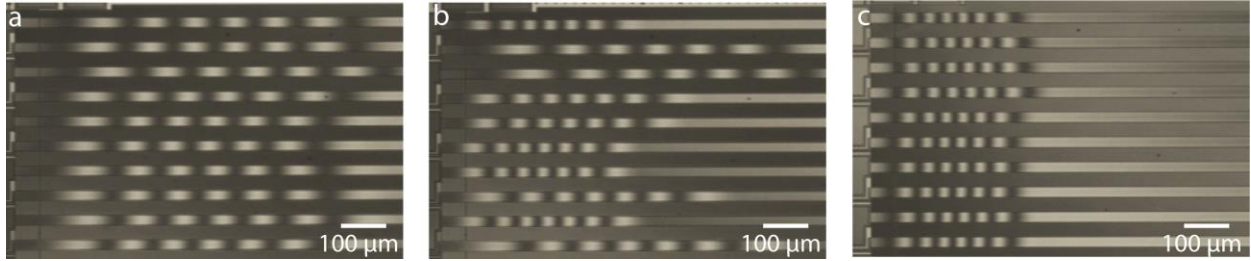


**Figure 2.8:** Interferograms of crack length  $s$  vs. time at 61% RH ( $p/p_s$ ) for sample 3. a) At 0<sup>th</sup> min. b) At 25<sup>th</sup> min. c) At 100<sup>th</sup> min.

In Figure 2.8 interferograms are shown that indicate crack healing over time for the sample 3 at 61% RH. Deflection curves are extracted for each cantilever using phase stepping interferometry, and the energy release rate,  $G$ , of a given cantilever was calculated in the following equation

$$G = \frac{3}{2} E \frac{h^2 t^3}{s^4} \quad . \quad (2.1)$$

The Young’s Modulus,  $E$ , of the polysilicon is 164 GPa [118].

**Table 2.1:** Experiments performed

| Sample | Initial $p/p_s$ | Steady State $p/p_s$ | $p/p_s$ Equilibrium Time (min) | Time to achieve equilibrium crack length (min) | Time between interferograms (min) |
|--------|-----------------|----------------------|--------------------------------|--|-----------------------------------|
| 1      | 0.35            | 0.54                 | 13.6                           | 500  | 10                                |
| 2      | 0.32            | 0.51                 | 11.3                           | 600  | 10                                |
| 3      | 0.30            | 0.61                 | 6.4                            | 150  | 1                                 |
| 3      | 0.61            | 0.88                 | 17.8                           | 90   | 1                                 |

Energy release rate data over time for individual microcantilevers are presented in Figures 2.9, 2.10, 2.11 and 2.12. The adhesion dependence on time for sample 1 from 0.35 to 0.54 RH is shown in Figure 2.9, where it can be seen that adhesion increased from 50  $\mu\text{J}/\text{m}^2$  to 280 to 350  $\mu\text{J}/\text{m}^2$  over  $\sim 8$  hours.

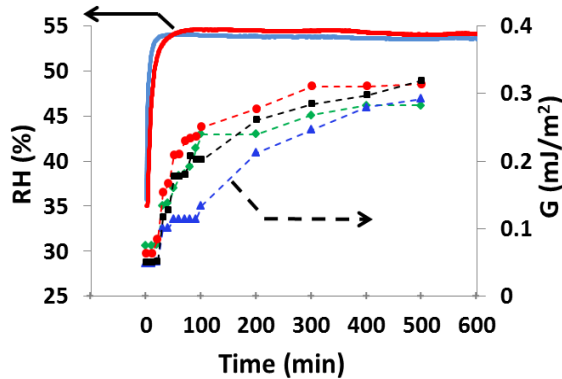


**Figure 2.9:** Sample 1 RH and adhesion data over time. Solid lines represent RH data at the chamber entrance (blue) and exit (red), and dashed lines represent adhesion data for different individual microcantilevers.

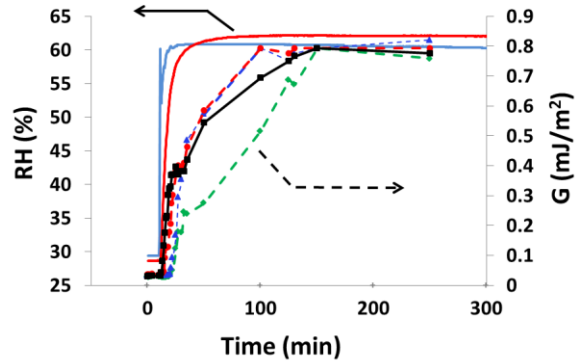


**Figure 2.11:** Sample 3 RH and adhesion data over time. Solid lines represent RH data at the chamber entrance (blue) and exit (red), and dashed lines represent adhesion data for different individual microcantilevers.

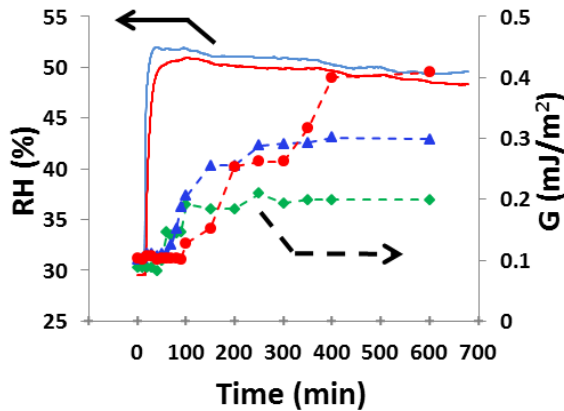


**Figure 2.10:** Sample 2 RH and adhesion data over time. Solid lines represent RH data at the chamber entrance (blue) and exit (red), and dashed lines represent adhesion data for different individual microcantilevers.

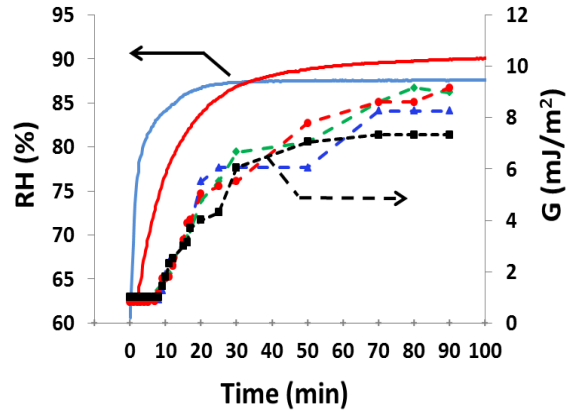


**Figure 2.12:** Sample 3 RH and adhesion data over time. Solid lines represent RH data at the chamber entrance (blue) and exit (red), and dashed lines represent adhesion data for different individual microcantilevers.

The adhesion data for sample 2 from 0.32 to 0.51 RH is shown in Figure 2.10, where it can be seen that  $G$  increased from  $100 \mu\text{J}/\text{m}^2$  to 200 to  $400 \mu\text{J}/\text{m}^2$  in 150 min. For sample 3 from 0.30 to 0.61 RH the data is plotted in Figure 2.11,  $G$  increased from  $50 \mu\text{J}/\text{m}^2$  to  $800 \mu\text{J}/\text{m}^2$ . And for the same sample when we increase the RH to 0.88,  $G$  values increase with time in 90 min duration from  $800 \mu\text{J}/\text{m}^2$  to  $8000\text{-}9000 \mu\text{J}/\text{m}^2$ . All of these figures illustrate that capillary forces enable crack healing against progressively higher values of  $G$  as RH increases. Also, they show that after steady state environment conditions are attained, crack healing continues. This implies the capillary nucleation until the equilibrium can be detected with this system.

## 2.4 CONCLUDING REMARKS

A versatile chamber with a high degree of environmental control has been constructed for the purpose of studying environmental effects on micro- and nanostructures. The chamber includes pumping to pressure as low as  $10^{-9}$  Torr, four electrical probes for MEMS device actuation, a load lock with *in-situ* plasma clean, long working distance interferometry for nanometer scale metrology and the ability to introduce vapors under controlled partial pressure conditions. Sample heating has been implemented using a boroelectric heater (Momentive part number 2110072), similar to shown in Figure 2.3a. With this newly constructed chamber, we have presented experimental results for microcantilever crack healing with time at a fixed RH level. Besides the adhesion studies which are the focus of this thesis study, we envision other uses of the chamber such as studies of friction in various environments, of adsorbed film thickness versus partial pressure, and of creep of metal thin films.

# Chapter III: Experiments of Water, *n*-Pentanol, and Ethanol Capillary Bridge Kinetics at Multi Asperity Surfaces

In the previous chapter, we showed preliminary data for the energy release rate ( $G$ ), also known as the crack driving force, versus time. In this chapter, we take a detailed look at such data. We find that crack healing occurs in discrete events, rather than continuously. It is seen that the average crack healing rate,  $\bar{v}$ , decreases with increasing  $G$ . A plot of  $\bar{v}$  versus energy release rate,  $G$ , reveals log-linear behavior, while the slope  $|d[\log(\bar{v})]/dG|$  decreases with increasing relative humidity. However, the log-linear trend does not continue indefinitely. Instead,  $\bar{v}$  abruptly goes to 0 at a sufficiently high value of  $G$  for a given RH.

## 3.1 INTRODUCTION

The relatively long capillary *nucleation time* between non-contacting surfaces can be understood in terms of a thermally activated first order gas-liquid phase transition theory. Information on capillary *nucleation* across a gap can be gained directly and unambiguously from the SFA [56], which is capable of controlling the distance of counterfacing surfaces of atomic smoothness as precisely as 1 Å. In this case, the index of refraction is monitored versus separation distance [56]. However, in the SFA, the sphere radius is ~2 cm. A quartz tuning fork AFM has recently been used to measure capillary nucleation times across a gap between a substrate and a tip with 10 nm radius of curvature [86]. In this experiment, Arrhenius behavior was also measured, similar to the AFM friction or force curve works [57,58,85], and also as predicted theoretically[77]. However, nucleation was observed at gaps as large as 3.4 nm at RH=30% [86], whereas  $2|r_K|=1$  nm at that RH value. Also, a drift rate of 10 pm/s compared to an approach rate of 75 pm/s introduces some uncertainty into the reported results.

Both the SFA and the AFM have been used to measure capillary meniscus *growth times* for surfaces that have just come into contact [37,56,73,74]. In these experiments, the pull-off force is measured after a certain contact time. At the macroscale and nanoscales, measured

growth times are on the order of seconds and milliseconds, respectively. Theories that account for vapor diffusion in the gas phase [73] and transport of adsorbed surface water molecules in the liquid phase [37], have been advanced for the meniscus growth. Theory agrees with the experimental results at the macroscale [73], but under-predicts measured growth times by three or more orders of magnitude at the nanoscale [37].

Besides the spherical geometry, model adhesion experiments between nominally parallel surfaces can be performed on double cantilever beams [119,120] and microcantilevers [68,115,121,122]. In such experiments, the surface separation is free of drift. In this chapter, we measure the crack length of plasma-cleaned microcantilevers with nanometer scale surface roughness as a function of time at fixed humidity after an abrupt increase in humidity. We plot average crack healing velocity ( $\bar{v}$ ) versus the energy release rate ( $G$ ), also known as the crack driving force. The experiments are then interpreted within the framework of capillary nucleation.

## 3.2 WATER EXPERIMENTS

As in the previous chapter, chamber cleanliness was evaluated with respect to hydrocarbon contamination by measuring the water contact angle (WCA) of deionized water on silicon (100) blank samples. Before the plasma treatment, the WCA was approximately 70°. After plasma cleaning for 30 min (frequency -- 76.6 kHz, power -- 2.9 W, pressure -- 250 mTorr), samples were transferred to the main chamber while a continuous flow of nitrogen was running, or placed in laboratory air. After 24 h, the WCA was measured. Approximately 0° and 24° WCA was observed for the samples kept in the main chamber and in laboratory air, respectively.

As imaged by interferometry, twenty freestanding cantilevers of lengths from 1,050 to 2,000  $\mu\text{m}$  in 50  $\mu\text{m}$  increments were obtained from a given chip. As illustrated in Figure 3.1a, the height of the step-up support post is  $h=1.8 \mu\text{m}$ , the cantilever width is  $w=20 \mu\text{m}$ , and the cantilever thickness is  $t=2.5 \mu\text{m}$ . The substrate and the cantilevers are electrically connected through the highly doped polysilicon, and are therefore at the same potential.

The freestanding cantilevers were placed in the load lock chamber and O<sub>2</sub> plasma-treated. After plasma cleaning, the sample was transferred to the main chamber under vacuum, which was then vented with dry nitrogen. It has been shown that rapid gas flow within a vacuum chamber causes compliant MEMS samples to contact and remain adhered [123]. Here, we took advantage of that effect. During venting using high purity nitrogen, the cantilevers became adhered in the “S-shape” in which the cantilever is in nominal contact with the substrate beyond the crack tip at crack length  $s$ , as schematically illustrated in Figure 3.1b.

The cantilever beam deflection is [124]

$$w(x)=h\left(\frac{x}{s}\right)^2\left(3-\frac{2x}{s}\right) \quad (3.1)$$

which has the symmetrical “S” shape as in Figure 3.1b. Near the crack tip, the distance between surfaces is nominally less than  $2|r_K|$  over a distance of many micrometers; this enables meniscus nucleation between opposing asperities in the counterfaces. The RH was increased to a desired level by changing the ratio of dry to wet nitrogen introduced into the chamber. For sufficiently high RH, *spontaneous* crack healing was observed. The RH was then maintained until no further change was detected. It was then increased further, as shown in Figures 3.1c-3.1f (Figure 2.8 is reinserted as Figure 3.1c-f because they will now be discussed in detail). Phase shifting interferometry [112] at 1 min intervals enabled determination of  $s$  versus time for all 20 microcantilevers. With a 5X objective (NA=0.14),  $s$  could be determined with  $\pm 5.5 \mu\text{m}$  ( $\pm 2$  pixels) uncertainty. With Young’s Modulus  $E=164 \text{ GPa}$ , [118] the energy release rate  $G \text{ (J/m}^2\text{)}$  [125] of a given cantilever was calculated according to [124]

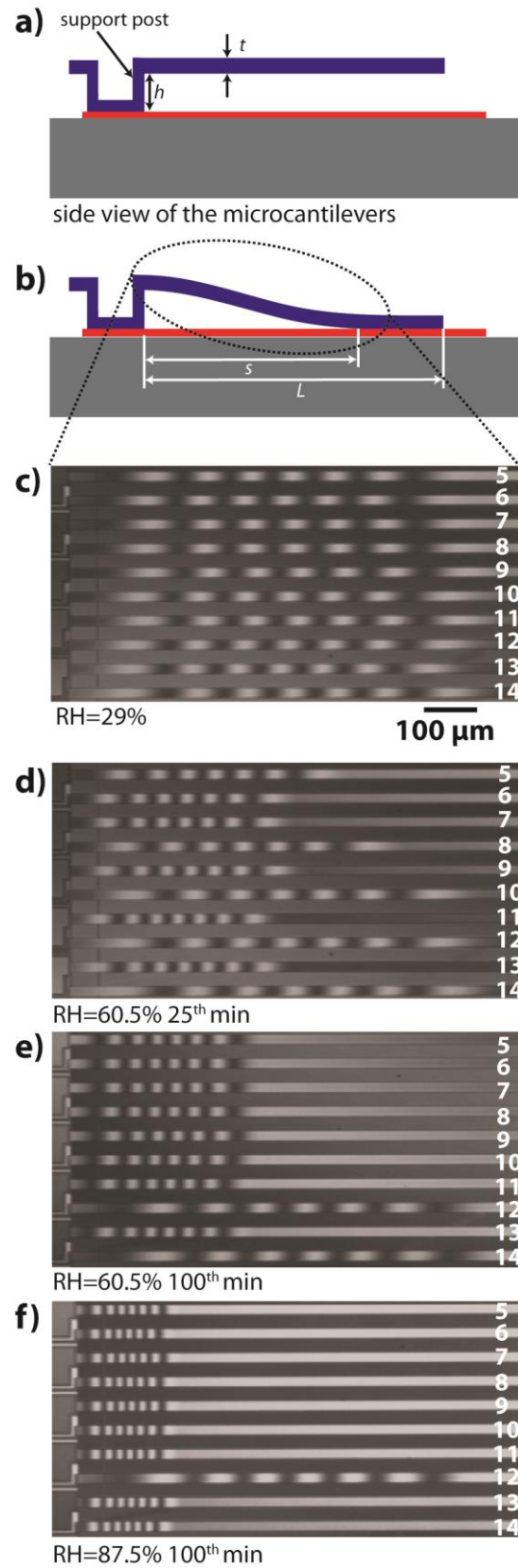


**Figure 3.1:** Cross-section schematic geometry of the microcantilever (a) standing freely and (b) in the *S* shape. Interferograms (c) of Cantilevers 5-14 at 29% RH (no crack healing) and (d)-(f) after increasing exposure to humid conditions.

$$G = \frac{3}{2} E \frac{h^2 t^3}{s^4} \quad (3.2)$$

In equilibrium,  $G = \Gamma$ , the adhesion energy per unit area. The value of  $\Gamma$  in dry nitrogen was from 0.02 to 0.06 mJ/m<sup>2</sup> ( $s = 890$  to  $675$   $\mu\text{m}$ ). These low values can be attributed to van der Waals forces and are typical of dry rough interfaces in MEMS [126]. The freestanding cantilever curvature is small ( $< 1 \text{ m}^{-1}$ ) because of a small internal moment; and exerts a negligible influence on the adhesion calculation [122]. The RH first was increased to 29%, but no crack healing was observed, as shown in Figure 3.1c. The RH was then increased further. As defined by achieving 95% of the change in set point, the RH value reached steady state at a  $60.5 \pm 0.5\%$  RH level (hereafter referred to as 60.5% RH) in 6.4 minutes. Significant crack healing occurred, as seen in Figures 3.1d and 3.1e. Crack healing continued until 200 min, indicating that the new steady-state RH level was attained in a time much shorter than the time required to reach the minimum crack length. The minimum value of  $s$  was 340  $\mu\text{m}$ ; no further crack healing occurred for any cantilever over the following 400 min. The RH was then increased to 87.5%, and a steady state RH condition was achieved in 17.8 min. Now crack healing continued for another 82 min. As seen in Figure 3.1f, the minimum value of  $s$  was 185  $\mu\text{m}$ .

Cantilevers 5-14 are numbered in Figures 3.1c-f. Figure 3.2a shows crack length  $s$  versus time data for Cantilevers 9 and 10 after RH was increased to 60.5%. The solid vertical bar at 6.4 minutes indicates the time at which RH achieved a steady state condition. Little change in crack length occurred during the RH transient, but  $s$  began to decrease after 12 and 20 minutes for Cantilevers 9 and 10, respectively. Figure 3.2b shows  $s$  versus time data for Cantilevers 10 and 14 after RH was increased to 87.5%. The solid vertical bar at 17.8 min again indicates the RH steady state. Here, it is seen that Cantilever 10 already began healing during the RH transient, while Cantilever 14 did not begin to heal until approximately 56 minutes. Cantilever 14 also did not heal during the exposure to 60.5% RH, as can be seen in Figures 3.1c-e.

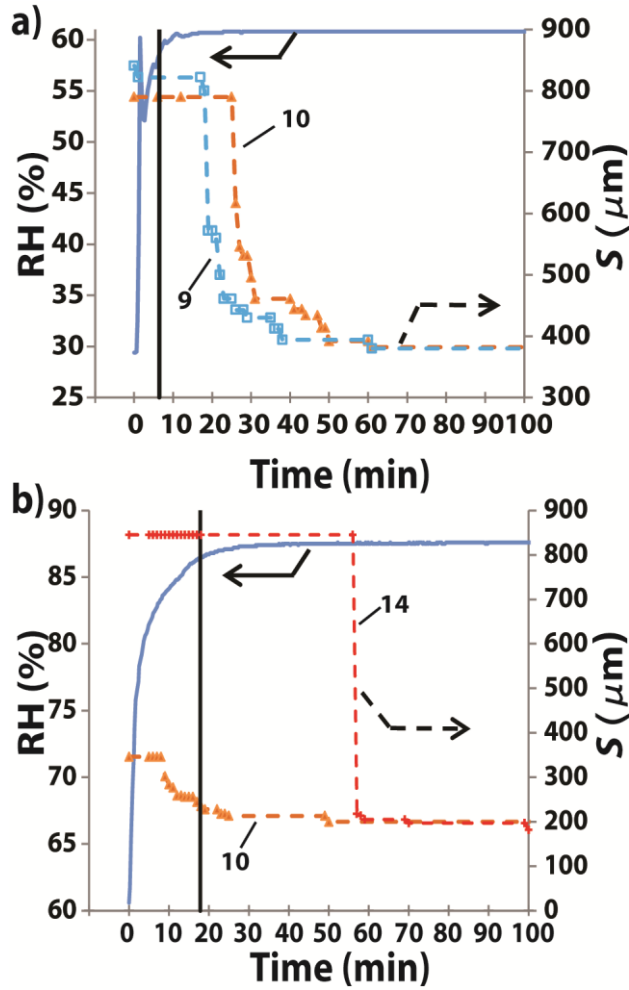


**Figure 3.2:** RH and crack length data over time. The solid blue lines indicate RH, while the dashed lines represent crack length data for different individual microcantilevers. The vertical solid black line represents onset of steady state RH. (a) Crack healing data of Cantilever 9 (blue squares) and Cantilever 10 (orange triangle markers) when RH is increased to 60.5% RH from 29% RH. (b) Crack healing data of Cantilever 10 (orange triangles) and Cantilever 14 (red crosses) when the 60.5% RH is increased to 87.5% RH.

Using the data for  $s$  and equation 3.2,  $G$  versus time can be plotted. Figure 3.3a shows the results from 12 microcantilevers at 60.5% RH.  $G$  is seen to increase from 0.02 to 0.06  $\text{mJ}/\text{m}^2$  to 0.7-0.9  $\text{mJ}/\text{m}^2$  over 150 minutes. The  $G$  data over time at 87.5% RH for 13 cantilevers are shown in Figure 3.3b. Here,  $G$  further increases to  $\sim 9 \text{ mJ}/\text{m}^2$  over 100 minutes.

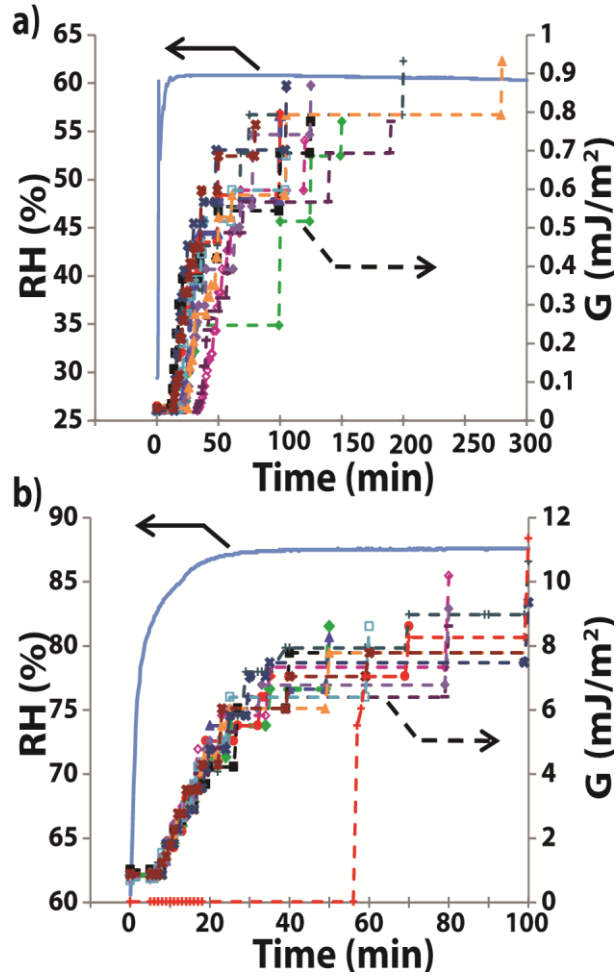


**Figure 3.3:** Crack healing data over time. The solid lines indicate RH at the chamber entry, while dashed lines represent energy release rate  $G$  data for different individual microcantilevers. Data for  $G$  after increasing RH (a) from 29 to 60.5%. (b) from 60.5 to 87.5%.

It is important to identify whether the crack healing trend is discrete or continuous with respect to time. Within the resolution of the interferometry measurement, it is apparent that crack lengths often do not decrease in each 1 min time interval. This is indicated in Figure 3.2 by horizontal portions of the  $s$  versus time trend that are greater than 1 min. On the other hand, in some time intervals,  $s$  consecutively decreases. Experiments were repeated with 5 s and 10 s time intervals (Figures F1 and F2, Appendix F). In most cases the time between measurable crack length reductions was greater than the time interval. Therefore, the changes in crack length tend to occur in discrete jumps.

When the separation or healing process is considered to be continuous,  $v - G$  curves are plotted, where  $v$  is the crack velocity. This characteristic has been studied both for crack propagation in ceramics subject to stress corrosion cracking [101,127,128] and for crack healing due to surface forces or capillary condensation [129,130]. Because within experimental resolution, the crack healing here is discrete in nature, we shall characterize the results with  $\bar{v} - G$  curves. Then  $\bar{v}$  is defined as

$$\bar{v} = \frac{s_j - s_{j+n}}{\Delta t} \quad (3.3)$$

Here,  $s_j$  is the crack length after  $j$  minutes, and  $s_{j+n}$  is an experimentally resolvable shorter crack length that occurs after  $j + n$  minutes. The time  $\Delta t$  is then  $n$  minutes. The  $G$  value is calculated at the average value of  $s$ , that is, at  $s = (s_j + s_{j+n})/2$ .

The discrete nature of the crack healing is indicative of nucleation events. The nucleation time for a crack healing event could be affected by exposure to wet conditions before steady state RH has been reached. Therefore,  $\bar{v}$  is also only calculated once steady-state RH has been achieved. Furthermore, the first  $\bar{v}$  is calculated for a given microcantilevers only after crack healing has initiated, i.e.,  $s_j < s_{initial}$ .

Results reflecting 13 different cantilevers and 202 calculated values at RH=60.5% and 87.5% are shown in Figure 3.4. As indicated by the solid lines (semi-empirical fits to be described later), log-linear trends of  $\bar{v}$  versus  $G$  are observed. It is seen at 60.5% RH that  $\bar{v}$  decreases from  $\sim 2 \mu\text{m/s}$  to  $\sim 10^{-3} \mu\text{m/s}$  while  $G$  increases from 0.06 to 0.85  $\text{mJ/m}^2$ . At 87.5% RH,  $\bar{v}$  decreases from  $\sim 0.2 \mu\text{m/s}$  to  $\sim 4 \cdot 10^{-4} \mu\text{m/s}$  at higher  $G$  values from 4 to 9  $\text{mJ/m}^2$ . The scatter in  $\bar{v}$  for a given value of  $G$  is approximately the same at the two RH levels (this is more readily seen if the  $G$  scale is expanded). The slope  $|d[\log(\bar{v})]/dG|$  in Figure 3.4 is smaller at the higher 87.5% RH than at 60% RH. Values of  $\bar{v}$  for  $G$  values between 1 and 4  $\text{mJ/m}^2$  are not calculated because the cracks healed during the transition regime from 60.5% to 87.5% RH. To check for any difference in the trend due to time resolution, experiments were conducted on other samples at 62% and 89.5% RH level with 5 s and 10 s intervals, respectively. Data from

the shorter intervals were similar to that presented in Figure 3.4 (Figures F3 and F4, Appendix F).

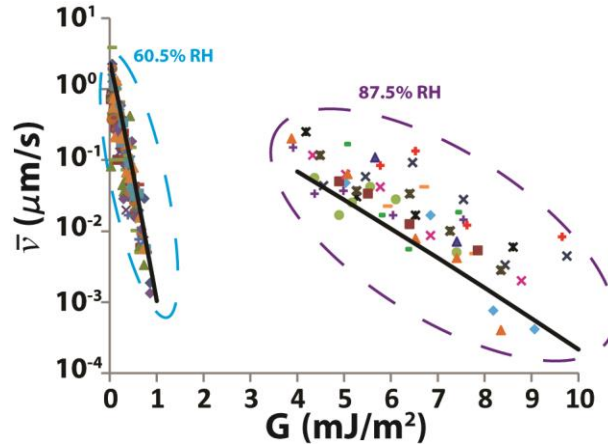


**Figure 3.4:** Average crack healing velocity  $\bar{v}$  as a function of energy release rate  $G$ . Different cantilever responses are plotted with different color and marker types for 60.5% and 87.5% RH cases. Solid lines are semi-empirical fit.

### 3.3 DISCUSSION

Let us now make the following *experimental observations*.

- (1) *Crack healing takes place when the RH increases.* When RH increases,  $|r_K|$  increases, encouraging crack healing because the capillaries can bridge and nucleate across larger gaps.
- (2) *At RH=60.5% and 87.5%, the slope  $|d[\log(\bar{v})]/dG|$  is observed to be approximately constant.* Also, at larger RH, the slope decreases.
- (3) *Figure 3.4 data exhibits a large degree of scatter.* This discrepancy can be explained by considering (a) that nucleation is a stochastic process and (b) that asperities encountered as the crack heals are at different heights.

Let us further contemplate the scatter in the Figure 3.4 data. In Figure 3.1c,  $s \approx 860$  to  $765 \mu\text{m}$ . However, in Figure 3.1d,  $400 \leq s \leq 550 \mu\text{m}$  for many cantilevers, but for Cantilevers 10, 12 and 14,  $s$  remains at  $\approx 800 \mu\text{m}$ . In Figure 3.1e,  $s \approx 800 \mu\text{m}$  persists for Cantilevers 12 and 14, while  $s \approx 350$ - $400 \mu\text{m}$  for all other cantilevers. Local barriers, for example anomalous asperities that protrude above others, can pin the crack open [131]. They may prevent the rapid onset of healing

of Cantilevers 10, 12 and 14. To explore this hypothesis, data points from Cantilever 14 are indicated by the red cross data markers at 87.5% RH in Figure 3.4. Once healing has begun, its  $\bar{v}$  values are similar to those of other cantilevers at the same  $G$  values.

(4) *In the experiments, there is no apparent healing after a certain amount of time.* Strictly, the time to attain equilibrium is limited by the condition that all suspended asperities in the healing process zone (HPZ) possess gaps greater than  $2|r_K|$ : in which case,  $\tau \rightarrow \infty$ . If asperities of non-uniform densities and of differing heights are allowed, it is much more likely that crack healing will abruptly end at a certain  $s$  value.

The decrease of  $\bar{v}$  with  $G$  can also be considered *qualitatively* in terms of the increasing cantilever stiffness while the crack is healing. In order to continue healing, a greater number of asperities must nucleate per unit area as the cantilever becomes stiffer. This, in turn, requires that capillary bridges nucleate across larger gaps, which involves greater times, thereby lowering  $\bar{v}$ .

Then, a useful, though simplified, visualization of the effect of the actual surface roughness is illustrated in Figure 3.5. In Figure 3.5a, contacting and bridging asperities are represented in red. Also, suspended green asperities are shown. An HPZ spans a certain cantilever deflection, arbitrarily to be defined at a deflection of  $2\sigma$ . To the left of the HPZ, it is assumed that all asperity gaps are larger than  $2|r_K|$ , so that capillary nucleation cannot occur. However, because of the surface roughness, suspended asperities even at the extreme left of the HPZ can be bridged. Suspended asperities closer to the crack tip than bridged also exist. For low  $G$  values, the bridged asperities in Figure 3.5a are sufficient to cause crack healing. As  $G$  increases, asperities with larger gaps must become bridged and, hence, the crack healing time increases. In the simplest visualization as in Figure 3.5b, the crack healing occurs when a number of asperities, each at some larger height, are bridged. Of course, in reality, the asperities are all at different heights and the density of bridged green asperities statistically will become smaller as they are further from the crack tip.

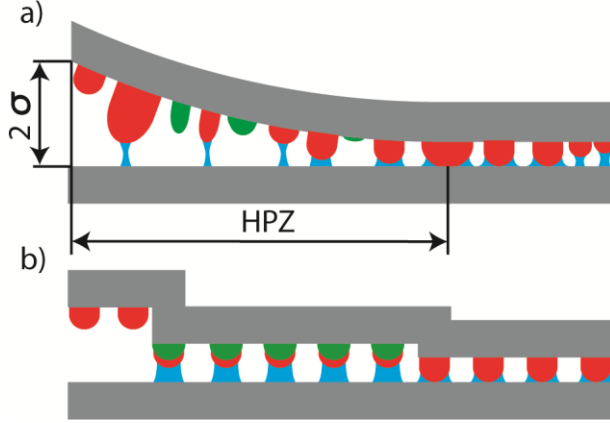


**Figure 3.5:** (a) Idealized crack tip region schematic to help visualize the effect of roughness. (b) The crack tip region is further simplified so that all suspended asperities in the HPZ nucleate at the same time due to the roughness.

In terms of the Figure 3.5 visualization, an equation can be found to fit the crack healing time versus adhesion trend. Accordingly,

$$H = \left( 0.53 \exp\left(\frac{RH}{100}\right) + \frac{0.01G}{(RH/100)^{4.3}} \right) \text{ nm} \quad (3.4)$$

where  $RH$  is in percent and  $G$  is in  $\text{mJ/m}^2$ . Once  $H$  is found from equation 3.4, equation 1.59 determines the energy barrier  $\Delta\Omega$ , and then equation 1.62 is used to calculate the nucleation time. Then,  $10 \mu\text{m}$ , which is on the order of the HPZ length, is divided by  $\tau$  to calculate  $\bar{v}$ . The results are represented by the solid lines in Figure 3.4.

Quantitative agreement with the semi-empirical equation 3.14 is reasonable. Besides specific roughness characteristics, many other factors deserve more detailed consideration. One is the effect of the adsorbed film layer. It increases the capillary meniscus area, thus increasing the capillary force [55]. More importantly, it will fill partially the gaps between asperities. The counterfacing adsorbed film layers may overlap and instantaneously nucleate a capillary bridge, or they will reduce the gap distance between the asperities, reducing  $\tau$ . Literature data on the details of adsorption isotherms vary significantly. For example, the water film thickness on an oxidized silicon wafer  $\sim 1.2$  and  $\sim 1.65$  nm for 60.5% and 87.5% RH respectively [132]. In contrast, on a silica surface, a  $\sim 0.3$  nm thick water accumulated in 600 min, then from 40 to 80% RH film thickness increases to  $\sim 0.5$  nm in 600 min [133].

More experimental data on different surfaces are also needed to understand water accumulation on polysilicon. Theillet and Pierron used a single crystal silicon MEMS resonator to determine the adsorbed film layer thickness in response to frequency changes as a function of temperature at constant RH [105]. The water film thickness dropped as the temperature increased from 20 °C to 80 °C at constant RH levels (>50%). Liu and Bhushan showed that single asperity adhesive force decreases significantly at a 50% RH level above 50 °C [134]. These experiments suggested that as temperature increases at constant RH, lower adhesion energy is expected due to the water film thinning. In contrast, according to the Arrhenius Equation 1.62, at higher temperature capillary condensation occurs faster. To sort out the dominant effect, temperature-controlled experiments are recommended for future work. Another factor to consider is that the adsorbed layer thins because the disjoining pressure is in equilibrium with the capillary pressure [32].

### **3.4 ALCOHOL EXPERIMENTS**

Vapor-phase lubrication, in which a supply of lubricant is immediately available through the gas phase to passivate a worn area, is another approach of interest. Although less experimental research has been reported on vapor-phase lubricants in MEMS, they are at the heart of the overwhelming success of the Texas Instruments Digital Mirror Device (DMD).

The micromirrors are encapsulated with perfluorodecanoic acid in a hermetic environment [89]. The aluminum micromirrors have small springs that store mechanical strain energy. They not only provide restoring force to the micromirror switches, but also are thought to induce wear marks due to a few nanometers of sliding upon contact between the mirror and substrate. At an operating temperature of about 80 °C, which may be attained because of the bright light source illuminating the DMD, the acid melts and the high vapor pressure easily re-passivates these wear tracks. The vapor pressure at 0 °C is 10 mm Hg [135], and therefore even the solid phase may provide passivation. The main purpose of the springs is to overcome adhesive rather than frictional forces. The carboxylic acid group forms a strong acid-base bond to the alumina surface (formed by plasma ashing the aluminum), improving its wear characteristics [136].

Recently, Kim, Dugger and colleagues have shown initial data indicating that alcohol-based vapors (ethanol through pentanol, i.e., C2-C5) provide effective wear prevention on a *microscale* MEMS tribology test structure made of polysilicon [90,137]. These results also apply to *nanoscale* oxidized Si asperities as measured by AFM and to *macroscale* quartz (SiO<sub>2</sub>) ball-on-flat linear wear tests in a conventional tribometer. Although alcohol-vapor is promising to reduce the wear effects, it is crucial to identify the  $p/p_s$  range over which MEMS can operate successfully in vapor-phase environments.

Crack healing experiments will reveal information on adhesion forces of alcohol vapors between multi-asperity surfaces. The experimental set up described for water experiments needs some modification to run these experiments. A flow meter can adjust the partial pressure, but equilibrium time can only be observed with sensors. RH sensors will be damaged for alcohol-vapor  $p/p_s$  measurements. To observe the equilibrium times, we attempted to implement a Chilled Mirror Hygrometer to the flow line to monitor the dew point temperatures that corresponds to partial pressures. Although Chilled Mirror Hygrometers are precise and accurate for the relative humidity measurements, they need further improvements for alcohol dew point measurement and hence ultimately could not be used. Our attempt is described in the Appendix D.

We conducted the experiments as described in the section 3.2. Water is highly soluble in alcohol solvents. To ensure the “wet” N<sub>2</sub> line was free of water, we placed 3 Å molecular sieves into the fritted bubblers, and waited 24 h prior to the experiment [138] to allow time for the water to be absorbed by the molecular sieves. To maximize the likelihood that the data was taken after steady state  $p/p_s$  was attained, we ignored the initial healing events. The first experiments were with *n*-pentanol vapor because it has the highest lubrication effect on the inorganic solid surfaces due to the long molecular chain [139].

The value of  $\Gamma$  in dry nitrogen was from 0.025 to 0.040 mJ/m<sup>2</sup> ( $s=840$  to 746  $\mu\text{m}$ ) similar to water experiments initial condition. The  $p/p_s$  first was increased to 30%, and after 10 min crack healing started. Eventually, healing occurred for 13 cantilevers out of 20, as seen in Figure 3.6a.  $G$  is seen to increase from 0.02 to 0.04 mJ/m<sup>2</sup> to 0.03-0.08 mJ/m<sup>2</sup> over 250 minutes. The

$p/p_s$  was then increased to 50%, and for some of the cantilevers healing events started in 30 s. Crack healing continued for 1000 min. As seen in Figure 3.6b,  $G$  further increases to 0.1-0.2  $\text{mJ}/\text{m}^2$ . Again 13 cantilevers responded to the  $p/p_s$  variation; however, this time some of the cantilevers had healed in the previous step didn't heal, and some non-responsive cantilevers healed at this step first time. Figure 3.6 plots the healing data for each  $p/p_s$ , and each colored line represents one individual cantilever. The next step reaches  $p/p_s=0.6$ . The slight increment of the partial pressure leads fewer cantilever responses as shown in Figure 3.6c. With this step most of the cantilevers reaches  $\sim 0.2 \text{ mJ}/\text{m}^2$ . However, at this point there are still cantilevers that did not heal since the beginning of the experiment. All of the cantilevers heal in the next step  $p/p_s=0.8$ . Here,  $G$  increases to 0.3-1.1  $\text{mJ}/\text{m}^2$  over  $\sim 200$  minutes, as shown in Figure 3.6d. Next,  $p/p_s=0.9$  has been tested.  $G$  climbs to 1-5  $\text{mJ}/\text{m}^2$  over  $\sim 60$  minutes, as seen in Figure 3.6e. Finally,  $p/p_s$  reaches to 0.95.  $G$  values equilibrate to  $\sim 20 \text{ mJ}/\text{m}^2$  in a much shorter time (35 min), as seen in Figure 3.6.

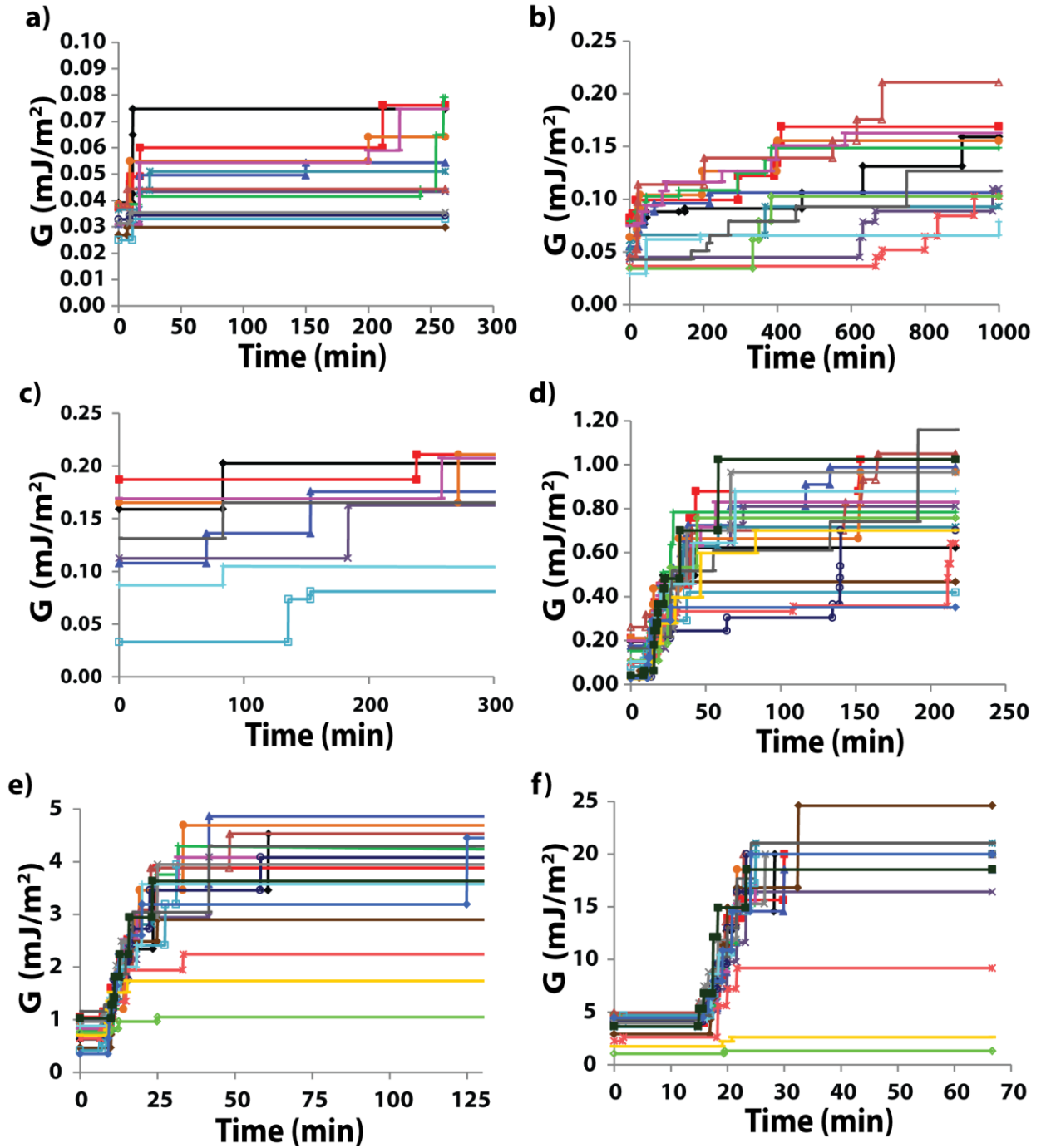


**Figure 3.6:** Crack healing data over time. Colored lines represent energy release rate  $G$  data for different individual microcantilevers. Data for  $G$  after increasing  $p/p_s$  (a) from 0 to 0.3. (b) from 0.3 to 0.5. (c) from 0.5 to 0.6. (d) from 0.6 to 0.8. (e) from 0.8 to 0.9. (f) from 0.9 to 0.95.

Results reflecting 20 different cantilevers at  $p/p_s=0.3, 0.5, 0.8, 0.9,$  and  $0.95$  are shown in Figure 3.7. Log-linear trends of  $\bar{v}$  versus  $G$  are again observed. It is seen at  $p/p_s=0.3$  that  $\bar{v}$  decreases from  $\sim 7 \mu\text{m/s}$  to  $\sim 10^{-3} \mu\text{m/s}$ , as shown in Figure 3.7a. At  $p/p_s=0.5$ ,  $\bar{v}$  decreases from  $\sim 2 \mu\text{m/s}$  to  $\sim 7 \cdot 10^{-4} \mu\text{m/s}$  at  $G$  values from  $0.07$  to  $0.20 \text{ mJ/m}^2$  plotted in Figure 3.7b. At  $p/p_s=0.8$ ,  $\bar{v}$  decreases from  $\sim 16 \mu\text{m/s}$  to  $\sim 2 \cdot 10^{-4} \mu\text{m/s}$  at  $G$  values from  $0.07$  to  $0.98 \text{ mJ/m}^2$  plotted in Figure 3.7c. Initially average velocity is higher compared to other partial pressure cases because the increment of  $p/p_s$  (from  $0.5$  to  $0.8$ ) is high. The adhesion values for the  $p/p_s=0.8$  is weak initially. Thus, compliant cantilever heals faster. Figure 3.7d and 3.7e show the  $\bar{v}$  versus  $G$  data for  $p/p_s=0.9$  and  $0.95$ , respectively.  $G$  values from  $0.8$  to  $4.2 \text{ mJ/m}^2$  and  $5.2$  to  $20.2 \text{ mJ/m}^2$  correspond to  $p/p_s=0.9$  and  $0.95$ , respectively. Figures 3.7 a-e illustrate the slope  $|d[\log(\bar{v})]/dG|$  decrease of the  $\bar{v}$  versus  $G$  curves while  $p/p_s$  increases.

The second alcohol tested was ethanol which is a shorter chain alcohol compared to *n*-pentanol, and it has been studied for a possible lubricant in the literature [140]. We followed the same experimental procedures; however, we could only observe the healing events starting at  $p/p_s=0.9$ . The response of only 5 cantilevers response data presented. When the  $p/p_s$  first was increased to  $0.9$ , cantilevers responded in 10 minutes. Figure 3.8a shows that  $G$  increases from  $0.16$  to  $0.21 \text{ mJ/m}^2$  to  $0.42\text{-}0.55 \text{ mJ/m}^2$  over 70 minutes. Then, at  $p/p_s=0.95$   $G$  increases from  $0.42$  to  $0.55 \text{ mJ/m}^2$  to  $1.37\text{-}2.08 \text{ mJ/m}^2$  over 33 minutes. Log linear trends of  $\bar{v}$  versus  $G$  curves again show slope decrease while increasing partial pressures, as shown in Figure 3.9.

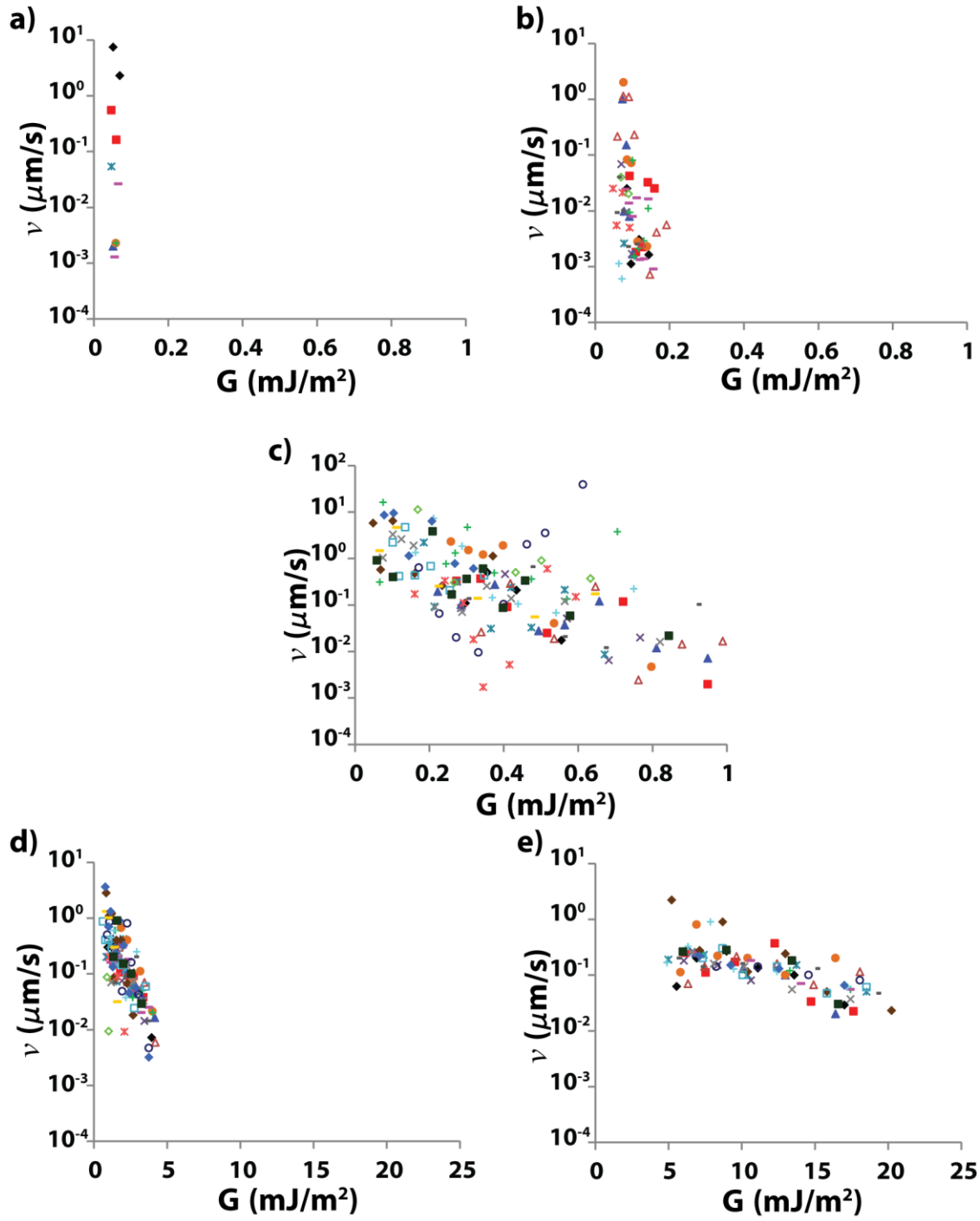


**Figure 3.7:** Average crack healing velocity  $\bar{v}$  as a function of energy release rate  $G$ . Different cantilever responses are plotted with different color and marker types. (a) for  $p/p_s=0.3$  case. (b) for  $p/p_s=0.5$  case. (c) for  $p/p_s=0.8$  case. (d) for  $p/p_s=0.9$  case. (e) for  $p/p_s=0.95$  case. It is again seen that  $|d[\log(\bar{v})]/dG|$  decreases as  $p/p_s$  increases.

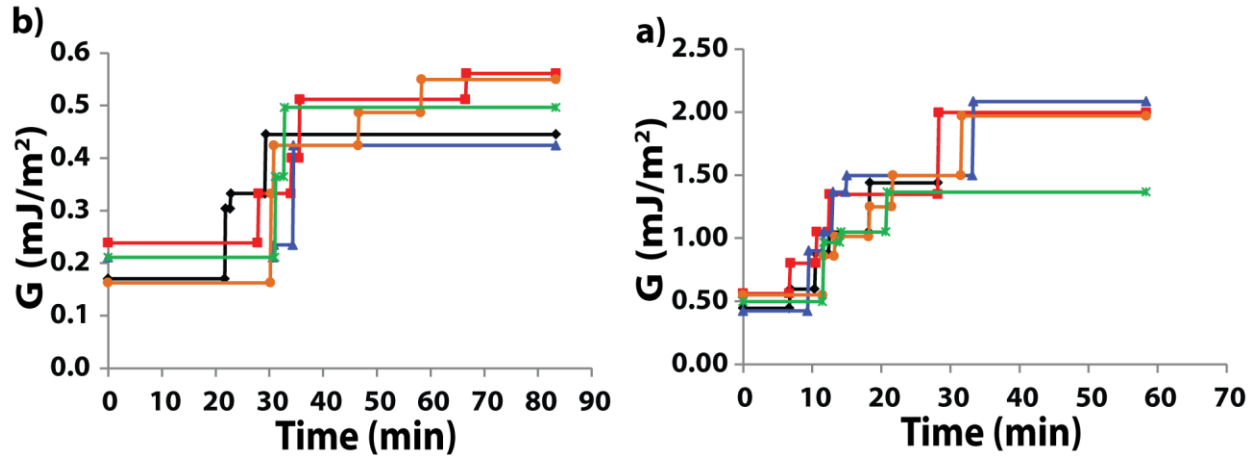


**Figure 3.8:** Crack healing data over time. Colored lines represent energy release rate  $G$  data for different individual microcantilevers. Data for  $G$  after increasing  $p/p_s$  (a) from 0 to 0.9. (b) from 0.9 to 0.95.

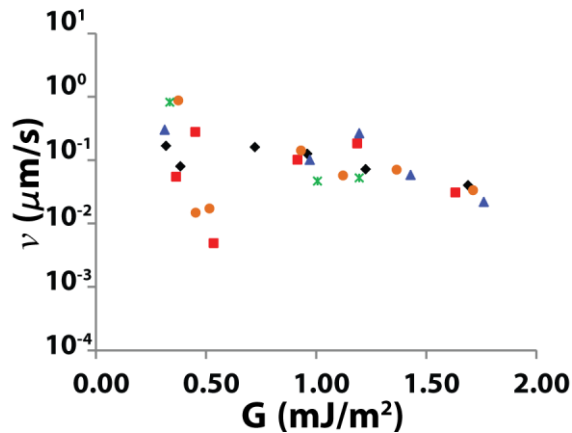


**Figure 3.9:** Average crack healing velocity  $\bar{v}$  as a function of energy release rate  $G$ . Different cantilever responses are plotted with different color and marker types. (a) for  $p/p_s=0.9$  case. (b) for  $p/p_s=0.95$  case.

### 3.5 COMPARISON OF EQUILIBRIUM ADHESION VALUES OF WATER, *n*-PENTANOL, AND ETHANOL

In this section, we collect the results of the equilibrium adhesion energy  $\Gamma$  vs.  $p/p_s$  in one chart from various experiments for water, *n*-pentanol, and ethanol, as seen in Figure 3.10.

Water experiments data shown with blue circle markers in Figure 3.10 are gathered from three different samples. One of the data sets presents the response of three cantilevers at  $p/p_s=0.35, 0.54, 0.66, 0.72, 0.77, 0.85, 0.92, 0.97,$  and  $0.99$ . The other sample data display the response of five cantilevers at  $p/p_s=0.61$  and  $0.88$ . The last sample data show the response of four cantilevers at  $p/p_s=0.34, 0.54, 0.69, 0.80, 0.87, 0.95,$  and  $1.00$ . There are more cantilevers that heal on these samples. However, the sample response is summarized with fewer cantilevers. Also, there are cantilevers that don't heal until very high partial pressure conditions due to higher surface roughness or particles.

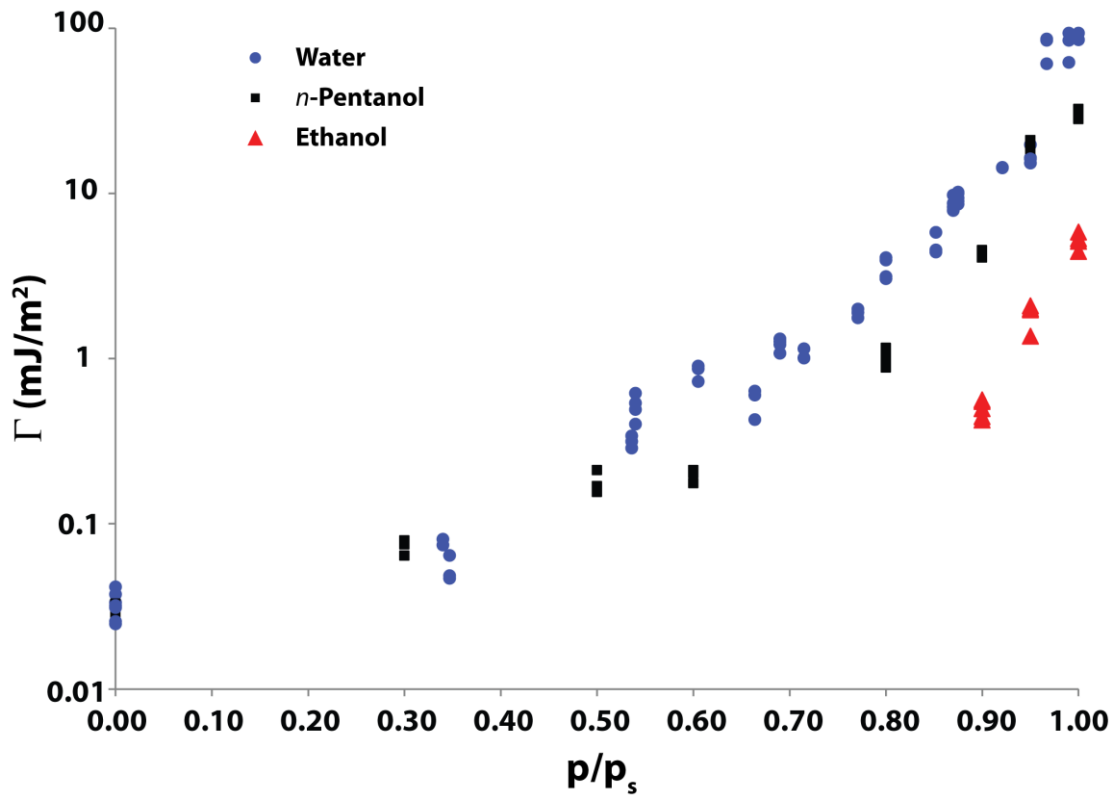


**Figure 3.10:** Adhesion energy at equilibrium vs partial pressure data. Water, *n*-pentanol and ethanol were represented by marks with blue circle, black square and red triangle, respectively.

The black square data markers represent *n*-pentanol experiments, as also seen in Figure 3.10. The data has been collected from the experiment described in section 3.4. The partial pressures are  $p/p_s=0.30, 0.50, 0.60, 0.80, 0.90, 0.95,$  and  $1.00,$  and data for five cantilevers are shown in Figure 3.10. In a similar way, ethanol experiment data, also, from section 3.4 were presented in Figure 3.10 with red triangle markers for the cases of  $p/p_s=0.90, 0.95, 1.00.$

To make a comparison of the data for different vapors, we need to understand the effects of surface roughness and Kelvin radius to the adhesion.

### 3.5.1 Surface Roughness Effect

Surface roughness effect has been studied for single asperity vs. flat surface [141] and between the multi-asperity surfaces [126] at the nanoscale. Small changes of the surface roughness effectively alter the adhesion energy of the surfaces. We scanned the upper and lower counterfaces of the cantilevers using tapping mode AFM. Between the polysilicon grains, there are deep grain boundary grooves that affect the roughness results. These grooves do not play a role during the capillary nucleation so only the intragrain roughness was characterized. Root mean square (rms) roughness for the lower counterfaces was  $\sim 1.4, \sim 1.8$  and  $\sim 1.4$  nm for the water, *n*-pentanol and ethanol experiments samples, respectively. The root mean square roughness for the upper counterfaces was  $\sim 1.7, \sim 1.8$  and  $\sim 2.0$  nm for the water, *n*-pentanol and ethanol experiments samples, respectively. Although there is some variation of the rms roughnesses, we can assume that the surface roughness values are very close to each other.

Over the  $5 \times 5 \mu\text{m}^2$  area, the surface features are relatively uniform for the samples of water and *n*-pentanol experiments, as seen in Figure 3.11 and 3.12. Upper counterface scans present holes on the surfaces because polysilicon grains protrude during the thermal oxidation. Protruded grains causes the hole formation due to the nature of chemical vapor deposition [126]. However, sample used in ethanol experiment have particles with 4-10 nm heights as indicated by red circles in Figure 3.13. These particles may be silicon carbide (SiC) particles, and they can form during the annealing processes of the sample fabrication steps described in detail by DelRio et al [142]. These high particles decrease the contacting areas, or they open larger gaps between

the surfaces. As a result, the adhesion values decrease. Cantilevers in the ethanol experiments did not heal until higher partial pressure, and the adhesion values are much smaller compared to water and n-pentanol experiments, as seen in Figure 3.10.

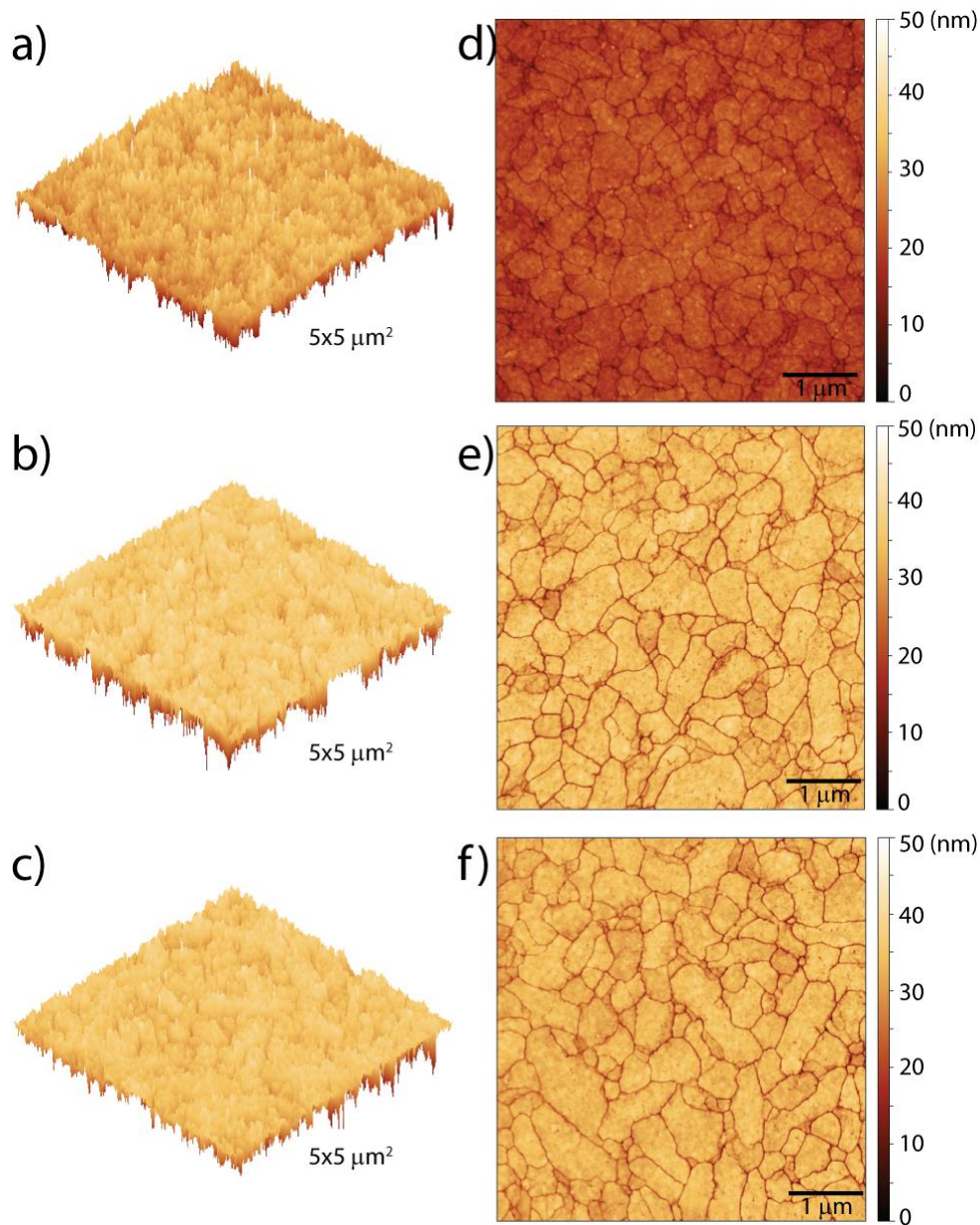


**Figure 3.11:** AFM images of the lower counterfaces over  $5 \times 5 \mu\text{m}^2$ . **a&d)** 3D&2D of the topography for the sample of the water experiment. **b&e)** 3D&2D illustration of the topography for the sample of the n-pentanol experiment. **c&f)** 3D&2D illustration of the topography for the sample of the ethanol experiment.

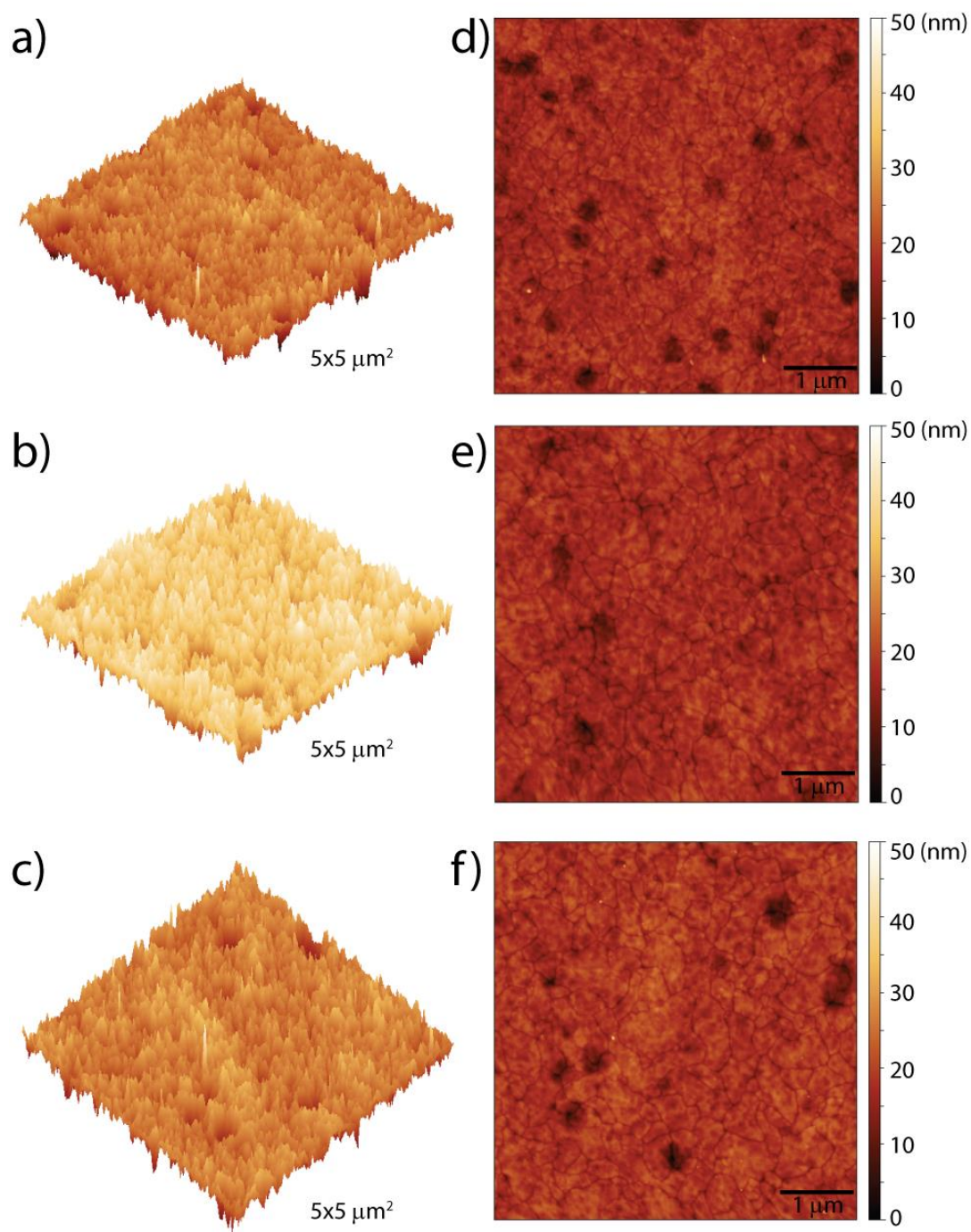


**Figure 3.12:** AFM images of the upper counterfaces over  $5 \times 5 \mu\text{m}^2$ . **a&d)** 3D&2D of the topography for the sample of the water experiment. **b&e)** 3D&2D illustration of the topography for the sample of the n-pentanol experiment. **c&f)** 3D&2D illustration of the topography for the sample of the ethanol experiment.

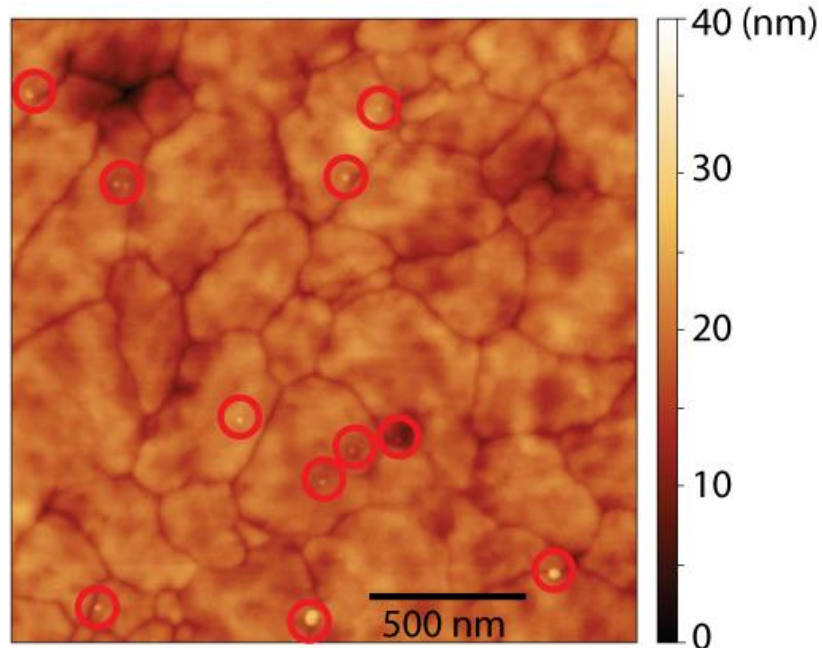


**Figure 3.13:** AFM image of the upper counterface of ethanol experiment's sample over  $2 \times 2 \mu\text{m}^2$ . Red circles indicate the possible SiC particles.

### 3.5.2 Kelvin Radius and Surface Tension Effects

The Kelvin equation (1.14) was described in section 1.2.2. The  $r_K$  value for water is calculated by  $0.53 \text{ nm}/\ln(p/p_s)$ . The 0.53 nm coefficient changes for the *n*-pentanol and ethanol due to different surface tension and molar volume values.  $V_m$  equals to 0.108 and 0.058 l/mol for *n*-pentanol and ethanol, respectively; and  $\gamma_L$  equals to 0.026 and 0.023 N/m for *n*-pentanol and ethanol, respectively [143]. Thus,  $r_K$  coefficient becomes 1.15 nm and 0.54 nm for *n*-pentanol and ethanol, respectively.

The *n*-pentanol coefficient of 1.15 nm gives approximately a factor of two larger  $r_K$  values compared to the water. This suggests that the number of nucleated capillary bridges are higher for the *n*-pentanol experiments. On the other hand, the surface tension of water is approximately a factor of three bigger than *n*-pentanol. When we compare our experimental results between water and *n*-pentanol, surface roughness effect is negligible. Dry condition

adhesion values (Figure 3.10 at  $p/p_s=0$ ) are very close to each other that leads to very similar surface roughnesses for these samples through the whole area of the cantilever surfaces.

At  $p/p_s=0.3$ , adhesion values of the cantilevers exposed to *n*-pentanol are 0.06-0.08  $\text{mJ}/\text{m}^2$ . At slightly higher  $p/p_s$  values, 0.34 and 0.35, adhesion values are 0.05-0.07  $\text{mJ}/\text{m}^2$  for the samples exposed to water. This suggests that nucleation capability at larger gaps is responsible for the higher adhesion values. As  $p/p_s$  increases, adhesion energies from the water experiments become higher than those in the *n*-pentanol experiments. This is because the surface tension difference becomes more significant. If we calculate the  $W_{asp}$  by taking the integral of the force vs. gap curves of water and *n*-pentanol cases as seen in Figure 3.14, at  $p/p_s=0.6$  using  $R=62$  nm, work of adhesion is calculated  $5.9 \times 10^{-17}$  J for water and  $4.6 \times 10^{-17}$  J for *n*-pentanol. As a result, factor of three difference from the surface tension becomes more important. Contradictory data from the *n*-pentanol experiments appear at  $p/p_s=0.95$ . *n*-pentanol experiment adhesion values seem higher than water experiments results. The possible explanation is the *n*-pentanol partial pressure might be higher than it is adjusted through the flow meters. Since we don't have the partial pressure sensor for the alcohols, we rely on the flow meter mixing ratios read by naked eye. This is a reliable system, but at high partial pressures  $r_K$  becomes very sensitive. For example,  $r_K=0.95$  and  $0.98$  nm at  $p/p_s=0.30$  and  $0.31$ , and  $r_K=22.42$  and  $28.17$  nm at  $p/p_s=0.95$  and  $0.96$  for *n*-pentanol vapor. One percent fluctuation may affect the results negligibly at low partial pressure case, but at higher values the variation affects significantly.

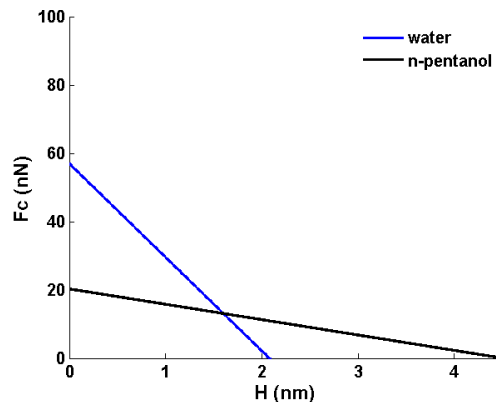


**Figure 3.14:** Comparison of the water and *n*-pentanol force values (equation 1.15) as a function of  $H$ . Blue line represents water, and black line represents *n*-pentanol.  $R=62$  nm and  $p/p_s=0.6$ .

### 3.6 CHAPTER SUMMARY

We have investigated the crack healing experiments for water, ethanol and *n*-pentanol vapors at different partial pressures. Crack healing occurs in discrete events, rather than continuously. It is seen that the average crack healing rate,  $\bar{v}$ , decreases with increasing  $G$ . A plot of  $\bar{v}$  versus energy release rate,  $G$ , reveals log-linear behavior, while the slope  $|d[\log(\bar{v})]/dG|$  decreases with increasing relative humidity.

We compared experimental data of ethanol and *n*-pentanol vapor adhesion energies with water vapor experimental data. We showed the surface roughness and Kelvin radius effects on adhesion between multi-asperity surfaces.

## Chapter IV: First Order Model of the Crack Healing at Various Partial Pressures

In this chapter, the crack healing experiments of chapter 3 are interpreted within the framework of capillary nucleation using a simple model in which all asperities are equally spaced and at the same height. Although the interface model is oversimplified, the log-linear trend and decreasing slope in increasing RH behaviors are captured qualitatively.

### 4.1 SURFACE ROUGHNESS CHARACTERIZATION

The actual surface in the experiments in the previous chapters II and III consists of polysilicon grains, which exhibit roughness at the nanometer scale. The surface topography can be measured using AFM, as seen in Figure 4.1. The surface topography is complex and has been modeled in many different ways. These include a fractal approach [144], or a Fourier series approach using a power spectrum [145]. Another high fidelity approach is to import the AFM data from the counterfaces and use it directly [126]. However, the most common method is to approximate the surface as consisting of asperities of a single radius of curvature but with different heights [146]. In this chapter, first order model uses the surface is modeled as asperities that are all of the same height, and complex model uses the surface as consisting of asperities of a single radius of curvature but with different heights.

It is further assumed that the interface can be modeled a rough surface on a smooth surface. Images of the lower counterface in the experiment, as scanned by tapping mode AFM, are shown in Figure 4.1. The lower surface asperity radius of  $R_l=124\pm 43$  nm (one standard deviation, 10 measurements) was found by fitting the AFM topography data of the asperities into the circular arc shapes[147] (Figure F5, Appendix F). A root mean square roughness inside the boundary of the grains  $\sigma \cong 1.9$  nm was found on the surface of the landing pad. Figure 4.1a unveils polysilicon grains as delineated by the grain boundaries. Over the  $5 \times 5 \mu\text{m}^2$  area, the surface features are relatively uniform. The magnified Figure 4.1b reveals that each grain is composed of small asperities, while Figure 4.1c is a linescan indicating hills and valleys. The

upper counterface has a similar value for the asperity radius  $R_u$ . The effective asperity radius is then

$$R = \left( \frac{1}{R_l} + \frac{1}{R_u} \right)^{-1} \quad (4.1)$$

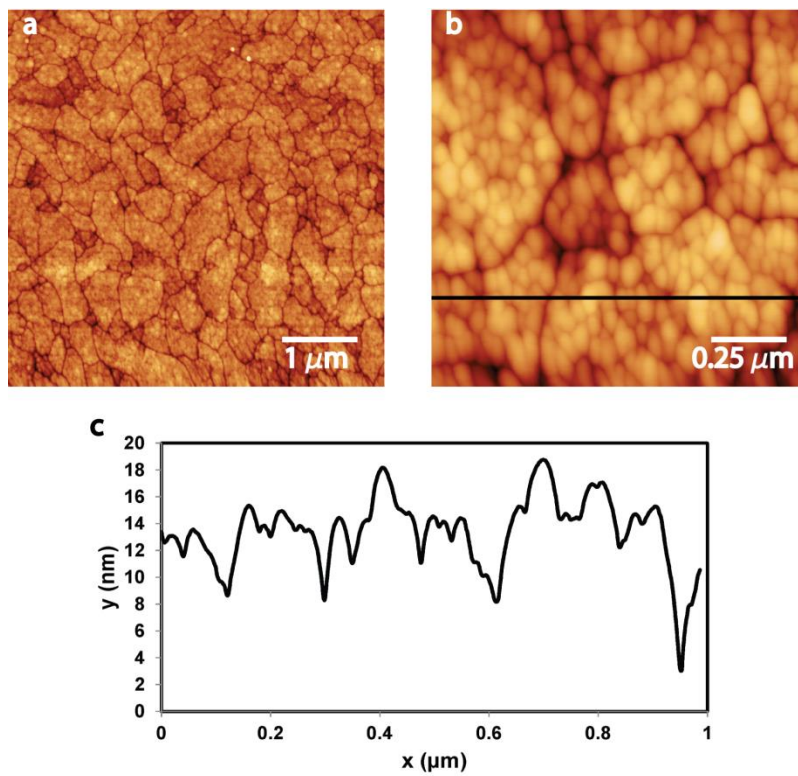


**Figure 4.1:** AFM images of polysilicon surface of sample 1. **a)**  $5 \mu\text{m}^2$  surface area **b)**  $1 \mu\text{m}^2$  surface area **c)** Cross sectional image along the black line shown in (b).

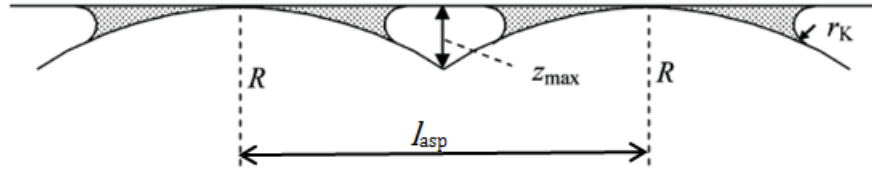


**Figure 4.2:** Array of uniform asperities with areal density  $n_{asp}=1/(8Rz_{max})$  contacting a plane, with liquid bridges of radius  $r_K$  providing adhesive energy[68].  $z_{max}$  is the largest separation between the substrate and the rough surface.  $l_{asp}$  is the asperity spacing along the length.

In Figure 4.2, the largest separation between the substrate and the rough surface,  $z_{max}$ , is related by geometry to areal density ( $n_{asp}$ ). According to Archard [148],

$$n_{asp} = \frac{0.05}{R\sigma} \quad (4.2)$$

estimates the asperity density per unit area. With  $R=62$  nm and  $\sigma =1.9\cdot\sqrt{2}$  nm (for two rough surfaces),  $n_{asp}\approx 300$  asperity/ $\mu\text{m}^2$ . This gives an upper limit to the asperity density relating to Figure 4.2.

For a square array of asperities as in Figure 4.2, it can be shown from geometrical considerations that

$$n_{asp} = \frac{1}{8Rz_{max}}. \quad (4.3)$$

According to this, we assign a value of  $z_{max}=7$  nm.

If  $z_{max}$  is smaller than  $2|r_K|$  for the corresponding vapor condition, individual asperity bridge activation is not possible because total area floods the interface. For  $p/p_s=0.61$ ,  $z_{max}=7$  nm is greater than  $2|r_K| = 2.1$ , so the interface is not flooded.

## 4.2 MODEL DESCRIPTION

The interface can be considered to consist of two rough surfaces in close proximity. Surface roughness can be described with increasing levels of fidelity [15,146,149]. We shall explore in this section a surface description that is more simple, but that already gives rise to a

rich variety of crack healing rate dependencies. Let us identify three different states for a given asperity (as designated parenthetically): (i) contacting and wetted (contacting), (ii) non-contacting and wetted (bridged), and (iii) non-contacting and not wetted (suspended). Capillary growth, either by a gas diffusion [73] or a surface molecule transportation mechanism [37], is fast compared to nucleation of capillaries across gaps on the order of the Kelvin radius.

Let us make the following considerations, and analyze a specific sequence of events. Figure 4.3 illustrates crack healing of uniformly distributed asperities all of the same height and radius  $R$ . Crack length equilibrium is represented in Figure 4.3a at a low RH level. There, Asperities 1 and 2 do not contact the surface, but are bridged by capillaries. Asperities to the right of 1 contact the substrate and are wetted, while those to the left of 2 are not bridged. In equilibrium, the radius of each capillary is governed by the Kelvin equation. When RH is increased, the meniscus volume of contacting Asperities 1 and 2 will *grow*, a fast process on the ms time scale or less for nanoasperities. Increased surface tractions will cause the beam to deflect towards the substrate. However, Asperity 1 may not yet make contact, as in Figure 4.3b. Therefore, capillary *nucleation*, a slow process, must occur. A capillary first nucleates at Asperity 3, the suspended asperity with the smallest gap. The nucleation event is rapidly succeeded by capillary growth with a concomitant force, which brings the beam and, hence, the asperities closer to the surface. The Asperity 3 capillary bridge still may not provide sufficient force to bring the Asperity 1 into contact. Therefore, the nucleation process repeats at Asperities 4 and 5, as illustrated in Figure 4.3c. Without displaying all the details at each successive nucleation and deflection, the final situation in which Asperity 1 has contacted the substrate is represented in Figure 4.3d. This sequence of events describes the crack healing time for a single asperity,  $\tau_{SA}$ , and then

$$\bar{v} = \text{pitch}/\tau_{SA} \tag{4.4}$$

where *pitch* is the center-to-center spacing of neighboring asperities.

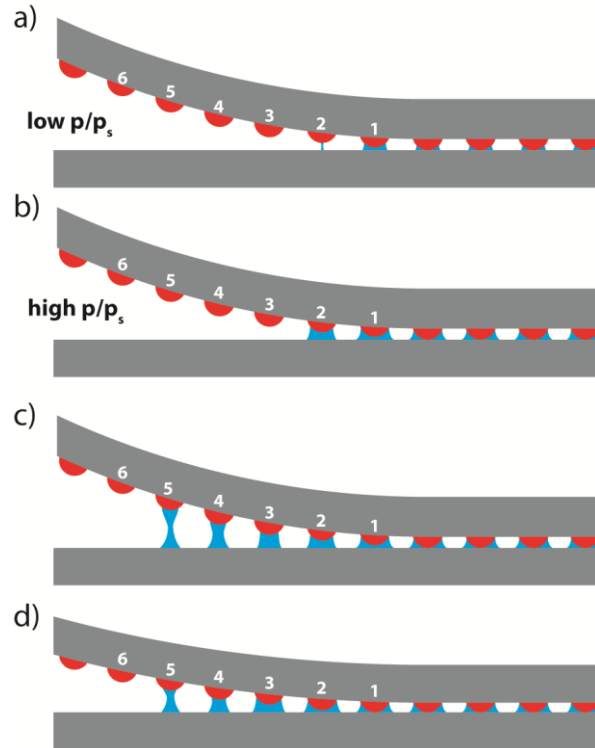


**Figure 4.3:** Illustration of crack healing with uniformly distributed asperities of equal height. (a) At low RH, the crack tip region is illustrated in equilibrium. (b) When RH is increased, capillaries at Asperities 1 and 2 grow, but induce only a small beam deflection. (c) Asperities 3 to 5 are nucleated sequentially, but Asperity 1 does not yet make contact. (d) The capillary force at each asperity brings the beam closer to the substrate. The resulting deflection due to the forces at Asperities 1-5 cause Asperity 1 to make contact.

### 4.3 MODEL IMPLEMENTATION

The picture just described provides an algorithm for a numerical model. This model does not capture quantitatively the experimental results, but lends insight into the strong parametric dependencies of  $\bar{\nu}$ . For a particular simulation, the asperities are spaced by a *pitch* value that is taken to be equal to the width of the cantilever. Individual point loads from each capillary bridge are linearly superposed to estimate the cantilever deflection. The cantilever thickness is  $t=2.5$   $\mu\text{m}$ , and the asperity radius  $R=62$  nm. The latter two values represent the experiment. The assumption that the width is equal to the asperity pitch is accounted for because adhesion is measured per unit area. The model takes into account only capillary forces according to equation 1.15 and cantilever beam elasticity. Asperity elasticity, asperity-asperity adhesion, and the

surface water layer are important second-order effects that are neglected in this model. This is justified quantitatively because the dimensionless parameter [150]

$$\lambda = \frac{1}{r_K} \left[ \frac{(2\gamma)^2}{\frac{4}{9R}\pi\left(\frac{E}{1-v^2}\right)^2} \right]^{1/3} \quad (4.5)$$

where  $v$  is Poisson's ratio, is much less than 1 ( $\lambda = 0.03$  and  $0.008$  at RH=60.5% and 87.5%, respectively). Hence the capillary pressure outside the solid-solid contact area dominates the adhesion forces [150].

The numerical model initiates with  $s=800 \mu\text{m}$ . The left end of the cantilever is at height  $h$ , and the right end is fixed to the substrate as in Figure 3.1b. All asperities with  $x \geq s$  contact the substrate and are assumed to be wetted. For such a large  $s$  value, the boundary condition is equivalent to a clamp condition, forcing the beam into contact with the substrate with zero slope at  $x=s$ , and the beam deflection is described by equation 3.1. In Figure 4.3a, the situation would be represented with Asperities 1-6 all in the suspended state. The energy barrier for nucleating Asperity 1 is found from equation 1.59, where  $H$  is the asperity-substrate gap. The nucleation time is then calculated from

$$\tau = \tau_0 \exp[\Delta\Omega/k_B T] \quad (4.6)$$

where  $1/\tau_0$  is the attempt frequency,  $k_B$  is the Boltzmann constant and  $T$  is the temperature (K). We use  $\tau_0=100$  GHz, similar to Boyd et al [82]. Its choice is not important given the qualitative results presented below.

Figure 4.4 indicates the force-displacement curve for a single asperity according to equation 1.15. The asperity nucleation is represented by traversing from B to C. At C, a force brings the cantilever closer to the substrate, ramping the force towards D. The force increases,

causing the gap to close further. The stable point D in Figure 4.4 is found by iteration. It is assumed that the time to equilibrate forces is short compared to the nucleation time. So far, this corresponds to Figure 4.3b with only Asperity 1 bridged.

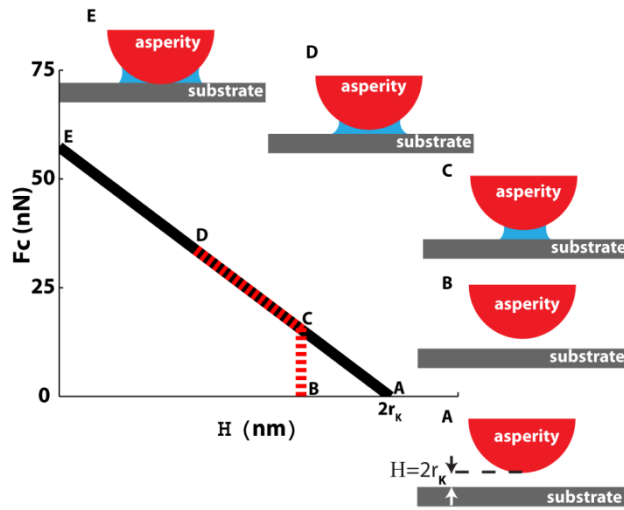


**Figure 4.4:** Force-displacement curve according to Eq. (1.15) with  $R=62$  nm and  $RH=60.5\%$ . At  $H=2r_k$ , no capillary bridge can form. With decreasing  $H$  (A→B), a liquid capillary bridge nucleates after time  $\tau$  determined by equation 1.59 (B→C). This will exert force on the microcantilever, causing capillary growth, further increasing the force (D). As other capillaries nucleate, point D will move further up the curve. The maximum capillary force between two surfaces occurs at contact (E).

Because of the short distance, however, the moment arm from Asperity 1 to the previous crack tip at  $s$  is small, and the change in beam deflection is miniscule. Therefore, Asperity 2 must nucleate and achieve mechanical equilibrium. It traverses a similar path from BCD in Figure 4.4. Iteration is required to ensure Asperities 1 and 2 are now both in mechanical equilibrium at their respective points D. Once equilibrium is found, Asperity 1 may be closer to the substrate, but not yet in contact. Therefore,  $\tau$  for Asperity 3 is calculated, and the force iteration is conducted on Asperities 1, 2 and 3. This process repeats until Asperity 1 is brought into contact at E. The total time involved with nucleating all bridges is taken to be the single asperity healing time,  $\tau_{SA}$ . The algorithm just describes takes into account more detail than is

represented by Figure 4.3, but Figure 4.3d illustrates a completed crack healing step for Asperity 1 in which five asperities were required to achieve a crack healing step.

For the next single asperity healing event, the situation begins with Figure 4.3d. The time  $\tau$  for Asperity 6 to nucleate is calculated, and mechanical equilibrium is determined. This time will generally be larger than the previous  $\tau_{SA}$ , but now because the moment arm is greater, nucleation of Asperity 6 may be sufficient to bring Asperity 2 into contact. Thus, the crack healing time for Asperity 2 may be associated only with  $\tau$  for Asperity 6. In fact, only a single asperity nucleation event is needed in most modeled situations, and  $\tau_{SA}$  usually reflects the process described in the current paragraph. Once  $\tau_{SA}$  is known, equation 4.4 is used to find  $\bar{v}$ .

## 4.4 MODEL RESULTS

Figure 4.5 shows the numerical model results for various parameters (RH=60.5% or 87.5%, asperity pitch of 75, 125 or 250 nm, and  $R=62$  nm). As seen,  $\bar{v}$  generally decreases rapidly with  $G$ , and exhibits a wide range of 9 decades. At the top of the range, an approximate limit where meniscus growth rather than nucleation limits the velocity is denoted by the horizontal dashed red line. The approximate range of the experiments is indicated by the shaded regions, and the data trends by the solid lines in them.

Let us consider the modeled 87.5% RH lines with 75 nm asperity pitch. At intermittent points, there is a vertical downward excursion in  $\bar{v}$ . This reflects events in which a single nucleation was insufficient to bring the next asperity into contact. In such cases, two asperities need to nucleate, which increases  $\tau_{SA}$  for the same *pitch* value. Also, at low velocity, say  $\bar{v}=10^{-6}$   $\mu\text{m/s}$ , the theoretical equilibrium adhesion value [26,68],

$$\Gamma = n_{asp} W_{asp} = 4\pi n_{asp} R |r_K| \gamma_L \cos\theta^2 \quad (4.7)$$

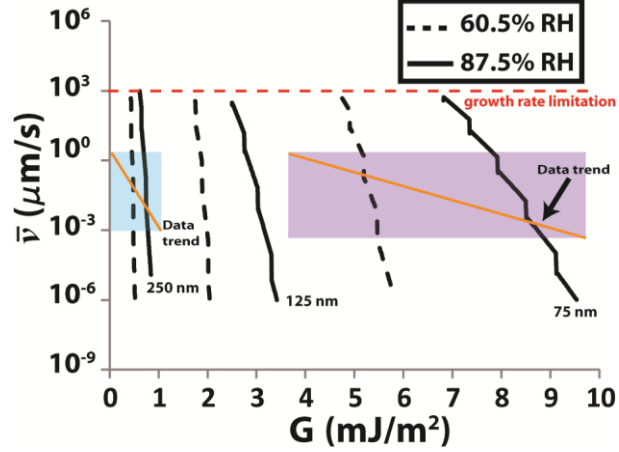


**Figure 4.5:** Numerical model results. The average velocity  $\bar{v}$  for the cases of RH=60.5% and 87.5%, and pitch=75, 125 and 250 nm are calculated. Shaded rectangular areas indicate the experimental adhesion and time realms, and the solid line within indicates the approximate experimental trend.

is approached but not met. For example, at RH=60.5% with  $pitch=75$  nm,  $n_{asp}=1/pitch^2=177/\mu m^2$ ,  $R=62$  nm,  $|r_K|=1.05$  nm,  $\gamma_L=72$  mJ/m<sup>2</sup>, and  $\theta=0^\circ$ ,  $\Gamma=10.5$  mJ/m<sup>2</sup>. However, at  $\bar{v}=10^{-6}$   $\mu m/s$ , in the numerical model  $G=6$  mJ/m<sup>2</sup>. This is because  $\Gamma$  is determined only by the asperity density, and rather than by the dynamics of how crack equilibrium is achieved.

Comparing the three different  $pitch$  values at 87.5% RH in Figure 4.5, it is clear that  $|d[\log(\bar{v})]/dG|$  increases strongly as  $pitch$  increases. This is associated with the very strong dependence of  $\tau$  on  $H$  in equation 4.6. As pitch increases, the next asperity is further away from the crack tip. Consequently,  $H$  increases, strongly increasing  $\tau$ . For the same  $G$ , the slope  $|d[\log(\bar{v})]/dG|$  again increases as RH decreases from 87.5% to 60.5%. This is again due to the nonlinearity in equation 4.6.

## 4.5 CHAPTER SUMMARY

First order model demonstrated that crack healing takes place when the RH increases. The model indicates that  $|d[\log(\bar{v})]/dG|$  increases as RH increases. This model can be used to

qualitatively explain the experimental trends. The model assumes that the driving force for crack healing is due to capillary nucleation across asperity gaps. For a quantitative agreement with the experiments more complex model is needed, and it will be introduced in Chapter V.

# Chapter V: Modeling of Crack Healing at Various Partial Pressures Between the Rough Nanoscale Surfaces

## 5.1 INTRODUCTION

In the previous chapter, a simple model was developed to gain insight into the experimentally measured average crack healing rate  $\bar{v}$  versus energy release rate  $G$  as a function of relative humidity and surface roughness. Although the surface roughness model was highly oversimplified, the model provided *qualitative* insight into important experimental observations such as the log linear trend in  $\bar{v}$  versus  $G$ , and the decrease in the slope of  $|d[\log(\bar{v})]/dG|$  with increasing RH. However, *quantitative* agreement with the data was utterly lacking.

By incorporating important details, such as a better description of the interface roughness and the presence of an adsorbed water layer, this chapter aims to predict *quantitatively* the behavior of capillary force dynamics. Beside gaining better agreement, other goals that are of interest are to understand the variation in  $\bar{v}$ , and also to understand why the crack stops healing once a certain  $G$  value has been attained.

The first issue that needs to be addressed is how to obtain a good description of the interface roughness. Of course, AFM topography maps can give us a good idea of the actual surface topography, and we immediately examine such maps of the counterfaces. However, importing and employing such data directly into computations is numerically intensive. Therefore, we seek a surface model that captures the surface details in a sufficiently satisfactory fashion. We shall assume that a topography in which asperities are modeled as elastic spherical caps, but now with a distribution of heights, is a good first step in this direction. The distribution will be assumed to be normal, but the importance of a cutoff in asperity height will be postulated and investigated.

Next, constitutive laws for single asperities under *dry conditions* will be explored. These necessarily incorporate long range van der Waals forces because even though relatively weak,

they are crucial especially in the dry adhesion case for promoting surface attraction. Both a simple (Derjaguin-Muller-Toporov) DMT [22] and a modified Maugis Dugdale (MD) [24] model will be developed. These models will be assessed using multi-asperity interfaces using two techniques. The first is a **parallel plate** model. Here, the asperities are attached to a *rigid* backing plate, and the force-displacement curve is calculated. Second, a **beam model** is developed. Here the asperities are attached to an *elastic* beam. The crack length is set to a long length, and then the surface forces perform work against the beam to heal the crack spontaneously until it reaches equilibrium. The beam model enables insight into adhesion variations, which develop when the asperity heights along the length of the beam are randomized. It is also seen how asperities of different heights and distances from the crack tip influence the crack healing, or on the other hand, pin it open. Using the AFM topography maps as a starting point, and comparing the results of the different models with the experimental value of  $\approx 0.03 \text{ mJ/m}^2$ , a best choice for surface topography is rationalized.

Finally, we develop constitutive laws for *wet conditions*. Using Restagno's activated energy model for capillary nucleation [77], crack healing rates are calculated using both the parallel plate and the beam models. The results significantly underestimate the experimental crack healing rates. Therefore, an adsorbed water layer, well known to exist on clean surfaces in wet environments [105,132,133], is introduced. This has the effect of reducing the effective gap between the surfaces, enhancing the crack healing rates. However, agreement with experiments remains unsatisfactory. Therefore, a new capillary nucleation rate models are investigated. It is seen that a model that agrees relatively well with recently-reported single asperity measurements [87], gives good agreement with the crack healing data.

## **5.2 SURFACE TOPOGRAPHY MAPS AND INTERFACIAL PARAMETERS**

As a starting point for the interface description, measurements of the lower and upper counterfaces were made using tapping mode atomic force microscopy (AFM). The lower surface asperity radius of  $R_l=124\pm 43 \text{ nm}$  (one standard deviation, 10 measurements) was found

by fitting the AFM topography data of the asperities into the circular arc shapes [147]. A root mean square (rms) roughness  $\sigma \cong 1.4$  nm was found on the lower counterface, as seen in Figures 5.1a and 5.1c. The upper counterface was measured by peeling the microcantilevers from the substrate using cellophane tape. It has a slightly larger rms roughness value of  $\sigma \cong 1.6$  nm, as seen in Figures 5.1b,d, and a similar value for the asperity radius  $R_u = 124 \pm 43$  nm (one standard deviation, 10 measurements). These values were calculated by removing deep grooves due to grain boundaries, which can be seen as dark lines in Figure 5.1, to better reflect the operative distribution.

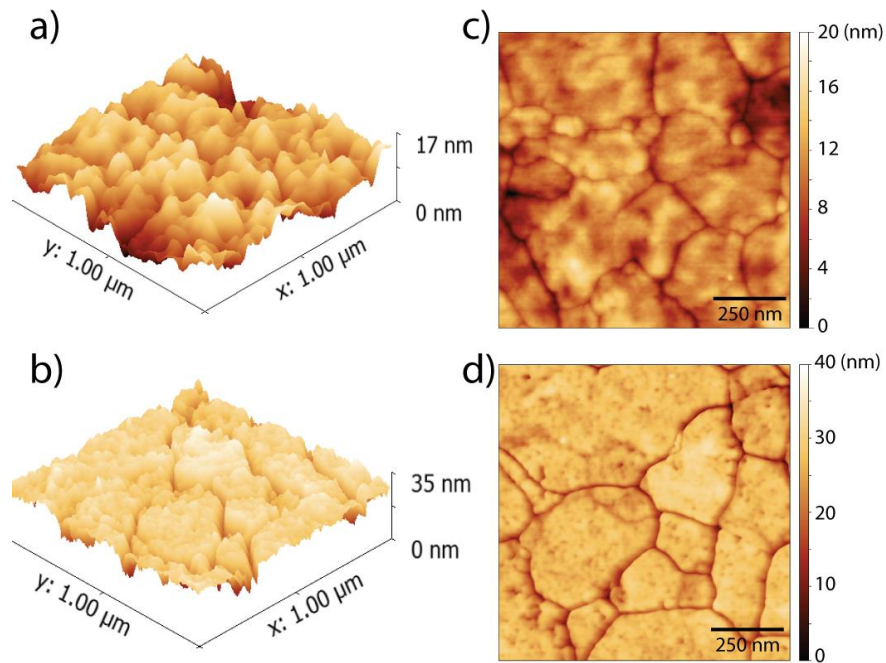


**Figure 5.1:** Topography of the sample that has been used at the experiment. **a&c)** 3D&2D AFM images of the lower counterface over  $1 \times 1 \mu\text{m}^2$ . **b&d)** 3D&2D AFM images of the upper counterfaces over  $1 \times 1 \mu\text{m}^2$ .

Surface roughness can be described with increasingly elaborate models [15,146,149]. Here, we use the standard Greenwood-Williamson model [146] as a point of departure. It assumes that the surface consists of spherical asperity caps of radius  $R$  and of variable height, distributed according to a normal distribution with root mean square roughness  $\sigma$ . We model the two counterfacing rough surfaces as one elastic rough surface pressed against a rigid plate [151]. The effective asperity radius is then

$$R = \left( \frac{1}{R_l} + \frac{1}{R_u} \right)^{-1}. \quad (5.1)$$

Therefore, a value of  $R=62$  nm is the input parameter as an asperity radius at simulations. Also, the effective rms roughness is

$$\sigma = \sqrt{\sigma_l^2 + \sigma_u^2}, \quad (5.2)$$

which gives  $\sigma = 2.1$  nm. Over the  $1 \times 1 \mu\text{m}^2$  area, 20 asperities arise along the  $1 \mu\text{m}$  linescan in the AFM image. This corresponds to an asperity density of  $n_{asp}=400/\mu\text{m}^2$ , which was implemented as a constant in the model.

The reduced Young's modulus is  $E^* = [(1 - \nu_u)^2/E_u + (1 - \nu_l)^2/E_l]^{-1}$  is where  $E_u, \nu_u$  and  $E_l, \nu_l$  are the Young's modulus and Poisson coefficient of the upper and lower layer, respectively. In our case, both layers are polycrystalline silicon (polysilicon) with  $E=164$  GPa [118] and  $\nu=0.23$ , and then  $E^*=86.5$  GPa.

### 5.3 CONSTITUTIVE LAWS FOR DRY CONDITIONS

We considered several constitutive models for single asperity versus flat plane under dry conditions to investigate the dependence of the results on the particular model, and to assess which model was most appropriate. In each, the repulsive force is taken from the Hertz model. In order to attain self-consistent models in which attractive surface forces do not diverge at contact, it is necessary to consider the intermolecular separation  $z_o$ , as indicated in Figure 5.2. There, the parameter  $\omega$  is the distance from the tip of the undeformed sphere to  $z_o$ . Note that  $\omega < 0$  represents interpenetration, as shown in Figure 5.2b. Also, the sphere-surface separation is

$$H = z_o + \omega \quad (5.3)$$

as seen in Figures 5.2a and 5.2b. The repulsive force acts for  $\omega < 0$ , i.e.,  $H < z_o$ . It grows non-linearly as the  $\omega$  decreases [22].

$$F_H = \frac{4}{3} E^* \sqrt{R} (-\omega)^{3/2} \quad \text{for } \omega < 0 \quad (5.4)$$

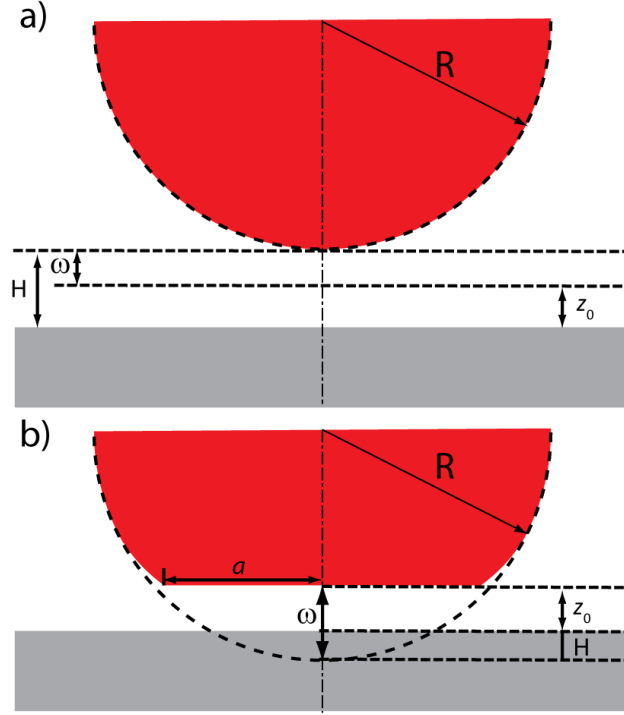


**Figure 5.2:** Schematic of a deformable elastic sphere and a rigid flat surface.  $z_0$  is the interatomic distance. **(a)** Non-contacting illustration  $H \geq z_0$ , **(b)** contacting  $H < z_0$ .

In detail, a further correction is made to the repulsive force. According to continuum theory, at a critical penetration ( $-\omega_c$ ), plastic deformation begins. Therefore, we modify  $F_r$  to include plasticity effects. The equation for the critical penetration is given by

$$\omega_c = -\left(\frac{\pi K \mathbb{H}}{2E^*}\right)^2 R, \quad (5.5)$$

where  $K = 0.454 + 0.41\nu$  is a hardness coefficient [152], and  $\mathbb{H}=10.5$  GPa [153] is the polysilicon hardness. With  $\nu=0.23$  and  $E^*=86.5$  GPa for silicon, the value of  $\omega_c$  is 0.68 nm. The repulsive forces as a function of penetration are calculated by applying the equations that are derived from FEA simulations [154]. Hence, for  $\omega < 0$  the repulsive force is

$$\frac{F_r}{F_c} = \begin{cases} (-\omega/-\omega_c)^{1.5}, & 0 \leq -\omega/-\omega_c \leq 1 \\ 1.03(-\omega/-\omega_c)^{1.425}, & 1 \leq -\omega/-\omega_c \leq 6, \\ 1.40(-\omega/-\omega_c)^{1.263}, & 6 \leq -\omega/-\omega_c \leq 110, \end{cases} \quad (5.6)$$

where  $F_c$  is the critical contact force corresponding to  $\omega_c$  in Equation 5.4. Given that the power law exponent is now smaller (1.425 or 1.263 versus 1.5 for Hertz), this law represents a gradual reduction in the repulsive force as penetration  $-\omega$  increases beyond  $-\omega_c$ , as would be expected once plasticity initiates.

The DMT model we study is taken to be a combination of van der Waals attractive forces and the repulsive forces [24]. Although the sphere is elastic-plastic, it is assumed, due to its relatively high modulus, that van der Waals forces acting across a gap are insufficient to distort its shape. Once the sphere encounters higher forces, such as those from Hertz repulsion, it does deform. Before contact ( $H > z_0$ ) and after contact ( $H \leq z_0$ ), the attractive forces are described by

$$F_{\text{vdW}} = \begin{cases} -\frac{A_H R}{6H^2} g_f & H > z_0, \omega > 0 \\ -\frac{A_H R}{6z_0^2} & H \leq z_0, \omega \leq 0 \end{cases} \quad (5.7)$$

Here,  $A_H$  is the Hamaker constant. A value  $A_H = 5 \times 10^{-20}$  J [155] for  $\text{SiO}_2$  is assumed because the surface is coated by a 2-3 nm thick native oxide after an oxygen plasma clean, while  $z_0$  is taken to be 0.2 nm. The closest separation at  $z_0$  sets the maximum adhesion force according to equation 5.7. The transition function  $g_f$  gives the retarded van der Waals forces,

$$g_f = \left[ 1 - \frac{2H}{b} + \frac{6H^2}{b^2} + \frac{12H^3}{b^3} - \frac{12H^3}{b^4} [H + b] \ln\left(1 + \frac{b}{H}\right) \right] \quad (5.8)$$

Here,  $b = 3.1\lambda/2\pi$ ,  $\lambda=100$  nm is a characteristic wavelength and 3.1 is a constant for the correction function [156].

Once contact occurs ( $H \leq z_0$ ), asperity deformation are as are shown in Figure 5.2b. As  $H$  becomes less than  $z_0$ ,  $\omega$  becomes negative. Hence  $-\omega$  is the apparent sphere penetration. The force  $F_{DMT}$  [22] is then given by the sum of equation 5.6 and the second of equations 5.7. Hence, the complete DMT model is

$$F_{DMT} = \begin{cases} -\frac{A_H R}{6H^2} g_f & H > z_0, \omega > 0 \\ F_r - \frac{A_H R}{6z_0^2} & H \leq z_0, \omega \leq 0 \end{cases} \quad (5.9)$$

The advantage of the above DMT model is that forces between non-contacting surfaces are included, unlike the Johnson-Kendall-Roberts (JKR) [21] model. This is needed because van der Waals forces are known to be important for adhesion between rough surfaces [126]. However, in the above interpretation, the adhesion force does not increase as the sphere penetration increases. This may be important to consider because the details of the crack healing may be sensitive to the constitutive law assumed. Therefore, the second model we investigate accounts for this effect. It is a combined Maugis-Dugdale (MD)–van der Waals model.

We first discuss the MD model alone (ignoring for the moment the van der Waals forces), which accounts for increasing adhesion as penetration increases and further accounts for the adhesive force dependence on the type of contact -- DMT, JKR, or an intermediate situation [24]. The adhesion forces are calculated by a constant stress,  $\sigma_0$ , over a range  $\delta_t$  [157]. The work of adhesion  $\Gamma_{ff}$  for smooth flat surfaces [155] is

$$\Gamma_{ff} = -\sigma_0 \delta_t = \frac{A_H}{12 \pi z_0^2} \quad (5.10)$$

With  $A_H=5 \times 10^{-20}$  J,  $\Gamma_{ff}$  is 33 mJ/m<sup>2</sup>. Using  $\delta_t=0.971z_0$ , the value for  $\sigma_0$  is -171 MPa, a negative value for attractive stress. The value of 0.971 is calculated from the minimum stress in a Lennard-Jones potential with equilibrium separation of  $z_0$  [157].

For all models, contact is considered to occur when the sphere tip reaches  $z_0$ . This bears further discussion when the Dugdale zone is operative. As the sphere approaches the Dugdale zone in the MD model, it senses no attraction. Once it contacts the Dugdale zone, the attractive stress  $\sigma_0$  will cause it to deform towards the rigid surface. Then  $h_0$ , which is the separation accounting for elastic deformation, is the distance from  $z_0$  to the tip of the asperity, as indicated in Figure 5.3a. The sphere cannot penetrate beyond  $z_0$ , as indicated in Figure 5.3b. However, if the sphere were retracted,  $h_0$  can reach  $\delta_t$ . Hence  $h_0 > 0$  is the non-contacting condition while  $h_0 = 0$  is the contacting condition for the MD model.

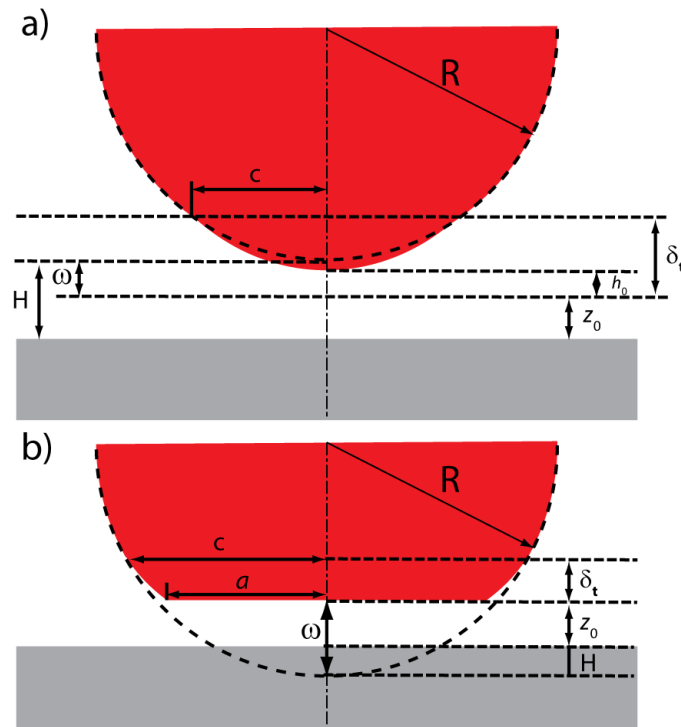


**Figure 5.3:** Schematic of a deformable elastic sphere and a rigid flat surface.  $z_0$  is the interatomic distance,  $\delta_t$  is the range of the constant attractive region for MD model. **(a)** Non-contacting illustration  $h_0 > 0$ , **(b)** contacting  $h_0 < 0$ .

For  $0 < h_0 < \delta_t$  as shown in Figure 5.3a, using the MD model we first find the value for the interacting area as defined by  $c$ , the radius of the Dugdale potential-limited area. Accordingly,

$$\frac{c^2}{2R} + \frac{2\sigma_0 c(\pi-2)}{\pi E^*} + h_0 - \delta_t = 0 \quad (5.11)$$

Equation 5.11 accounts for the effect of uniform attractive pressure on the sphere deformation [18]. The adhesive force is then given by

$$F_{MD\_A} = \pi \sigma_0 c^2 \quad (5.12)$$

and  $\omega$  is determined from

$$\omega = h_0 - \frac{2c \sigma_0}{E^*} \quad (5.13)$$

Note that a minus sign is used in equation 5.13 because the attractive stress is taken as negative.

Once the sphere makes contact with the flat rigid plane ( $h_0=0$ ), the following equations apply. First, Maugis' adhesion parameter,  $\lambda$ , is calculated, where

$$\lambda = \sigma_0 \left( \frac{9R}{2\pi\Gamma_{ff}E^{*2}} \right)^{1/3} . \quad (5.14)$$

The JKR model applies for  $\lambda > 5$ , while the DMT model applies for  $\lambda < 0.1$  [150]. For the present case,  $\lambda=0.12$ , which closely approaches the DMT situation. For a given ratio of  $c/a = m$ , the MD model yields the relations (5.15) to (5.18).

$$\frac{\lambda a^{*2}}{2} \left[ \sqrt{m^2 - 1} + (m^2 - 2) \tan^{-1} \sqrt{m^2 - 1} \right] + \frac{4\lambda^2 a^*}{3} \left[ \sqrt{m^2 - 1} \tan^{-1} \sqrt{m^2 - 1} - m + 1 \right] = 1 , \quad (5.15)$$

where  $a^*$  is the normalized contact radius,

$$a^* = a \left( \frac{4E^*}{3\pi\Gamma_{ff}R^2} \right)^{1/3} . \quad (5.16)$$

The normalized approach depends on contact radius

$$\omega^* = \omega \left( \frac{16E^{*2}}{9\pi^2\Gamma_{ff}^2R} \right)^{1/3} = a^{*2} - \frac{4}{3} a^* \lambda \sqrt{m^2 - 1} . \quad (5.17)$$

In this work,  $\omega$  is taken to be the independent parameter. By iteration,  $m$  and  $a^*$  values that satisfy both equations 5.15 and 5.17 can be found for a given value of  $\omega$ . Then, the total adhesive force is calculated as

$$F_{MD\_A} = 2\sigma_0 a^2 (m^2 \tan^{-1} \sqrt{m^2 - 1} + \sqrt{m^2 - 1}) \quad (h_0 = 0) \quad (5.18)$$

The repulsive force is now added to the attractive force to obtain the total MD force. In summary,

$$F_{MD} = \begin{cases} 0 & h_0 > 2\delta_t \quad (h_0 = \omega) \\ \pi\sigma_0 c^2 & 0 < h_0 \leq 2\delta_t \quad (\text{Eq. 5.13 relates } h_0 \text{ to } \omega) \\ F_{MD\_A} + F_r & h_0 = 0 \quad \left( \omega = -\frac{2c\sigma_0}{E^*} \right) \end{cases} \quad (5.19)$$

When  $h_0$  becomes zero according to equation 5.13 in the second expression, the value of  $\omega$  will be greater than zero. This marks the transition to the third expression. Inside the contacting region, the adhesive stress remains equal to  $\sigma_0$ .

Both the DMT and MD models are normalized to the work of adhesion. That is, both would exhibit the same work per unit area,  $\Gamma_{ff}$ , to separate the materials if the opposing surfaces were nominally flat. However, in detail, the single asperity force-displacement curves depend on the particular model. Figure 5.4 compares the curves for different models, with  $\omega$  as the independent parameter. In Figures 5.4a, and 5.4b, the adhesive force in the contacting regime is indicated by blue dashed lines. In Figure 5.4a, the dashed blue line is constant, while in Figure 5.4b, it becomes more negative representing the increasing attraction of the Dugdale zone. Compared to the DMT model (Figure 5.4a), the adhesive force in the MD model (Figure 5.4b) is larger at  $\omega=0$  because the deformation increases the interacting area with the flat. The effect is seen in Figure 5.4d, where the models are compared directly. The difference, however, is small. For the DMT and MD models, the forces at  $\omega = 0$  are 12.9 nN and 13.5 nN, respectively. In Figure 5.4a, the long range  $F_{vdW}$  is shown up to 0.5 nm but in the model is taken to extend to 100 nm. In Figure 5.4b,  $F_{MD\_A}$  is 0 for  $\omega > 0.194$  nm, and once contact is made it increases because the interaction area increases. For a single asperity, surface forces across a gap may seem small. However, they become significant when considering that  $n_{asp}=400/\mu\text{m}^2$  and the surface forces are acting to heal a compliant beam.

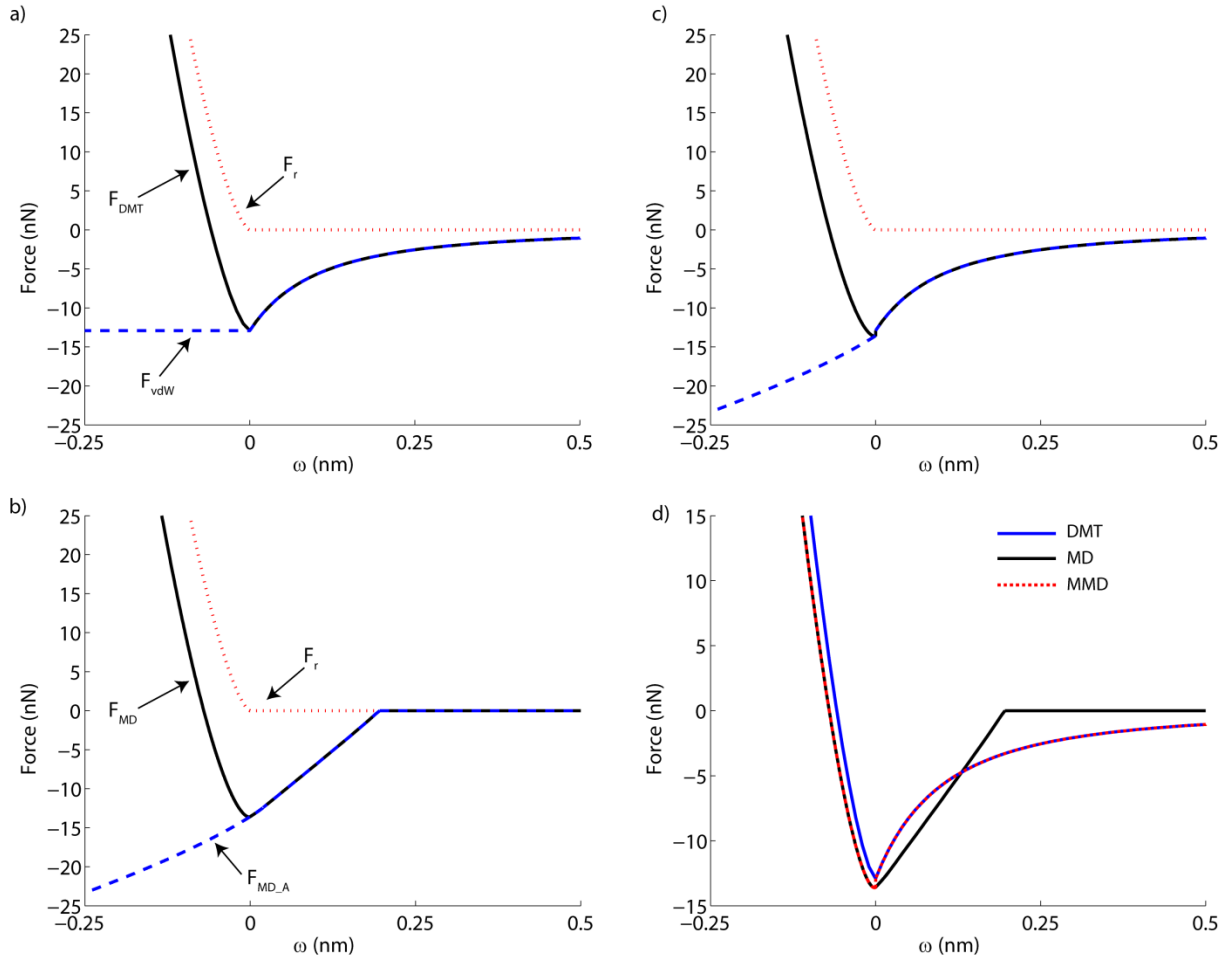


**Figure 5.4:** Blue dashed lines are the curves for adhesive force versus  $\omega$  for the (a) DMT, (b) MD and (c) MMD models. Red dotted lines are the repulsive forces due to Hertzian contact. Black solid lines are the sum of the attractive and repulsive forces. (d) shows the total force applied for each model.

We see that neither of the above approaches, as represented in Figures 5.4a and 5.4b, is entirely satisfactory. The DMT model does not account for the effect of surface forces on the asperity deformations, while the MD model does not account for long-range attractive forces. Therefore we propose a hybrid DMT-MD, model to capture the important physics. We call this the modified MD, or MMD model.

The MMD model incorporates van der Waals forces per equation 5.7 from separations of 100 nm to  $z_0$ . After this point, the contacting asperity deforms and the interacting area increases.

The MMD model then follows equation 5.19 to include this effect. Thus, it ignores the attractive forces due to the Dugdale zone until the asperity reaches  $z_0$ , because the Dugdale zone represents the entire range of attractive forces. The effect due to the entire range is accounted for by starting at  $H=100$  nm. While in the Dugdale zone, the asperity remains rigid. Once it reaches  $z_0$ , the asperity becomes elastic and the deformations and contact area are calculated according to the MD model. The MMD model adhesive force equation is

$$F_{MMD\_A} = \begin{cases} -\frac{A_H R}{6H^2} g_f & \text{for } \omega > 0 \\ 2\sigma_0 a^2 (m^2 \tan^{-1} \sqrt{m^2 - 1} + \sqrt{m^2 - 1}) & \text{for } \omega \leq 0 \end{cases}. \quad (5.20)$$

The full MMD model is then

$$F_{MMD} = \begin{cases} -\frac{A_H R}{6H^2} g_f & \text{for } \omega > 0 \\ F_r + 2\sigma_0 a^2 (m^2 \tan^{-1} \sqrt{m^2 - 1} + \sqrt{m^2 - 1}) & \text{for } \omega \leq 0 \end{cases}. \quad (5.21)$$

The force-displacement curve of the MMD model is shown in Figure 5.4c, where the blue dashed line indicates the attractive forces once contact is made.  $F_{MMD}$  exhibits a small discontinuity at  $\omega = 0$  (from 12.9 nN to 13.5 nN) because  $F_{MD\_A}$  differs from  $F_{vdW}$  after including the deformation effect on adhesion.

Figure 5.4d compares the total force curves for the three cases. The difference between  $F_{MMD}$  and  $F_{DMT}$  is small for a single asperity, and is due to a force discontinuity at  $\omega = 0$ . In the following model results sections we will explore whether this difference is important in evaluating the adhesion of the rough interface.

## 5.4 PARALLEL PLATE MODEL

### 5.4.1 Parallel Plate Model Description

The DMT and MMD constitutive laws were now implemented in two different multi-asperity surface descriptions. First, we describe the parallel plate model, which consists of an upper, nominally flat counterface with spherical asperity caps, while the lower counterface is

rigid flat. The asperity height distribution is assumed to be Gaussian (models with a cutoff are also explored) and the asperities are spaced laterally by 50 nm. A representative area of  $2.5 \times 2.5 \mu\text{m}^2$  was chosen, and so was modeled with  $50 \times 50$  asperity caps. The average separation between the top and bottom surfaces is  $\bar{H}$ , as shown in Figure 5.5, while the local separation from the rigid surface to a given asperity is  $H_i$ , where “ $i$ ” represents the  $i^{\text{th}}$  asperity. This data is stored in a  $50 \times 50$  matrix. Changes in  $\bar{H}$  are directly associated with changes in the rigid plate separation. The asperity deformation is described through  $\omega_i = H_i - z_o$ , per equation 5.3.

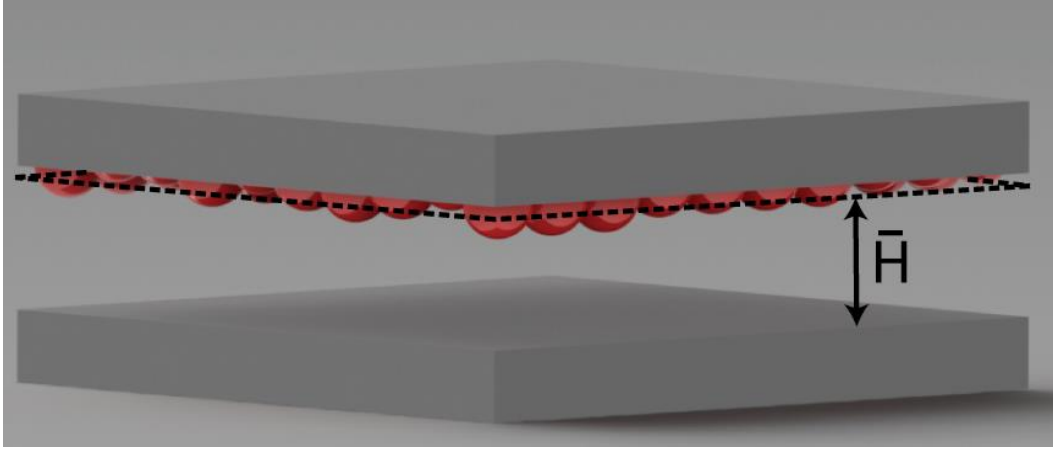


**Figure 5.5:** Parallel plate schematic. The plates are rigid bodies, while the spheres, distributed at different heights with constant radius, are elastic. Dimension  $\bar{H}$  is the average surface separation.

The parallel plate model initially places the upper surface at an average separation  $\bar{H}$  of 100 nm, as indicated in Figure 5.5. The upper surface travels down to  $\bar{H} = -1$  nm in step sizes of 1 pm. At each step, the force between the rigid parallel plates is found by summing the individual asperity forces. Then, the force-distance curve is obtained. The equilibrium separation  $\bar{H}_{eq}$  is the position where the total force equals to zero. Integrating the force-distance curve from  $\bar{H}_{eq}$  to infinity (taken to be  $\bar{H} = 100$  nm) gives the adhesion energy  $\Gamma$ .

## 5.4.2 Parallel Plate Model Results for Dry conditions

The experimental value of  $\Gamma$  in dry nitrogen ranged from 0.02 to 0.06 mJ/m<sup>2</sup> ( $s=890$  to 675  $\mu\text{m}$ ) [87]. Maintaining a normal distribution,  $\sigma$  in the model was considered as a free parameter to match adhesion at  $\Gamma=0.036$  mJ/m<sup>2</sup> ( $s=765$   $\mu\text{m}$ ). It was found using the DMT model that with  $\sigma=1.29$  nm, the measured adhesion value was found. However, this value is significantly smaller than the AFM-measured value of  $\sigma=2.1$  nm.

While the normal distribution is a reasonable description of the asperity height distribution, its extension beyond many multiples of  $\sigma$  is questionable. This is because the asperities are formed from a thin film deposition, and there is no physical reason that a normal distribution will extend indefinitely to large heights. It is important to make this observation, because a cutoff at some multiple of  $\sigma$  has a dramatic effect on the calculated adhesion. This is illustrated in Figure 5.6. Here,  $\sigma=1.29$  nm, and the blue line represents the data without a cutoff, while the red dashed line cuts off the asperity height distribution at  $2\sigma$ . We identify a cutoff parameter,  $n$ . As a cutoff at  $n\sigma$  eliminates repulsive forces for the asperities higher than  $n\sigma$ , the adhesion is significantly larger. Integration of the curve with the cutoff at  $2\sigma$  triples  $\Gamma$  from 0.0371 to 0.1058 mJ/m<sup>2</sup>. While the peak is high, it is also narrow. Furthermore, the contribution out to 100 nm is significant.

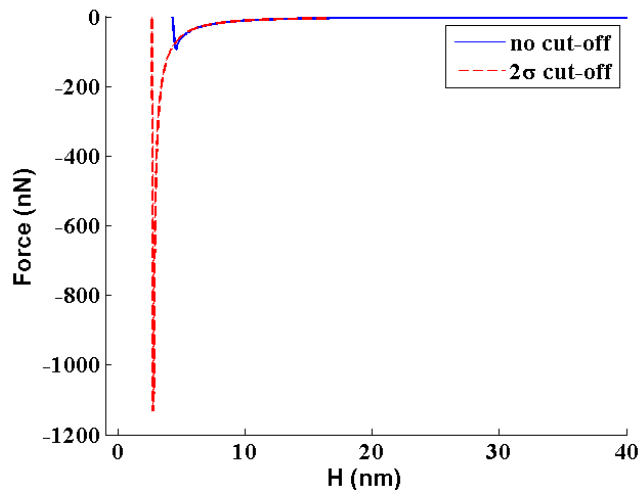


**Figure 5.6:** Force-average separation curve for a parallel plate model with different asperity normal height distribution. Blue line represents the results with no cut-off, and red line represents for the same distribution with  $2\sigma$  cut-off.

Indeed, for the same value of  $\Gamma$ ,  $\sigma$  depends on the cutoff parameter. For example, a normal distribution with  $\sigma = 1.29$  nm gives  $\Gamma = 0.0371$  mJ/m<sup>2</sup>. With a cutoff at  $2.6\sigma$ ,  $\sigma = 2.1$  nm and  $\Gamma = 0.0370$  mJ/m<sup>2</sup>. However, the measured rms roughness as in Figure 5.1 will be essentially the same for each of these values.

The value of the cutoff parameter  $n$  is extremely important in determining  $\sigma$  value for a given value of  $\Gamma$ . However, once  $\sigma$  and  $n$  are decided, the value of  $\Gamma$  depends only weakly on the choice of the constitutive model - DMT or MMD. For the simulations just described, the difference is on the order of 1%, as seen by comparing model results for DMT versus MMD in Table 5.1. This may be expected because the Tabor parameter is 0.12, which is effectively a DMT situation. The small difference is because with the cutoff there are more contacting asperities that have higher attraction forces with the MMD model.

**Table 5.1:** Summary of model results for dry conditions

| Model      | $\sigma$ (nm) | $n$ (cutoff param) | $\Gamma$ (mJ/m <sup>2</sup> ) |
|------------|---------------|--------------------|-------------------------------|
| DMT (PP)   | 1.29          | $\infty$           | 0.0371                        |
|            | 1.29          | 2                  | 0.1058                        |
|            | 2.1           | 2.6                | 0.0370                        |
|            | 7.4           | 2.0                | 0.0369                        |
| MMD (PP)   | 1.29          | $\infty$           | 0.0374                        |
|            | 2.1           | 2.6                | 0.0375                        |
|            | 2.1           | 2.6                | 0.0369                        |
| DMT (Beam) | 7.4           | 2.0                | $0.024 \pm 0.002$             |

## 5.5 S-SHAPED BEAM MODEL

### 5.5.1 S-shaped Beam Model Description

The parallel plate model gives a reasonable idea of the required asperity distribution, but independent of how the asperities are placed, the result will be the same. However, as the crack heals in a real beam, tall asperities will tend to pin crack open, while short asperities will tend to promote healing. This can be expected to affect the measured values of  $s$  and hence the apparent adhesion. Therefore, a beam model was developed to gain insight into the effect of asperity placement near the crack tip.

The S-shaped beam model includes the cantilever beam crack tip region where capillary nucleation occurs (as described in the following section), as illustrated in Fig. 5.7. The S-shaped adhered cantilever is modeled as a fixed-fixed beam with one side higher than the other by a gap  $h$ . One end is fixed at the support post, while the other end is fixed at the crack tip. Only reaction forces and moments at the beam ends exist. The initial cantilever beam deflection  $w_i$  is [124]

$$w_i(x) = \frac{1}{EI} \left( \frac{-R_A x^3}{6} + \frac{M_A x^2}{2} + E I h \right) \quad (5.22)$$

which has the symmetrical “S” shape. Here,  $R_A$  is the reaction force at the support post,  $M_A$  is the reaction moment at the support post,  $I$  is the moment of inertia.

The simulation begins with some assumed value of  $s$  greater than the value that would be predicted by the parallel plate model, but with the same asperity height distribution. Therefore, it might be expected that on average, cracks will heal to the value predicted by the parallel plate model, but will exhibit some variability.

In detail, there are 50 columns, each containing 50 asperities on the cantilever surface, and their heights  $H$  relative to the rigid flat are stored in a matrix, as represented in Figure 5.7.5. Figure 5.8 shows S-Shape beam model surface topography with a cutoff at  $2.6\sigma$ ,  $\sigma=2.1$  nm. The different distributions of the spherical caps that gave adhesion energy values at  $s=765\pm 5$   $\mu\text{m}$  in

the parallel plate model (see Table 5.1) were used. A column of the matrix gives the asperities in  $y$ -direction as seen in Figure 5.7b, while a row of the asperity matrix represents the  $x$ -direction from the crack tip towards to the support post as seen in Figure 5.7a. The asperity pitches in the  $y$ - and  $x$ - directions are 5 and 500 nm, respectively. The model covers 25  $\mu\text{m}$  in the  $x$ -direction because capillary nucleation (described in the following section) is possible in that region, as the  $w$  deflection is on the order of the Kelvin radius (just a few nm). Although the 0.5  $\mu\text{m}$  column separation is larger than the actual separation in the  $x$ -direction, it is representative of the real surface, as the density remains  $1/(0.5 \cdot 0.005 \mu\text{m}^2) = 400$  asperity/ $\mu\text{m}^2$ . The DMT constitutive law, described in the previous section, was implemented.

The crack length  $s$  is set to some value greater than that expected from the parallel plate model, and reaction loads  $M_A$  and  $R_A$  from beam theory are calculated. These are associated with the adhesion for the assumed value of  $s$ , and are applied to obtain the S-shape, as seen in Figure 5.9, giving shape  $w_i(x)$ . At the crack tip, the cantilever is set to the equilibrium separation  $\bar{H}_{eq}$  that comes from the parallel plate model, as illustrated in Figure 5.7a. Van der Waals forces alone, which operate in a dry environment, are now introduced in order to heal the cantilever. The forces are calculated as a function of the surface gaps. Each column force is calculated separately and is assumed to behave as a single load  $P$ . The load  $P_j$  from the  $j^{\text{th}}$  column gives a cantilever deflection shape

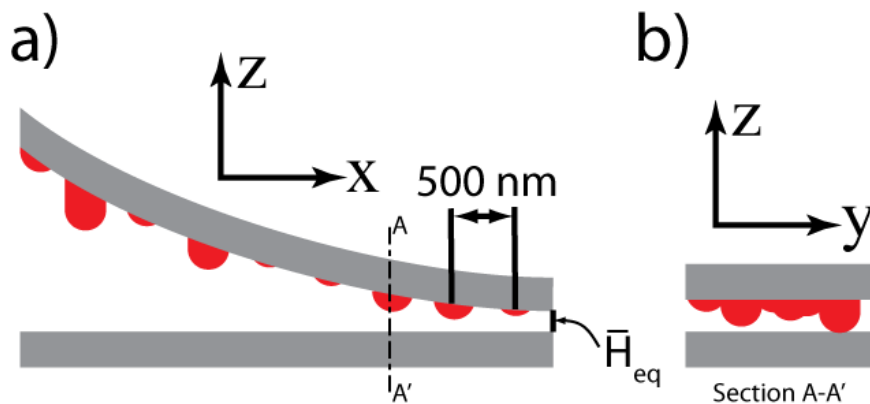


**Figure 5.7:** S-Shape beam model schematic with directions indicated. **a)** Slice of the S-Shape model in the longitudinal direction. **b)** Cross section schematic of A-A'.

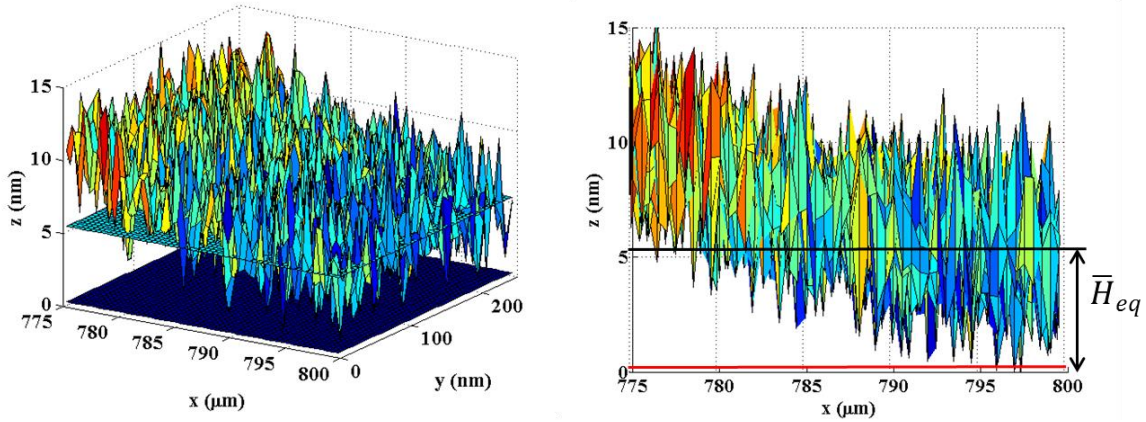


**Figure 5.8:** S-Shape beam model simulated surface topography with a cutoff at  $2.6\sigma$ ,  $\sigma=2.1$  nm. **a)** 3D view of the asperity distribution. **b)** Front view of the asperity distributions. Right end is near the crack tip.  $\bar{H}_{eq}$  sets the gap at the right end between the flat surface and the average height of the asperities. Red line represents the plane of the  $z_0$  distance where the repulsive forces start to apply when the asperities contact.

$$\begin{aligned}
 w_j(x) &= \frac{1}{EI} \left( \frac{-R_{Aj}x^3}{6} + \frac{M_{Aj}x^2}{2} + Eih \right) & \text{for } (0 < x < a) \\
 w_j(x) &= \frac{1}{EI} \left( \frac{-R_{Aj}x^3}{6} + \frac{P_j(x-a)^3}{6} + \frac{M_{Aj}x^2}{2} + Eih \right) & \text{for } (a < x < L)
 \end{aligned} \tag{5.23}$$

where  $w_j$  is the beam deflection due to the  $j^{\text{th}}$  column,  $R_{Aj}$  is the reaction force at the support post,  $M_{Aj}$  is the reaction moment at the support post, and  $a$  is the position where the load is applied as seen in Figure 5.9 (Appendix E). Here,  $R_{Aj}$  and  $M_{Aj}$  are the total reaction forces. After finding the deflection shapes corresponding to each column's load, the deflection  $w_i(x)$  is subtracted from  $w_j(x)$  to find the vertical deflection  $\Delta w_j(x)$  due to applied load. Linear superposition of  $\Delta w_j$  from all the columns gives a new shape of the cantilever according to

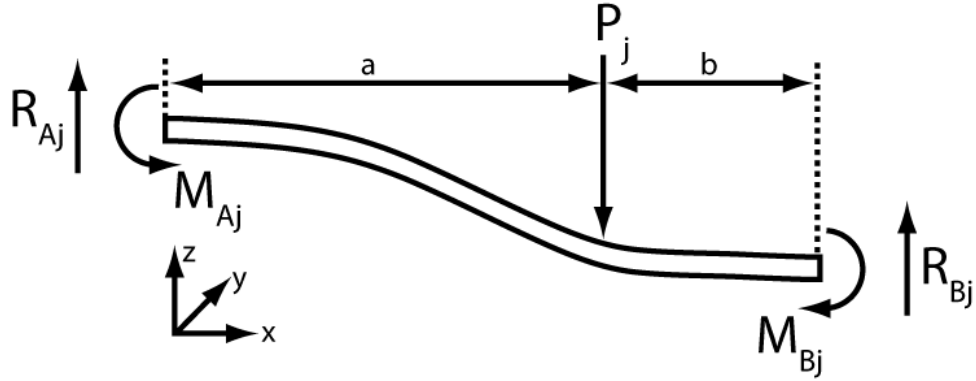


**Figure 5.9:** Free-body diagram for an *s*-shaped beam. The force and moment are provided by the support post on the left-hand side. On the right-hand side, the moment and the reaction force occur at the crack tip.

$$w_f(x) = w_i(x) + c \sum_{j=1}^{50} \Delta w_j(x) . \quad (5.24)$$

Here,  $c$  is a damping factor that enables smooth convergence by preventing numerical instabilities. Specifically, the maximum value of summed vertical deflections  $\Delta w_{max} = \max(w_i(x) - \sum \Delta w_j(x))$  is set to a limit  $\Delta w_{limit}$  of 0.01 nm, after which, the vertical deflection is normalized. Hence, Equation 5.24 is modified to represent the actual implementation in each iteration as follows

$$w_f(x) = w_i(x) + \frac{\Delta w_{limit}}{\Delta w_{max}} \sum_{j=1}^{50} \Delta w_j(x) . \quad (5.25)$$

With this new deflected shape, the surface gaps decrease. Thus, the applied loads  $P_j$  increase. This process was repeated iteratively until mechanical equilibrium is achieved. Mechanical equilibrium here is defined to occur when the cantilever deflection becomes about  $10^{-8}$  smaller than the largest gap of about 2 nm. As convergence is approached, the repulsive forces become larger than the adhesive forces because of the nonlinear force-displacement relationships, causing the cantilever to deflect upwards. After the gap matrix upgrade, it deflects again towards the substrate due to adhesive forces. In the iteration, this cycle continues 1000 times, at which

point the amplitude is typically  $<10^{-8}$  nm, or until the maximum deflection between steps is  $10^{-11}$  nm, whichever is first.

Once mechanical equilibrium is reached, the model tests whether a crack healing event has occurred. Figure 5.10 illustrates a healed crack. The black line represents the initial deflection  $w_i$ , while the red line represents the final cantilever shape  $w_f$  after reaching mechanical equilibrium. The right end is the crack tip with the equilibrium separation  $\bar{H}_{eq}$  shown by the black bar. If any location other than the crack tip has the same  $\bar{H}_{eq}$  average gap or less, then the crack has healed up to that point. The red bar illustrates a case in which healing has occurred.

If crack healing has occurred, then we reset the initial crack length and run a new simulation. This continues until no healing is observed.

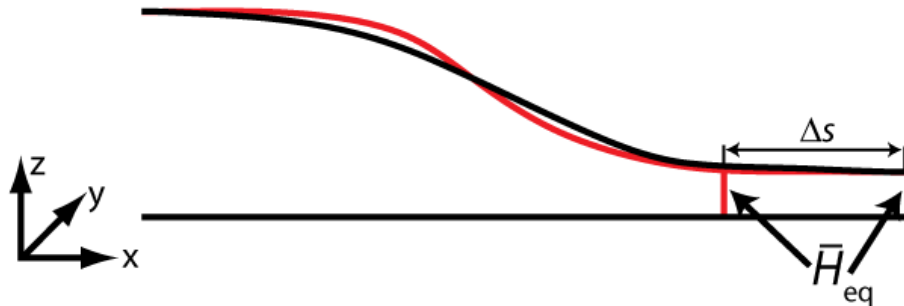


**Figure 5.10:** Illustration of the crack healing at the model. Black line represents the initial deflection  $w_i$ , and red line represents the final cantilever shape  $w_f$ .

### 5.5.2 S-shaped Model Results

To exercise the S-shaped model, we imported the same asperity distributions that were used for parallel plate models. In each case,  $\Gamma=0.0037$  mJ/m<sup>2</sup> as in Table 5.1, but the cutoff value was changed. We ran simulations expecting to see healing corresponding to the adhesion energy from the parallel plate model. The initial  $s$  value was 850  $\mu\text{m}$ . When we used the distribution data without any cut-off ( $\sigma=1.29$  nm,  $n\rightarrow\infty$ ), no healing occurred whatsoever. To check the effect of varying asperity distributions, the asperity columns were then shifted to the adjacent column and the column closest to the crack tip was moved to the furthest location, as

illustrated in Figure 5.11. This was done for each of 50 cases, and no healing occurred for any shifted distribution. This was traced to high asperities in the upper tail of the Gaussian distribution. They cause large repulsive forces, inducing a large resisting moment especially when the contacting asperity is far from the crack tip [131].

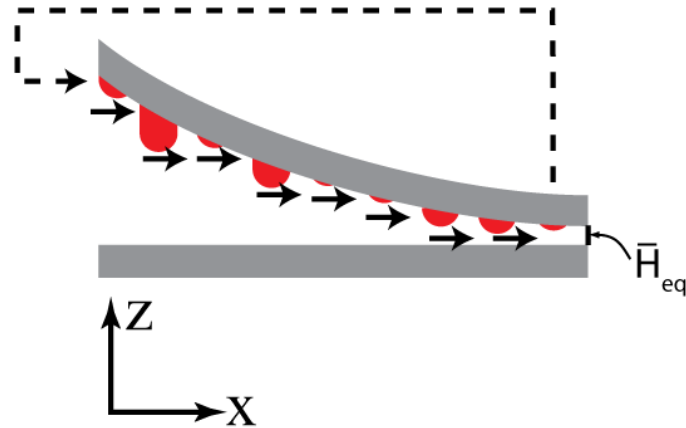


**Figure 5.11:** Illustration of the asperity column shifting to simulate different distributions.

On the other hand, when we apply a distribution with a small cutoff ( $\sigma=7.4$  nm,  $n=2$ ), healing initially occurs for any distribution, as seen in Figure 5.12. Here, the horizontal axis gives the initial crack length, while the left vertical axis shows the healed crack length for a given initial crack length,  $s_{init}$ . The distribution of black dot markers indicates the variability in  $\Delta s$  depending on  $s_{init}$ . For example, for  $s_{init}=850$   $\mu\text{m}$ ,  $\Delta s$  ranges from 12 to 17  $\mu\text{m}$ . In this case, all 50 distributions exhibited healing, as indicated by the blue line which is referred to the right vertical axis. For  $s_{init}=825$   $\mu\text{m}$ ,  $\Delta s$  ranges from 10 to 14.5  $\mu\text{m}$ , and in this case only 12 of the distributions healed. For  $s_{init}=840$   $\mu\text{m}$ , there was a range of  $\Delta s$  from 0.5 to 17  $\mu\text{m}$ . The measured  $s$  values for experiments in dry conditions vary from 840 to 733  $\mu\text{m}$ . Although chemical vapor deposition was used to fabricate the layers, roughness of the local areas may vary. The observation that no healing is observed when there is no cutoff, but healing is observed for  $n=2$  qualitatively shows how sensitive the cantilever is to a surface topography deviations. Simulations run with different asperity distributions illustrate this sensitivity. The healing of the cantilevers in simulations with the same surface roughness do not match with the experimental

results. The asperity distribution may not represent the real surface perfectly. It may be worthwhile to try asperity distribution other than Gaussian in order to gain more insight.

In general, as  $s_{init}$  decreases in Figure 5.12, the number of distributions that heal decreases, as indicated by the blue line, and distance they heal also reduces, as indicated by the black markers. Those distributions with only a few high asperities concentrated near the crack tip still heal, as they cannot apply big bending moments. Thus, crack healing happens for these cases as plotted in Figure 5.13b. In different shifted distributions, the bending moment becomes large enough to resist crack healing. As the initial  $s$  value decreases, healed crack length  $\Delta s$  decreases as a result of increasing stiffness. They still do not heal to the location predicted by the parallel plate model. Compared to the previous case ( $n \rightarrow \infty$ ) the cutoff at  $2\sigma$  encourages healing because surface is artificially polished with cut-off. This means there is now a portion of area with perfect flat surface. If we simulate the same cases with cut-off at  $1.9\sigma$ , the polished surface area increases. Thus healing continues until smaller crack length with a greater number of distributions, as shown in Figure 5.14. However, the sigma value (17.5 nm) is now much higher than the measured value of 2.1 nm. This will limit the possible capillary nucleation because  $\bar{H}_{eq}$  is 33.4 nm for  $1.9\sigma$  cut-off case, and the asperity caps distributes much wider. Therefore, asperity gaps with gaps less than  $2r_K$  decreases.

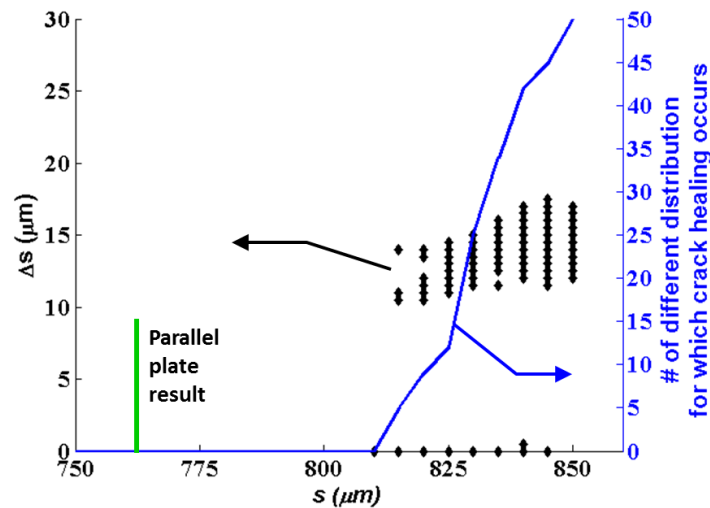


**Figure 5.12:** S-Shape Beam model crack healing result with  $n=2$  cutoff ( $\sigma = 7.40$  nm) (using DMT model). 50 different asperity distributions have been simulated.

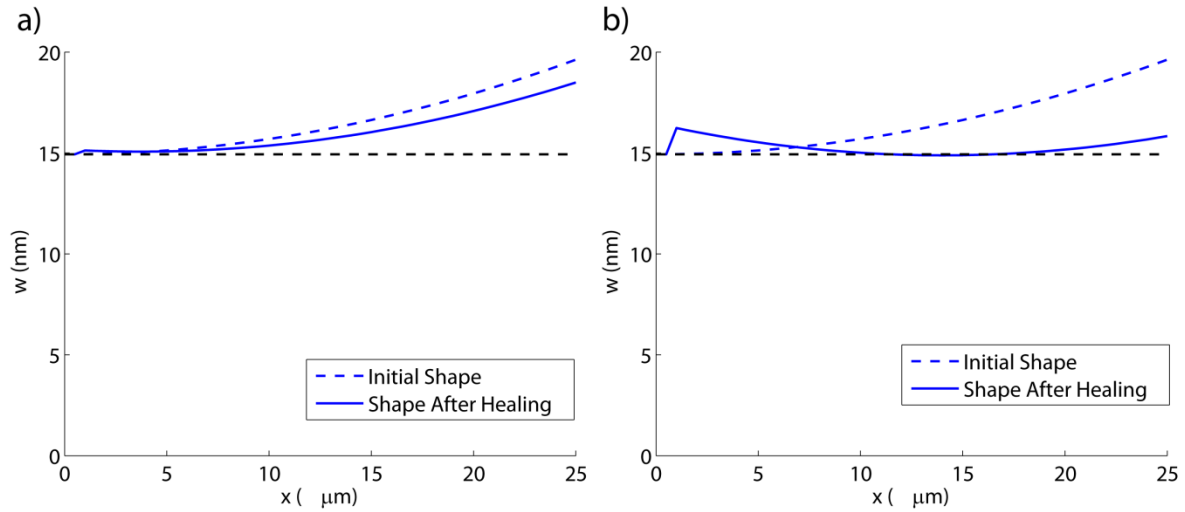


**Figure 5.13:** Cantilever deflection shapes are shown according to Figure 5.12 data. **a)** Cantilever shape without healing event, **b)** cantilever shape after healing occurs. Black dashed line is the axis showing the  $\bar{H}_{eq}$  level.

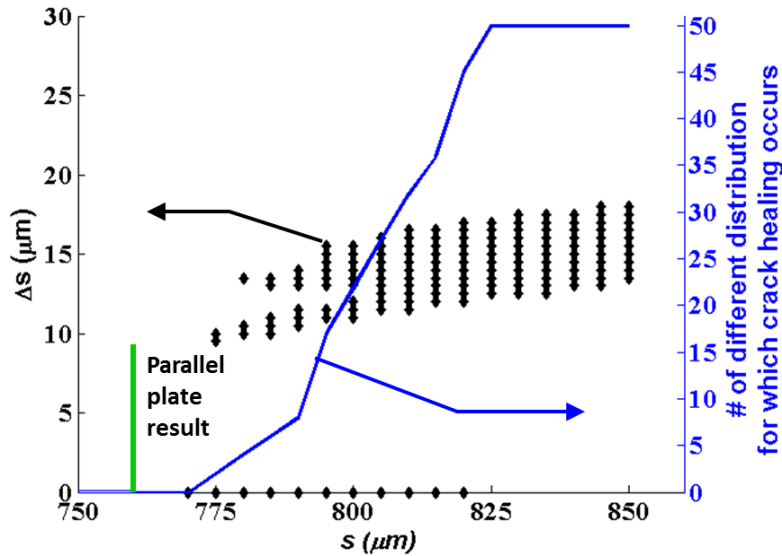


**Figure 5.14:** S-Shape Beam model crack healing results with  $1.9\sigma$  cutoff ( $\sigma = 17.5$  nm) (using DMT model). 50 different asperity distributions have been simulated.

Hence, it is difficult to achieve good agreement between the measured surface roughness and the measured adhesion under dry conditions using the beam model. The likely reason is the high sensitivity to a surface roughness of the beam model. High asperity caps apply large repulsive

forces causing the high resistance to healing. We will apply a cut-off at  $n=2.6$  in the following section. This is for two reasons. First, the actual measured surface is reasonably described by this. Second, capillary forces play a far stronger role than van der Waals forces in healing cracks, and therefore are not as sensitive to topography details.

## 5.6 WET CONDITIONS – CRACK HEALING BEAM MODEL

After obtaining the mechanical equilibrium shape in dry conditions with  $\sigma=2.1$  nm and  $n=2.6$ , humidity is introduced by adding capillary forces into the surface interaction forces. For a sphere-flat geometry, with the assumption that the sphere radius  $R \gg |r_K|$ , the capillary force  $F_c$  under thermodynamic equilibrium can be found from the Laplace and Kelvin equations as [28]

$$F_c = -4\pi R\gamma_L \left[ 1 - \frac{\omega}{2|r_K|} \right] \quad \text{for } \omega > 0 \quad (5.26)$$

We used equation 5.26 for  $\omega > 0$  corresponding to non-contacting case. To keep the dry and humid cases logically consistent, we also added intermolecular distance to the capillary bridge gap, as shown in Figure 5.15a. This means that, capillary bridge can nucleate at  $H = H_c + z_0$ , and contact happens at  $H = z_0$ .

We used the improved meniscus model of Xue and Polycarpou for the contacting case  $\omega < 0$  [114,150], which is based on the MD model. The MD model in dry conditions applies attractive forces when the sphere contacts the Dugdale zone. In humid conditions, the capillary bridge substitutes for the Dugdale zone. Then,  $\delta_t$  becomes  $H_c = 2r_K$ , the maximum capillary bridge height. Also, the Laplace pressure  $\Delta P$  substitutes for the attractive stress in the Dugdale zone. Equation 5.18 is modified for humid conditions according to

$$F_{C\_MD} = 2\Delta P a^2 (m^2 \tan^{-1} \sqrt{m^2 - 1} + \sqrt{m^2 - 1}) \quad \omega < 0 \quad . \quad (5.27)$$

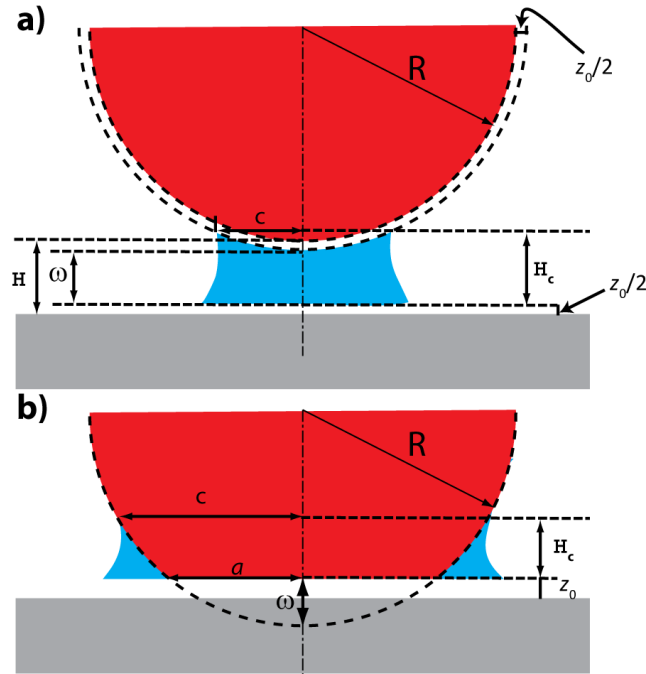


**Figure 5.15:** Schematic of an elastic sphere and a rigid flat surface.  $z_0$  is the intermolecular separation,  $H_c$  is the range of the constant Laplace pressure. (a) Non-contacting illustration  $\omega > 0$ , (b) contacting  $\omega < 0$ .

First, dry condition forces were applied, and the cantilever deflects. Then, capillary forces were applied sequentially according to a nucleation time, beginning with the asperity that has the smallest gap between the tip and the surface. Mechanical equilibrium is then found. If  $\bar{H} = \bar{H}_{eq}$  for one of the column of the gap matrix, then, the cantilever is brought to the same level with crack tip at another location as described earlier at section 5.5.1. It represents the crack healing, and simulation stops. Otherwise, the next nucleation event is calculated, and this is repeated until  $\bar{H} = \bar{H}_{eq}$  for one of the column of the gap matrix. We sum up each nucleation time to heal the cantilever, nucleation times for the asperities with  $H \leq z_0$  are taken as 1 ms, corresponding to the time for a capillary to grow. The average value of 1 ms is chosen corresponding to studies in the literature [37,57]. The relatively long capillary *nucleation time* between non-contacting surfaces can be understood in terms of a thermally activated first order gas-liquid phase transition theory. The energy barrier is found to be [77],

$$\Delta\Omega = \pi \gamma_{LV}(H - z_0)^2 \left( \frac{\pi^2 [1 - ((H - z_0)/2H_c)]^2}{8 [1 - ((H - z_0)/H_c)]} + \frac{(H - z_0)}{3H_c} - 1 \right) \quad (5.28)$$

where  $H_c$  is the critical separation, which can be equated with  $2|r_K|$ , while  $H$  is the surface separation. Each energy barrier calculation for new capillary bridge has been done after the cantilever deflection from the previous step.

The nucleation time is then calculated as follows

$$\tau = \tau_0 \exp[\Delta\Omega/k_B T] \quad (5.29)$$

where  $1/\tau_0$  is the attempt frequency,  $k_B$  is the Boltzmann constant and  $T$  is the temperature (K). We use  $\tau_0=100$  GHz, similar to Boyd et al. [82] The sum of the nucleation times,  $\Delta t$ , in each loop gives the time to reach the corresponding energy release rate with nucleated capillary meniscus bridges. Also, the corresponding  $s$  value can be calculated after each loop. Then crack healing velocity  $\bar{v}$  is defined as

$$\bar{v} = \frac{s_i - s_{i+n}}{\Delta t} \quad (5.30)$$

Here,  $s_i$  is the crack length for the dry conditions, and  $s_{i+n}$  is a corresponding crack length after  $n$ th loop. The  $G$  value is calculated at the average value of  $s$ , that is, at  $s=(s_i + s_{i+n})/2$ .

## 5.7 CRACK HEALING MODEL RESULTS

Figure 5.16 shows the results of the crack healing model at 60.5% RH. For each value of  $s$  as an initial condition, fifty possible shifted distributions have been simulated. Scattering effect of the data is due to the shifted distributions. Gray shaded area shows the experimental trend. Simulation results are quickly diverging from the experimental trend at  $0.25 \text{ mJ/m}^2$ , and it never heals up to  $1 \text{ mJ/m}^2$  as in the experimental results.

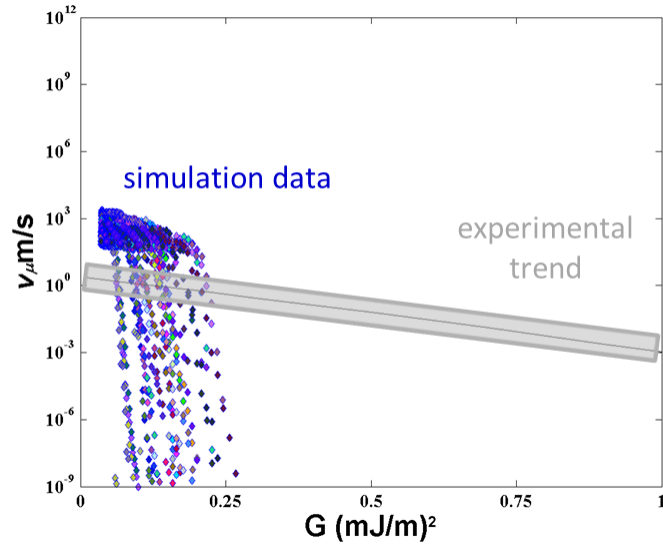


**Figure 5.16:** Crack healing model results at RH=60.5%. Average velocity calculations are based on equation 5.30. Markers show the results for fifty different shifted distributions of the asperities. Gray shaded area represents the experimental trend.

One reason might be the adsorbed liquid layer on the surfaces. To this point, we have neglected this effect. However, recent study showed that capillary nucleation at nanoscale occurs at a larger gap than  $2r_K$  [86]. Experiments at 30% RH sensed the capillary nucleations at  $2.1 \pm 1.3$  nm gaps. At 30% RH,  $2r_K = 0.8$  nm, and adsorbed liquid film thickness  $h_f = 0.75$  nm [132]. This supports the adsorbed liquid film role at capillary nucleation.

We assume ice-like adsorbed water layer behaves as a solid surface as shown in Figure 5.17. Therefore,  $2r_K$  gap may nucleate between two ice-like layers. At 60 and 87% RH, the ice-like layer thickness is  $\sim 1$  nm [132]. We have run the simulations with this effect. This helps to nucleate more bridges between the surfaces. A horizontal line is obtained as seen in Figure 5.18 because closing the gaps with the liquid film caused instantaneous capillary nucleations. Then, we tried  $h_f = 0.5$  nm due to asperity cap curvature film thinning effect [32] and different surface effect. There is also a different study that reports the film thickness on silica at 80% RH as 0.5 nm [133]. Still, the scattering is too much to predict the experimental trend; it can not heal up to  $1 \text{ mJ/m}^2$ ; and the initial healing events happen too fast, as shown in Figure 5.18.

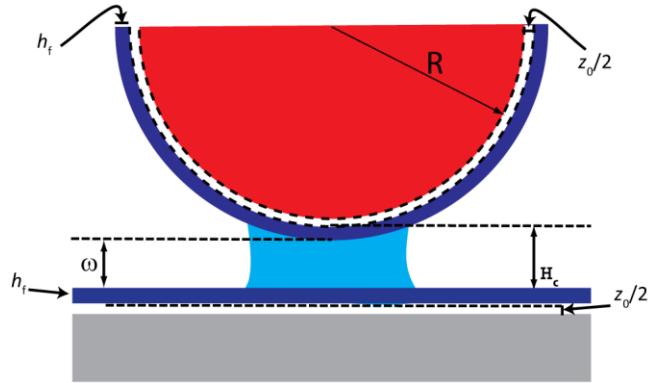


**Figure 5.17:** Schematic of a capillary bridge with adsorbed liquid film between an elastic sphere and a rigid flat surface.  $z_0$  is the intermolecular separation,  $H_c$  is the range of the constant Laplace pressure.  $H = \omega - z_0$ .

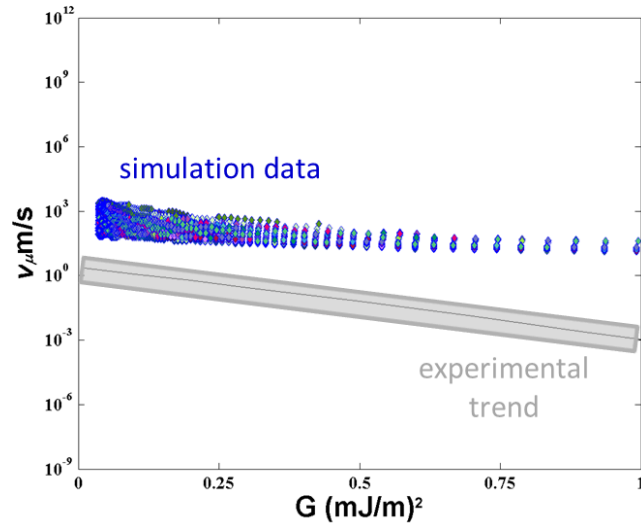


**Figure 5.18:** Crack healing model results at RH=60.5% with  $h_f = 1$  nm. Average velocity calculations are based on equation 5.30. Markers show the results for fifty different shifted distributions of the asperities. Gray shaded area represents the experimental trend.

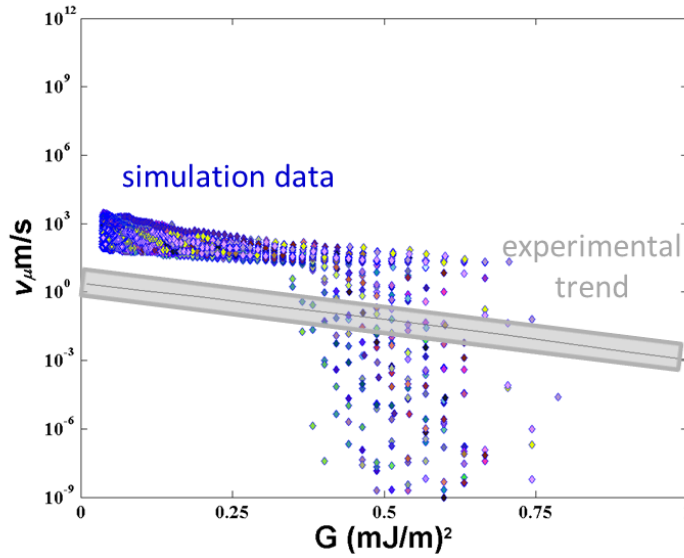


**Figure 5.19:** Crack healing model results at RH=60.5% with  $h_f = 0.5$  nm. Average velocity calculations are based on equation 5.30. Markers show the results for fifty different shifted distributions of the asperities. Gray shaded area represents the experimental trend.

Energy barrier equation is the key equation to estimate the nucleation times. It would be beneficial to fit an alternative equation to eliminate the high sensitivity of a gap variation. We suggest the following empirical equation

$$\Delta\Omega_{FIT} = \pi \gamma_{LV} H_c^2 C \left( \frac{H-z_0}{H_c} \right)^{0.4}, \quad (5.31)$$

where  $C = 0.151$  and  $0.010$  for RH=60.5 and 87.5%, respectively. Nucleation time equation has been modified also

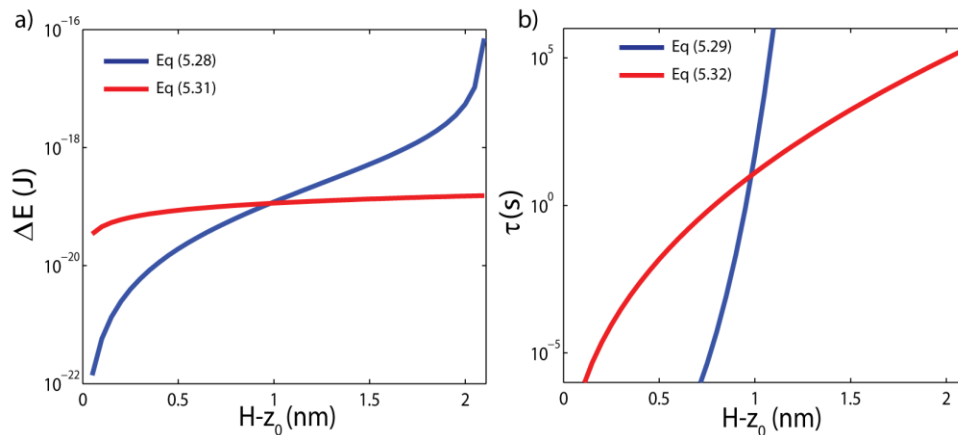
$$\tau_{FIT} = \tau_0 \exp[\Delta\Omega_{FIT}/k_B T]. \quad (5.32)$$

Figure 5.20b shows the steep nucleation time function of equation 5.29 at 60.5%RH. The gap change from  $\sim 0.75$  nm to  $\sim 1$  nm sweeps the time range from microseconds to  $\sim 12$  days. However, quartz tuning force microscopy experiments illustrated the  $2.1 \pm 1.3$  nm gap capillary

nucleations in the 0 to 2 s range. This supports the activation energy barrier modification necessity. Figure 5.20a shows the equation 5.31 plot, it limits the energy barrier between  $10^{-20}$  to  $10^{-19}$  J. Experimental studies that presented the activation energy barrier values help to validate equation 5.31. Some estimates from the literature are  $\Delta\Omega=(7.8\pm 0.9)\times 10^{-20}$  J at  $37\%\pm 2\%$  RH [57],  $\Delta\Omega=(4.7\pm 1.3)\times 10^{-20}$  J at 15-35% RH [85], and  $\Delta\Omega=(7.65)\times 10^{-20}$  J at 27-29% RH [86].

Crack healing model was simulated by using equation 5.32, and the predicted results are now following the experimental trend, as shown in Figure 5.21. The shifted asperity distribution still causes data scattering, but this is also observed in the experimental data. Also, not all the shifted distribution setting heals up to  $1\text{ mJ/m}^2$ , and this explains the different cantilever responses at the experiments.

Figure 5.22 shows the activation energy barrier and nucleation time curves for 87.5% RH condition. Equation 5.32 was used for the 87.5% RH conditioned crack healing simulation. Results of the average velocity vs energy release rates are seen in Figure 5.23. It predicts the experimental trend, and it show less scattering because equation 5.32 curve in Figure 5.22b is less sensitive to small gap variations at higher humidity.



**Figure 5.20:** Energy barrier and nucleation time curves at 60.5% RH level in the range of 0 to  $H_c$ . **a)** Energy barrier vs gap is plotted with blue and red lines by equation 5.26 and 5.29, respectively. **b)** Nucleation time vs gap is plotted with blue and red lines by equation 5.27 and 5.30, respectively.

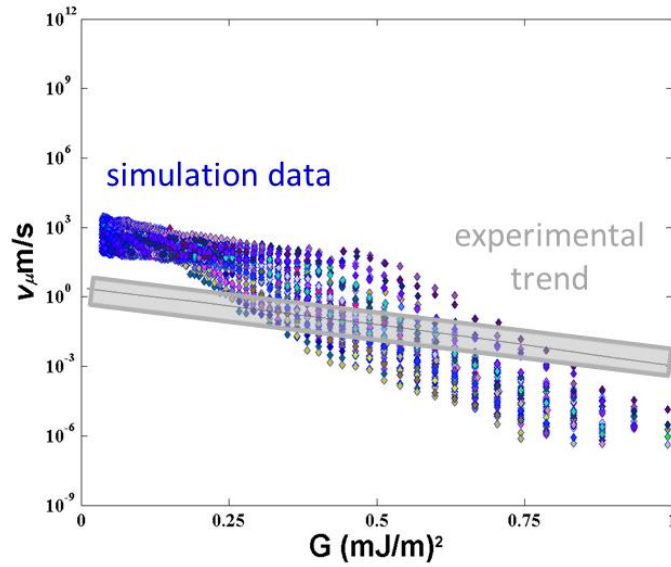


**Figure 5.21:** Crack healing model results at RH=60.5% with  $h_f = 0.5$  nm. Average velocity calculations are based on equation 5.30. Markers show the results for fifty different shifted distributions of the asperities. Gray shaded area represents the experimental trend.

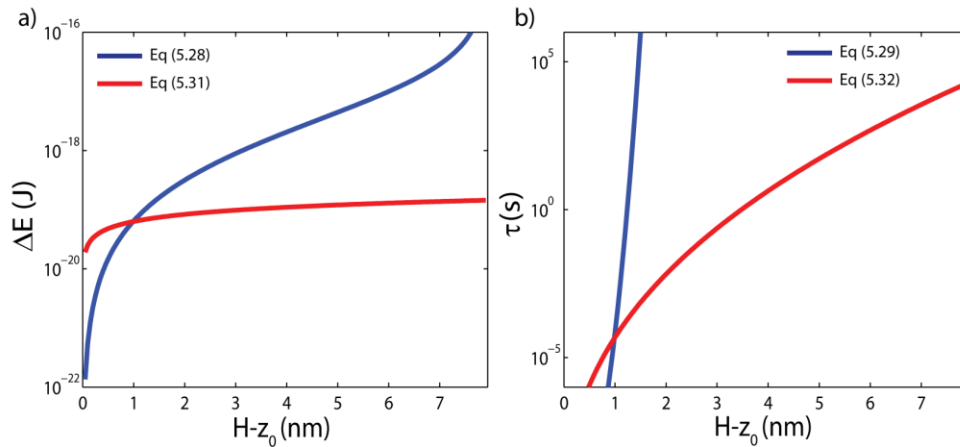


**Figure 5.22:** Energy barrier and nucleation time curves at 87.5% RH level in the range of 0 to  $H_c$ . a) Energy barrier vs gap is plotted with blue and red lines by equation 5.26 and 5.29, respectively. b) Nucleation time vs gap is plotted with blue and red lines by equation 5.27 and 5.30, respectively.

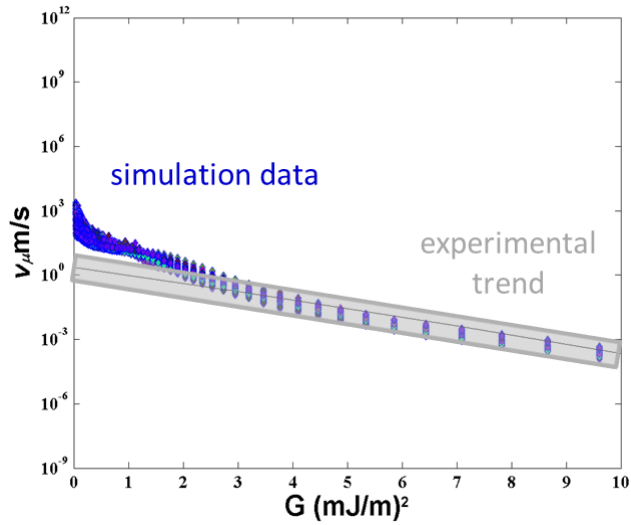


**Figure 5.23:** Crack healing model results at RH=87.5% with  $h_f = 0.5$  nm. Average velocity calculations are based on equation 5.30. Markers show the results for fifty different shifted distributions of the asperities. Gray shaded area represents the experimental trend.

## 5.8 CHAPTER SUMMARY

This chapter has demonstrated numerical modeling can lend significant insight into capillary crack healing experiments. First, single asperity contact models have been detailed. Then, a parallel plate model has been assembled to create a surface asperity distribution consistent with deflected cantilever beams in dry conditions at experiments. An S-shaped beam model was developed to simulate crack healing. This model revealed extreme sensitivity to surface roughness characteristics even for the same value of adhesion. The capillary model is less sensitive, but still did not model the crack healing well without refinement. In particular, an improved meniscus model was implemented in which an adsorbed liquid film better captures the experimental results. To fully capture the results, however, the model for nucleation time required an empirical modification. The modification is in reasonable agreement with experimental results. However, more work is necessary to understand whether this proposed theoretical energy barrier equation has a physical basis.

## Chapter VI: Summary and Suggestions for Future Work

First the major findings from Chapters II through V are summarized. Then, future studies that might enlighten capillary dynamics further are suggested.

This dissertation explores the capillary dynamics between multi-asperity surfaces. Microcantilever crack healing experiment method is chosen to observe the capillary condensation effects between non-contacting asperities.

It has been demonstrated that an experimental setup can be built to run the microcantilever crack healing experiments in a controlled environment (Chapter II). Microcantilever samples with smooth surfaces ( $\sim 2$  nm rms roughness) responded to low vapor partial pressure conditions. AFM scans of the top and bottom counterfaces have been conducted to characterize the surface roughness.

We have found that crack healing occurs in discrete events (Chapter III), rather than continuously. Discrete healing steps suggests the capillary condensation events in the crack healing experiments. We showed that a plot of  $\bar{v}$  versus energy release rate,  $G$ , reveals log-linear behavior, while the slope  $|d[\log(\bar{v})]/dG|$  decreases with increasing relative humidity.

In addition to the dynamics of the capillary studies, we have investigated the alcohols (ethanol and *n*-pentanol) vapor adhesion energies (Chapter III). These alcohols are used in MEMS devices to reduce wearing of rubbing surfaces. We studied their adhesion energies at various partial pressures to understand how to control the partial pressure of the environment without entering the critical range for failure.

We introduced multi-asperity surfaces to simple S-shaped beam models to gain insight into the results (Chapter IV). A first order model with equally spaced same height asperities predicted the log-linear trends and decreasing slope in increasing RH qualitatively.

Then, a more advanced numerical model has been proposed and studied for improved quantitative agreement (Chapter V). This model included more realistic surface roughness

descriptions in the interface. It accounts the contact interaction forces and improved meniscus model forces. With this model, the importance of the adsorbed liquid film contribution to the crack healing has been revealed. Finally, with the introduction of an empirical energy barrier equation, the model has captured the behaviors quantitatively.

To understand the capillary adhesion mechanisms better, liquid film adsorption experiments can be the possible future study. MEMS resonator can be fabricated with identical surface to microcantilever surface in the same wafer. Then, microcantilever crack healing and liquid adsorption experiments can be run simultaneously. This type of experiment would answer the main driving force behind the crack healing. Also, high temperature experiments would be a good illustration to show nucleation characteristics consistent with the Arrhenius equation. Moreover, high temperature experiments might answer if the adsorbed film layer is a dominant force or a negligible force on crack healing because the adsorbed liquid film layer thins with increasing temperature [105,134].

It would also be worthwhile to investigate other vapors. Differences in their chemistry would help us to understand the capillary adhesion driving mechanisms between multi-asperity surfaces.

A theoretical study to estimate the capillary nucleation and growth times is needed, and this thesis would be a good guidance with its wide range of experimental data. Both intuitive physics-based analytical as well as sophisticated molecular dynamics or density functional theory models [158,159] would be extremely useful.

## BIBLIOGRAPHY

- [1] Mounier, E., and Robin, L., 2013, Status of the MEMS Industry 2013.
- [2] Romig, A. D., Dugger, M. T., and McWhorter, P. J., 2003, “Materials issues in microelectromechanical devices: science, engineering, manufacturability and reliability,” *Acta Mater.*, **51**(19), pp. 5837–5866.
- [3] Dudley, D., Duncan, W. M., and Slaughter, J., 2003, “Emerging digital micromirror device (DMD) applications,” *Micromachining and Microfabrication*, H. Urey, ed., International Society for Optics and Photonics, pp. 14–25.
- [4] Cummings, W., 2010, “The Impact of Materials and System Design Choices on Reflective Display Quality for Mobile Device Applications,” *SID Symp. Dig. Tech. Pap.*, **41**(1), p. 935.
- [5] Brand, V., Baker, M. S., and Boer, M. P., 2013, “Impact of Contact Materials and Operating Conditions on Stability of Micromechanical Switches,” *Tribol. Lett.*, **51**(3), pp. 341–356.
- [6] Puyal, V., Dragomirescu, D., Villeneuve, C., Pons, P., and Plana, R., 2009, “Frequency Scalable Model for MEMS Capacitive Shunt Switches at Millimeter-Wave Frequencies,” *IEEE Trans. Microw. Theory Tech.*, **57**(11), pp. 2824–2833.
- [7] Fonseca, D. J., and Sequera, M., 2011, “On MEMS Reliability and Failure Mechanisms,” *Int. J. Qual. Stat. Reliab.*, **2011**, pp. 1–7.
- [8] Pederson, A., and Solgaard, O., 2000, “Free space communication link using a grating light modulator,” *Sensors Actuators A*, **83**, pp. 6–10.
- [9] Yeh, R., Hollar, S., and Pister, K. S. J., 2002, “Single mask, large force, and large displacement electrostatic linear inchworm motors,” *J. Microelectromechanical Syst.*, **11**(4), pp. 330–336.
- [10] Smith, J. H., Rodgers, M. S., Sniegowski, J. J., Miller, S. L., Hetherington, D., McWhorter, P. J., and Warren, M. E., 1998, “Microelectro-Optical Devices in a 5-Level Polysilicon Surface Micromachining Technology,” Part of the SPIE Conference on Micromachined Devices and Components IV, pp. 42–47.
- [11] Lal, A., 2008, “Information Tethered Micro Automated Rotary Stages (ITMARS),” pp. 1–32.

- [12] Reyes, D., Schildkraut, E. R., Kim, J., Connors, R. F., Kotidis, P., and Cavicchio, D. J., 2008, "A Novel Method of Creating a Surface Micromachined 3-D Optical Assembly for MEMS-Based, Miniaturized FTIR Spectrometers," SPIE, S.S. Olivier, T.G. Bifano, and J.A. Kubby, eds., p. 68880D-1:68880D-8.
- [13] Fisher, L. R., and Israelachvili, J. N., 1981, "Experimental studies on the applicability of the Kelvin equation to highly curved concave menisci," *J. Colloid Interface Sci.*, **80**(2), pp. 528-541.
- [14] Prokopovich, P., and Starov, V., 2011, "Adhesion models: from single to multiple asperity contacts.," *Adv. Colloid Interface Sci.*, **168**(1-2), pp. 210-22.
- [15] Maugis, D., 1996, "On the contact and adhesion of rough surfaces," *J. Adhes. Sci. Technol.*, **10**(2), pp. 161-175.
- [16] Bhushan, B., 2003, "Adhesion and stiction: Mechanisms, measurement techniques, and methods for reduction," *J. Vac. Sci. Technol. B Microelectron. Nanom. Struct.*, **21**(6), p. 2262.
- [17] Hertz, H., 1881, "Uber die Beruhrung fester elastischer Korper," *J. fur die reine und Angew. Math.*, **92**, pp. 156-171.
- [18] Johnson, K. L., 1987, *Contact Mechanics*, Cambridge University Press.
- [19] Schwarz, U. D., 2003, "A generalized analytical model for the elastic deformation of an adhesive contact between a sphere and a flat surface," *J. Colloid Interface Sci.*, **261**(1), pp. 99-106.
- [20] Popov, V., 2010, *Contact Mechanics and Friction*, Springer.
- [21] Johnson, K. L., Kendall, K., and Roberts, A. D., 1971, "Surface energy and the contact of elastic solids," *Proc. R. Soc. Lond. A.*, **324**, pp. 301-313.
- [22] Derjaguin, B. V., Muller, V. M., and Toporov, Y. P., 1975, "Effect of Contact Deformations on the Adhesion of Particles," *J. Colloid Interface Sci.*, **53**(2), pp. 314-326.
- [23] Tabor, D., 1977, "Surface forces and surface interactions," *J. Colloid Interface Sci.*, **58**(1), pp. 2-13.
- [24] Maugis, D., 1992, "Adhesion of Spheres : The JKR-DMT Transition Using a Dugdale Model," *J. Colloid Interface Sci.*, **150**(1), pp. 243-269.
- [25] Adamson, A. W., and Gast, A. P., 1997, *Physical Chemistry of Surfaces*, Wiley-Interscience.
- [26] Israelachvili, J. N., 1992, *Intermolecular and Surface Forces*, Academic Press.

- [27] Thomson, W., 1870, "On the equilibrium of vapour at a curved surface of liquid.," Proc. R. Soc. Edinburgh, **7**, p. 63.
- [28] De Boer, M. P., and de Boer, P. C. T., 2007, "Thermodynamics of capillary adhesion between rough surfaces.," J. Colloid Interface Sci., **311**(1), pp. 171–85.
- [29] Bowles, A. P., Hsia, Y.-T., Jones, P. M., Schneider, J. W., and White, L. R., 2006, "Quasi-equilibrium AFM measurement of disjoining pressure in lubricant nano-films I: Fomblin Z03 on silica.," Langmuir, **22**(26), pp. 11436–46.
- [30] Fisher, L. R., Gamble, R. A., and Middlehurst, J., 1981, "The Kelvin equation and the capillary condensation of water," Nature, **290**(5807), pp. 575–576.
- [31] Derjaguin, B. V., Churaev, N. V., and Muller, V. M., 1987, SURFACE FORCES, Consultants Bureau, New York.
- [32] Mate, C. M., 1992, "Application of disjoining and capillary pressure to liquid lubricant films in magnetic recording," J. Appl. Phys., **72**(7), p. 3084.
- [33] Butt, H.-J., Cappella, B., and Kappl, M., 2005, "Force measurements with the atomic force microscope: Technique, interpretation and applications," Surf. Sci. Rep., **59**(1-6), pp. 1–152.
- [34] Hecht, E., 2002, OPTICS, Addison Wesley.
- [35] Ciullo, P. A., 1997, Industrial Minerals and Their Uses: A Handbook and Formulary, William Andrew.
- [36] Wei, Z., and Zhao, Y.-P., 2007, "Growth of liquid bridge in AFM," J. Phys. D. Appl. Phys., **40**(14), pp. 4368–4375.
- [37] Sirghi, L., 2012, "Transport mechanisms in capillary condensation of water at a single-asperity nanoscopic contact.," Langmuir, **28**(5), pp. 2558–66.
- [38] Mate, C. M., Lorenz, M. R., and Novotny, V. J., 1989, "Atomic force microscopy of polymeric liquid films," J. Chem. Phys., **90**(12), p. 7550.
- [39] Halsey, T., and Levine, A., 1998, "How Sandcastles Fall," Phys. Rev. Lett., **80**(14), pp. 3141–3144.
- [40] Crassous, J., Bocquet, L., Ciliberto, S., and Laroche, C., 1999, "Humidity effect on static aging of dry friction," Europhys. Lett., **47**(5), pp. 562–567.
- [41] Qian, J., and Gao, H., 2006, "Scaling effects of wet adhesion in biological attachment systems.," Acta Biomater., **2**(1), pp. 51–8.

- [42] Bachmann, J., and van der Ploeg, R. R., 2002, “A review on recent developments in soil water retention theory: interfacial tension and temperature effects,” *J. Plant Nutr. Soil Sci.*, **165**(4), p. 468.
- [43] Rozhok, S., Piner, R., and Mirkin, C. A., 2003, “Dip-Pen Nanolithography: What Controls Ink Transport?,” *J. Phys. Chem. B*, **107**(3), pp. 751–757.
- [44] De Lazzar, A., Dreyer, M., and Rath, H. J., 1999, “Particle–Surface Capillary Forces,” *Langmuir*, **15**(13), pp. 4551–4559.
- [45] Mastrangelo, C. H., and Hsu, C. H., 1993, “Mechanical Stability and Adhesion of Microstructures Under Capillary Forces-Part II: Experiments,” *J. Microelectromechanical Syst.*, **2**(1), pp. 44–55.
- [46] Mastrangelo, C. H., and Hsu, C. H., 1993, “Mechanical Stability and Adhesion of Microstructures Under Capillary Forces-Part I : Basic Theory,” *J. Microelectromechanical Syst.*, **2**(1), pp. 33–43.
- [47] Carpick, R. W., Batteas, J., and de Boer, M. P., 2007, *Scanning Probe Studies of Nanoscale Adhesion Between Solids in the Presence of Liquids and Monolayer Films*, Springer.
- [48] Kohonen, M. M., and Christenson, H. K., 2000, “Capillary Condensation of Water between Rinsed Mica Surfaces,” (11), pp. 7285–7288.
- [49] Weeks, B. L., Vaughn, M. W., and Deyoreo, J. J., 2005, “Direct imaging of meniscus formation in atomic force microscopy using environmental scanning electron microscopy,” *Langmuir*, **21**(18), pp. 8096–8098.
- [50] Van Honschoten, J. W., Brunets, N., and Tas, N. R., 2010, “Capillarity at the nanoscale,” *Chem. Soc. Rev.*, **39**(3), pp. 1096–1114.
- [51] Donald, A. M., 2003, “The use of environmental scanning electron microscopy for imaging wet and insulating materials,” *Nat. Mater.*, **2**(8), pp. 511–516.
- [52] Christenson, H. K., 1988, “Adhesion between surfaces in undersaturated vapors—a reexamination of the influence of meniscus curvature and surface forces,” *J. Colloid Interface Sci.*, **121**(1), pp. 170–178.
- [53] Xiao, X., and Qian, L., 2000, “Investigation of Humidity-Dependent Capillary Force,” *Langmuir*, **16**(21), pp. 8153–8158.
- [54] Butt, H.-J., and Kappl, M., 2009, “Normal capillary forces,” *Adv. Colloid Interface Sci.*, **146**(1-2), pp. 48–60.

- [55] Barthel, A. J., Al-Azizi, A., and Kim, S. H., 2013, “Fundamental Understanding of Environmental Effects on Adhesion and Friction: Alcohol and Water Adsorption Cases,” *Tribol. Lett.*, **50**(2), pp. 157–168.
- [56] Maeda, N., Israelachvili, J. N., and Kohonen, M. M., 2003, “Evaporation and instabilities of microscopic capillary bridges,” *Proc. Natl. Acad. Sci. U. S. A.*, **100**(3), pp. 803–808.
- [57] Szoszkiewicz, R., and Riedo, E., 2005, “Nucleation Time of Nanoscale Water Bridges,” *Phys. Rev. Lett.*, **95**(13), pp. 135502–1:135502–4.
- [58] Bocquet, L., Charlaix, E., Ciliberto, S., and Crassous, J., 1998, “Moisture-induced ageing in granular media and the kinetics of capillary condensation,” *Nature*, **396**(December), pp. 735–737.
- [59] Soylemez, E., Plass, R. A., Ashurst, W. R., and de Boer, M. P., 2013, “Probing microelectromechanical systems in an environmentally controlled chamber using long working distance interferometry,” *Rev. Sci. Instrum.*, **84**(7), pp. 075006–1:075006–6.
- [60] Christenson, H. K., 2001, “Confinement effects on freezing and melting,” *J. Phys. Condens. Matter*, **13**(11), pp. R96–R133.
- [61] Maeda, N., and Israelachvili, J. N., 2002, “Nanoscale Mechanisms of Evaporation, Condensation and Nucleation in Confined Geometries,” *J. Phys. Chem. B*, **106**(14), pp. 3534–3537.
- [62] Koehler, W. F., 1958, “Multiple-Beam Fringes of Equal Chromatic Order. Part VIII. Method of Coincidence,” **48**(1955), pp. 55–57.
- [63] Israelachvili, J. N., 1973, “Thin Film Studies Using Multiple-Beam Interferometry,” *J. Colloid Interface Sci.*, **44**(2), pp. 259–271.
- [64] Cappella, B., and Dietler, G., 1999, “Force-distance curves by atomic force microscopy,” *Surf. Sci. Rep.*, **34**(1-3), pp. 1–104.
- [65] Rabinovich, Y. I., Esayanur, M. S., and Moudgil, B. M., 2005, “Capillary forces between two spheres with a fixed volume liquid bridge: theory and experiment,” *Langmuir*, **21**(24), pp. 10992–10997.
- [66] Farshchi-Tabrizi, M., Kappl, M., Cheng, Y., Gutmann, J., and Butt, H.-J., 2006, “On the adhesion between fine particles and nanocontacts: an atomic force microscope study,” *Langmuir*, **22**(5), pp. 2171–2184.
- [67] De Boer, M. P., and Michalske, T. a., 1999, “Accurate method for determining adhesion of cantilever beams,” *J. Appl. Phys.*, **86**(2), pp. 817–827.

- [68] De Boer, M. P., 2007, “Capillary Adhesion Between Elastically Hard Rough Surfaces,” *Exp. Mech.*, **47**(1), pp. 171–183.
- [69] Kim, H., Smit, B., and Jang, J., 2012, “Monte Carlo Study on the Water Meniscus Condensation and Capillary Force in Atomic Force Microscopy,” *J. Phys. Chem. C*, **116**(41), pp. 21923–21931.
- [70] Choi, H. J., Kim, J. Y., Hong, S. D., Ha, M. Y., and Jang, J., 2009, “Molecular simulation of the nanoscale water confined between an atomic force microscope tip and a surface,” *Mol. Simul.*, **35**(6), pp. 466–472.
- [71] Leroch, S., and Wendland, M., 2013, “Influence of Capillary Bridge Formation onto the Silica Nanoparticle Interaction Studied by Grand Canonical Monte Carlo Simulations,” *Langmuir*, **29**, pp. 12410–12420.
- [72] Cheng, S., and Robbins, M. O., 2014, “Capillary adhesion at the nanometer scale,” *Phys. Rev. E*, **89**(6), pp. 062402–1:062402–14.
- [73] Kohonen, M., Maeda, N., and Christenson, H., 1999, “Kinetics of Capillary Condensation in a Nanoscale Pore,” *Phys. Rev. Lett.*, **82**(23), pp. 4667–4670.
- [74] Rabinovich, Y. I., Singh, A., Hahn, M., Brown, S., and Moudgil, B., 2011, “Kinetics of liquid annulus formation and capillary forces,” *Langmuir*, **27**(22), pp. 13514–13523.
- [75] Li, T.-D., Gao, J., Szoszkiewicz, R., Landman, U., and Riedo, E., 2007, “Structured and viscous water in subnanometer gaps,” *Phys. Rev. B*, **75**(11), pp. 115415–1:115415–6.
- [76] Feibelman, P. J., 2004, “Effect of High-Viscosity Interphases on Drainage between Hydrophilic Surfaces,” *Langmuir*, **20**(4), pp. 1239–1244.
- [77] Restagno, F., Bocquet, L., and Biben, T., 2000, “Metastability and nucleation in capillary condensation,” *Phys. Rev. Lett.*, **84**(11), pp. 2433–2436.
- [78] Riedo, E., Lévy, F., and Brune, H., 2002, “Kinetics of Capillary Condensation in Nanoscopic Sliding Friction,” *Phys. Rev. Lett.*, **88**(18), pp. 185505–1:185505–4.
- [79] Riedo, E., Palaci, I., Boragno, C., and Brune, H., 2004, “The 2 / 3 Power Law Dependence of Capillary Force on Normal Load in Nanoscopic Friction,” *J. Phys. Chem. B*, **108**, pp. 5324–5328.
- [80] Barel, I., Filippov, A. E., and Urbakh, M., 2012, “Formation and rupture of capillary bridges in atomic scale friction,” *J. Chem. Phys.*, **137**(16), pp. 164706–1:164706–6.
- [81] Tamura, A., and Ichinokawa, T., 1984, “LIQUID DROP MODEL OF A SMALL PARTICLE IN A LIQUID STATE,” *Surf. Sci.*, **136**, pp. 437–448.

- [82] Boyd, J., Briskman, A., Colvin, V., and Mittleman, D., 2001, "Direct Observation of Terahertz Surface Modes in Nanometer-Sized Liquid Water Pools," *Phys. Rev. Lett.*, **87**(14), pp. 147401–1:147401–4.
- [83] Sirghi, L., Szoszkiewicz, R., and Riedo, E., 2006, "Volume of a nanoscale water bridge.," *Langmuir*, **22**(3), pp. 1093–1098.
- [84] Iwamatsu, M., and Horii, K., 1996, "Capillary Condensation and Adhesion of Two Wetter Surfaces," *J. Colloid Interface Sci.*, **406**, pp. 400–406.
- [85] Greiner, C., Felts, J. R., Dai, Z., King, W. P., and Carpick, R. W., 2010, "Local nanoscale heating modulates single-asperity friction.," *Nano Lett.*, **10**(11), pp. 4640–4645.
- [86] Sung, B., Kim, J., Stambaugh, C., Chang, S.-J., and Jhe, W., 2013, "Direct measurement of activation time and nucleation rate in capillary-condensed water nanomeniscus," *Appl. Phys. Lett.*, **103**(21), pp. 213107–1:213107–4.
- [87] Soylemez, E., and de Boer, M. P., 2014, "Capillary-Induced Crack Healing between Surfaces of Nanoscale Roughness.," *Langmuir*, **30**(39), pp. 11625–11633.
- [88] Gellman, A. J., 2004, "Vapor Lubricant Transport in MEMS Devices," *Tribol. Lett.*, **17**(3), pp. 455–461.
- [89] Henck, S. A., 1997, "Lubrication of digital micromirrordevices™," *Tribol. Lett.*, **3**(3), pp. 239–247.
- [90] Asay, D. B., Dugger, M. T., Ohlhausen, J. A., and Kim, S. H., 2008, "Macro- to nanoscale wear prevention via molecular adsorption.," *Langmuir*, **24**(1), pp. 155–159.
- [91] Asay, D. B., and Kim, S. H., 2006, "Effects of adsorbed water layer structure on adhesion force of silicon oxide nanoasperity contact in humid ambient.," *J. Chem. Phys.*, **124**(17), p. 174712.
- [92] Jensen, B. D., Chow, L. L.-W., Saitou, K., Volakis, J. L., and Kurabayashi, K., 2005, "Effect of nanoscale heating on electrical transport in RF MEMS switch contacts," *J. Microelectromechanical Syst.*, **14**(5), pp. 935–946.
- [93] Tringe, J. W., Uhlman, T. A., Oliver, A. C., and Houston, J. E., 2003, "A single asperity study of Au/Au electrical contacts," *J. Appl. Phys.*, **93**(8), pp. 4661–4669.
- [94] Walker, M. J., Berman, D., Nordquist, C., and Krim, J., 2011, "Electrical Contact Resistance and Device Lifetime Measurements of Au-RuO<sub>2</sub>-Based RF MEMS Exposed to Hydrocarbons in Vacuum and Nitrogen Environments," *Tribol. Lett.*, **44**(3), pp. 305–314.

- [95] DelRio, F. W., Dunn, M. L., Phinney, L. M., Bourdon, C. J., and de Boer, M. P., 2007, "Rough surface adhesion in the presence of capillary condensation," *Appl. Phys. Lett.*, **90**(16), p. 163104.
- [96] Barnette, A. L., Asay, D. B., Kim, D., Guyer, B. D., Lim, H., Janik, M. J., and Kim, S. H., 2009, "Experimental and density functional theory study of the tribochemical wear behavior of SiO<sub>2</sub> in humid and alcohol vapor environments.," *Langmuir*, **25**(22), pp. 13052–13061.
- [97] Tanner, D. M., and Dugger, M. T., 2003, "Wear mechanisms in a reliability methodology," SPIE, R. Ramesham, and D.M. Tanner, eds., *International Society for Optics and Photonics*, pp. 22–40.
- [98] Timpe, S. J., and Komvopoulos, K., 2007, "Microdevice for measuring friction and adhesion properties of sidewall contact interfaces of microelectromechanical systems," *Rev. Sci. Instrum.*, **78**(6), p. 065106.
- [99] French, P., Hon, M., DelRio, F. W., White, J. T., Kendig, M., Carraro, C., and Maboudian, R., 2008, "Cathodic corrosion of polycrystalline silicon MEMS," *Sensors Actuators A Phys.*, **145**, pp. 323–329.
- [100] Plass, R. A., Walraven, J. A., Tanner, D. M., and Sexton, F. W., 2003, "Anodic oxidation-induced delamination of the SUMMiT poly 0 to Silicon Nitride Interface," SPIE, R. Ramesham, and D.M. Tanner, eds., *International Society for Optics and Photonics*, pp. 81–86.
- [101] Michalske, T. A., and Freiman, S. W., 1983, "A Molecular Mechanism for Stress Corrosion in Vitreous Silica," *J. Am. Ceram. Soc.*, **66**(4), pp. 284–288.
- [102] Alsem, D. H., Stach, E. A., Muhlstein, C. L., and Ritchie, R. O., 2005, "Fatigue failure in thin-film polycrystalline silicon is due to subcritical cracking within the oxide layer," *Appl. Phys. Lett.*, **86**(4), pp. 041914–1:041914–3.
- [103] Heuer, A., Kahn, H., Kahn, H., Avishai, A., Ballarini, R., and Heuer, A. H., 2008, "Surface oxide effects on failure of polysilicon MEMS after cyclic and monotonic loading," *Scr. Mater.*, **59**(9), pp. 912–915.
- [104] Shrotriya, P., Allameh, S. M., and Soboyejo, W. O., 2004, "On the evolution of surface morphology of polysilicon MEMS structures during fatigue," *Mech. Mater.*, **36**(1), pp. 35–44.
- [105] Theillet, P.-O., and Pierron, O. N., 2011, "Quantifying adsorbed water monolayers on silicon MEMS resonators exposed to humid environments," *Sensors Actuators A Phys.*, **171**(2), pp. 375–380.

- [106] Yang, Y.-S., Lin, Y.-H., Hu, Y.-C., and Liu, C.-H., 2009, "A large-displacement thermal actuator designed for MEMS pitch-tunable grating," *J. Micromechanics Microengineering*, **19**, pp. 1–12.
- [107] Zook, J. D., Burns, D. W., Guckel, H., Sniegowski, J. J., Engelstad, R. L., and Feng, Z., 1992, "Characteristics of polysilicon resonant microbeams," *Sensors Actuators A Phys.*, **35**(1), pp. 51–59.
- [108] Gong, S., Shen, H., and Barker, N. S., 2009, "Study of Broadband Cryogenic DC-Contact RF MEMS Switches," *IEEE Trans. Microw. Theory Tech.*, **57**(12), pp. 3442–3449.
- [109] Miller, D. C., Gall, K., and Stoldt, C. R., 2005, "Galvanic Corrosion of Miniaturized Polysilicon Structures," *Electrochem. Solid-State Lett.*, **8**(9), pp. G223–G226.
- [110] Andersen, H. H., and Bay, H. L., 1981, "Sputtering Yield Measurements," *Top. Ina. Phys.*, **47**, pp. 145–218.
- [111] Sinclair, M. B., de Boer, M. P., and Corwin, A. D., 2005, "Long-working-distance incoherent light interference microscope," *Appl. Opt.*, **44**(36), pp. 7714–7721.
- [112] Greivenkamp, J. E., and Bruning, J. H., 1992, *Optical Shop Testing*, Wiley and Sons, New York.
- [113] Persson, B. N. J., 2008, "Capillary adhesion between elastic solids with randomly rough surfaces," *J. Phys. Condens. Matter*, **20**(31), p. 315007.
- [114] Xue, X., and Polycarpou, A. a, 2007, "An improved meniscus surface model for contacting rough surfaces.," *J. Colloid Interface Sci.*, **311**(1), pp. 203–11.
- [115] DelRio, F. W., Dunn, M. L., and de Boer, M. P., 2008, "Capillary adhesion model for contacting micromachined surfaces," *Scr. Mater.*, **59**(9), pp. 916–920.
- [116] Sniegowski, J. J., and de Boer, M. P., 2000, "IC-COMPATIBLE POLYSILICON SURFACE MICROMACHINING," *Annu. Rev. Mater. Sci.*, **30**(1), pp. 299–333.
- [117] Mulhern, G. T., Soane, D. S., and Howe, R. T., 1993, "Supercritical carbon dioxide drying of microstructures," *Proc. Transducers*, pp. 296–299.
- [118] Jensen, B. D., Boer, M. P. De, Masters, N. D., Bitsie, F., and Lavan, D. A., 2001, "Interferometry of Actuated Microcantilevers to Determine Material Properties and Test Structure Nonidealities in MEMS," (September), pp. 336–346.
- [119] Wan, K.-T., and Lawn, B. R., 1990, "Surface forces at crack interfaces in mica in the presence of capillary condensation," *Acta Metall. Mater.*, **38**(11), pp. 2073–2083.

- [120] Wan, K.-T., Smith, D. T., and Lawn, B. R., 1992, “Fracture and Contact Adhesion Energies of Mica-Mica, Silica-Silica, and Mica-Silica Interfaces in Dry and Moist Atmospheres,” *J. Am. Ceram. Soc.*, **75**(3), pp. 667–676.
- [121] De Boer, M. ., Knapp, J. ., Michalske, T. ., Srinivasan, U., and Maboudian, R., 2000, “Adhesion hysteresis of silane coated microcantilevers,” *Acta Mater.*, **48**(18-19), pp. 4531–4541.
- [122] Knapp, J. A., and de Boer, M. P., 2002, “Mechanics of microcantilever beams subject to combined electrostatic and adhesive forces,” *J. Microelectromechanical Syst.*, **11**(6), pp. 754–764.
- [123] Meinhart, M., Miller, N., and Saif, M. T. A., 2006, “Dry stiction of micro structures— theory and experiment,” *Proc. R. Soc. A Math. Phys. Eng. Sci.*, **462**(2066), pp. 567–585.
- [124] De Boer, M. P., and Michalske, T. A., 1999, “Accurate method for determining adhesion of cantilever beams,” *J. Appl. Phys.*, **86**(2), pp. 817–827.
- [125] Lawn, B., 1993, *Fracture of Brittle Solids*, Cambridge University Press.
- [126] Delrio, F. W., de Boer, M. P., Knapp, J. A., David Reedy, E., Clews, P. J., and Dunn, M. L., 2005, “The role of van der Waals forces in adhesion of micromachined surfaces,” *Nat. Mater.*, **4**(8), pp. 629–634.
- [127] Wan, K.-T., Lathabai, S., and Lawn, B. R., 1990, “Crack velocity functions and thresholds in brittle solids,” *J. Eur. Ceram. Soc.*, **6**(4), pp. 259–268.
- [128] Wiederhorn, S. M., 1967, “Influence of Water Vapor on Crack Propagation in Soda-Lime Glass,” *J. Am. Ceram. Soc.*, **50**(8), pp. 407–414.
- [129] Michalske, T. A., and Fuller, E. R., 1985, “Closure and Repropagation of Healed Cracks in Silicate Glass,” *J. Am. Ceram. Soc.*, **68**(11), pp. 586–590.
- [130] Wan, K., Aimard, N., Lathabai, S., Horn, R. G., and Lawn, B. R., 1990, “Interfacial energy states of moisture-exposed cracks in mica,” *J. Mater. Res.*, **5**(1), pp. 172–182.
- [131] Wan, K., Lawn, B. R., and Horn, R. G., 1992, “Repulsive interaction between coplanar cracks in the double-cantilever geometry,” *J. Mater. Res.*, **7**(6), pp. 1584–1588.
- [132] Asay, D. B., and Kim, S. H., 2005, “Evolution of the adsorbed water layer structure on silicon oxide at room temperature,” *J. Phys. Chem. B*, **109**(35), pp. 16760–16763.
- [133] Wang, X., Zhao, M., and Nolte, D. D., 2010, “Ambient molecular water accumulation on silica surfaces detected by a reflectance interference optical balance,” *Appl. Phys. Lett.*, **97**(18), pp. 183702–1:183702–3.

- [134] Liu, H., and Bhushan, B., 2003, "Adhesion and friction studies of microelectromechanical systems/nanoelectromechanical systems materials using a novel microtriboapparatus," *J. Vac. Sci. Technol. A Vacuum, Surfaces, Film.*, **21**(4), p. 1528.
- [135] SIGMA-ALDRICH, "Perfluorodecanoic acid" [Online]. Available: <http://www.sigmaaldrich.com/catalog/product/aldrich/177741?lang=en&region=US>.
- [136] Wallace, R. M., 1995, "Adsorption of perfluorinated n-alkanoic acids on native aluminum oxide surfaces," *J. Vac. Sci. Technol. A Vacuum, Surfaces, Film.*, **13**(3), pp. 1345–1350.
- [137] Asay, D. B., Dugger, M. T., and Kim, S. H., 2007, "In-situ Vapor-Phase Lubrication of MEMS," *Tribol. Lett.*, **29**(1), pp. 67–74.
- [138] Williams, D. B. G., and Lawton, M., 2010, "Drying of organic solvents: quantitative evaluation of the efficiency of several desiccants," *J. Org. Chem.*, **75**(24), pp. 8351–8354.
- [139] Barthel, A. J., and Kim, S. H., 2014, "Lubrication by Physisorbed Molecules in Equilibrium with Vapor at Ambient Condition: Effects of Molecular Structure and Substrate Chemistry," *Langmuir*, **30**, pp. 6469–6478.
- [140] Marchand, D. J., Chen, L., Meng, Y., Qian, L., and Kim, S. H., 2013, "Effects of Vapor Environment and Counter-Surface Chemistry on Tribochemical Wear of Silicon Wafers," *Tribol. Lett.*, **53**(1), pp. 365–372.
- [141] Rabinovich, Y. I., Adler, J. J., Esayanur, M. S., Ata, A., Singh, R. K., and Moudgil, B. M., 2002, "Capillary forces between surfaces with nanoscale roughness," *Adv. Colloid Interface Sci.*, **96**(1-3), pp. 213–230.
- [142] DelRio, F. W., Dunn, M. L., and de Boer, M. P., 2007, "Growth of Silicon Carbide Nanoparticles Using Tetraethylorthosilicate for Microelectromechanical Systems," *Electrochem. Solid-State Lett.*, **10**(1), pp. H27–H30.
- [143] Yaws, C. L., 2003, *Yaws' Handbook of Thermodynamic and Physical Properties of Chemical Compounds*, Knovel.
- [144] Komvopoulos, K., and Yan, W., 1997, "A Fractal Analysis of Stiction in Microelectromechanical Systems," *J. Tribol.*, **119**(3), pp. 391–400.
- [145] Persson, B. N. J., Albohr, O., Heinrich, G., and Ueba, H., 2005, "Crack propagation in rubber-like materials," *J. Phys. Condens. Matter*, **17**(44), pp. R1071–R1142.
- [146] Greenwood, J. A., and Williamson, J. B. P., 1966, "Contact of nominally flat surfaces," *R. Soc.*, **295**(1442), pp. 300–319.

- [147] Thoreson, E. J., and Burnham, N. a., 2004, “Standard-deviation minimization for calibrating the radii of spheres attached to atomic force microscope cantilevers,” *Rev. Sci. Instrum.*, **75**(5), pp. 1359–1362.
- [148] Archard, J. F., 1974, “Surface topography and tribology,” *Tribology*, **7**(5), pp. 213–220.
- [149] Persson, B. N. J., Albohr, O., Tartaglino, U., Volokitin, A. I., and Tosatti, E., 2005, “On the nature of surface roughness with application to contact mechanics, sealing, rubber friction and adhesion,” *J. Phys. Condens. Matter*, **17**(1), pp. R1–R62.
- [150] Maugis, D., and Gauthier-Manuel, B., 1994, “JKR-DMT transition in the presence of a liquid meniscus,” *J. Adhes. Sci. Technol.*, **8**(11), pp. 1311–1322.
- [151] Greenwood, J. A., and Tripp, J. H., “Proceedings of the Institution of Mechanical Engineers THE CONTACT OF TWO NOMINALLY FLAT.”
- [152] Chang, W. R., Etsion, I., and Bogy, D. B., 1987, “An Elastic-Plastic Model for the Contact of Rough Surfaces,” *J. Tribol.*, **109**(2), p. 257.
- [153] Bhushan, B., and Li, X., 1997, “Micromechanical and tribological characterization of doped single-crystal silicon and polysilicon films for microelectromechanical systems devices,” *J. Mater. Res.*, **12**(1), pp. 54–63.
- [154] Kogut, L., and Etsion, I., 2002, “Elastic-Plastic Contact Analysis of a Sphere and a Rigid Flat,” *J. Appl. Mech.*, **69**(5), p. 657.
- [155] Israelachvili, J. N., 1992, *Intermolecular and Surface Forces*, Academic Press.
- [156] Anandarajah, A., and Chen, J., 1995, “Single Correction Function for Computing Retarded van der Waals Attraction,” *J. Colloid Interface Sci.*, **176**(2), pp. 293–300.
- [157] Carpick, R. W., Ogletree, D. F., and Salmeron, M., 1999, “and Friction vs Load Measurements,” **400**, pp. 395–400.
- [158] Men, Y., and Zhang, X., 2012, “Physical basis for constrained lattice density functional theory,” *J. Chem. Phys.*, **136**(12), p. 124704.
- [159] Men, Y., Zhang, X., and Wang, W., 2009, “Capillary liquid bridges in atomic force microscopy: formation, rupture, and hysteresis,” *J. Chem. Phys.*, **131**(18), p. 184702.

# APPENDICES

## Appendix A

### Interferometer Quick-Start Guide

#### Introduction

Long-working-distance incoherent-light interference microscope has been used for the in-plane and out of plane geometry measurements of the MEMS samples. A schematic of the optical layout of the interferometer is shown in Figure A1. Components to build the microscope setup were gathered from various vendors. This user manual aims to present clear instructions to use the interferometer microscope and also to align the microscope properly. To understand the steps clearly and to comprehend the physics of the instrument, it is strongly suggested to first reading the Sinclair et al.[111].

Note: To increase clarity in these instructions  $x$ ,  $y$ , and  $z$  coordinates are defined as shown in Figure A1. The  $x$ -axis runs parallel to the image, and when looking at the instrument from the front is equivalent to left and right. The  $y$ -axis is equivalent to up and down, and the  $z$ -axis refers to front to back.

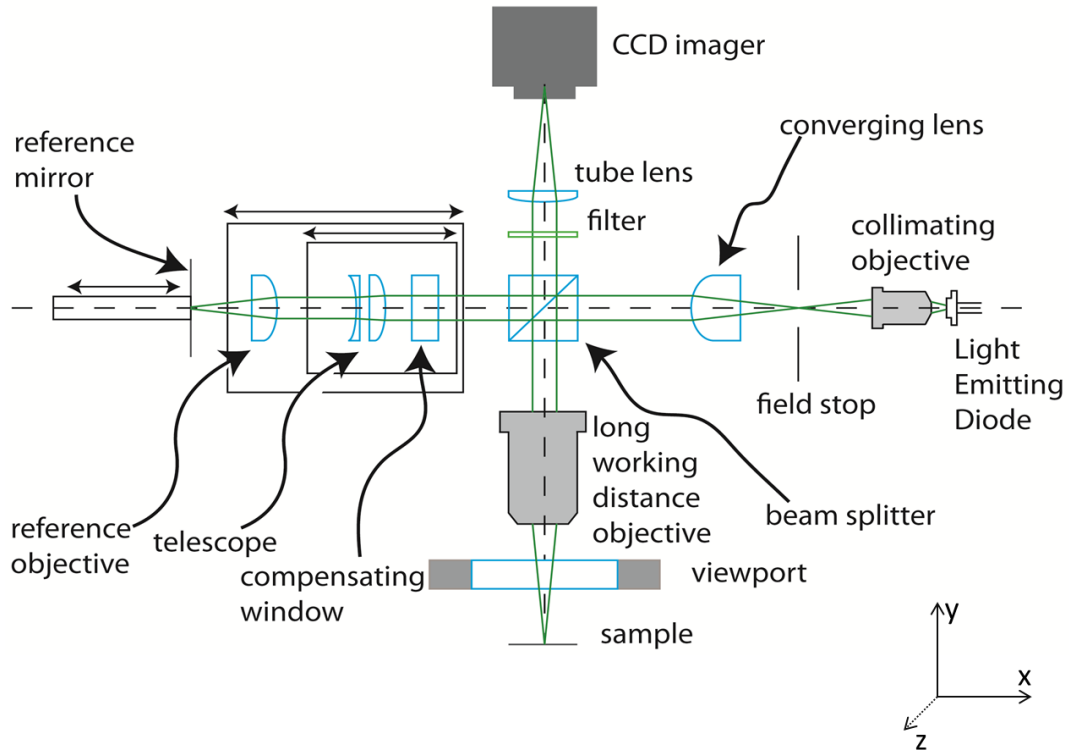


**Figure A1:** Schematic layout of the interference microscope.

## Pre-Alignment

### Turn on the LED

1. Flip the switch on the controller DC Power Supply to the “on” position
  - The DC Power Supply is located above the computer monitor



**Figure A2:** Picture of the DC power supply.

2. From the computer desktop, double click on “TalkToLED.bat”



**Figure A3:** “TalkToLED.bat” shortcut symbol.

3. A prompt will appear as shown in Figure A4. In the “Send String” field, type “vset” followed by the desired voltage to determine LED brightness
  - A typical voltage range is 2.7-3
4. Once voltage is set, click “Write”



**Figure A4:** Command window for LED brightness.

Note: The green LED light located on the far right end of the instrument should now be turned on.

## Close the Shutter

1. Open NIMAX Program on desktop



**Figure A5:** NIMAX shortcut symbol.

2. Click “Devices and Interfaces”
3. Click “Traditional NI-DAQ (Legacy) Devices”
4. Double click on “PCI-6733 (Device 1)” as shown in Figure A6.

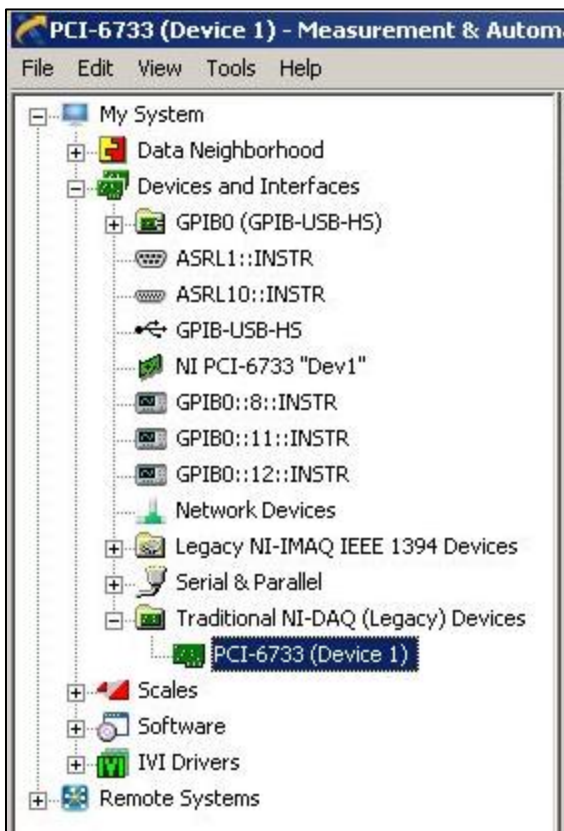


**Figure A6:** Screenshot of the “PCI-6733 (Device 1)” in the menu.

5. Click “Test Panel” tab in the main section of the screen at the top of the device window
6. Under Channel Selection, select channel 6
  - This channel controls the shutter
7. Set the DC Voltage to 3 and click “Update Channel”
  - DC Voltage of 3 closes the shutter, shutter open at voltage of 0

Note: The reference side shutter is now closed. The shutter is closed in order to avoid interference from the reference sample. In this way, it is easier to align the sample side of the instrument. The sample side alignment can be begun.

## Microscope (Sample side) Alignment

Note: Before the alignment process is begun, it is important to assemble the following materials shown in Figure A7: two small paper circles (1.5" and 1" in diameter) each with a small pinhole in its center, a bull's eye level, and a set of Allen wrenches.

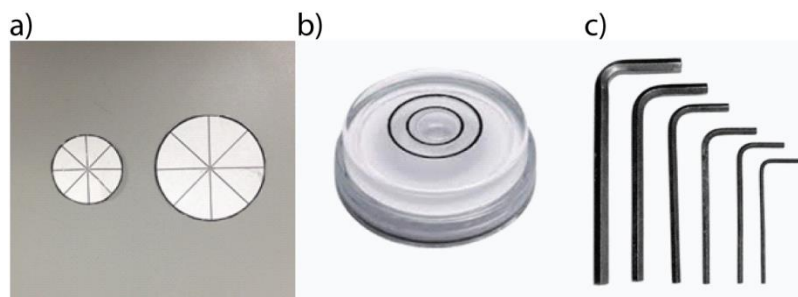


**Figure A7:** Alignment tools. (a) two small paper circles (1.5" and 1" in diameter) each with a small pinhole in its center. (b) a bull's eye level. (c) a set of Allen wrenches.

## Adjust the Light Source

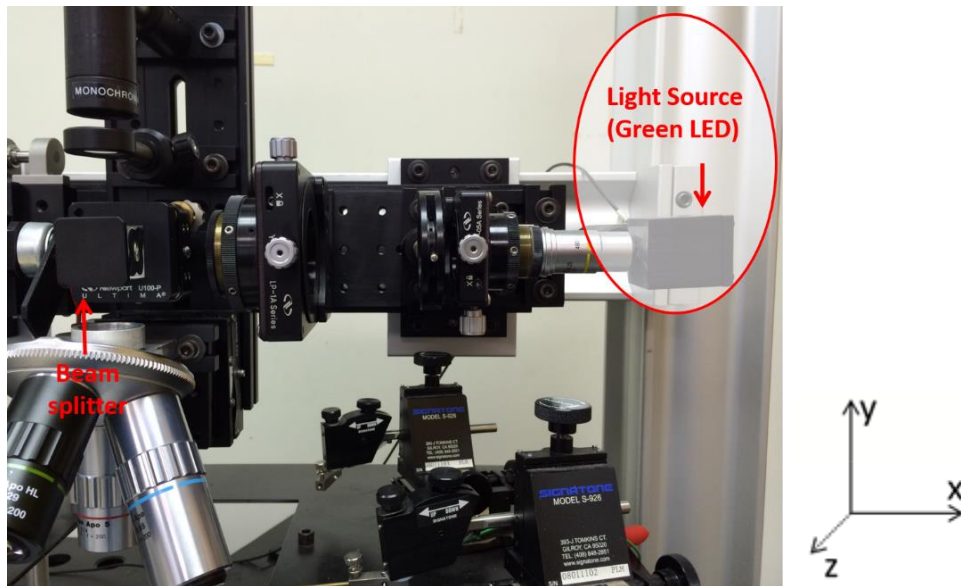


**Figure A8:** Interferometer microscope right hand side picture.

1. First, ensure the light source is on the same level with beam splitter by using a bull's eye level
2. If the light source is leveled, hold the 1" diameter paper with the pinhole on the right side of the beam splitter and check to see if the light axis is through the pinhole and centered
3. If light source is not on the same level with the beam splitter, loosen the screws that holds the post holder of the light source using the Allen wrench , and adjust light source to bring it to the same level
4. Once the light source is leveled, again hold the 1" diameter paper on the right side of the beam splitter, and check to see if the light is through and centered
5. Lock the light source in place by retightening the screws with the Allen wrench

Note: These post holders are the cylinders attached to the mounting plate. In order to loosen them, an Allen wrench needs to be used.

## Adjust the Collimator

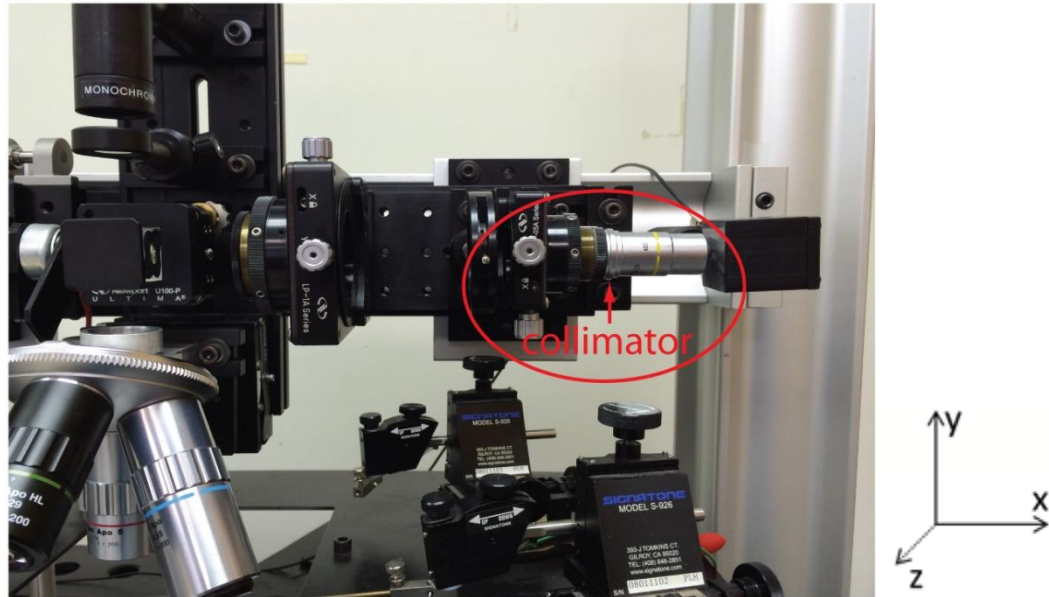


**Figure A9:** Interferometer microscope right hand side picture.

1. First, ensure the collimator is at the same level with the light source using a bull's eye level
2. If it is not leveled, loosen the collimator post holder, adjust its position so it is leveled, and tighten the post holders
3. Next, move the collimator in the x direction by rotating the knob so it is almost touching the light source
4. Once the collimator is brought to the position, adjust the collimator in the z and y directions so it is in the center of the light source using the appropriate knobs. Perform this step by rotating the knobs on the collimator and ensure it is centered by inspection with the eye

Note: It is important that the collimating objective is positioned so that the light of the LED hits the center of the collimator.

## Adjust the Converging lens

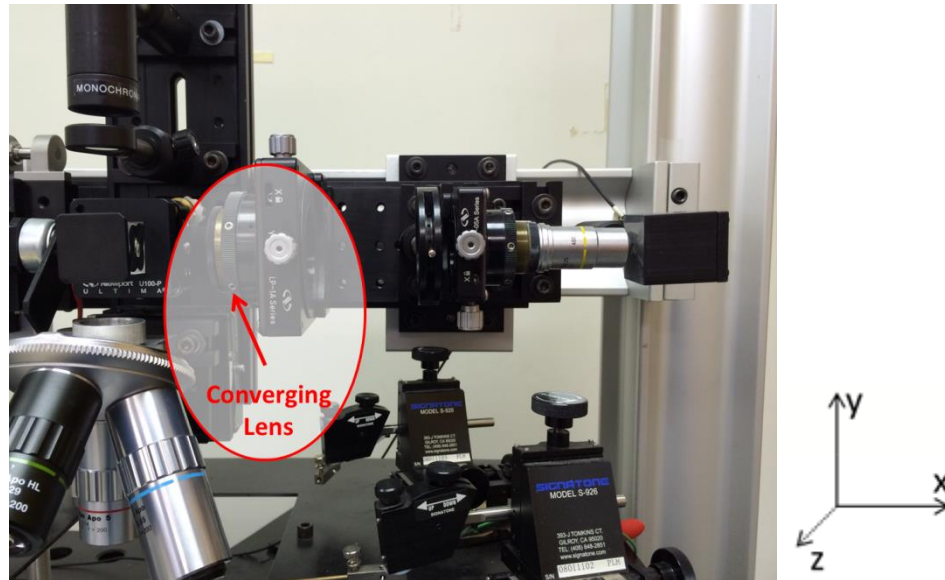


**Figure A10:** Interferometer microscope right hand side picture.

1. First, ensure the converging lens is leveled using the bull's eye level
2. If it is not leveled, loosen the post holder, level the converging lens using the bullseye level, and then tighten the post holder
3. Place the 1.5" paper circle inside the circular cutout of the XYZ lens positioner and leave it there
  - This step decreases the size of the diameter of the beam drastically, which is needed to get a precise alignment
4. Adjust z and y using the knobs so the converging lens is centered on the pinhole

## Adjust the Beam Splitter

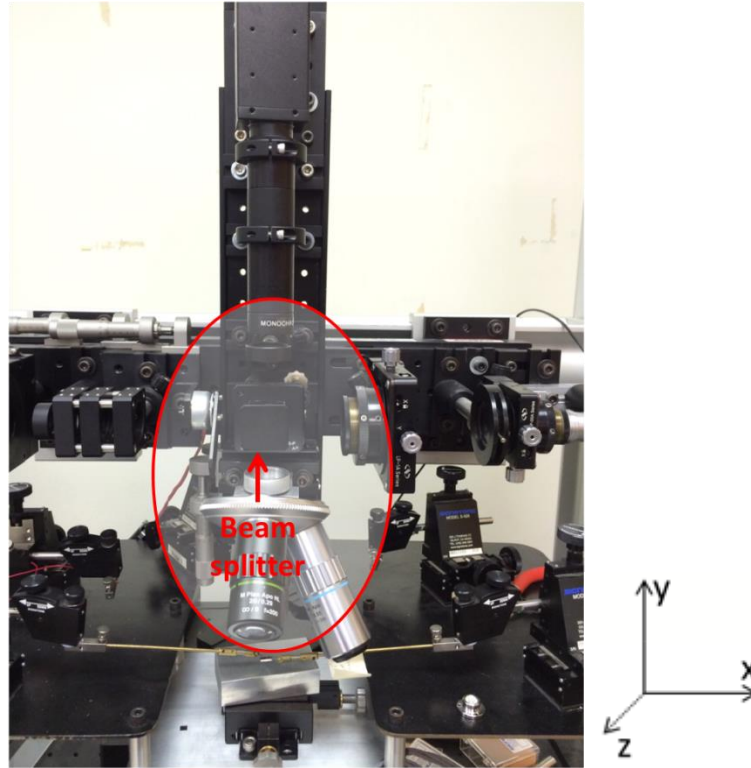


**Figure A11:** Interferometer microscope center picture.

1. First, ensure the beam splitter is leveled
2. If the beam splitter is not leveled, loosen the post holder, level the beam splitter using a bull's eye level, and tighten the post holder

## Adjust the Compensating Plate Holder

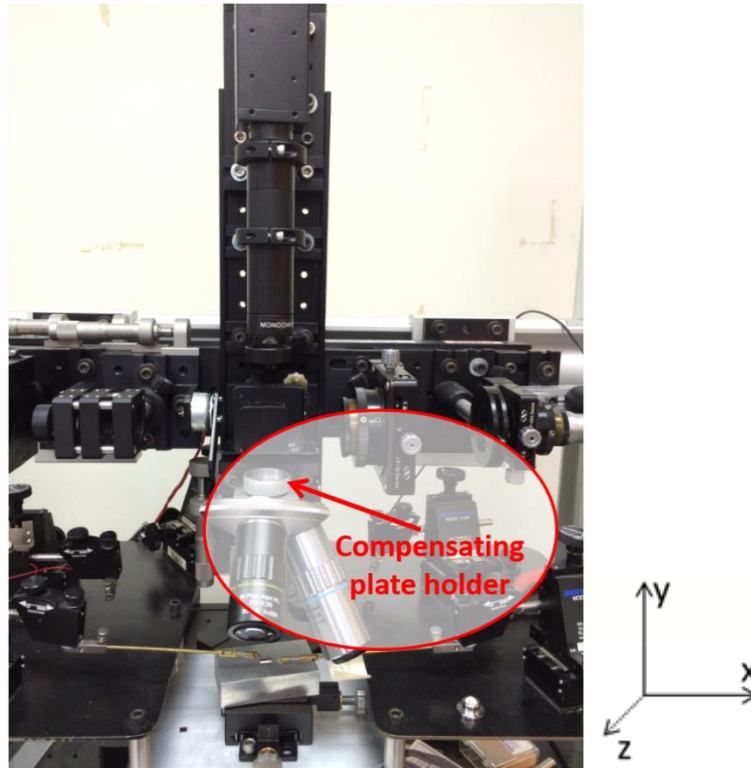


**Figure A12:** Interferometer microscope center picture.

1. First, place the 1" paper circle with a small pinhole on top of the compensating plate holder
2. Next, turn off the light in the room, and check to make sure the green LED light is coming through under the objective lens of the microscope using a second piece of paper

Note: If necessary, it is possible to go back and increase the intensity of the light using vset.

## Adjust the Objective Lens

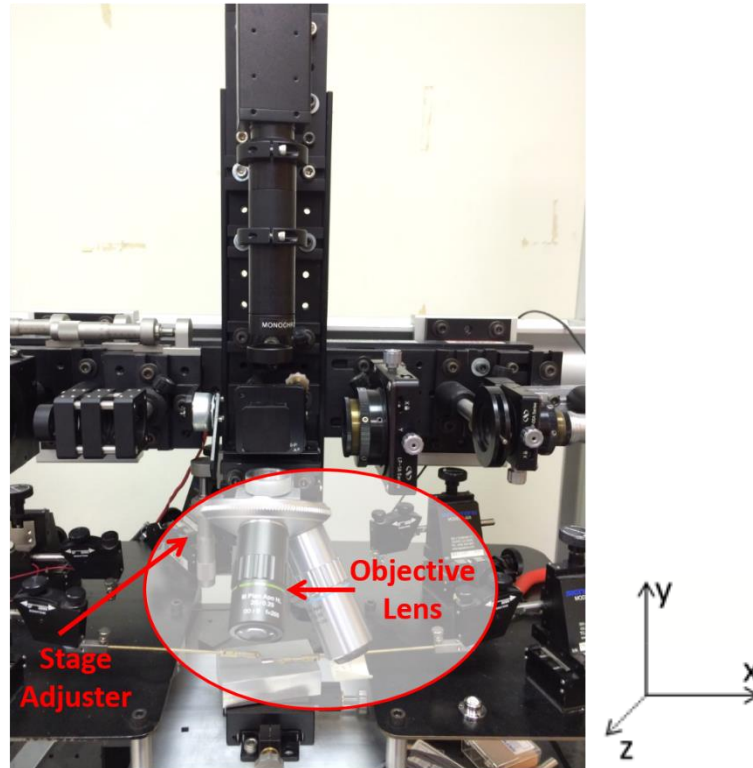


**Figure A13:** Interferometer microscope center picture.

1. First, ensure the transition stage position is at “14.77” using the stage adjuster as shown in Figure A13. This value corresponds to the reference condition
2. Next, place the paper circle with the small pinhole under the objective and check if the reflection light is coming through the pinhole
3. If the light is not coming through the pinhole, tilt the objective lens. Adjust the angle until the reflection shines through the pinhole

## Adjust the Camera

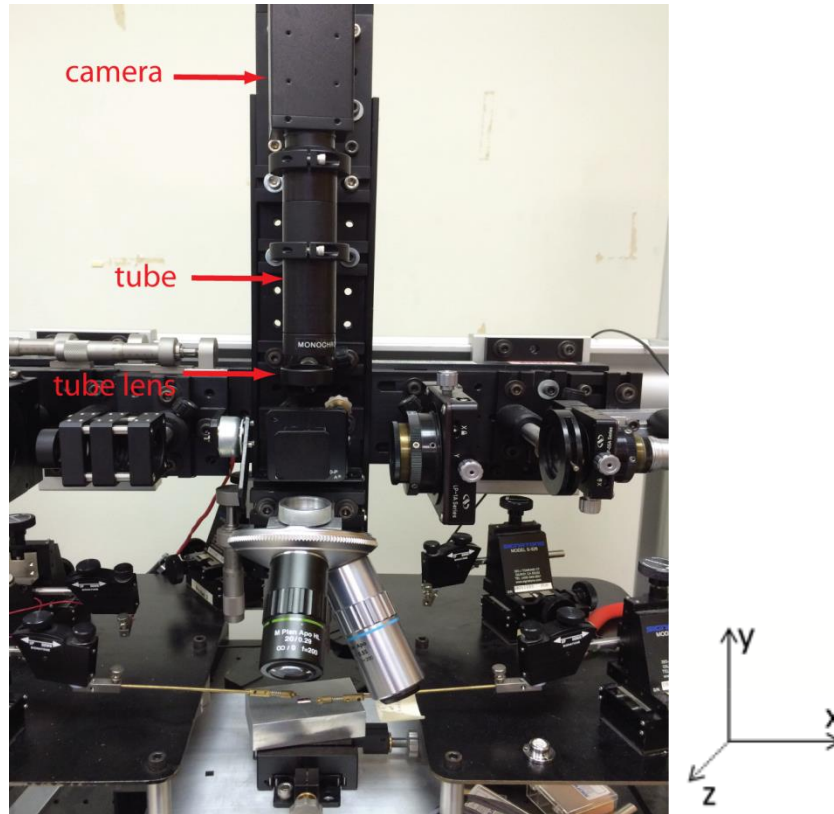


**Figure A14:** Interferometer microscope center picture.

1. First, align the tube lens. In doing so, loosen the lens tube clamps, level the tube lens using a bull's eye level, and tighten the post holder
2. Next, align the tube in the z direction
3. Go to the computer desktop and open 1394Camera Demo



**Figure A15:** Shortcut symbol of 1394Camera Demo

4. Click “Grab” and a black screen should appear

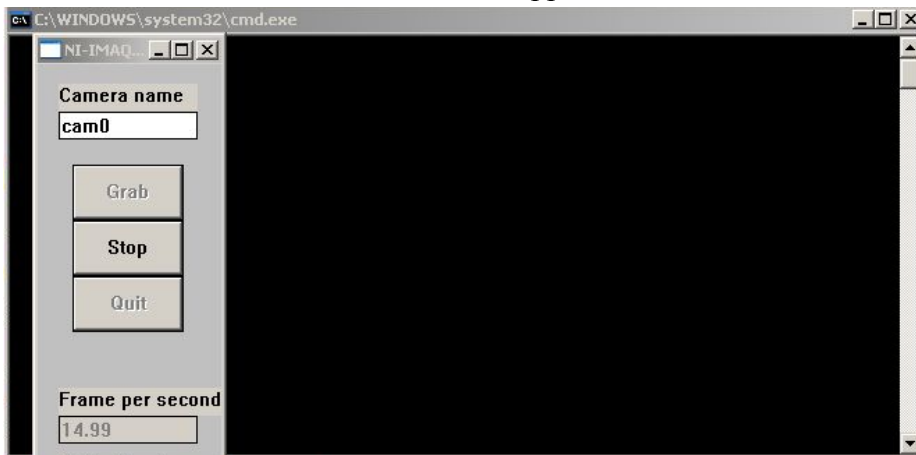


**Figure A16:** Grabbed image

5. If the instrument is properly aligned, a small light spot should appear on the screen a few seconds after the program boots up
6. Adjust the camera in the z direction by loosening its post holder until there is a light on the screen. Once this light is found, tighten the poster holder on the lens tube

### **Adjust the Sample Stage in the y Direction**

1. Turn the power of the motion controller on
2. From the computer desktop, open the ESP-util program



**Figure A17:** Shortcut of ESP-util

3. Under Select Port type, select “GPIP,” then click “Open Port,”



**Figure A18:** ESP-util menu

4. A new prompt will appear asking “Do you want to reset controller.” Click “Yes”



**Figure A19:** ESP-util pop up window

Note: This step initializes the controller and moves the sample stage in the y direction.

5. Next, a new prompt will appear. Click “enable,” then click “All On”

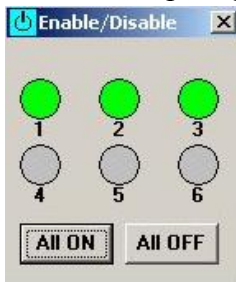


**Figure A20:** ESP-util controlling is enable for three channels

6. Click “Jog” from the toolbar



**Figure A21:** Symbol of Jog

7. A new window will appear. Under Mode, select “Indexed”
8. In this same window, adjust the Index Distance as needed to define the size of the adjustment steps
9. Under Jog, click on -X or +X to adjust the focus. This adjustment occurs in real time, so one can see how it is adjusted on the camera
10. Repeat steps 8 & 9 until the sharp image is obtained

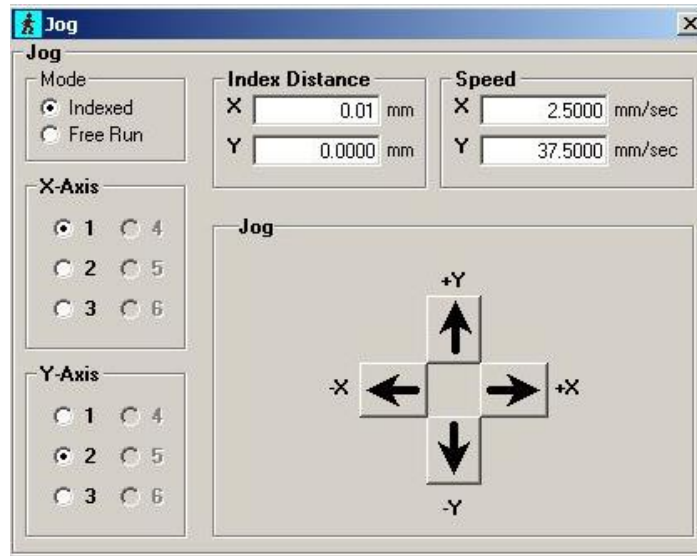


**Figure A22:** Jog window

## Close the Iris

Note: This step allows one to be able to see the edge of the holes in the screen.

1. First, ensure the iris is at the center of the screen
2. If the iris is not at the center of the screen, loosen the post holder, move the iris so that it is at the center of the screen, and tighten the post holder
3. Next, adjust the x position of the converging lens so that the edge of the iris is focused

Note: Sample side alignment has successfully been completed.

## Interferometer (Reference Side) Alignment

### Open the Shutter

1. Set the DC Voltage to 0 and click “Update Channel”
2. Put a paper on top of a compensating plate to close the sample side imaging.

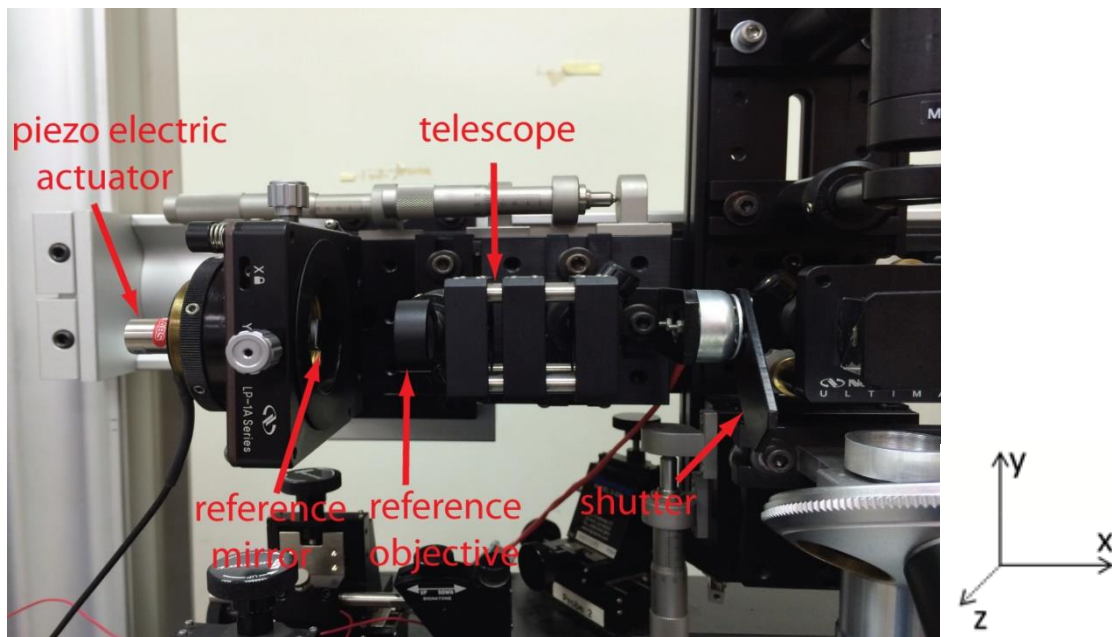


**Figure A23:** Reference side picture of the interferometer.

### Adjust the Reference Mirror

1. Close the iris until a small diameter size
2. Remove the telescope and reference objective
3. Level the reference mirror holder X-Y-Z positioner
4. After the leveling, make sure the reference mirror is perpendicular to the light ray. Tilt the mirror with knobs, and check with the paper circles if the reflection gets in through the pinhole

## **Adjust the Reference Objective and Telescope**

1. Put the reference objective back to its location
2. Make sure the light source hit at the center of the objective
3. Rotate it until the reflection light from the mirror gets through the pinhole of the circle paper stands at the left side of the lens
4. Adjust the reference mirror in x direction to focus the mirror surface.
5. Repeat steps 2 to 4 for the telescope.

## **Bring Two Images Together**

1. Open the sample side
2. There are two images forming on the camera; one is the sample image with circling iris image, and the other is the reference image with circling iris image. These two circles should be on top of each other. If not, tilt the reference mirror to bring the reference side image on top of sample side image.

## **Finding Fringes**

1. Carefully and slowly move the reference side in the x direction with the reference side positioner until you see the fringes
2. Once you find the fringes, check if you see the bull's eye pattern as shown in Figure A25. If you can't see the bull's eye pattern, loosen the post holder of the telescope and rotate it until you find the bull's eye. When you find it, tighten the post holder.
3. Each fringe in the bull's eye pattern adds artificial slope to the surface. To get rid of this, you need to move the telescope in the x direction with telescope positioner until you magnify the bull's eye and eventually lose it.

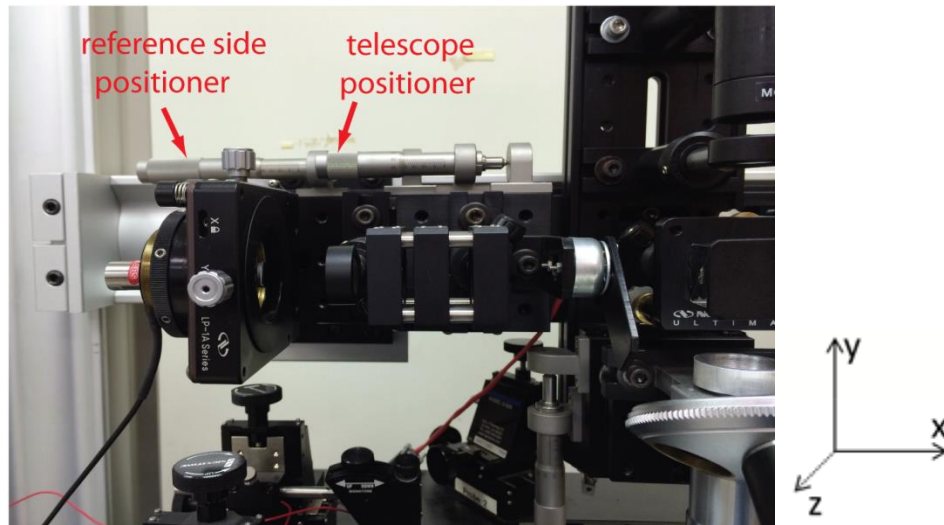


**Figure A24:** Reference side picture of the interferometer.

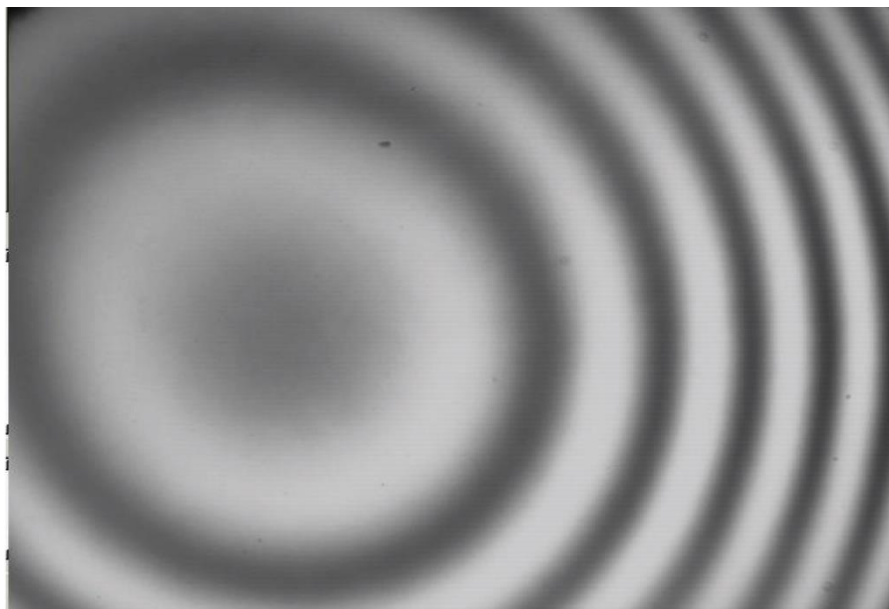


**Figure A25:** Bull's eye patterned fringes.

Note: Interferometer alignment has successfully been completed.

## Compensating Plates

Mismatch of the back focal planes of the reference and sample sides causes a bull's eye. To eliminate this distortion, we move the telescope in the x direction. However, it may not be sufficient for each objective on the sample side. For this reason, we add compensating plates (Fused Silica) as seen in Figure A26 according to which objective is being used in the system. Compensating plate locations are shown in Figure A27. Table A1 lists the combination of compensating plates according to used objective in the system.



**Figure A26:** Compensating plates.

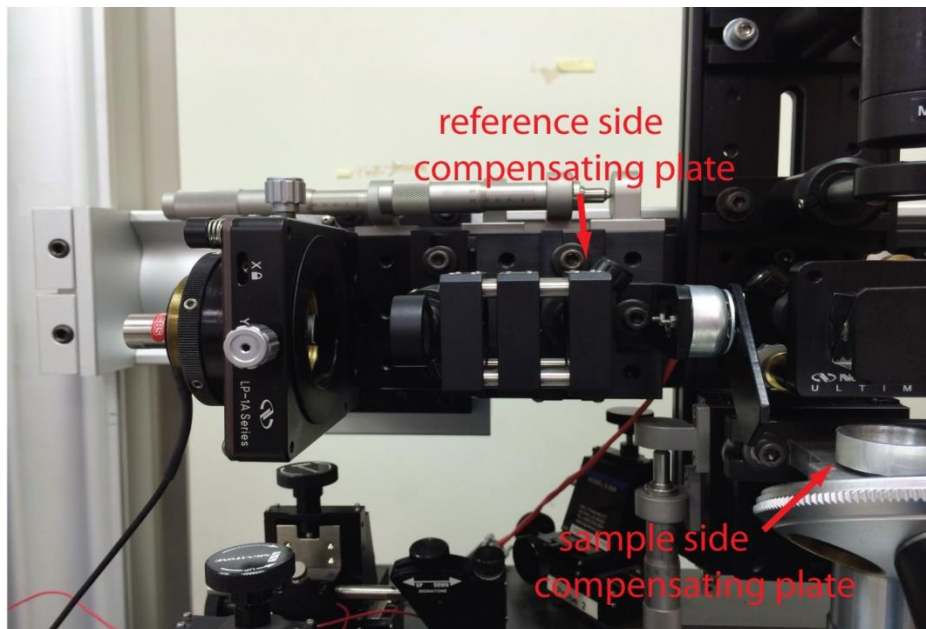


**Figure A27:** Compensating plate locations.

**Table A1:** Compensating plate selection to eliminate the bull's eye.

| Objective | Compensating Plate Side | Compensating Plate Thickness (mm) |
|-----------|-------------------------|-----------------------------------|
| 5X        | Sample Side             | 6.4                               |
| 10X       | Reference Side          | 6.4                               |
| 20X       | Reference Side          | 3.9                               |

## WinLens3D Basic

If you need to modify the system with new optic elements, you need to make sure that back focal planes of each side will match after the modification. The way to simulate it is to use a geometrical optics software. WinLens3D is a free software, and it is capable to handle simple simulations. Figure A28 shows the simulation schematic to see the component variation effect and x variation effect on the back focal plane.

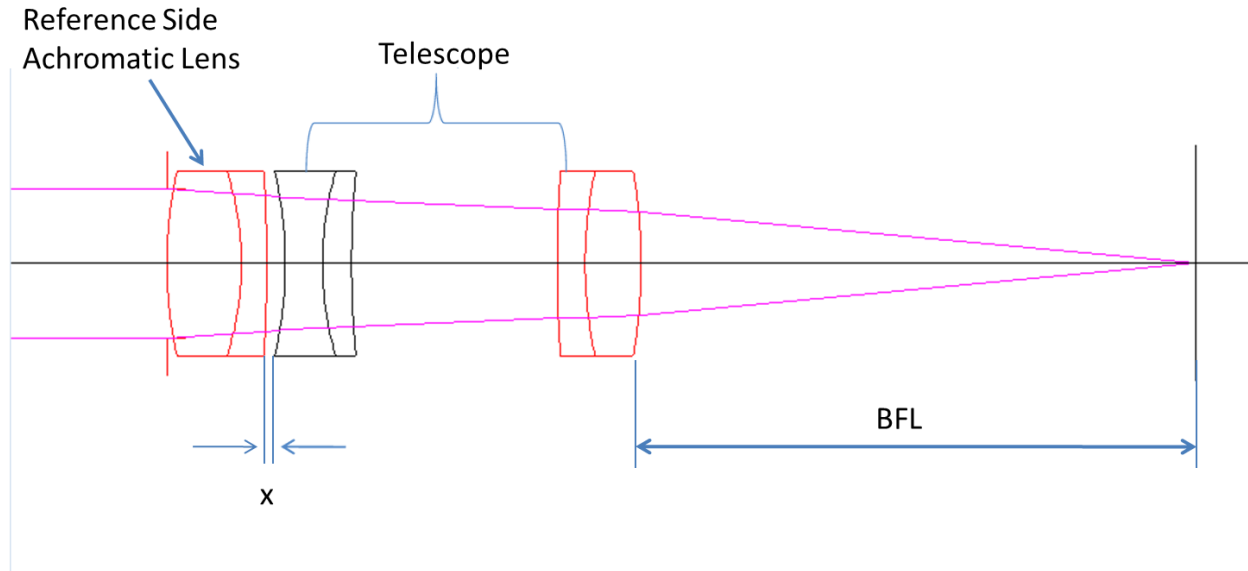


**Figure A28:** WinLens3D screenshot for a specific schematic.

## Final Adjustment Tips

1. When you finish aligning the system, you should have the intensity contrasts in the range of 100. If you don't have, make sure you have a good focus on both sides.
2. Make sure all the clamps holding the system is tight.
3. Make sure the iris images are focused.
4. Adjust the light intensity to obtain the maximum contrast.

## Incoherent Light Source LED Replacement Procedure

First the old LED needs to be removed from the case. Since, it is glued with epoxy, drilling machine is used to obtain the appropriate hole for the new LED. After obtaining a smooth surface, cathode and anode leads of LED are soldered. Anode lead is soldered through the plug's cable connector. Cathode lead is soldered through cable lug, and it is connected through a screw, which holds the metal plate of plug. Following to these steps, 5 min epoxy fills in the hole and LED is mounted in it. Until the glue gets stiffer, support on the back of LED is needed. After drying the epoxy, LED top face is polished with sand papers. Then, it is polished with micro-particles in materials science department laboratory to obtain a shining smooth surface.

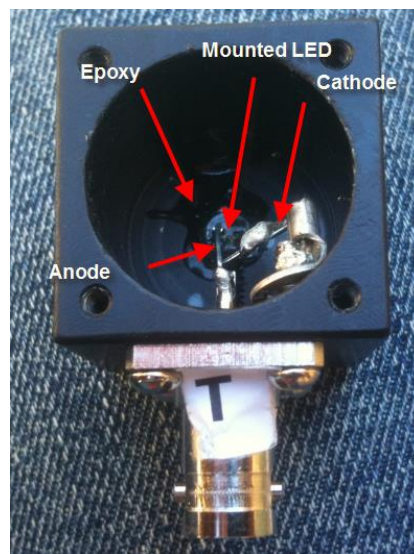


**Figure A29:** Image of replaced LED Light Source.

## Appendix B

### Contact Angle Goniometer

Custom made low cost contact angle goniometer set up is described in this section. The design and the assembly of the setup have been conducted first at University of Mexico by Khawar Abbas and Zayd Leseman. I reassembled the setup in CMU and verified the working conditions. Contact angle goniometer measures contact angle of a liquid droplet to predict the surface energy of the surfaces.

The components used in the set up listed in the table B1. The main body that holds the components is made out of aluminum as shown in Figure B1. Ball bearing linear stage is mounted to the bottom layer. Then, support post (SP3) is engaged to the stage. The camera front lens has been removed, and Fujinon lens is mounted to the camera. This camera is engaged to the support post standing on the linear stage. Post holder is mounted in front of the camera. Support post and tilting stage (precision platform optical mount) are assembled and were engaged to the post holder. Samples have been put on the tilting stage. A syringe is suspended at the top of the tilting stage to inject a liquid droplet during the experiment. Red LED light source is connected to the power source, and it is mounted to the metal frame as shown in the Figure B1.

**Table B1:** Components list

| Description  | Model     | Vendor        |
|--|-----------|---------------|
| Miniature Ball Bearing Linear Stage, 0.5 inch Travel                         | 411-05S   | Newport       |
| Translating Post Holder, 2 - 2.28 in., 0.5 in. Dia Post, 1/4-20              | VPT-2     | Newport       |
| Precision Platform Optical Mount, 1.76 x 1.76 in., 3 Locking Knob Adjustment | U200-P3K  | Newport       |
| Horizontal Adaptor, 2 inch, For U200-P                                       | UPA-PA2   | Newport       |
| Standard Post, 0.5 in. Diameter x 2 in., 8-32 & 1/4-20 Tapped Holes          | SP-2      | Newport       |
| Standard Post, 0.5 in. Diameter x 3 in., 8-32 & 1/4-20 Tapped Holes          | SP-3      | Newport       |
| Red, 0.315 Inch LED Spot Light   | NT62-817  | Edmund Optics |
| Variable Current, Single Output Basic Current Source                         | NT56-440  | Edmund Optics |
| C-mount extension tube 40mm  | NT54-631  | Edmund Optics |
| 1750LTN 500ul SYR(22/2"/3) (P# 81216 Hamilton)                               | 60376-672 | VWR           |
| FUJINON TV lens 1:1.8C-mount   |           | ebay          |
| Logitech quick cam pro 4000  |           | ebay          |

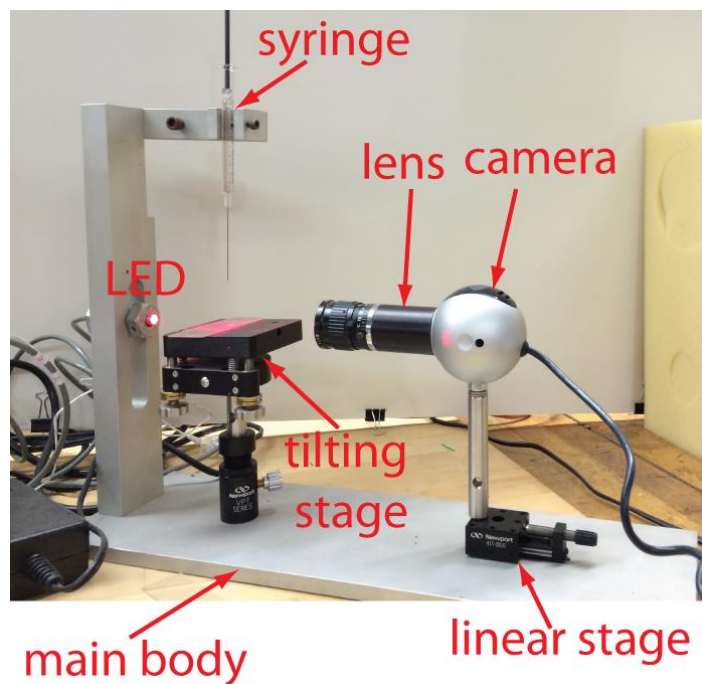


**Figure B1:** Picture of the contact angle goniometer set up.

During the measurement process, light source, sample, and camera should be on the same axis. To adjust this, we monitor the image of the camera. Light source from the backside of the sample forms a dark sample and droplet image on the screen. Focusing can be done through lens and linear stage.

After obtaining the sharp image, we open the CAM 100 (Contact Angle Meter) software. Red as seen in Figure B2 should be brought to the substrate level. Then, blue dashed rectangular should surround the droplet image as shown in Figure B3. When we click the “Rec”, CAM 100 calculates the contact angles as shown in Figure B4.

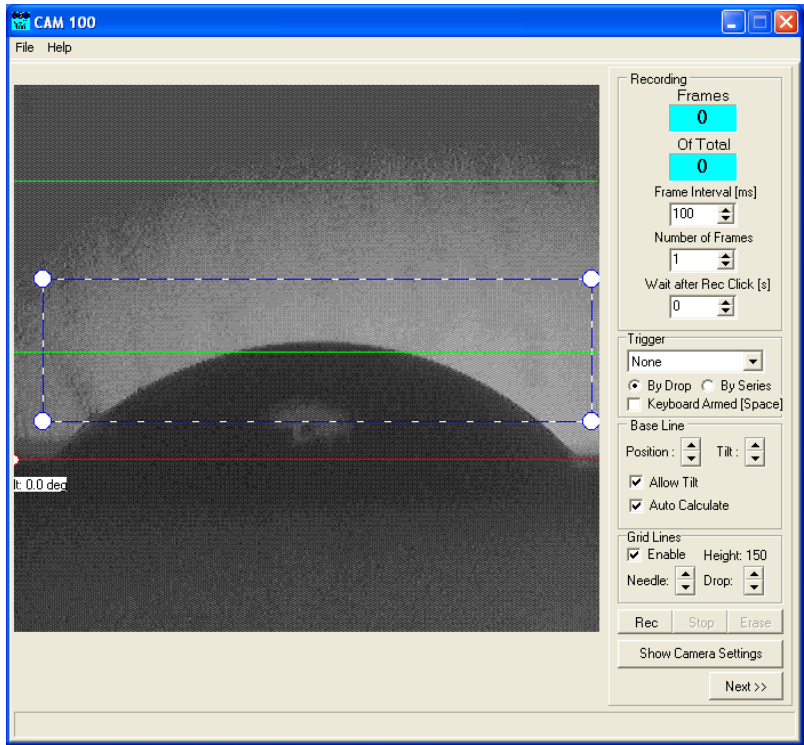


Figure B2: CAM 100 window. Red line is aligned with the substrate.

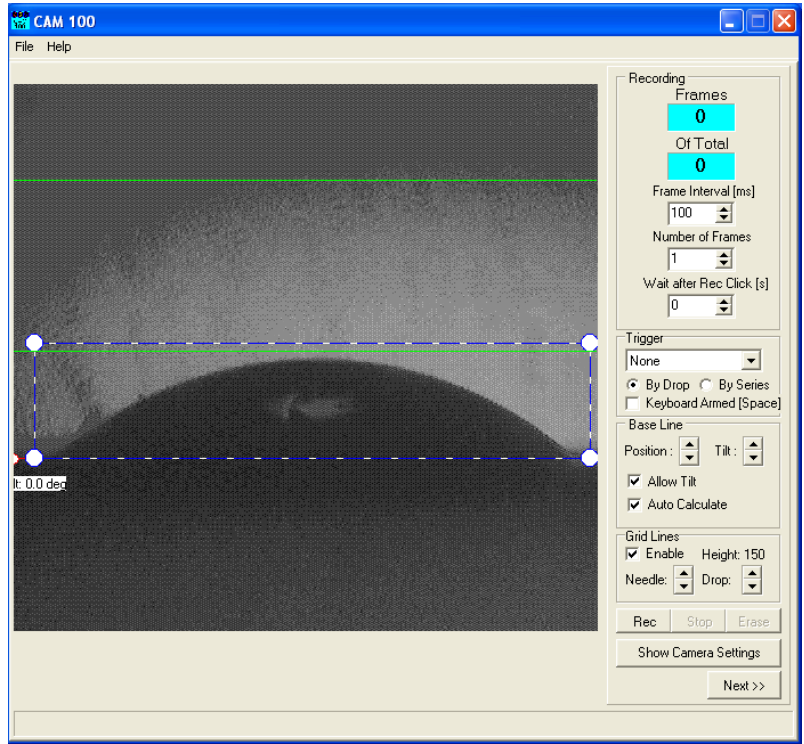
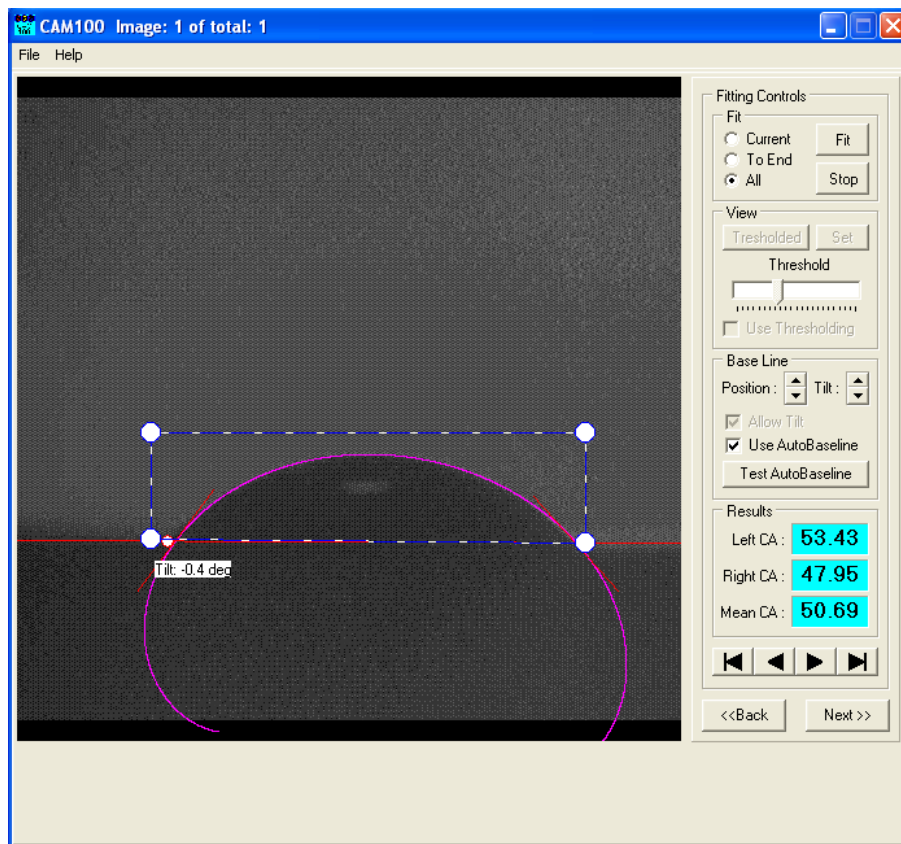


Figure B3: CAM 100 window. Blue rectangular is aligned according to the droplet.



**Figure B4:** CAM 100 window. Calculated contact angles: left CA=53.43, right CA=47.95 and mean CA=50.69.

## Appendix C

### Sample Releasing Procedure

#### HF Etch

- Put the samples into a glass beaker filled with acetone for 5 minutes.
- Transfer the samples to another glass beaker filled with isopropanol for 5 minutes.
- Then, transfer the sample into DI filled glass beaker for 5 minutes.
- Pick the samples after the wait, and dry the sample by either blowing air or vacuuming the excess water.
- Check the samples under objective microscope to inspect particle free conditions.
- Pick the samples with either Polytetrafluoroethylene (PTFE) or Chlorotrifluoroethylene (CTFE) tweezers, and immerse them into the 49% HF filled PTFE beaker.
- Wait for 1 hour.
- When wet etching process is finished, pick the samples with tweezers and soak into DI water for 5 minutes.
- Transfer the sample to the second DI rinse beaker, and rinse for another 5 mins.

#### RCA Cleaning

- Into 400ml PTFE beaker add 85 ml DI water.
- Add 30 ml of  $\text{NH}_4\text{OH}$  (27%).
- Bring the mixture up to  $75^\circ\text{C}$  ( $\pm 5^\circ\text{C}$ ) on a hot plate.
- Measure with a stainless steel thermometer to verify the solution temperature.
- Add 5 ml  $\text{H}_2\text{O}_2$  (30%).
- Solution will bubble vigorously after 1–2 minutes, indicating that it is ready for use.
- When the solution is at desired temperature, immerse the samples in the beaker using the PTFE or CTFE tweezers.
- Wait for 30 minutes. Once heated the solution is only effective for 30 minutes.
- When the clean is complete, transfer the sample to the first DI water glass beaker.
- Transfer the sample to the second DI rinse beaker, and rinse for another 5 minutes.
- Put all the tools that have been used during the process into DI water for 5 minutes
- To dispose of the RCA-1 solution, dilute with cold water. There should be no bubbles left in the solution.
- Drain the waste through the sink while the water flows through the tap. Let the water flow continue for a minute after the pouring the waste.

## **Critical Point Dryer**

- Put the sample into high purity isopropanol for 5 minutes. Then, repeat the same step for two more times.
- Leave the samples in the third beaker for an hour to dry any water in the solution.
- Sink the critical point dryer tools and 4 inch wafer holder into the isopropanol for 10 minutes.
- After this step, follow the instructions of the critical point dryer to proceed.

## **Appendix D**

### **Chilled Mirror Hygrometer Setup**

Chilled mirror hygrometer is a device that measures the dew point of the vapor flow. Dew point is the temperature that the moisture of the flow starts condensing. There is a correlation between a dew point and a vapor pressure. Thus, we can find the partial pressure of the flow.

The working principle of the device is described in here. The mirror surface is cooled down to condensate the vapor. There is a photo detector measures the reflected light from the mirror surface. When the intensity of the measured light drops due to the condensation, temperature is controlled at that level to keep the liquid film on the surface. This controlled temperature corresponds to dew point temperature.

Chilled mirror hygrometers are mainly used for reliable humidity measurements. However, any vapor can be cooled to its dew point temperature. Theoretically, any solution's partial pressure can be measured. From this thought, we tried Edgetech DewMaster Chilled Mirror Hygrometer in our system. Schematic of the system upgrade is shown in Figure D1. The lines are modified to sense both exit and entry lines when it is necessary. Figure D2 shows the pictures of the sensor.

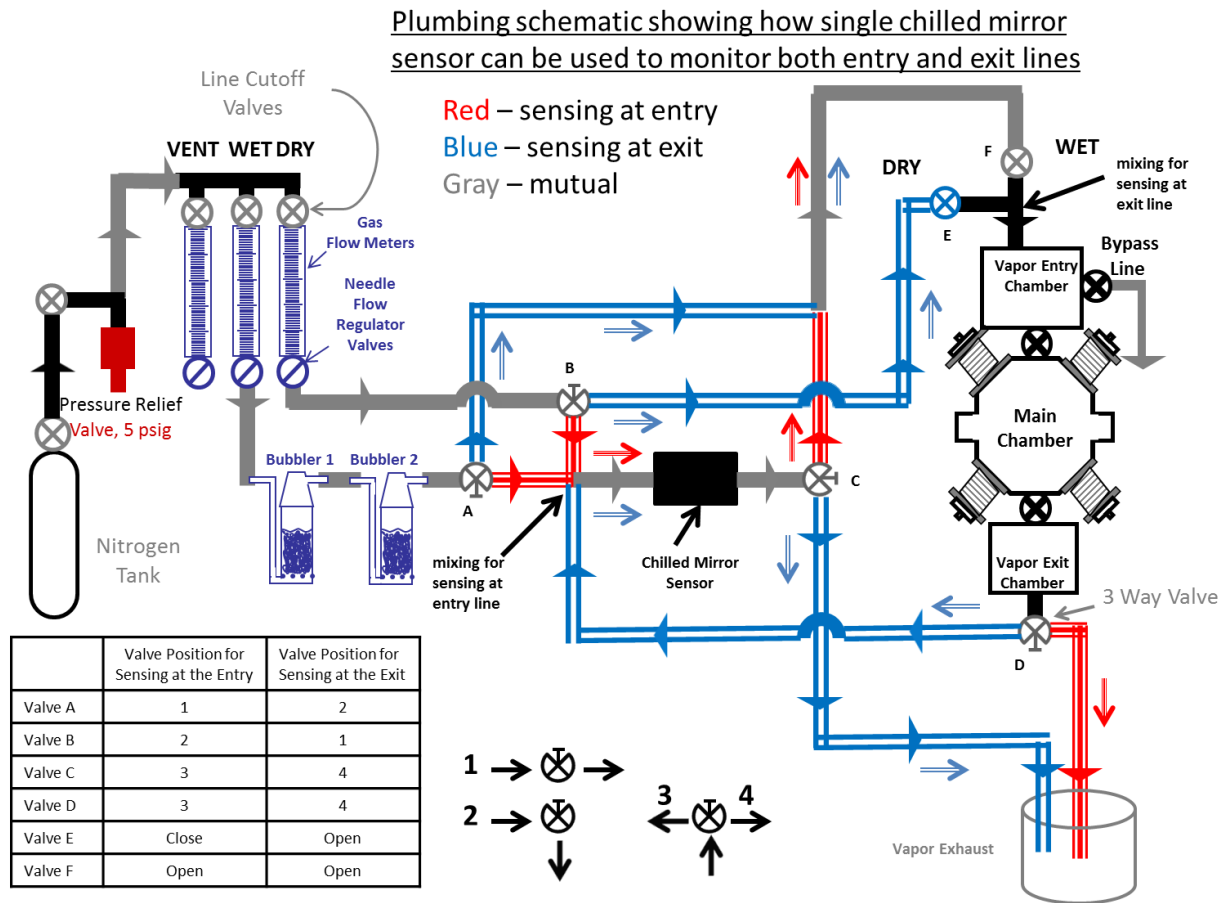


**Figure D1:** Flow line schematic after chilled mirror hygrometer adaptation.

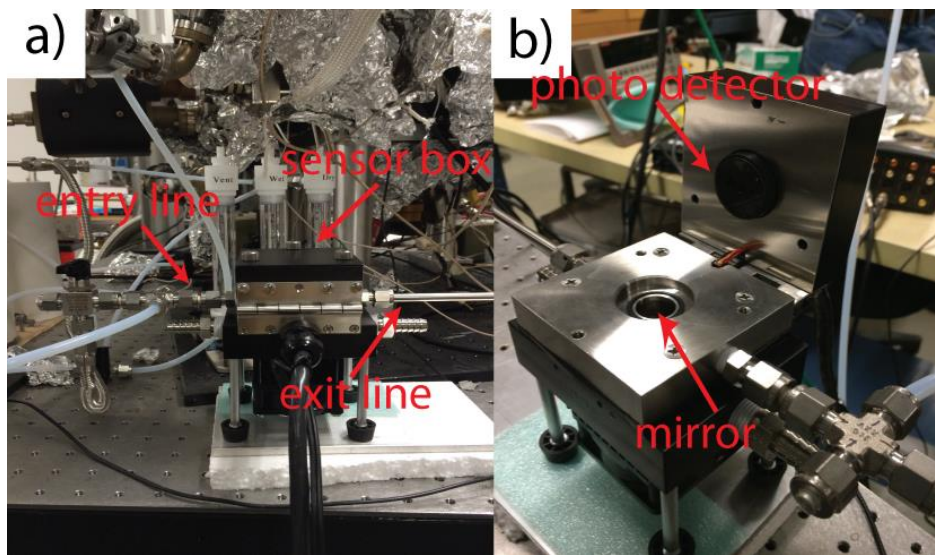


**Figure D2:** a) Sensor box image. b) Image of the sensor box interior.

The mirror surface of the sensor is made out of stainless steel, and it works well with water flows. However, it couldn't measure the dew points for alcohols. We investigated the possible reason. It measures the reflectivity change of the mirror surface. When water liquid forms on the stainless steel, it scatters the light. Since we are trying to form a different solution on the mirror surface, the scattering effect might not be as big as water. We measured contact angles of the water droplet and alcohols to understand if the formed liquid has similar geometry, which behaves as an optical lens. While we measure  $\sim 75^\circ$  for water, the contact angle too small to be measured for alcohols. Surface energy differences cause the poor system performance. Vendor tried to apply coatings to mirror surface to change the surface energies compatible for alcohol experiments. Although they worked for a few minutes, they eventually disposed.

In conclusion, a well understood surface treatment on the mirror or a different material mirror surface can give accurate partial pressure measurements for alcohol solutions.

## Appendix E

### Fixed-Fixed Beam with Single Point Load Deflection Derivation

Consider Figure E1 as a free body diagram of the  $s$ -shaped beam. Cantilever beam length  $L$  corresponds to the  $s$ . The post and the substrate are assumed to be rigid. Left-hand side of the cantilever end attaches to the support post, and right-hand side of the cantilever adheres to the substrate. Deflection of the beam is represented by  $w(x)$ , and the slope is the derivative of the deflection  $dw(x)/dx$ . Bending moment in the beam is

$$EI \frac{d^2w}{dx^2} = -R_A x + M_A \quad \text{for } (0 < x < a)$$

$$EI \frac{d^2w}{dx^2} = -R_A x + P(x - a) + M_A \quad \text{for } (a < x < L)$$
(E1)

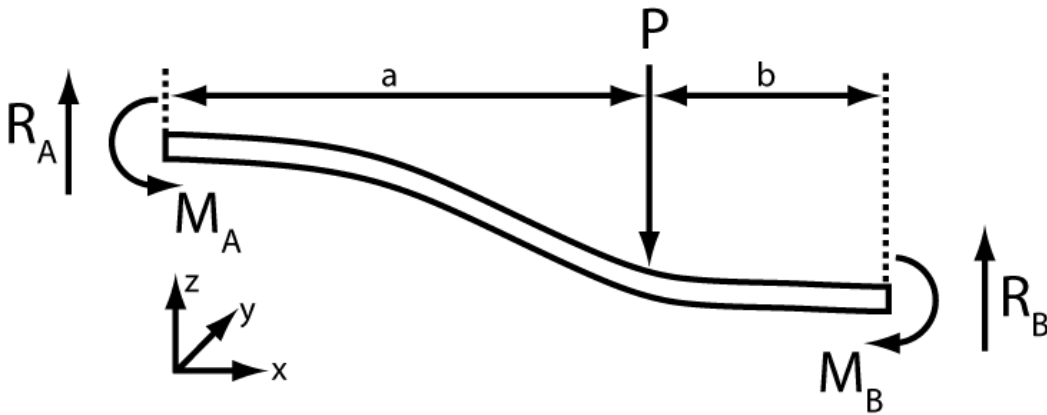


**Figure E1:** Free-body diagram for an  $s$ -shaped beam. The force and moment are provided by the support post on the left-hand side. On the right-hand side, the moment and the reaction force occur at the crack tip.

Integrating results with the beam slope equation

$$\begin{aligned}
 EI \frac{dw}{dx} &= -R_A \frac{x^2}{2} + M_A x + C_1 && \text{for } (0 < x < a) \\
 EI \frac{dw}{dx} &= -R_A \frac{x^2}{2} + \frac{P(x-a)^2}{2} + M_A x + C_1 && \text{for } (a < x < L)
 \end{aligned}
 \tag{E2}$$

One more integration gives the deflection equation

$$\begin{aligned}
 EI w &= -R_A \frac{x^3}{6} + M_A x^2 + C_1 x + C_2 && \text{for } (0 < x < a) \\
 EI w &= -R_A \frac{x^3}{6} + \frac{P(x-a)^3}{6} + M_A x^2 + C_1 x + C_2 && \text{for } (a < x < L)
 \end{aligned}
 \tag{E3}$$

$C_1$  and  $C_2$  are the unknown constants can be found through the boundary conditions. The boundary conditions are

$$\begin{aligned}
 w(0) &= h, \frac{dw(0)}{dx} = 0, \\
 w(L) &= 0, \text{ and } \frac{dw(L)}{dx} = 0.
 \end{aligned}
 \tag{E4}$$

Solving for the constants in terms of known quantities  $C_1 = 0$  and  $C_2 = Eih$ .

Equation E2 and equation E3 can be solved now because we have two equations with two unknowns,  $R_A$  and  $M_A$ . Therefore

$$R_A = -\frac{12Eih}{L^3} + P + \frac{2a^3P}{L^3} - \frac{3a^2P}{L^2},
 \tag{E5}$$

$$M_A = -\frac{6Eih}{L^2} + aP + \frac{a^3P}{L^2} - \frac{2a^2P}{L}.
 \tag{E6}$$

The deflection equation is then

$$\begin{aligned} w(x) &= \frac{1}{EI} \left( \frac{-R_A x^3}{6} + \frac{M_A x^2}{2} + EIh \right) && \text{for } (0 < x < a) \\ w(x) &= \frac{1}{EI} \left( \frac{-R_A x^3}{6} + \frac{P(x-a)^3}{6} + \frac{M_A x^2}{2} + EIh \right) && \text{for } (a < x < L) \end{aligned} \quad (E7)$$

## Appendix F

### Supporting Information

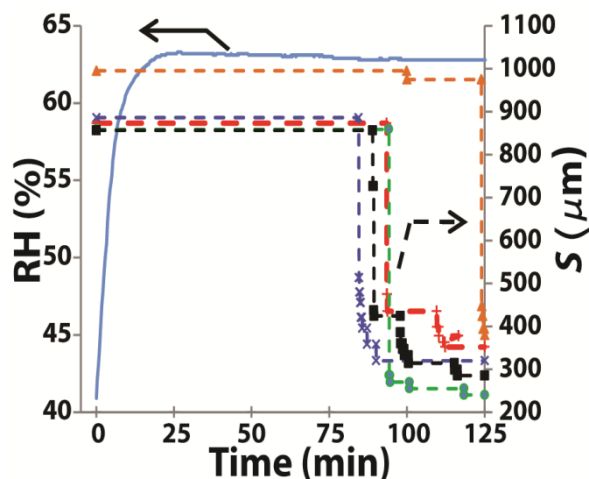


**Figure S1.** Crack length  $s$  versus time on five different cantilevers taken at 5 s intervals after increasing RH from 0 to 62%. The solid line indicates RH at the chamber entry, while dashed lines represent crack length  $s$  data for different individual microcantilevers. In this particular experimental trial, the exit line reached steady state at 27 min (not shown), and the environment temperature was 21°C, which is 3°C less than the conditions for the 1 min resolution experiments shown in the main text. These differences may explain the longer period before crack healing begins. In any case, the crack healing velocity is only calculated after previous healing had already been observed, as explained in the main text. The plot clearly shows that crack healing occurs in discrete steps.

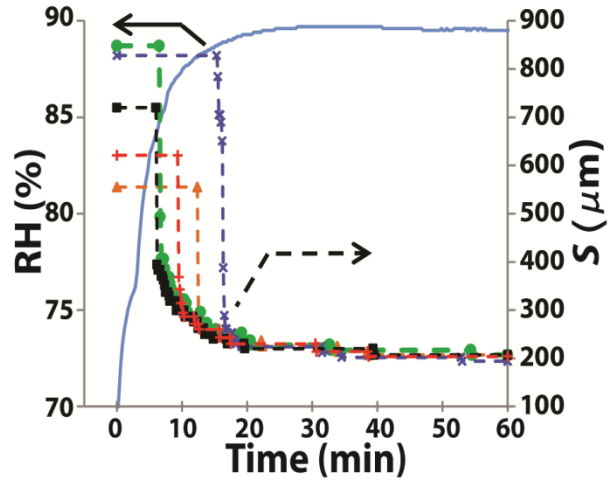


**Figure S2.** Crack length  $s$  versus time on five different cantilevers taken at 10 s intervals after increasing RH from 69 to 89.5%. The solid line indicates RH at the chamber entry, while dashed lines represent crack length  $s$  data for different individual microcantilevers. The plot again shows that crack healing occurs in discrete steps.

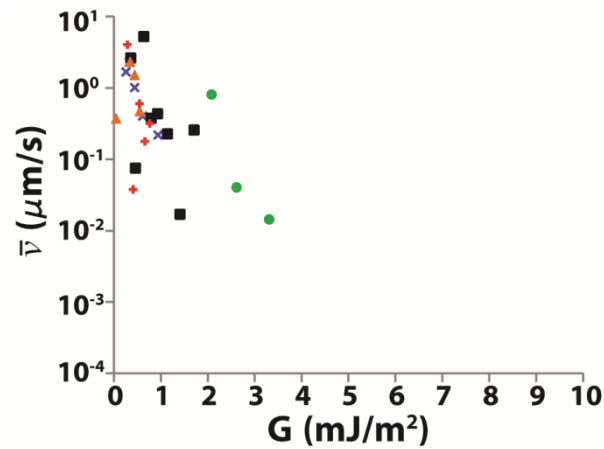


**Figure S3.** Average crack healing velocity  $\bar{v}$  as a function of energy release rate  $G$ . Different cantilever responses are plotted with colors and marker types corresponding to Figure S1. In this case, a non-zero  $\bar{v}$  extends out nearly to  $G=4$  mJ/m<sup>2</sup>, possibly indicating a smaller surface roughness.

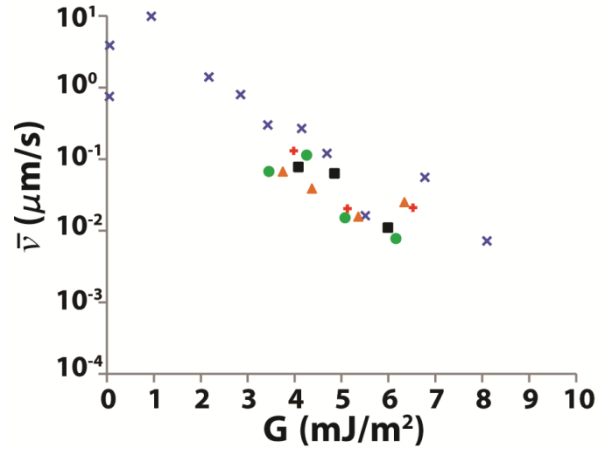


**Figure S4.** Average crack healing velocity  $\bar{v}$  as a function of energy release rate  $G$ . Different cantilever responses are plotted with colors and marker types corresponding to Figure S2.

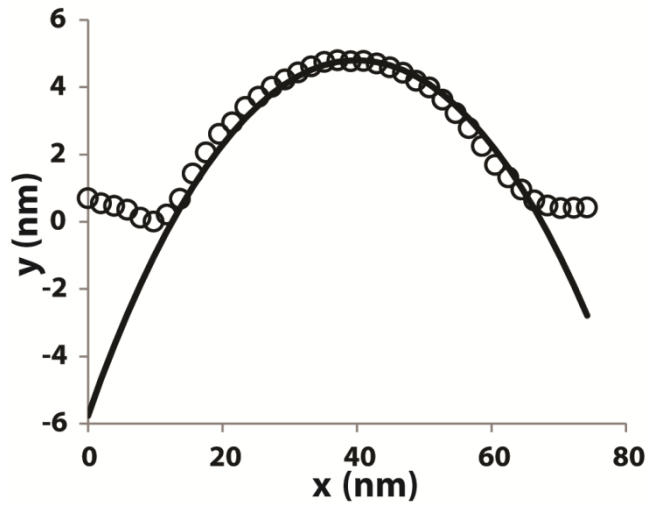


**Figure S5.** Circle data points represent the AFM topography data across the asperity. Solid line is a curve fit by using a circular arc shape assumption.  $R=81.3$  nm for this given data. As stated in the main text, the average value of  $R$  is 124 nm and the standard deviation is 43 nm.